

Department of Materials
University of Oxford

Radiation Damage and Transmutation in Tungsten-Alloys for Nuclear Fusion Applications

Matthew J. Lloyd

Supervised by: David E.J. Armstrong, Duc Nguyen–Manh,

Enrique Martinez, Paul A.J. Bagot and Michael P. Moody

This thesis is submitted for the degree of

Doctor of Philosophy

13th January 2021

for Emily

Dedicated to my Grandfather

William Edward Smith

1942-2020

Preface

The work presented in this thesis is submitted for the degree of doctor of philosophy. This was was carried out at the Department of Materials, University of Oxford between October 2016 and September 2020. All of the work presented is original and where the work of others has been included, it has been clearly labelled and the author acknowledged. No part of this thesis has been submitted for a degree at this, or any other university. This project has received funding from the European Union's Horizon 2020 research and innovation programme under grant agreement number 633053. The views expressed herein do not necessarily reflect those of the European Commission. This work is also supported by the UK Engineering and Physical Sciences Research Council [EP/N509711/1] and the Culham Centre for Fusion Energy, United Kingdom Atomic Energy Authority through an Industrial CASE scholarship, [Project Reference Number 1802461].

The following peer reviewed articles and conference presentations were made during the research period:

Publications

M. J. Lloyd, R. G. Abernethy, M. R. Gilbert, I. Griffiths, P. A. Bagot, D. Nguyen-Manh, M. P. Moody and D. E. J. Armstrong, 2019. Decoration of voids with rhenium and osmium transmutation products in neutron irradiated single crystal tungsten. Scripta Materialia, 173, pp.96-100.

M. J. Lloyd, R. G. Abernethy, D. E. J. Armstrong, P. A. Bagot, M. P. Moody, E. Martinez and D. Nguyen-Manh, 2019. Radiation-induced segregation in W-Re: from kinetic Monte Carlo simulations to atom probe tomography experiments. The European Physical Journal B, 92(10), p.241.

Conference Presentations

M. J. Lloyd, R. G. Abernethy, J. Haley, I. Griffiths, E. Martinez, P. A. Bagot, D. Nguyen-Manh, M. P. Moody and D. E. J. Armstrong, 2019. Nanoscale Characterisation of Re/Os Precipitation in Neutron Irradiated W, **The 19th International Conference on Fusion Reactor Materials, La Jolla, USA, 2019**

M. J. Lloyd, D. E. J. Armstrong, M. P. Moody, P. A. Bagot, E. Martinez and D. Nguyen-Manh, 2018. KMC and APT of Tungsten-Rhenium Alloys for Nuclear Fusion, **The 9th International Conference on Multiscale Materials Modelling, Osaka, Japan, 2018**

Acknowledgements

I am thankful for a great number of people who have directly or indirectly contributed to the work in this thesis. I am grateful for everyone that made this project possible, and that helped me in my work. Firstly, to my supervisors: David Armstrong, Michael Moody, Paul Bagot, Enrique Martinez and Duc Nguyen-Manh; thank you for your support and guidance over the past few years, and for giving me such excellent opportunities. This thesis would not have been possible without all of your help. I am also thankful for everyone in the MFFP, APT and Micromechanics groups with whom I have had many discussions about the different aspects of this work. I am thankful also to everyone at UKAEA and the MRF that made me feel welcome during my regular visits. I am extremely grateful also to everyone in the DCCEM and APT groups that have frequently supported my work with technical assistance and by troubleshooting problems; including Gareth Hughes, Graham Wyatt and Jenny Holter.

Many people from different institutions contributed to the work that is discussed in this thesis, and I am grateful to all of them for their contributions. Thanks to Jack Haley, Ian Griffiths and Andy London for carrying out the TEM/STEM experiments that I have discussed, and to Hazel Gardener for carrying out APT experiments on my behalf when the Covid-19 pandemic prevented me from accessing the lab. I am very grateful to Robbie Abernethy, not only for helping with the FIB preparation, but also for providing the neutron irradiated samples which formed the main focus of this work. Thanks also to Mark Gilbert for running FISPACT simulations for the neutron irradiated samples and to Osman El-Atwani for helping with the ion irradiation experiments.

Thank you to Enrique, Romain, Diana, Anna, and the many others who made me feel welcome during my visits to Los Alamos. I am grateful to those at LANL that contributed to this work, but also for those that made my time in the US such an enjoyable and memorable experience. The same goes for everyone I met during my collaboration with Rolls-Royce in Singapore. Everyone in the Failure Analysis laboratory and the Repair Technology teams made me feel very welcome and I thoroughly enjoyed my time there. Thanks to Kei Lin Chin, Yanan Wang, Iulian Marinescu and Anna Tai to name just a few. Thanks as well to everyone in the corner office, and my housemates from Copse Lane for making the past four years such an enjoyable experience.

To my family and friends, including those who are sadly no longer with us, thank you for your constant support and encouragement during my DPhil studies and during my time as an undergraduate. To my parents in particular, thank your for all of your help and for always encouraging me to pursue my studies - I would not be in the position I am today without you. Thanks also to Beccie and Morgan for giving us a welcome break from our studies. Finally to Emily, thank you for your constant love and support, and for always inspiring me to have confidence in myself.

List of Abbreviations

AKMC	Atomistic Kinetic Monte Carlo
APT	Atom Probe Tomography
ASDEX	Axially Symmetric Divertor Experiment
ASTM	American Society for Testing and Materials
BCA	Binary Collision Approximation
bcc	Body Centred Cubic
CALPHAD	Computer Coupling of Phase Diagrams and Thermochemistry
CVD	Chemical Vapour Deposition
DBTT	Ductile to Brittle Transition Temperature
DEMO	DEMOnstration Fusion Power Station
DFT	Density Functional Theory
DONES	DEMO Oriented NEutron Source
DT	Deuterium-Tritium Fusion
EBR-II	Experimental Breeder Reactor II
EELS	Electron Energy-Loss Spectroscopy
EDX	Energy Dispersive X-Ray
ENDF	Evaluated Nuclear Data File
EU	European Union
EXTREMAT	New Materials for Extreme Environments
FEI	Field Electron and Ion company
FEM	Finite Element Modelling
FIB	focussed Ion Beam
FIM	Field Ion Microscopy
FW	First Wall
GB	Grain Boundary
GIF	Gatan Imaging Filter
HAADF	High Angle Annular Dark Field
hcp	Hexagonal Close Packed
HFIR	High Flux Isotope Reactor
HFR	High Flux Reactor
IFMIF	International Fusion Materials Irradiation Facility
ITER	International Thermonuclear Experimental Reactor
IVAS	Integrated Visualization and Analysis
JANNuS	Joint Accelerators for Nanosciences and NUclear Simulation
JET	Joint European Torus
JMTR	Japan Materials Test Reactor
KMC	Kinetic Monte Carlo
LANL	Los Alamos National Laboratory
LEAP	Local Electrode Atom Probe
LOCA	Loss of Coolant Accident
LOVA	Loss of Vacuum Accident
MC	Monte Carlo
MCF	Magnetic Confinement Fusion
MD	Molecular Dynamics
MI	Mixed Interstitial Atom
MMC	Metropolis Monte Carlo
MRF	Materials Research Facility
NIST	National Institute of Science and Technology
NN	Nearest Neighbours
NRT	Norgett, Torrens and Robinsion Model
OKMC	Object Kinetic Monte Carlo
PFC	Plasma Facing Component
PHENIX	PFC evaluation by tritium Plasma, HEat, and Neutron Irradiation eXperiments
PKA	Primary Knock-on Atom
PWR	Pressurised Water Reactor
RED	Radiation Enhanced Diffusion
rfKMC	Rejection-Free Kinetic Monte Carlo
RID	Radiation Induced Segregation
ROI	Region Of Interest
RT	Room Temperature
RTA	Residence Time Algorithm
SEM	Scanning Electron Microscopy
SGMC	Semi-Grand Canonical Monte Carlo
SIA	Self-Interstitial Atom
SIBC	Surrey Ion Beam Centre
SME	Small-to-Medium sized Enterprise
SNL	Sandia National Laboratory
SPPARKS	Stochastic Parallel PARticle Kinetic Simulator
SRIM	Stopping Range of Ions in Matter
STEM	Scanning Transmission Electron Microscopy
TEM	Transmission Electron Microscopy
TENDL	TALYS Evaluated Nuclear Data Library
TKD	Transmission Kikuchi Diffraction
TST	Harmonic Transition State Theory
UKAEA	United Kingdom Atomic Energy Authority

Contents

1 Introduction **11**
- 1.1 Neutron Physics . . . 13
  - 1.1.1 Nuclear Fission and Fusion . . . 13
  - 1.1.2 Reaction Cross Sections . . . 15
  - 1.1.3 Neutron Capture and Moderation . . . 16
  - 1.1.4 Transmutation . . . 17
- 1.2 Fusion Energy . . . 19
  - 1.2.1 Choice of Fuel . . . 19
  - 1.2.2 Reactor Design . . . 21
  - 1.2.3 DEMO Plasma Facing Components . . . 23
- 1.3 Radiation Damage in Materials . . . 24
  - 1.3.1 The Collision Cascade . . . 24
  - 1.3.2 Stopping Power . . . 26
  - 1.3.3 Displacements per Atom . . . 28
  - 1.3.4 Physical Effects of Radiation Damage . . . 29
- 1.4 Engineering Challenges to Fusion Energy . . . 30
  - 1.4.1 Development of Plasma Facing Materials . . . 30
  - 1.4.2 Nuclear Waste and Reactor Safety . . . 32
  - 1.4.3 Fusion Neutron Sources . . . 34
- 1.5 Surrogates for Fusion Neutron Damage . . . 34
  - 1.5.1 Fission Neutrons . . . 35
  - 1.5.2 Heavy-Ion Irradiation . . . 36
  - 1.5.3 Proton Irradiation . . . 38
- 1.6 Summary . . . 39

2 Tungsten for Nuclear Fusion **41**
- 2.1 Physical Properties of Pure Tungsten . . . 41
- 2.2 Microstructural Evolution under Irradiation . . . 42
  - 2.2.1 Transmutation in Tungsten . . . 42
  - 2.2.2 Experimental Studies of Transmutation in W . . . 46
  - 2.2.3 Physical Properties of Pure Re, Os and Ta . . . 47
  - 2.2.4 Equilibrium W-(Re,Os,Ta) Phase Diagrams . . . 49
  - 2.2.5 Physical Properties of W-Re and W-Os . . . 54
  - 2.2.6 Neutron Induced Microstructural Evolution . . . 55
  - 2.2.7 Voids in APT . . . 65
  - 2.2.8 Ion Induced Microstructural Evolution . . . 67
  - 2.2.9 Summary of Irradiated Microstructures . . . 71
- 2.3 Modelling Microstructural Evolution in W . . . 72
  - 2.3.1 Defects in Pure W . . . 73
  - 2.3.2 Defects in W-(Re,Os) . . . 74
  - 2.3.3 Kinetic Studies of Radiation Damage in W . . . 76

2.4 Properties after Irradiation . . . 79
2.4.1 Irradiation Hardening . . . 79
2.4.2 Proton Irradiation . . . 84
2.4.3 Brittle to Ductile Transition . . . 86
2.4.4 Thermal Diffusivity . . . 87
2.4.5 Oxidation . . . 88
2.4.6 He/H Plasma Exposure . . . 90
2.4.7 Improving W Properties through Design . . . 91
2.5 Research Objectives . . . 92
2.5.1 Experimental Characterisation of Ion and Neutron Irradiated W . . . 92
2.5.2 Computational Study of Anomalous Re and Os Precipitation . . . 93

I Experimental Investigation 94

3 Neutron Irradiation 95
3.1 Irradiation . . . 95
3.1.1 Pre-Irradiation Sample Preparation . . . 95
3.1.2 High Flux Reactor . . . 96
3.1.3 Damage and Transmutation Quantification . . . 97
3.2 Post-Irradiation Sample Preparation . . . 98
3.2.1 FIB Lift-out Procedure . . . 98
3.2.2 Targeted Grain Boundary Sample Preparation . . . 99
3.3 Atom Probe Tomography . . . 100
3.3.1 Experimental Setup . . . 100
3.3.2 Mass Spectrum Analysis . . . 101
3.3.3 Validation of FISPACT-II . . . 106
3.4 Precipitation of Re and Os . . . 109
3.4.1 Single Crystal . . . 110
3.4.2 Polycrystalline . . . 110
3.4.3 Cluster Composition Analysis from APT . . . 114
3.4.4 Grain Boundary Decoration . . . 121
3.4.5 Dislocation Decoration . . . 124
3.5 Voids . . . 126
3.5.1 Density Artefacts in APT . . . 128
3.5.2 STEM Imaging of Single Crystal Sample . . . 130
3.5.3 STEM Imaging of Polycrystalline Sample . . . 133
3.6 Correlative TEM/APT . . . 136
3.7 Summary of Neutron Irradiation . . . 137

4 Ion Irradiation 143
4.1 Sample Production . . . 143
4.1.1 Simulated Transmutation Samples . . . 144
4.1.2 Other Samples used in this Study . . . 147
4.2 Ion Irradiation . . . 147

4.2.1 Procedure for Estimating Damage Profile 147
4.2.2 Sandia National Laboratory 148
4.2.3 JANNuS, Saclay 150
4.2.4 Surrey Ion Beam Centre 151
4.2.5 Comparison of Depth Profiles 151
4.3 APT Sample Preparation 155
4.3.1 FIB Lift-Out 155
4.3.2 APT Analysis Parameters and Reconstruction 156
4.4 Re and Os Clustering 157
4.4.1 Solute Clustering in Concentrated Alloy 157
4.4.2 Solute Clustering in Dilute Binary and Ternary Alloys 158
4.4.3 Grain Boundary Decoration 162
4.4.4 Thermal Stability of Re Clusters 163
4.4.5 Void Formation in Dilute Alloys 167
4.5 Comparison to Neutron Irradiation 169
4.5.1 Mass Spectrum Analysis 170
4.5.2 Precipitate Structure 172
4.5.3 Cluster Composition Comparison 175

Summary of Experiments **185**

II Computational Investigation 187

5 Introduction to Modelling **188**
5.1 Outstanding Questions and Modelling 188
5.2 Atomistic Monte Carlo 191
5.3 Pair Interaction Energy Model 193
5.4 SPPARKS Implementation 195
5.4.1 Metropolis Monte Carlo 196
5.4.2 Semi-Grand Canonical Algorithm 197
5.4.3 Canonical Algorithm 198
5.4.4 Kinetic Monte Carlo 199
5.4.5 Vacancy Migration 199
5.4.6 Interstitial Migration 200
5.4.7 Instantaneous Process and Deposition 203
5.4.8 Summary 204

6 W-Re-Os-Vac Energy Model **206**
6.1 Outline of Fitting Methodology 206
6.2 Fitting Interatomic Interactions 209
6.2.1 Atom-Atom Interactions 209
6.2.2 Cross Atom-Atom Interactions 210
6.3 Fitting Defective Interactions 212
6.3.1 Atom-Vacancy Interactions 212
6.4 Evaluating Fit Accuracy 217
6.5 Binding Energies 220

6.5.1 Calculation of Binding Energy . . . 220
6.5.2 Vacancy Clusters . . . 221
6.5.3 Vacancy Solute Clusters . . . 223
6.6 Phase Analysis . . . 226
6.6.1 W-(Re/Os) . . . 226
6.6.2 W-Vacancy . . . 228
6.7 Void Nucleation . . . 232
6.8 Summary . . . 233

7 Radiation Damage Simulations 235
7.1 Simulations of Binary W-Re . . . 235
7.1.1 SGMC Simulations of W-Re . . . 235
7.1.2 Kinetic Monte Carlo . . . 238
7.1.3 Calculation of Diffusion Coefficients . . . 238
7.1.4 Precipitation in W-Re . . . 242
7.1.5 Grain Boundary Decoration in W-Re . . . 247
7.1.6 Effect of Re Pre-Alloying on Precipitation . . . 250
7.1.7 Summary of W-Re Study . . . 253
7.2 Simulations of Ternary W-Re-Os . . . 253
7.2.1 Metropolis Simulations of W-Vac . . . 253
7.2.2 Canonical Simulations of Void Decoration . . . 256

Summary of Simulations 261

III Epilogue 263

8 Conclusions 264
8.1 Tungsten and Nuclear Fusion . . . 264
8.2 Effect of Neutron Irradiation on W . . . 265
8.3 Simulated Neutron Irradiation with Ions . . . 267
8.4 Computational Modelling of Tungsten . . . 268
8.5 Future Work . . . 269

Appendices 308

A Huang Energy Model 309

B W-Re-Os-Vac Energy Model 310

C FISPACT-II HFR Data 311

D APT Experimental Data 314

E ACI Alloy Samples 315
E.1 Chemical Analysis of Pure-W . . . 315
E.2 Chemical Analysis of W-1.4Re-0.1Os . . . 316

Abstract

In this work, the effect of neutron-induced radiation damage and transmutation on the microstructure of W is investigated. Samples irradiated in the High Flux Reactor to a dose of 1.67 dpa at 1173 K were characterised using a combination of atom probe tomography and electron microscopy based techniques. Characterisation showed a microstructure dominated by voids and precipitates rich in Re and Os atoms produced via transmutation. Voids were shown to be decorated with Re and Os. Samples with equivalent Re and Os concentrations were produced via arc melting by ACI alloys, and heavy-ion irradiated at Sandia National Laboratory, USA, to a peak dose of 1.7 dpa at 1173 K. Characterisation using APT and TEM was used to highlight key differences in the microstructure produced by ion and neutron irradiation, including a smaller average void size and weaker precipitate formation. The clusters observed under ion irradiation were smaller, more diffuse and consisted primarily of Os, with slight enrichment of Re measured using cluster analysis techniques. The clusters in the neutron irradiated material on the other hand were dense and comprised mainly of Re, but with a central Os rich core. Cluster analysis methods showed cluster compositions comparable to samples from the Joyo reactor, however, line profile analysis suggested that some of the clusters had a composition consistent with σ phase in the centre. Kinetic Monte Carlo simulations of W-Re showed that transport of Re to point defect sinks occurred via mixed interstitial defects. A new energy model including Os was developed in which more accurate vacancy interactions were modelled by introducing local vacancy concentration dependant interactions. Analysis of the binding energies showed that Re and Os bind strongly to vacancies, and that Os had the strongest binding. The new model was used to simulate the formation of voids in W under irradiation and forms the basis for further study of the phenomena observed experimentally in this thesis.

1 Introduction

The way the world generates its electricity is changing as countries struggle to reduce their greenhouse gas emissions. This combined with an increasing awareness of the negative impacts of air pollution on human health [1], is driving an acceleration in the rate of fossil fuel phase-out in post-industrial economies. Increased renewable production has already had an impact in the European Union, and is responsible for a 10% reduction in fossil fuel use between 2005 and 2015, and a saving of 447 Mt CO_2 [2]. Nuclear power plants have low life-cycle greenhouse gas emissions and can be used to offset some of the challenges associated with further large scale renewable deployment such as variable supply.

The benefits of nuclear power led to the prediction of a *Nuclear Renaissance* in Europe and North America in the early 2000s [3, 4], with widespread expansion of nuclear capacity envisaged. Instead, a rise in fracking, financial risks, negative public perception and the effects of the Fukushima Daiichi nuclear disaster in 2011 have led to a stagnation in new projects and a predicted decline in market share from around 10% in 2018 to 2-5% in 2050 [4, 5]. Some countries such as Germany went as far as to begin a phase out of nuclear by 2022, a decision which has implications for reducing emissions and preventing air pollution related deaths [6].

Nuclear fusion has been explored for decades as an alternative to nuclear

fission and has a number of clear advantages. Fusion does not produce long-lived radioactive waste, there is no possibility of a runaway chain reaction and subsequent meltdown and there are reduced proliferation risks. Ongoing public perception problems and the economic risks of fission, combined with a shift in emphasis to position fusion as a low-carbon energy source have led to increased interest in the development of fusion in recent decades. The UK in particular is aggressively pursuing fusion, and aims to build a commercially viable fusion power plant by 2040 [7, 8]. However, some have questioned the effectiveness of fusion energy as a means of reducing greenhouse gas emissions in the short-term [9]

In addition to large international collaborations, there are a growing number of privately funded small to medium sized enterprises (SMEs) which aim to accelerate the development of fusion energy. Smaller compact devices are lower cost, lower risk alternatives that could benefit from the economies of scale arguments that are applied to small modular reactors, if they can first be demonstrated [10]. However, there a number of critical engineering problems that need to be overcome if nuclear fusion is to be used to generate electricity.

One of the key problem areas is the development of novel material solutions to withstand extreme operating environments. This project focusses on tungsten (W), one of the candidate materials for the plasma facing components (PFCs) which are expected to receive the most intense temperature and neutron loading. The combined effects of high temperatures, radiation

damage and transmutation are explored in order to improve our understanding of how the physical properties of W will change over time in a reactor. In the first chapter, the concepts of radiation damage in materials and the challenges of studying materials for fusion are outlined. The second chapter will discuss W in more detail and outline the research that has gone into its development as a material for fusion.

1.1 Neutron Physics

Neutrons are small, electrically neutral particles that along with protons make up the nucleus of atoms. They are produced in both fission and fusion reactors and are one of the key contributors to in-service material degradation. Differences in the damage produced by fission and fusion neutrons make the simulation of fusion conditions challenging.

1.1.1 *Nuclear Fission and Fusion*

In a fission reaction, heavier nuclei are split into lighter fragments, whereas in nuclear fusion, two light nuclei are joined together. In both cases, energy is released due to a difference in the nuclear binding energy between the initial and final nuclei [11, 12]. Nuclear fission first began to be understood in the early 1900s, and eventually led to the development of atomic weapons, followed by nuclear power stations.

In a nuclear reactor, fission is sustained through a chain reaction of neutron absorption and emission. The chain reaction arises from the fact that the splitting of the fuel atom leads to the release of several neutrons, which

can go on to generate further fission events. Control in a reactor is achieved by removing neutrons (using control rods which are strong absorbers of neutrons) or by moderation which increases their absorption probability in the fuel. When the reactor is shut down, the control rods are inserted and the chain reaction stops. The decay of unstable atoms in the fuel continues to produce heat for a long time after this occurs, in most cases requiring active cooling to prevent overheating [11].

More powerful nuclear weapons developed during the cold war, utilised a conventional fission explosion to ignite a fusion reaction in a small pellet containing a mixture of deuterium (^{2}H or ^{2}D) and tritium (^{3}H or ^{3}T), two isotopes of hydrogen. It is this process of fusion, made possible in hydrogen bombs by the intense pressure and temperature created by the initial fission explosion, that has been explored for over 50 years as a means of producing heat to generate electricity. Achieving sustained nuclear fusion relies on providing the nuclei in the fuel with sufficient energy that they can overcome the repulsive forces between them, and as such there is no nuclear-chain reaction and therefore no risk of a runaway reaction, as is the case in fission. The challenge of fusion is creating and sustaining these extreme conditions, within a vessel that can also withstand them. While the control of neutrons is not necessary for sustaining the reaction, as is the case in fission, neutrons produced in fusion reactions are a primary source of degradation in the vessel materials.

1.1.2 *Reaction Cross Sections*

Nuclear processes including neutron absorption and nuclear fusion are typically discussed in terms of their *Reaction Cross Section,* σ, which is a measure of the relative probability for a reaction to occur. For a beam of particles incident on a detector, of current, I particles per unit time, the reaction cross section, σ is given by equation 1.1, where R is the reaction rate and N is the number of target nuclei per unit area [11]. The total cross section for a reaction can be expressed as the sum of these individual reaction cross sections, each of which is dependant on incident neutron energy and temperature.

$$\sigma = \frac{R}{IN} \tag{1.1}$$

The units of σ is area[1] per nuclide but it includes all of the different possible interactions with the incident beam, not just the area presented to it.

To illustrate the effects of temperature and incident neutron energy on σ, the cross section, σ_f for the neutron induced fission (n,f)[2], of a ^{235}U nucleus, as a function of the incident neutron energy, is plotted in figure 1.1b, as well as the absorption cross section for neutron interacting with ^{186}W [13, 14]. There is generally a linear dependence between the log of the incident neutron energy and the log of σ_f, with lower incidence energy

[1] This is typically expressed in units of barns (b), where 1b=10^{-28} m^2

[2] where nuclear reactions are written in the form of shortened notation, A(b,c)D refers to the reaction in which A+b→c+D

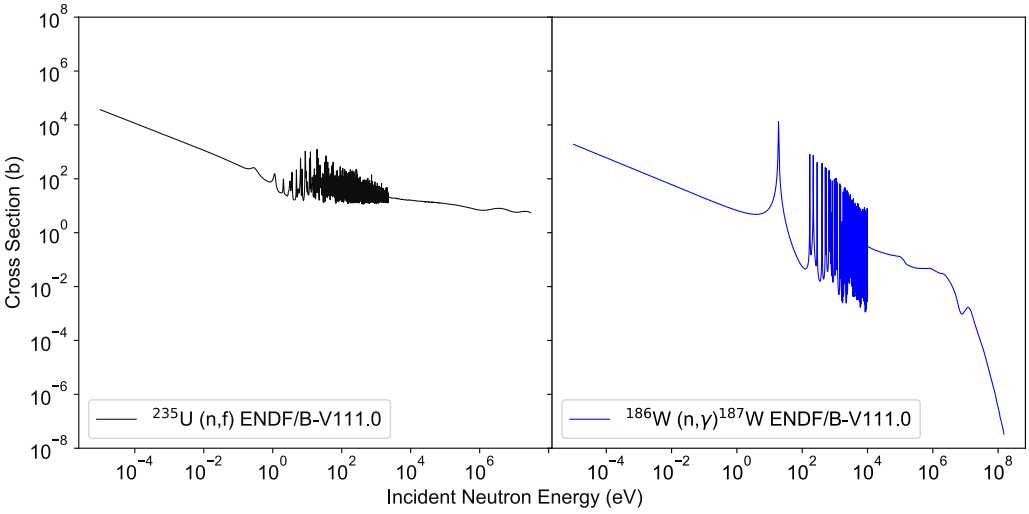


Figure 1.1: Neutron induced fission, and neutron absorption reaction cross sections for (a)^{235}U and (b)^{186}W targets respectively as a function of incident neutron energy. Plotted using data obtained from the Nuclear Energy Agency, Java-based Nuclear Data Information System (JANIS) [13]. Data plotted is taken from the Evaluated Nuclear Data File (ENDF) version B-V111.0 [14].

corresponding to an increase in σ_f. Large peaks in the central region of the plot are known as resonances, and are a result of the nuclear structure of the target. Increasing temperature results in an increase in the width of these resonance peaks due to a process called Doppler Broadening [11]. The effect of a large resonance in the cross section over a defined energy range leads to a reduction in the neutron population in the energies near to the resonance [15].

1.1.3 *Neutron Capture and Moderation*

Neutron capture reactions occurs when a nucleus absorbs a neutron, and releases energy via γ emission, in an (n,γ) reaction. This produces a different isotope of the original material. The decaying nucleus recoils as this emission occurs, with an energy that in some cases is sufficient to displace

the atom [16]. A neutron loss reaction refers to the case in which capture of the neutron leads to emission of a greater number of neutrons such as (n,2n) or (n,3n) [16, 17]. As with the (n,f) cross section discussed in section 1.1.2, the cross section or neutron capture depends strongly on the incident neutron energy and resonances can be broadened with an increased target temperature. To illustrate this the neutron absorption cross section for ^{186}W is plotted in figure 1.1.

Neutron moderation is the reduction in neutron energy through interaction with a moderating material. Moderation of neutrons is an effect used in a fission plant to increase reactivity, but in a fusion plant in which the neutrons are not used to induce the reaction, moderation can be a undesirable effect, leading to increased rates of transmutation and reducing the overall population of neutrons needed to produce tritium.[3]

1.1.4 *Transmutation*

Transmutation occurs in a reactor component through a series of neutron capture or neutron loss events, followed by subsequent decay of unstable isotopes of the original material [18, 19]. Neutron absorption or loss produce new isotopes of the original material. If these new isotopes are unstable, then they can undergo a decay process which can be grouped into those which result in light products (such as H and He) and those which result in a change of the material composition, through the production of heavy

[3] Tritium is produced by neutron absorption in Lithium, via the ${}^{6}_{3}\mathrm{Li} + {}^{1}\mathrm{n} \rightarrow {}^{4}_{2}\mathrm{He} + {}^{3}_{1}\mathrm{T}$ and ${}^{7}_{3}\mathrm{Li} + {}^{1}\mathrm{n} \rightarrow {}^{4}_{2}\mathrm{He} + {}^{3}_{1}\mathrm{T} + {}^{1}\mathrm{n}$ reactions. Modules containing Li surrounding the reactor core form a tritium breeding blanket in which the fuel will be produced and extracted.

elements.

Gaseous products are produced as a result of (n,α) and (n,p) reactions following capture or loss reactions. The emission of an alpha-particle ($^{4}He^{2+}$) in (n,α) reactions produces He in the material. Proton emission (n,p) reactions similarly produce $^{1}H^{+}$ particles [20]. The rate of H and He production depends on the target material, but even at low concentrations these dissolved gasses can have an impact on the physical properties of materials, due to their typically low solubility [16, 18–20].

Compositional changes in the target material occur as a result of beta decay following neutron capture or loss reactions. Equations 1.2–1.4 show the β^{-}, β^{+} and electron capture reactions respectively. A β^{-} decay, as shown in equation 1.2, results in the conversion of a neutron in the nucleus to a proton, increasing the proton number of the target atom. Similarly the reverse can occurs in a β^{+} reaction, decreasing the proton number of the target atom by converting a proton to a neutron [11, 16, 18, 19].

$$n \rightarrow p + e^{-} + \bar{\nu}_{e} \tag{1.2}$$

$$p \rightarrow n + e^{+} + \nu_{e} \tag{1.3}$$

$$p + e^{-} \rightarrow n + \nu_{e} \tag{1.4}$$

In a reactor component, this process results in a composition that varies with exposure time. The addition of impurity elements through this process

can be either beneficial or detrimental to the properties of the component, depending on the base material. Predicting the change in composition is complex, as it relies on a complete picture of all of the nuclear processes possible in a material, as well as an accurate description of the neutron energy spectrum from the reactor in question. Modern transmutation codes such as FISPACT-II [15, 21] rely on extensive nuclear reaction databases such as ENDF [14] and TENDL [22], and are capable of simulating a wide range of elements [18].

1.2 Fusion Energy

In this section, the design of current and future DEMOnstration fusion reactors will be discussed. The general goal of fusion research is to achieve a net energy gain from fusion (a Q-factor[4] greater than 1). No device has yet been able to achieve a greater amount of energy than was used to produce the reaction, and reaching this condition is crucial to the development of fusion as an energy source.

1.2.1 *Choice of Fuel*

In theory there are several fuel options for producing a fusion reaction. Practical limitations mean that the majority of fusion experiments and future concept power stations will use the reaction between two isotopes of Hydrogen: deuterium ^{2}H and tritium ^{3}H (D-T) as shown in figure 1.2. The

[4]The fusion energy gain factor, Q, is the ratio of power produced by nuclear fusion to the input power from auxiliary power sources [12]

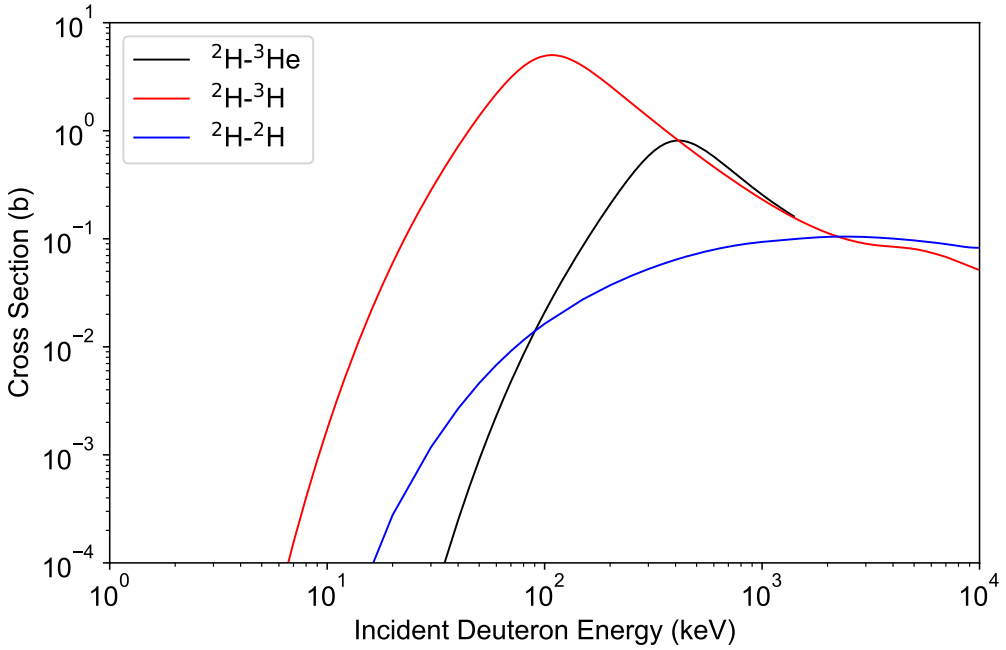


Figure 1.2: Fusion cross section in barns for various fuels as a function of incident deuteron energy. Plotted using data obtained from the Nuclear Energy Agency, Java-based Nuclear Data Information System (JANIS) [13]. Data plotted is taken from the Evaluated Nuclear Data File (ENDF) version B-V1.8 [14].

electrostatic barrier between two nuclei (or Coulomb barrier) is a function of the charge of the nucleus and therefore the number of protons in those nucleons. It is therefore lowest for isotopes of hydrogen [11].

Deuterium is stable and naturally occurring. Tritium, however, is radioactive: decaying via β^- with a half-life of around 12-13 years [18] and therefore needs to be carefully managed and produced. Equation 1.5 [12, 23] shows the fusion reaction between deuterium and tritium.

$$ {}^2_1\mathrm{D} + {}^3_1\mathrm{T} \xrightarrow{100\,\%} {}^4_2\mathrm{He}(\alpha) + {}^1_0\mathrm{n} \qquad [17.6\,\mathrm{MeV}] \tag{1.5} $$

The neutron is emitted with 14 MeV and the α with 3.6 MeV of kinetic energy [23], and is a result of the mass deficit between the incident and

product nuclei. The alpha particles which quickly deposit their energy over a short distance but the neutrons travel much further into the surrounding reactor components. Aneutronic fusion reactions, such as the ^{2}D–^{3}He reaction, shown in figure 1.2 do not produce neutrons, but are much harder to achieve.

1.2.2 *Reactor Design*

The most technologically advanced design for a nuclear fusion power station is based on Magnetic Confinement Fusion (MCF). MCF uses powerful magnets to constrain an ionised plasma, heated to hundreds of millions of degrees K. The world's largest MCF experiment, the Joint European Torus (JET), shown in figure 1.3, uses this configuration to create in-vessel temperatures as high as 325 million K [24]. JET holds the current world record with 16 MW of fusion power for 24 MW input [23, 25], giving a Q factor of 0.67. The successor to JET, ITER[5], is an even larger device currently under construction in the south of France, and could be the first device to achieve a net energy production (Q$>$ 1) with 500 MW fusion power for fractions of a second [23]. These reactors operate in a divertor configuration, which uses a particle dump to extract energy and remove waste ions produced during fusion. These reactors use an armoured first wall (FW) to protect the components behind from extreme heating and neutron damage. Together the FW and divertor make up the Plasma Facing Components (PFCs) of the

[5]originally the International Thermonuclear Experimental Reactor, now defined by the Latin word for "the way"

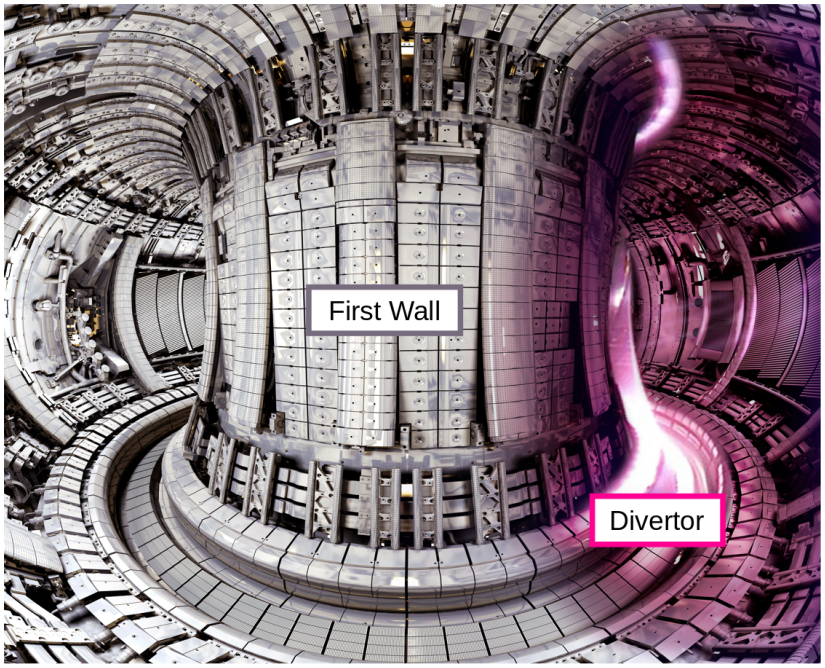


Figure 1.3: Photograph of the inside of the JET reactor, showing the position of the Beryllium first wall and W divertor, adapted from image obtained from [26].

reactor, and are highlighted in figure 1.3.

ITER is an experimental reactor, and despite a Q> 1, will not produce electricity. A DEMOnstration fusion power station, will use the knowledge gained in experiments like ITER and JET to supply electricity to the grid [25, 27]. Various countries are now working to address the technical challenges of a DEMO reactor: the governments of the European Union, South Korea, Russia and the UK have invested in conceptual design studies for electricity generating reactors. China, India and the USA are working on reactors which bridge the gap between ITER and DEMO and will be used for the testing and development of components for a power station [28, 29].

A DEMO reactor could operate under steady state conditions rather than pulsed operation as in ITER and JET and will experience greater

Table 1.1: Predicted operating conditions for the first wall and divertor of a demonstration fusion reactor. Units of full-power years are used to describe operational lifetimes, and refer to years of continued exposure to neutron loading at temperature without maintenance. Peak loading and operating temperature refers to the expected conditions under a disruption lasting a short period of time. The operating temperature of PFCs are subject to variation because of many outstanding design choices. The operating temperature of the components will also depend on the type of coolant used, for example He or water.

Operating Condition	First Wall	Divertor	Reference
Expected Lifetime (fpy)	1-5	1-5	[18, 30, 31]
Thermal Loading ($MW\,m^{-2}$)	1-2	10-20	[30, 31]
Operating Temperature (K)	823-1073	773-2000	[31, 32]
Peak Loading ($MW\,m^{-2}$)	N/A	10-20	[33]
Dose (dpa)	10-30	15	[18, 31]
Dose Rate (dpa/fpy)	5-9	3	[18, 31]

thermal loading and doses of neutrons. In addition, a DEMO reactor would also need to continuously produce its tritium fuel through a breeding process in blanket modules behind the FW.

1.2.3 *DEMO Plasma Facing Components*

The PFCs in DEMO will have to be durable, and withstand a significantly higher neutron dose and higher thermal loading than current reactors (1-2 $MW\,m^{-2}$ for the FW [30] and 10-20 $MW\,m^{-2}$ in the divertor [31]), as summarised in table 1.1. Crucially, they need to last long enough in service to maintain the availability of the reactor, so that economic viability can be achieved. Their performance in an accident scenario must also be justified.

Comparing the DEMO FW neutron spectrum to that of a typical Pressurised Water Reactor (PWR), as shown in figure 1.4, it is clear that for

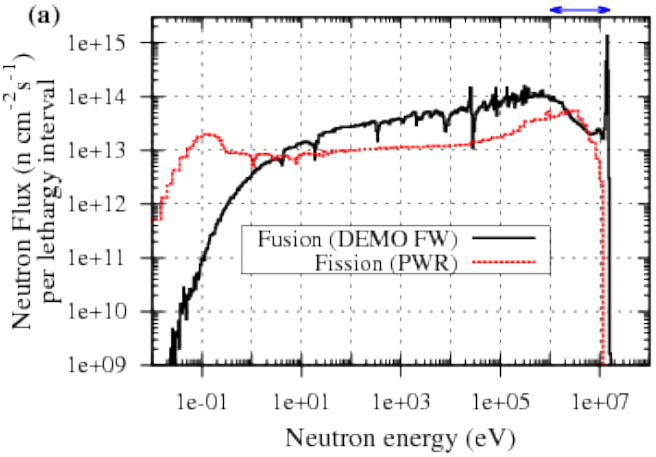
fusion there will be a much greater flux of high energy (14 MeV) neutrons, with a lower thermal neutron component [19, 34]. In terms of transmutation, this means that the PFCs can be expected to receive a significant neutron dose, whilst undergoing a lower transmutation rate than in a fission reactor.

1.3 Radiation Damage in Materials

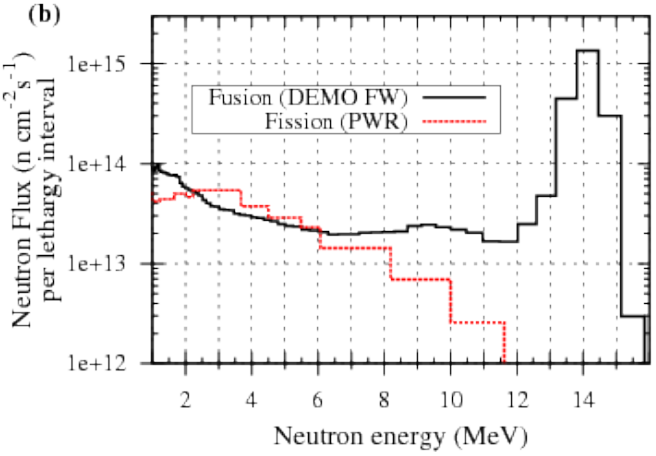
In this section, the fundamentals of radiation damage in materials will be outlined. Radiation damage in materials covers a wide range of interactions between incident radiation and matter, but in the context of this research this primarily concerns the interaction between neutrons and charged particles with crystalline metallic systems.

1.3.1 *The Collision Cascade*

Radiation damage in materials begins with an incident particle impacting an atom in the crystal lattice, transferring its energy to the primary knock on atom (PKA). If the energy transferred to the PKA is above the material's displacement threshold energy (E_d), it is displaced from its initial lattice site creating a vacant lattice site (vacancy) and a displaced interstitial atom (interstitial). If the energy of the PKA is high enough, further interactions between the PKA and other lattice atoms produces a cascade of displacements through the material, as shown schematically in figure 1.5. The cascade forms a central region of vacancies with a surrounding shell of displaced interstitial atoms. The structure left behind quickly relaxes



(a) log–log.



(b) log-scale.

Figure 1.4: First wall neutron energy spectrum in a concept fusion power station vs a typical Pressurised Water Reactor (PWR) energy spectrum shown on both (a) a log-log scale and (b) with a standard x-axis scale [34].

as recombination of interstitials and vacancies occurs, but a small population of defects are retained. Channelling and focussing effects increase the separation between defects, reducing the chance of their recombination [16].

The surviving defects produced in these picosecond scale cascades go on to influence material properties over years of in-service operation. As such, modelling the full process from neutron interaction to long-term property evolution using a single computational technique is impossible, and mutl-

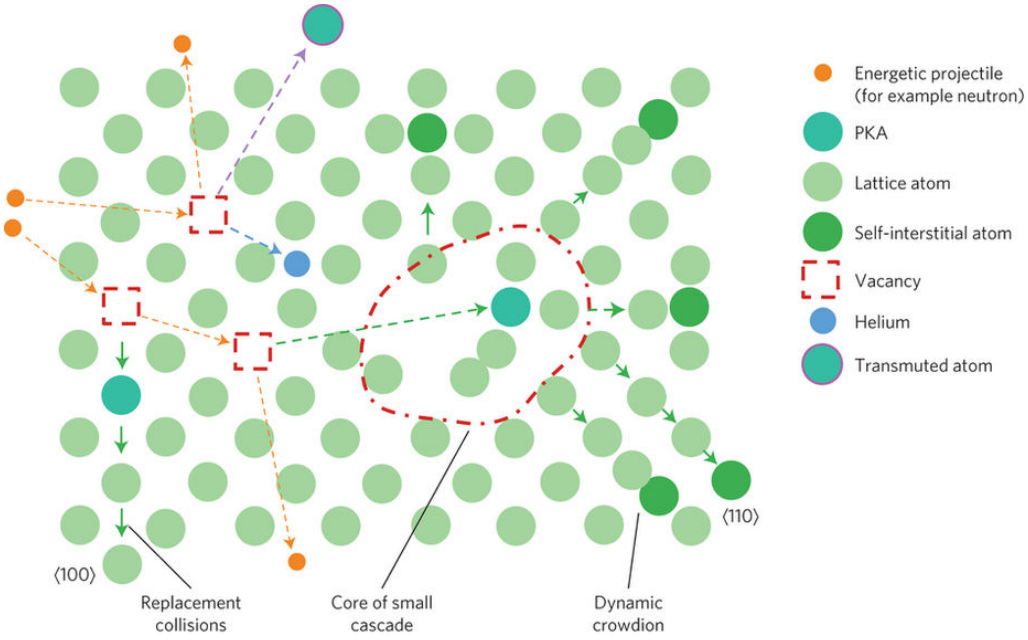


Figure 1.5: Schematic diagram of a damage cascade [35].

iscale modelling approaches are needed. Molecular dynamics (MD) is used to simulate the motion of atoms, which are treated as uniform spheres interacting according to an interatomic potential [36]. Diaz de la Rubia et. al were able to simulate the full evolution of a cascade in Cu, using PKA energies of 5 keV in 1987 [36, 37]. Since these early simulations, advances in computational power and more sophisticated modelling techniques have allowed the simulation of high energy cascades, such as those produced by the interaction with fusion neutrons [38].

1.3.2 *Stopping Power*

Charged particles lose energy through interactions with material via a range of processes including electronic excitation, ionisation or Bremsstrahlung radiation [16]. The *Stopping Power* is a measure of the force which acts to reduce the energy of the incident particles, and is an important consideration

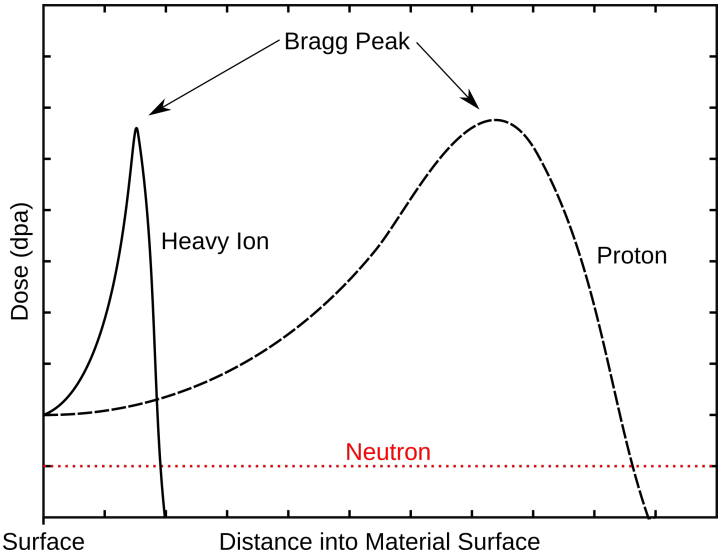


Figure 1.6: Schematic diagram showing the difference in dose/depth profiles for neutron, heavy-ion and proton irradiation. The approximate dose profile from a neutron irradiation is plotted in red and indicates that on average, the long mean free path of neutrons in the material means that there is no variation in the dose as a function of depth.

for ion irradiation studies, which, as will be discussed in section 1.5.2, are a commonly used surrogate for neutron irradiation.

The overall *Stopping Power*, $S(E)$ is defined as the energy loss, E, per unit length, x, and is given by $S(E) = dE/dx$ [16]. The total stopping power can be broken down into the contributions to the energy loss from different interaction mechanisms.

Electronic excitation refers to the inelastic collisions between the incident particle and the electrons of the material it is moving through. This results in excitation of the electrons as the incident particle traverses the material. Elastic collisions also occur between the incident particle and the nuclei of the material atoms, which is also referred to as *Nuclear Stopping Power*. At very high ion energies, Bremsstrahlung radiation in which x-rays are produced due to the deceleration of a charged particle in an elec-

tric field, become significant, however, the work presented in this thesis uses ion energies below the threshold needed to consider radiative losses.

As an ion traverses the material, the stopping power increases as it approaches the end of its range. The stopping power reaches a maximum at a point known as the *Bragg Peak*. At shallow depths electronic stopping is dominant but nearer to the end of the ion range elastic collisions begin to dominate, as the ion loses energy [16]. Therefore, the dose as a function of depth for a charged ion irradiation is characterised by a peak in dose at a given depth, with a lower dose region between the surface and this depth, as shown in figure 1.6. Neutron irradiation results in a comparatively uniform damage profile.

1.3.3 *Displacements per Atom*

The dose received by a material is commonly given in units of displacements per atom (where 1dpa corresponds to an average of 1 displacement for every atom in the sample) [16, 39]. This is typically estimated according to the Norgett, Torrens and Robinson (NRT) model for estimating the number of Frenkel pairs generated as a function of PKA energy [39, 40].

In practice, for ion irradiations, the dose as a function of depth into the sample surface is typically calculated using the Stopping Range of Ions in Matter (SRIM) [41] code, which utilises an approximation known as the Binary Collision Approximation (BCA). Under the BCA in SRIM, nuclei lose energy due to both elastic and inelastic collisions. The ion travels through the material is approximated as a sequence of independent bin-

ary collisions (between two nuclei), with inelastic losses between collisions estimated using the effective charge formalism [16].

The BCA method does not fully capture the effects of primary damage [42] but is a recommended standard for comparing between different experiments [39]. A standardised approach to these calculations is given by Stoller et. al [43], which provides a set of instructions on how to set up these simulations.

1.3.4 *Physical Effects of Radiation Damage*

Following the relaxation of the cascade, the surviving point defects diffuse through the lattice and create larger scale defects [16]. The agglomeration of point defects into clusters of vacancies (voids) or vacancy/interstitial loops, depends on the material and the crystal structure. Radiation damage increases the population of point defects that have negligible contributions at equilibrium, leading leading to the phenomenon known as Radiation Enhanced Diffusion (RED) [16, 44, 45].

Point defects can also have attractive or repulsive binding energies with solute or impurity atoms in an alloy. The drag of solute towards or away from sinks of point defects can lead to localised depletion or enrichment of different elements and the precipitation of phases not predicted under equilibrium conditions. This process is called Radiation Induced Segregation (RIS). Radiation damage can also stabilise phases that would not be seen in the equilibrium phase diagram, or destabilise those that would be expected [16, 44].

Maydet and Russell, in treating point defects as a chemical component in the material, were able to model incoherent phase stability under irradiation in 1977 [44]. Similarly, Cauvin and Martin, in 1981 were also able to predict the homogeneous formation of coherent precipitates, such as those expected in W-Re [45].

1.4 Engineering Challenges to Fusion Energy

There are several engineering challenges to the realisation of fusion as an energy source. These include the development of reduced activation structural steels, neutron damage resistant high heat flux components, tritium handling, breeding and recycling technology, and remote maintenance of reactor components [46]. For the PFCs, this involves the development of refractory alloys that are resistant to activation and with sufficient long-term properties. The materials under investigation for these applications are not currently certified for use in a nuclear environment.

1.4.1 *Development of Plasma Facing Materials*

Based on the anticipated operating conditions discussed in section 1.2.2, and summarised in table 1.1, the PFCs must have a high melting temperature, such that continued operation can be assured in the event of a disruption. They must have a good thermal conductivity in order to effectively transport heat away from the reactor core and prevent overheating in the FW and divertor, and they must be resistant to erosion under exposure to a H plasma [33, 49, 50]. Both Beryllium and W were trialled in JET however for DEMO,

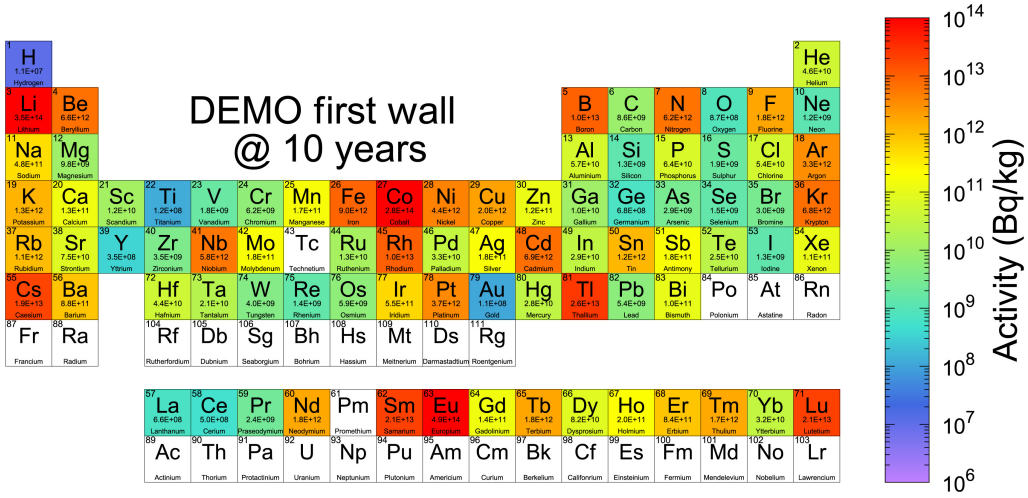


Figure 1.7: Periodic table presented by Gilbert et. al, showing the total activity in Bq for each element in the periodic table following a 2 full-power year neutron irradiation with a DEMO FW neutron spectrum, and following 10 years of cooling [47].

the erosion rate of Beryllium is predicted to be too high for commercial viability [24, 31, 51]. Silicon–Carbide compositions were investigated as a possibility but were found to erode too quickly and retain tritium [24, 52]. The PFC material must be low activation to limit the generation of long-lived radioactive waste.

Figure 1.7 shows the predicted activity of various elements after irradiation in DEMO and illustrates the difficulty of material selection for fusion [47]. Tungsten remains as the most suitable choice, in terms of cost, activity and weldability, and has been used in the JET and ASDEX tokamaks [24].

The design of DEMO isn't complete and multiple countries are pursuing their own DEMO designs, the majority of which include a W FW and divertor [7, 28, 29, 53]. Current designs for the ITER divertor tiles consist of a solid W monoblock, with a central copper pipe around which cooling water is circulated. Between the copper pipe and the W is a Cu-Cr-Zr inter-layer

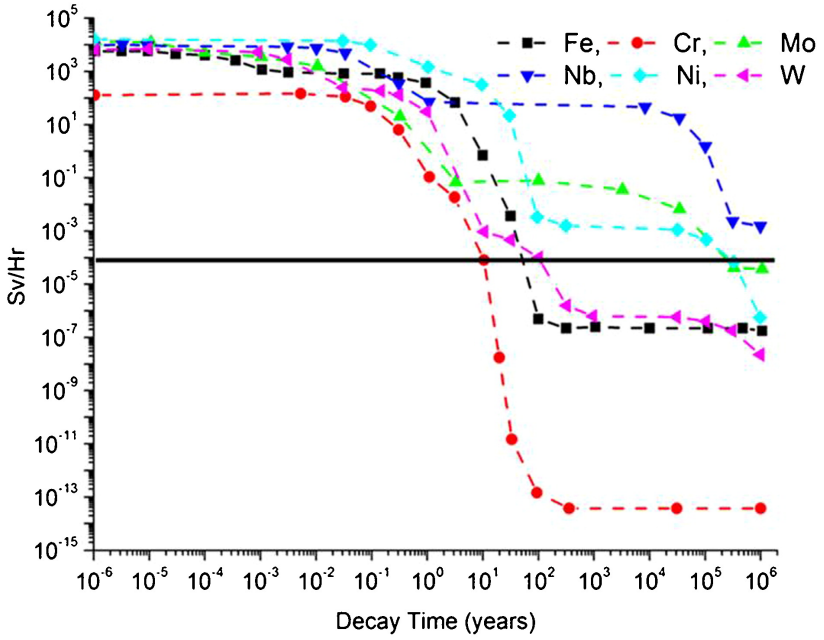


Figure 1.8: Level of activity in mSv from common elements found in steels, irradiated for 5 years in a 3.6 GW fusion power reactor, plotted as a function of time after removal from the reactor. Black line represents ITER administrative limit for hands on maintenance [48].

[50].

1.4.2 *Nuclear Waste and Reactor Safety*

Fusion reactors and power stations based on the DT reaction shown in equation 1.5, will inherently produce radioactive waste due to activation of the reactor components by neutron interactions [54]. Efforts began in the 1980s to reduce the amount of radioactive waste produced by a fusion reactor through the development of low or reduced-activation structural materials, severely limiting material selection options [48, 55, 56].

The details of this criteria are unclear but is stated explicitly by Gorley *"that these criteria require all materials used in a fusion reactor to be suitable for recycling or disposal in non-active landfills approximately 100*

years after removal from the reactor" [48]. Impurities are particularly important to consider, as even trace quantities of elements such as uranium in beryllium can lead to significant long-term activation implications [57].

One of the reasons for the selection of W as a PFC is its low, long-term, activation properties (discussed in more detail in section 2.2.1). It is used as a replacement for Mo in reduced activation steels [55], because as shown in figure 1.8, it has a lower long-term activity. While in the long-term, W has a lower activity than many other elements, in the short-term its high activity requires careful management, particularly when considering potential accident scenarios. Despite having no chain reaction, decay heating effects due to the activity of the reactor components are substantial (1473 K in the FW after 10 days following a LOCA [58]), and will require active cooling [58–60]. Though well below the melting temperature of W, this temperature could potentially threaten the integrity of the steel supporting structures.

Furthermore, in the event of a loss of vacuum accident (LOVA), either as a result of structural integrity issues following overheating of the FW components in a LOCA, or independently, significant quantities of tungsten-trioxide (WO_3) will be produced from activated W, and potentially released into the environment [58]. The low sublimation temperature of WO_3 (see section 2.4.5) makes a LOVA particularly important from a risk mitigation standpoint. The presence of Os in neutron irradiated tungsten is likely to result in the formation of the highly toxic, and volatile oxide OsO_4 in the event of a LOVA, as will be discussed further in section 2.4.5. The potential

for the release of toxic OsO_4 in substantial quantities during an accident scenario is another important factor for the development of a safety case, and something that needs further work to understand and mitigate against.

1.4.3 *Fusion Neutron Sources*

At present, there is no facility capable of reproducing the high heat fluxes, and intense neutron doses that will be produced in a fusion power station. But understanding how materials will perform is vital for developing the safety case and for designing an economically viable reactor. The need for a dedicated facility has been recognised for many years but has been in the discussion stage for over 30 years. The EU is planning the construction of an International Fusion Materials Irradiation Facility-DEMO Oriented Neutron Source (IFMIF-DONES) [61, 62] but until this facility is commissioned and constructed, studies of radiation damage and transmutation have to rely on surrogates for neutron damage.

1.5 Surrogates for Fusion Neutron Damage

In the absence of a source of a high flux of 14 MeV neutrons, alternative methods have to be used to study the effects of neutron damage on the materials. It is essential to understand material degradation so that accurate predictions can be made as to the performance of components.

1.5.1 *Fission Neutrons*

Compared to other methods, the use of fission neutrons has obvious advantages. Because the incident particles are the same, the scattering and energy deposition through the material is more comparable, though the neutrons will have a lower energy. The absence of coulomb interactions between the incident neutrons and the atoms in the material lattice means that large sample volumes are required, making bulk property measurements possible. A wide range of temperatures can be studied and reasonable doses can be achieved over several years [63, 64].

Neutron irradiation studies are time consuming, expensive and difficult. Sample handling is particularly challenging due to activation and samples typically needing a period of cooling after removal from the reactor before they are safe to transport. After transport, dedicated facilities with high activity limits are needed to process and test the material. Differences in the neutron energy spectrum introduce significant changes in the transmutation rate (as discussed in section 1.1.2) and result in a higher transmutation level per dpa of damage [18, 65]. Differences in the incident neutron energy also results in changes to the cascade structure. Furthermore, the dose rate can be slow and irradiation temperatures can be difficult to control and accurately report [63].

1.5.2 *Heavy-Ion Irradiation*

Heavy-ion irradiation is a well established technique for simulating neutron damage. Ion irradiation has the advantage of being quick and easy to carry out, and doesn't generate any activation that can create issues around handling and analysis. It is possible to achieve very high doses (>1 dpa) over short times scales (<1 day) [63] and it is possible to implant both self-ions and lighter ions such as helium or hydrogen to simulate both neutron damage and ion bombardment from a fusion reaction and gas production via transmutation reactions. The lack of transmutation allows for control over specimen compositions, facilitating systematic studies of composition. High incident energies are easily achievable because the ions are charged, and therefore can be accelerated by an electric field. Specimen temperature can be well controlled and in-situ examination of samples with TEM is possible [63].

Using charged particles means that the reactions between the incident particles and the lattice are inherently different. Long range coulomb interactions mean that a higher fraction of low angle, low energy collisions occur, resulting in a greater percentage of surviving defects for a given dpa [63]. The higher stopping power for charged particles means that a shallow implanted region at the surface of the sample is produced, necessitating the use of micromechanical testing techniques to study mechanical properties. The dose profile of a heavy-ion irradiation consists of a lower dose tail with a high dose Bragg peak, as shown in figure 1.6. Degrader foils and sequential

ion irradiation with different energies can be used to spread out the dose profile using multiple Bragg peaks [66].

Artefacts due to the proximity of the surface may also have an impact [63]. Transmutation is not produced by ion irradiation, so studies of the effect of transmutation rely on pre-alloying of the material. Though this means systematic studies can be carried out, the effect of pre-alloying on the cascade structure and defect migration needs to be fully understood. At the Bragg peak of an ion irradiation, where the injected atoms come to rest, there is a bias for interstitial formation, which can affect the phenomena observed there [67, 68]

Though the vastly increased dose rate for ion irradiations can make experiments easier, the effect of dose rate is not fully understood. Attempts to compensate for the reduced time for point defect diffusion in ion irradiation experiments by increasing the irradiation temperature have been used [16, 69]. There is no systematic study of the effect of dose-rate in W, but studies of Fe-Cr by Reese et. al, comparing ion and neutron damage have highlighted differences in the size of Cr clusters, with increasing dose rate correlated with decreased Cr cluster size [70]. Differences in hardening due to different dose rates were seen by Hardie et. al in Fe-Cr, linked to the size of Cr rich clusters [71].

Differences in the method used to estimate the dpa as a function of depth using SRIM, between different studies also reduces the repeatability of ion irradiation experiments, and makes comparison challenging, as will

be discussed further in section 2.4.1.2.

1.5.3 *Proton Irradiation*

Proton irradiation is a less commonly used approach to simulating neutron irradiation. Early investigations of protons as a surrogate for neutrons report that 16 MeV protons provide an accurate simulation for 14 MeV neutrons [72]. Charged particles can be accelerated using an electric field giving precise control over the incident beam energy. Unlike heavy-ion implantation, proton irradiation can induce some activation in the sample under certain conditions, and may therefore require additional risk controls during sample preparation. Protons have a shorter stopping range than neutrons, but considerably longer than that of heavy-ions. Through-thickness irradiation can be achieved in thin samples, allowing for bulk measurements to be carried out. The Bragg peak can positioned outside of the sample, with the dose coming from the tail of the peak and is the reason for its exploration as a targeted cancer therapy.

High energy, 800 MeV proton irradiations of W were carried out by Maloy et. al in 2005 [73], and the degradation of bulk mechanical properties were characterised. This study highlights the benefits of proton beam irradiation as doses as high as 21.9 dpa were achieved with minimal transmutation. This could allow for systematic studies of different alloy compositions, if the differences between proton and neutron irradiation could be established. The study does not take into account the effects of (n,f) reactions however, which could be significant at such high proton energies.

Rayaprolu et. al, suggest that the majority of the interactions between the incident radiation and the material are scattering reactions, and thus the dominant mechanism of damage creation should be similar between high energy proton and neutron irradiation. It is also highlighted that using a 30 MeV H^+ proton beam on W, similar Re transmutation rates to DEMO could be achieved: 700appm and 401appm Re for 1dpa in DEMO and under proton beam respectively [74]. The depth achieved is sill limited to 500 µm, with the Bragg peak beyond this depth, which means that bulk mechanical testing may still not be possible. The H production in the sample is reported as almost 30 times higher than a DEMO first wall, however, and the impact of this on the mechanical properties, and on the stabilisation of features such as voids needs to be understood.

1.6 Summary

Nuclear fusion is a promising technology with key advantages over nuclear fission, but is still dependant on the development of materials to address outstanding engineering problems. Despite being low-carbon, it is unclear whether it can be realised in a time frame that would allow it to contribute to decarbonisation. Despite public perception, a fusion reactor has a number of potential accident scenarios that could result in the release of radioactive material. This underlines the need for the development of reliable PFC materials that can withstand high temperature, high dose neutron irradiation. In the absence of a fusion spectrum neutron source, a combination of ion and neutron irradiation can be used to understand the processes of radi-

ation damage, transmutation and radiation induced/enhanced precipitation in W in order to predict the performance of components in-service.

2 Tungsten for Nuclear Fusion

▶ Synopsis: Tungsten has been investigated for many years for applications within fusion, after other materials like carbon were ruled out for the ITER divertor. W is not a commonly used engineering material because of its poor mechanical properties. It's degradation under neutron irradiation is a key focus of the fusion development program. In this section, the properties of pure W, and alloys of W-Re and W-Os are outlined, as well as a summary of studies that have attempted to understand how W will perform in a fusion reactor under neutron irradiation.

2.1 Physical Properties of Pure Tungsten

Tungsten is a refractory metal with melting temperature of 3695 K [75, 76], a room temperature thermal conductivity of 165 $W\,m^{-1}\,K^{-1}$ [77], and a sputtering threshold of E_{th}=100 eV for D, T and He [78]. W has a room temperature electrical resistivity of 0.05 $\mu\Omega$/m [77] and is a bcc metal with a density of 19.25 $g\,cm^{-3}$ [79], a theoretical atomic radius of 193 pm [80] (135 pm experimentally [81]) and a lattice parameter of 3.169 Å [82]. In its natural state, W has 5 isotopes, of atomic mass numbers 180, 182, 183, 184 and 186, as summarised in table 2.1 [18]. W is the chemical element with the highest melting temperature and is mined in the form of the mineral

Table 2.1: Natural abundances of W isotopes [18].

Nuclide	^{180}W	^{182}W	^{183}W	^{184}W	^{186}W
Abundance (at.%)	0.12	26.50	14.31	30.64	28.43

Wolframite (Fe,Mn)WO_4. It is most commonly used in tungsten-carbides for abrasive cutting tools, and as the filament in filament light bulbs.

Prior to irradiation, W has a high Ductile to Brittle Transition Temperature (DBTT) of between 623-723 K [66, 83], below which it has a low fracture toughness of 5 MPa/$\sqrt{\text{m}}$. Above the DBTT this value increases to between 20 and 100 MPa/$\sqrt{\text{m}}$ at temperatures of between 673 and 1073 K [84]. Failure in both annealed and recrystallised tungsten is predominantly inter-granular, even in high purity material [85, 86]. Analysis of different impurities in tungsten using Auger electron spectroscopy and electron microscopy suggests that the presence of grain boundary impurities does not have a significant influence on the resistance of grain boundaries to inter-granular fracture [85].

There are reports of a lower DBTT in W of 400 K in measurements taken by Steichen [66, 87] however, these appear to have been misinterpreted as the DBTT of 400 K is reported for a Molybdenum alloy TZM rather than W [87]. Other earlier studies by Raffo do report a lower DBTT of 490 K in arc-melted and recrystallised W, reduced to 430 K and 350 K by the alloying of 2at.%Re and 25at.%Re respectively [83].

2.2 Microstructural Evolution under Irradiation

2.2.1 *Transmutation in Tungsten*

As discussed in section 1.1.4, transmutation is a process that occurs under neutron irradiation due to the absorption of neutrons and decay of the

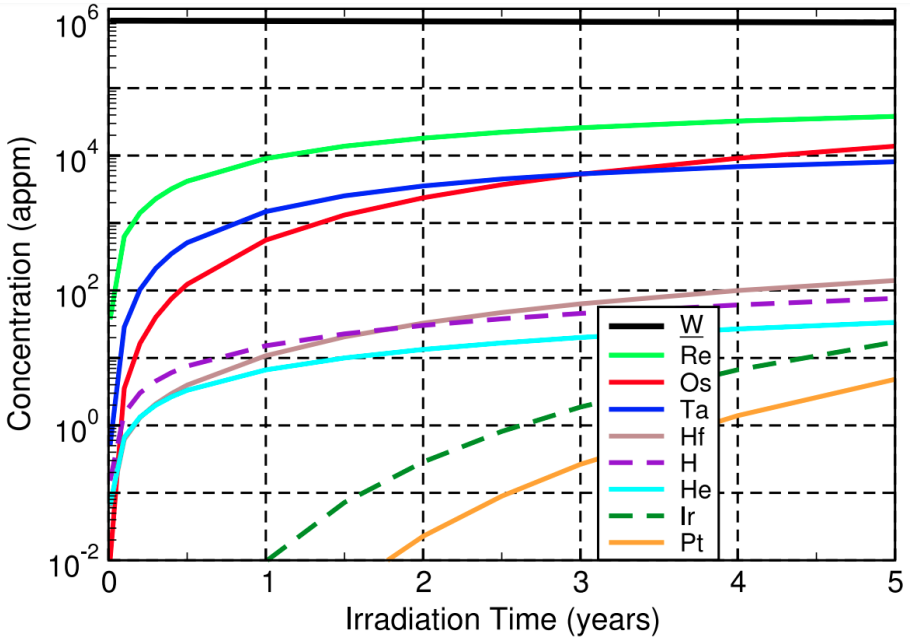


Figure 2.1: Transmutation of a W FW component during a 5-year irradiation under DEMO fusion power-plant conditions assuming a spatially homogenous reactor structure and neutron flux [18, 19].

subsequent isotopes. For W, the primary transmutation products are Re, Os and Ta, which are produced in varying quantities [17–19]. Table 2.1 shows the natural isotopic abundances of of W. The production of Re in W is primarily a result of the β^- decay of ^{187}W and ^{185}W, which are produced by the neutron absorption (n,γ) of ^{186}W and ^{184}W [18, 65]. Os is similarly produced via the β^- decay of Re isotopes. Ta, on the other hand is produced via β^+ reactions in isotopes of W, which are produced by (n,2n) and (n,3n) neutron loss reactions. For full details the reader is directed to [18].

2.2.1.1 *Modelling Transmutation in W*

Simulations of transmutation are complex and require large databases of interaction data such as ENDF [14] and TENDL [22]. The United Kingdom Atomic Energy Authority (UKAEA) has developed the FISPACT, nuclear

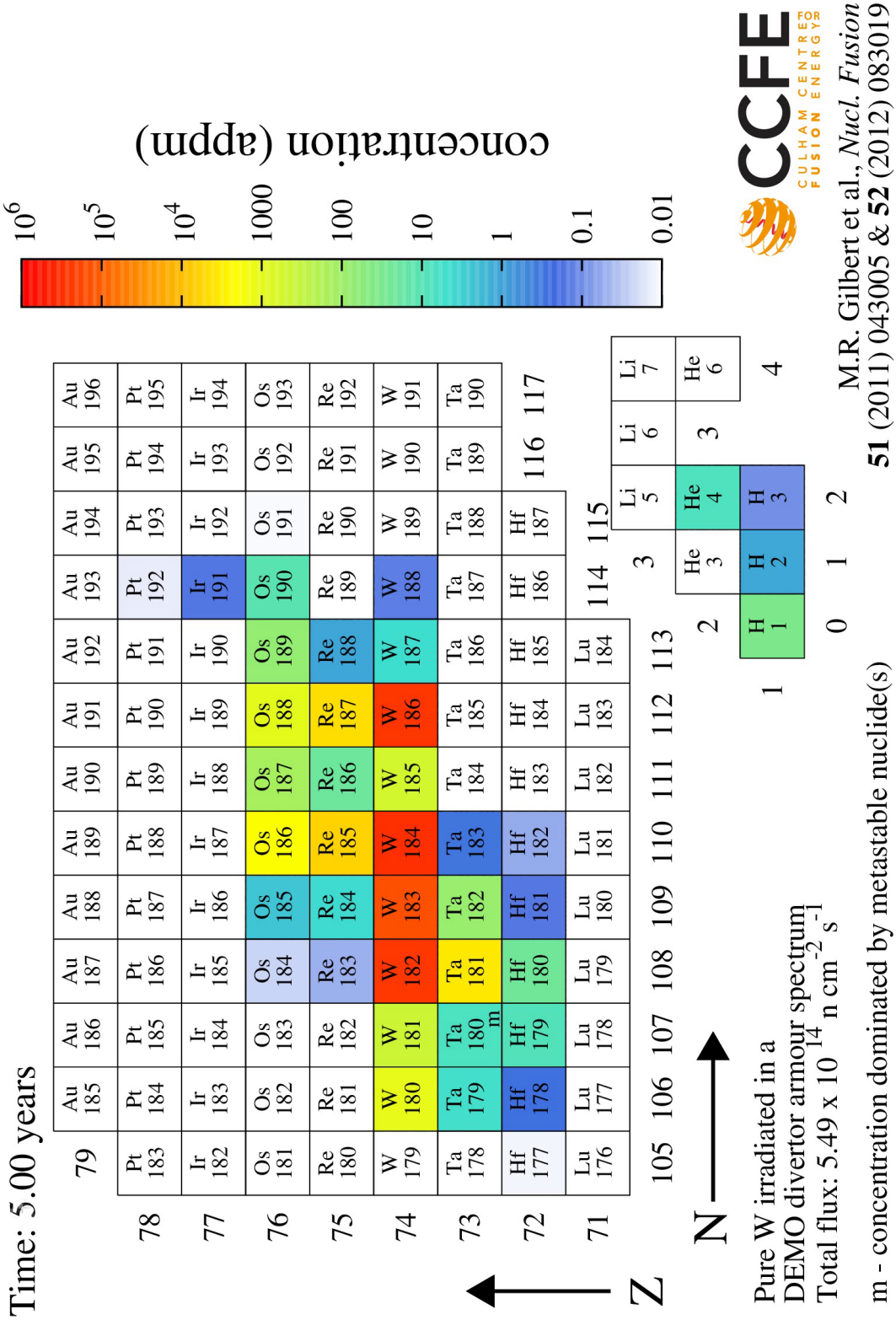


Figure 2.2: Transmutation of initially pure W under a DEMO neutron spectrum for 5 full-power years showing the production of Re, Os and Ta through β decay as well as He and H production [18–20].

inventory code over many years [15, 19, 21, 47]. This code uses the local neutron spectrum of the reactor along with an extensive database of nuclear libraries and accounts for self-shielding effects [15]. Gilbert et. al predicted transmutation levels in W for a DEMO FW of 3.8%Re, 1.38%Os and < 1%Ta after 5 years, as shown in figure 2.1. Figure 2.2 shows the spread of isotopes produced in W by 2 full-power years irradiation under DEMO conditions. The production of He and H via transmutation is comparatively small in W, and is 2 orders of magnitude lower than the equivalent production in Fe for example[1].

Gilbert et. al also study the impact of features such as coolant pipes which introduce spatial heterogeneity in the neutron spectrum. It was shown that large variations in the transmutation level can be expected due to local neutron moderation, but also that Re production varies significantly as a function of depth, due to the large resonances in ^{186}W [17]. A gradient in transmutation as a function of depth is seen despite the deep penetration depth of neutrons into W.

FISPACT-II simulations have also been applied to fission irradiation studies in which an accurate description of the neutron spectrum is available. The Re and Os production rates predicted by FISPACT simulations in W have been validated in multiple experimental studies [88, 89] demonstrating that FISPACT-II is an extremely reliable approach to quantifying

[1]He production in W after 5 years of irradiation under DEMO FW conditions is predicted to be 33appm (< 0.01%), whereas for Fe under the same neutron loading the level is 1090appm (0.11%H). A similar trend is predicted for H production, with 76 appm (< 0.01%) for W and 5010 appm (0.50%H) for Fe under equivalent FW neutron loading [19].

transmutation in W, provided an accurate description of the neutron spectrum is available. No simulations have yet been carried out for a full reactor, but simple simulations using coolant pipes highlight the complexity of this design process.

2.2.2 *Experimental Studies of Transmutation in W*

As discussed in section 1.5, transmutation is highly sensitive to the neutron energy spectrum, and fully simulating DEMO transmutation with fission spectrum neutrons is impossible. This is illustrated by figure 2.3 which shows the transmutation rate (averaged over the entire time at irradiation) as a function of dose for different reactors, compared to predicted transmutation per dpa for a DEMO reactor. In HFIR[2], the transmutation rate can be as high as 9.22at.%Re dpa^{-1}, and 5.02at.%Os dpa^{-1} for initially pure W [90]. Sodium-cooled, fast reactors like Joyo produce far less thermal neutrons, and thus induce a lower transmutation rate in pure W (0.95at.%Re dpa^{-1} and 0.03at.%Os dpa^{-1}) [90].

Transmutation is sensitive to the local neutron spectrum, not just the averaged reactor spectrum. In W samples irradiated at HFR, that will be analysed in this study, the transmutation rate is 0.72at.%Re dpa^{-1}, and 0.06at.%Os dpa^{-1} due to the presence of strong thermal neutron absorber being placed adjacent to the sample during irradiation [66, 91] . New irradiation campaigns are using canister design to change the effective neut-

[2]HFIR is a light water moderated and cooled, beryllium reflected, flux trap reactor operated by Oak Ridge National Laboratory (ORNL), USA

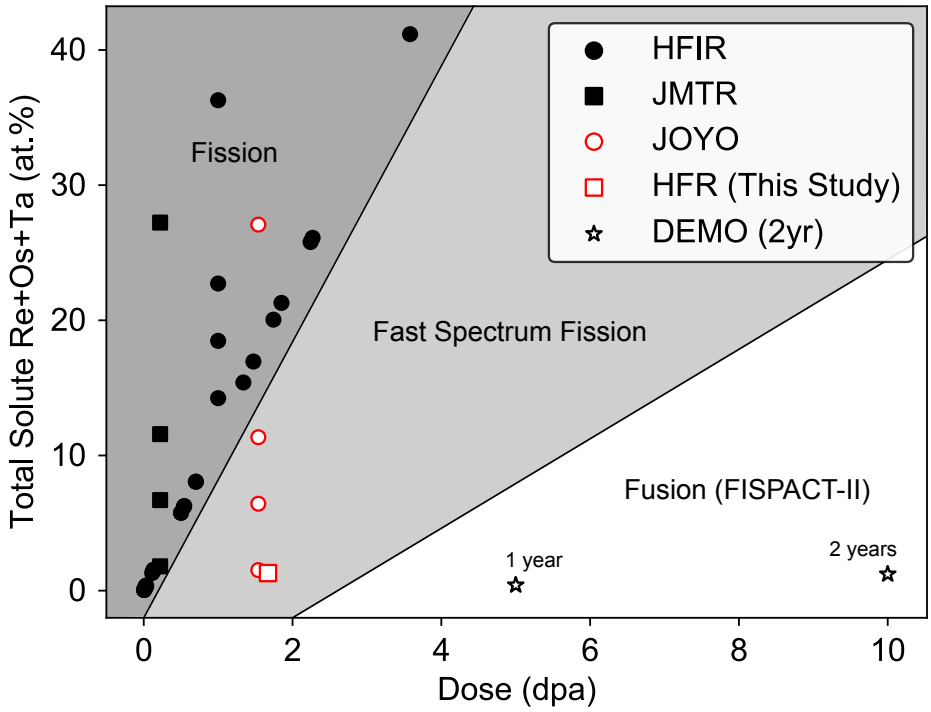


Figure 2.3: Comparison between transmutation rates in different fission irradiation experiments compared to the predicted transmutation level in a DEMO reactor after 1 and 2 years full-power irradiation at a dose rate of 5dpa/year [18].

ron energy spectrum received by the sample, such as in the Japanese-US PHENIX (Plasma facing components evaluation by tritium Plasma, HEat and Neutron Irradiation eXperiments) collaboration (2013–2018) [89, 92].

One proposed option to mitigate against transmutation effects in W is to isotopically enrich W in ^{184}W, as this isotope has a weaker neutron absorption cross section, however this would likely not be cost effective.

2.2.3 *Physical Properties of Pure Re, Os and Ta*

Both rhenium (Re) and osmium (Os) are platinum group metals adjacent to W in the periodic table (see figure 2.2), with high melting temperatures and a hexagonal close packed (hcp) crystal structure. Rhenium has a melting

Table 2.2: Natural abundances of Re, Os and Ta isotopes [18].

Element	Isotopes	Abundance (at.%)	$t_{1/2}$
Re	^{185}Re	37.40	stable
	^{187}Re	62.60	4.4×10^{10} yr
Os	^{184}Os	0.02	5.6×10^{13} yr
	^{186}Os	1.59	2.0×10^{15} yr
	^{187}Os	1.60	stable
	^{188}Os	13.29	stable
	^{189}Os	16.21	stable
	^{190}Os	26.36	stable
	^{192}Os	40.93	stable
Ta	^{181}Ta	99.99	stable

temperature of 3459 K, an electrical resistivity of 0.172 µΩ/m, a density of 20.02 g cm^{-3} [76], lattice parameters a =2.761 Å and c =4.446 Å and a theoretical atomic radius of 188 pm [80] (135 pm experimentally [81]). In its natural state, Re has two isotopes, of mass numbers 185 and 187, as shown in table 2.2 [18].

Rhenium is an expensive metal to mine to due its relatively low demand and low availability, primarily being used in the alloying of jet engine turbine blades to increase their maximum temperature capability and therefore improve engine efficiency. It is also alloyed with W for use in high temperature thermocouples [76].

Osmium is one of the rarest elements on earth, and is the densest naturally occurring element. It has a melting temperature of 3306 K, an electrical resistivity of 0.08 µΩ/m, and a density at room temperature of 22.59 g cm^{-3} [76]. Osmium also has a hcp crystal structure with lattice

parameters a =2.734 Å and c =4.317 Å. Osmium is typically alloyed with other platinum group metals to increase hardness [76]. Os is also added to Iridium and W in order to reduce spark resistance, for applications requiring a resistance to arc erosion. W-Os was investigated in 1981 as an improved cathode material [93]. This makes Os, and alloys of Os particularly difficult to machine with electric discharge machining (EDM). Os has 7 naturally occurring isotopes of mass numbers between 184 and 192, as shown in table 2.2 [18].

Tantalum (Ta) is a refractory metal with a bcc crystal structure. It has a melting temperature of 3290 K and a density at room temperature of 16.62 g cm^{-3} [76]. It is monoisotopic, as shown in table 2.2, with a single stable isotope: ^{181}Ta [18].

2.2.4 *Equilibrium W-(Re,Os,Ta) Phase Diagrams*

As discussed in section 2.2.1, Re, Os and Ta will be produced in W components in small quantities. In this section, the equilibrium phase diagrams of the different alloy systems are given to provide context to the discussion of anomalous precipitation of these elements, observed experimentally.

2.2.4.1 *W-Re*

Figure 2.5a shows the equilibrium phase diagram for the W-Re binary system, adapted from the figures published in [96]. The solubility limit in W is around 26-28at.% at 1773 K, the lowest temperature on the experimentally determined phase diagram. Beyond this, there is a large σ phase (WRe)

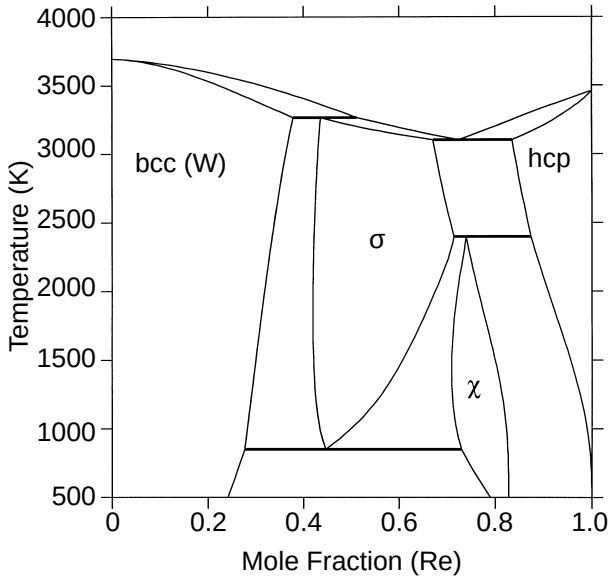
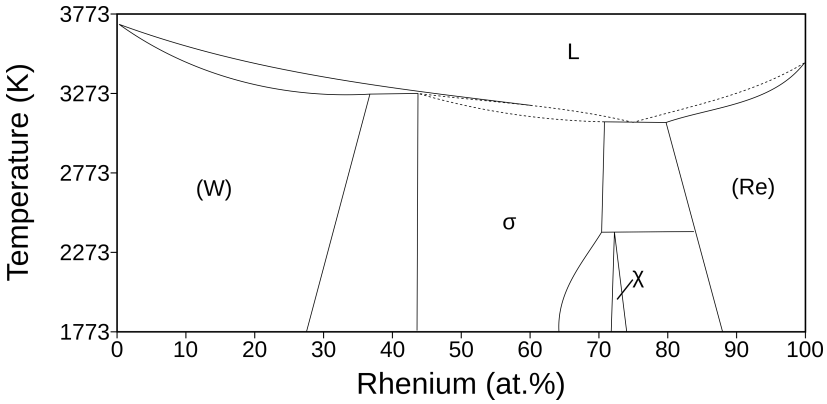


Figure 2.4: Computationally derived equilibrium W-Re phase diagram adapted from [94].

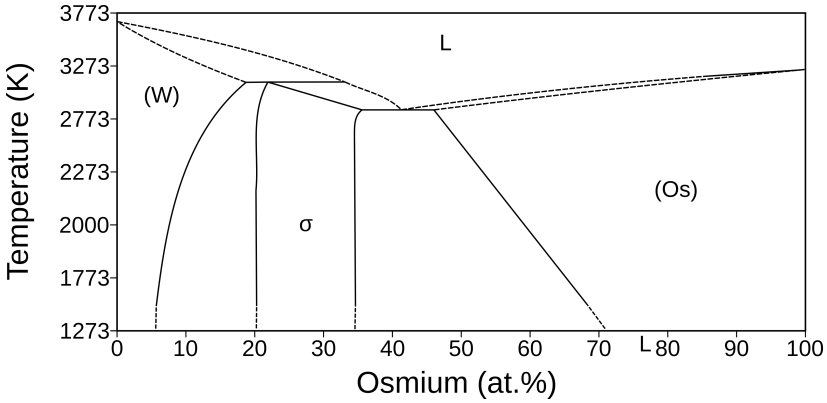
region between 43 and 64 at.%Re, after which is the χ phase associated with 75at.%Re (WRe_3). Both of these intermetallic phases have complex crystal structures not derived from the bcc crystal structure. In the intermediate region between complete Re solubility and σ phase is a mixture of W+σ associated with between 26 and 43 at.%Re. Figure 2.4, shows the phase diagram simulated with Computer Coupling of Phase Diagrams and Thermochemistry (CALPHAD) by Liu and Chang [94]. Their simulation predicts that at lower temperatures than 1773 K, the Re solubility limit in W is fairly stable (>25at.% at 1000 K) [84].

2.2.4.2 *W-Os*

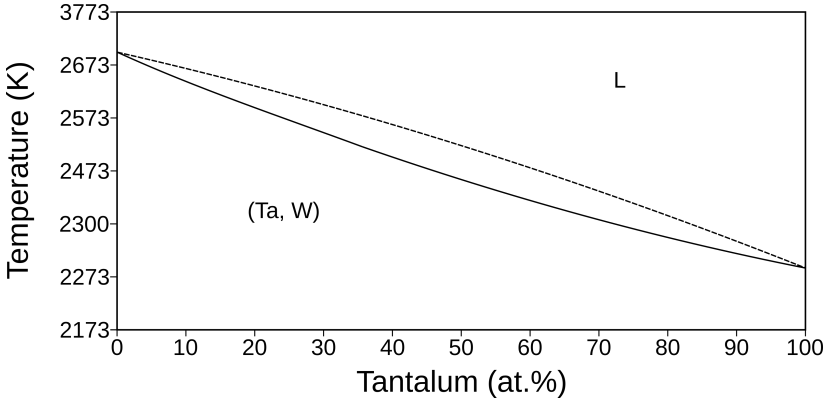
The equilibrium W-Os phase diagram shown in figure 2.5b shows that a σ phase intermetallic (WOs) forms at increasing Os concentration. Compared to W-Re, the solubility limit for Os in W is lower (6-10at.% at 1773 K) and



(a) Experimentally determined W-Re phase diagram shown between temperatures of 1773 and 3773 K.



(b) Experimentally determined W-Os phase diagram shown between temperatures of 1273 and 3773 K.



(c) Experimentally determined W-Ta phase diagram shown between temperatures of 2173 and 3773 K.

Figure 2.5: Equilibrium phase diagrams for binary W-Re, W-Os and W-Ta alloy systems. Adapted from the imaged reproduced in [84] and originally sourced from [95, 96].

there is no secondary χ phase visible on the diagram. The lower solubility limit of Os in W may indicate that RIS of Os should be stronger than with Re. Between the intermetallic σ phase and solid solution at low Os, there is a region in which a mixture of W+σ occurs around 10at.%Os (6-20at.% at 1773 K) [84].

2.2.4.3 *W-Ta*

Shown in figure 2.5c is the high temperature region of the W-Ta phase diagram. Ta shows complete solubility in W at this temperature range and does not form any of the intermetallic phases observed in W-Re or W-Os. Both metals have a bcc crystal structure. Based on this phase diagram and APT studied by A. Xu et. al on ion implanted W-Ta [84, 97], Ta would not be expected to form precipitates under irradiation. DFT calculations carried out at a temperature of 0 K for the W-Ta system have predicted the formation of complex intermetallic structures [98].

2.2.4.4 *Ternary W-Re-Os and W-Re-Ta Phase Diagrams*

Figures 2.6 and 2.7 show the equilibrium ternary phase diagrams for the W-Re-Os and W-Re-Ta systems respectively, both of which are adapted from the images reproduced in [84] and originally sourced from [95]. Figure 2.6 shows only part of the diagram in which data is available. The black region in figure 2.6 represents a σ phase intermetallic whereas the light grey section in the concentrated W corner, is the region in which solid solubility is predicted. The white region in-between σ phase and solution is a mixture of

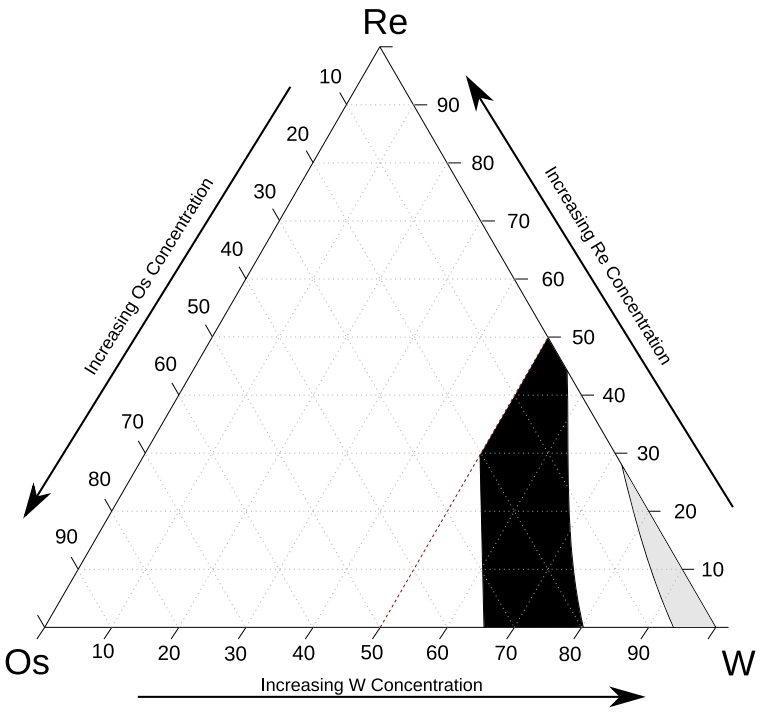


Figure 2.6: Ternary equilibrium phase diagram at 1873 K for the W-Re-Os system, showing partial phase region in which experimental data is available. Adapted from the images reproduced in [84] and originally sourced from [95].

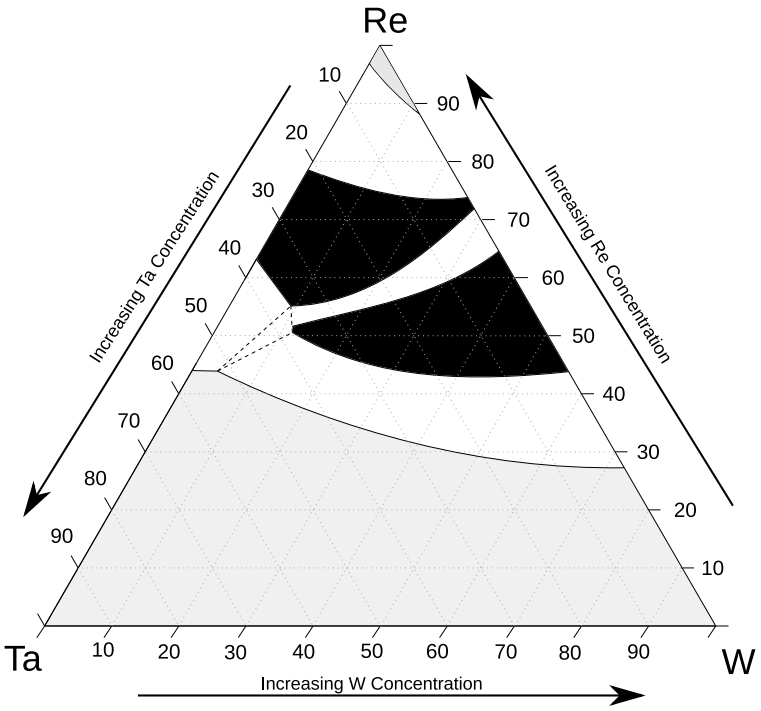


Figure 2.7: Ternary equilibrium phase diagram at 1473 K for the W-Re-Ta system. Adapted from the images reproduced in [84] and originally sourced from [95]. The χ and σ phase regions are shown in black.

σ and bcc W. The original data upon which the diagram is adapted is based on [95] and there remains a large region of the diagram that is unknown. For the study of transmutation, the material compositions investigated in this project are within the concentrated W corner of the diagram. More work is needed to understand this system fully. The region of the ternary phase diagram in which χ phase formation occurs is not visible in figure 2.6.

More data is available for the W-Re-Ta system, shown in figure 2.7. The majority of the diagram, with concentrated W and Ta shows mutual solubility within the bcc phase. Other intermetallic phases begin to emerge towards the Re concentrated corner of the diagram. Both χ and σ phase regions are visible, as is a small region of solubility in the Re concentrated corner. As with W-Re-Os, the alloys studied in this work are mainly based in the concentrated W corner of the diagram. The compositions of these samples are shown in figure 4.1 and are summarised in table 4.1.

2.2.5 *Physical Properties of W-Re and W-Os*

Alloying W with Re is known to increase its ductility and reduce its ductile to brittle transition temperature [99–101]. Figure 2.8 shows the effect of increasing Re solute content on the hardness of W-Re measured using Vicker's indentation. There is an initial reduction in hardness due to solid solution softening effects, following by a plateau and then an increasing hardness attributed to σ phase formation at higher Re concentrations [99].

Re, even in small quantities ($\approx$1at.%Re), has a positive effect on the poor DBTT of pure W, as shown in figure 2.9, reducing the DBTT by

over 100 K [99, 100, 102]. Re acts to reduce the average grain size, as shown in figure 2.9, further improving the DBTT, as well as increasing the recrystallisation temperature and improving fracture toughness properties. The presence of 3 and 5 at.%Re in recrystallised W investigated by Gilbert was shown to reduce the tendency for W to undergo inter-granular failure, instead promoting cleavage failure [86]. Re has also been shown to improve creep performance in W [100].

Studies of the effect of Os on W are limited: due to its rarity, alloying with Os over Re is unlikely to offer economic benefits. Studies of Os alloying in Mo did however, find similar hardening effects to Re in W shown in figure 2.8 [102].

2.2.6 *Neutron Induced Microstructural Evolution*

The post-neutron irradiation microstructure of W is characterised by a combination of voids, dislocation loops and Re/Os precipitates [90]. These features are typically identified using either Atom Probe Tomography (APT), Transmission Electron Microscopy (TEM), Scanning Transmission Electron Microscopy (STEM) or a combination of these techniques. The population density of each of these features depends on the irradiation conditions such as the dose and the irradiation temperature.

2.2.6.1 *TEM Studies*

W-Re was investigated as a material for high temperature thermocouples for use in nuclear reactors. As a result, there are several early neutron

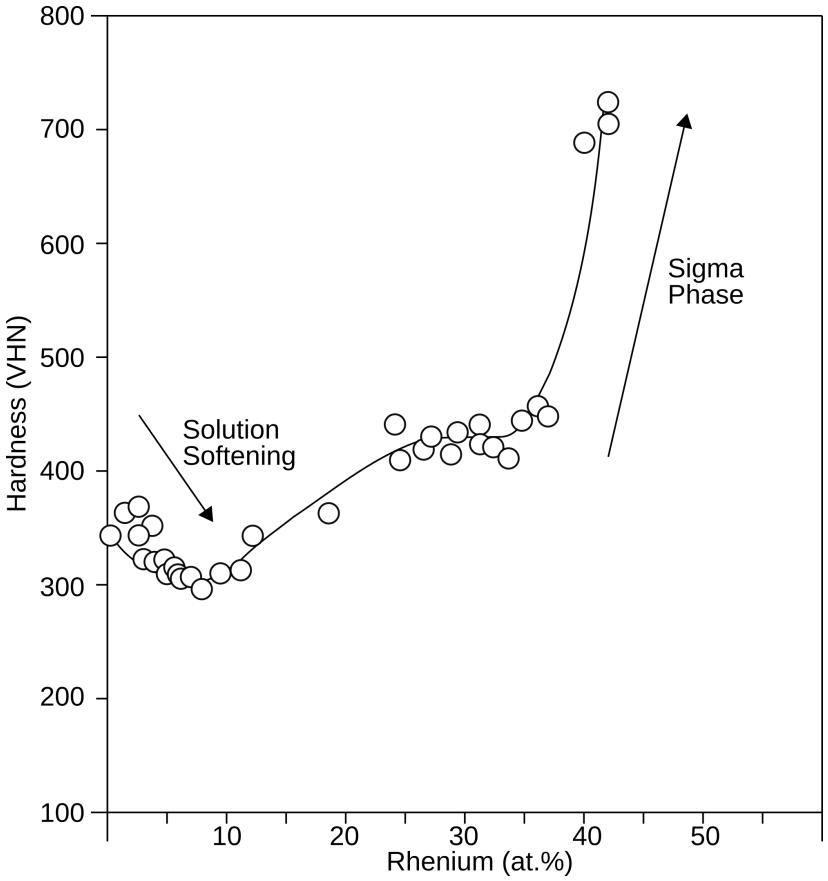


Figure 2.8: Vickers hardness measured at room temperature for W-Re as a function of Re concentration [99].

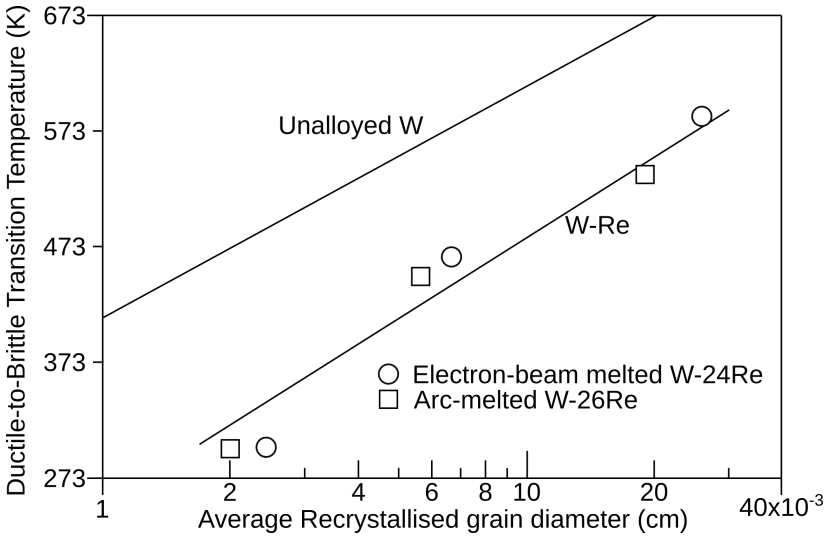


Figure 2.9: DBTT measured using 3-point bend testing in pure-W, W-26Re and W-24Re as a function of recrystallised grain size [99].

irradiation studies of pre-alloyed W-Re and initially pure W which observed precipitation of Re and the formation of voids, using TEM [103–106].

Dislocation loops were also observed in low temperature (343 K) neutron irradiation studies in 1967 [107]. Studies of void formation in samples irradiated at the EBR-II[3] in 1974 by Matolich et. al, suggested that Re acted to suppress void formation, as they measured a substantial reduction in swelling comparing W-25Re to Pure W [105]. Williams et. al found acicular precipitates in pre-alloyed W-Re samples from EBR-II in 1983.

Analysis of diffraction patterns led the authors to conclude that Re rich, WRe_3 χ-phase had formed, rather than the lower concentration WRe σ phase shown in figure 2.5a [103]. The conventional picture of RIS would predict the formation of σ phase rather than χ, leading to the precipitation of Re in W to be referred to as *Anomalous Precipitation*. Other studies use the term anomalous precipitation to describe the formation of σ phase well below its solubility limit. It is not clear from early studies of Re precipitation whether transmutation is fully accounted for, as it is unclear how the final Re and Os concentration was calculated. They do however, provide the first suggestion that precipitation in W-Re cannot be fully explained by the conventional picture of RIS. The effect of neutron irradiation on pre-alloyed W-Os was not studied, and therefore there is more limited data on this system.

Interest in neutron irradiated W-Re increased in the 1990's, when W was

[3]The Experimental Breeder Reactor II is a sodium fast cooled reactor operated by Argonne National Laboratory in the USA between 1964 and 1994

suggested as a candidate divertor material for ITER [108–110]. Nemoto et. al, found a combination of χ and σ phase precipitates in W-26Re, irradiated to 11dpa at 873 K [111], unlike in previous analyses by Williams et. al [103]. Pre-alloying the material with 26Re resulted in the suppression of void formation [111], as was observed previously [105]. Further neutron irradiation campaigns have subsequently been carried out using fast neutrons from mixed spectrum reactors such as JMTR [90, 112], JOYO [112–114], HFR [88, 91] and the HFIR[4]. [89, 90, 112, 114–116] on W-Re alloys at various temperatures ranging from 500–800°C and a range of ≈0.1–1.5 dpa. Hasegawa et. al summarise the evolution of the microstructure under neutron irradiation schematically, as shown in figure 2.10, reproduced from [90]. In pure W at low doses, voids and loops are observed, whereas with increasing dose, larger voids and an increasing population of precipitates emerge. In the pre-alloyed W-Re, void formation is suppressed, resulting in a microstructure dominated by precipitates. It is unclear how this relates to samples in which Re is produced only by transmutation, as void formation and transmutation happen concurrently. Diffraction pattern analysis of these precipitates was inconclusive, and thus they cannot be described as either χ or σ [90]. The role of small quantities of Os on these precipitates is also unknown, and there is a lack of data in irradiated samples with low nominal Os concentrations. There is virtually no data on neutron irradiated W-Os.

[4]JMTR is a light water moderated and cooled test reactor, and Joyo is a test sodium fast-cooled reactor operated, both of which are owned and operated by Japan's Atomic Energy Agency

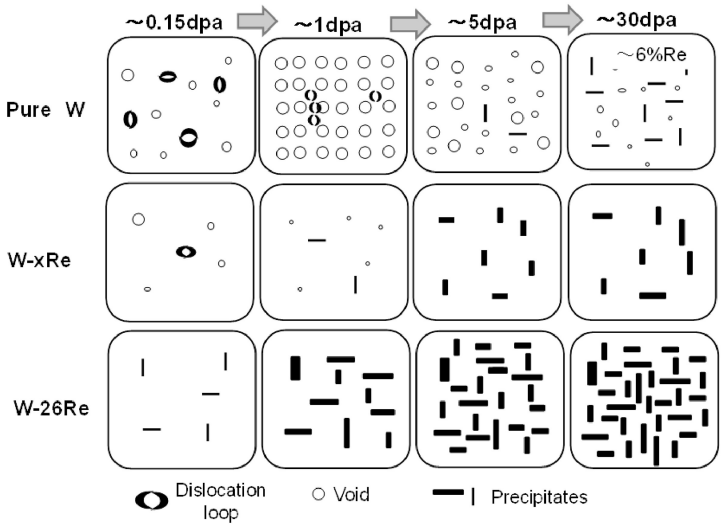


Figure 2.10: Schematic illustration of observed microstructural evolution under neutron irradiation, showing the effects of dose and Re concentration. Reproduced from [90].

Voids also act as point defect sinks and become decorated with Re and Os transmutation products under irradiation. Klimenkov observed this in the 1173 K, 1.67dpa sample from HFR, using High Angle Annular Dark Field imaging (HAADF) and EDX [91] (see figures 2.11 and 2.12), as did Lloyd et. al in 2019 [88][5]. Hu et. al. found needle shaped precipitates in samples from HFIR using EDX and showed that in some cases these precipitates were associated with voids identified with HAADF. In lower dose samples (0.44dpa), void decoration was seen rather than the association of needle shaped precipitates growing from the void [116], as shown in figure 2.13. Though strong diffraction contrast from precipitates was seen, the phase of these precipitates (ie χ or σ) is not currently reported. Hu et. al conclude that voids form prior to the formation of precipitates [116], which confirms the suggestion that voids or small vacancy clusters could act as sinks for

[5]This work was published during this research and is discussed further in chapter 3

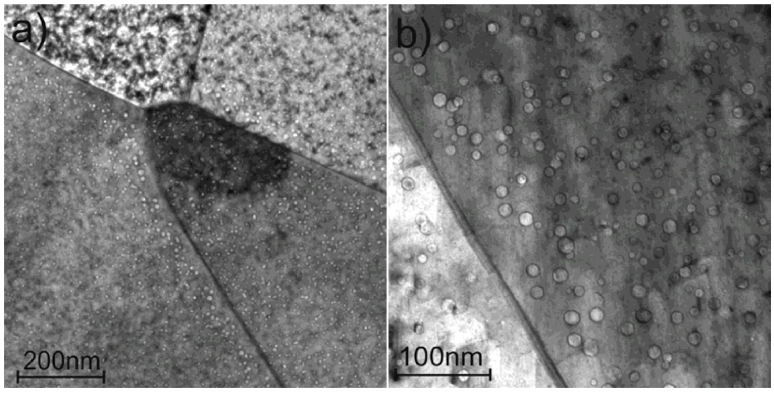


Figure 2.11: TEM image of polycrystalline W neutron irradiated at HFR to 1.67dpa at 1173 K showing voids and grain boundaries, reproduced from [91].

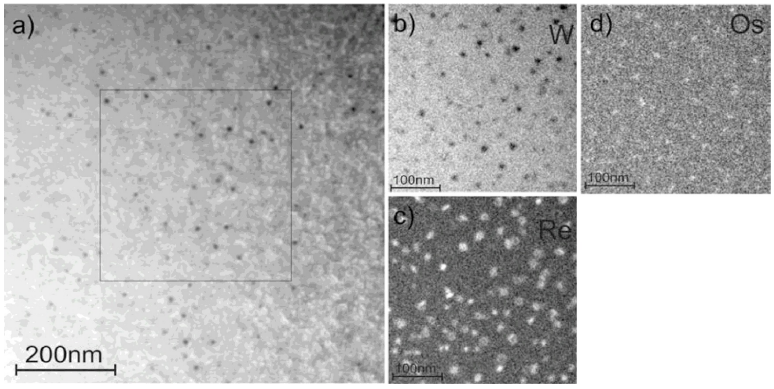


Figure 2.12: TEM images of single crystal W neutron irradiated at HFR to 1.67dpa at 1173 K showing (a) HAADF image of voids alongside EDX mapping of (b) W (c) Re and (d) Os, reproduced from [91].

point defects and allow for the local concentration of solute elements.

The thermal stability of Re clusters was investigated by Hu et. al by subjecting the samples from HFIR to annealing for 2h at 1473 K. Using EDX mapping they show that the clusters present in this sample dissolve back into solution under these conditions [116]. Damage in the PFCs of a reactor could therefore potentially be annealed to remove damage and increase component lifetimes, without causing significant precipitate growth. The response of more concentrated χ or σ phase precipitates to annealing still needs to be investigated.

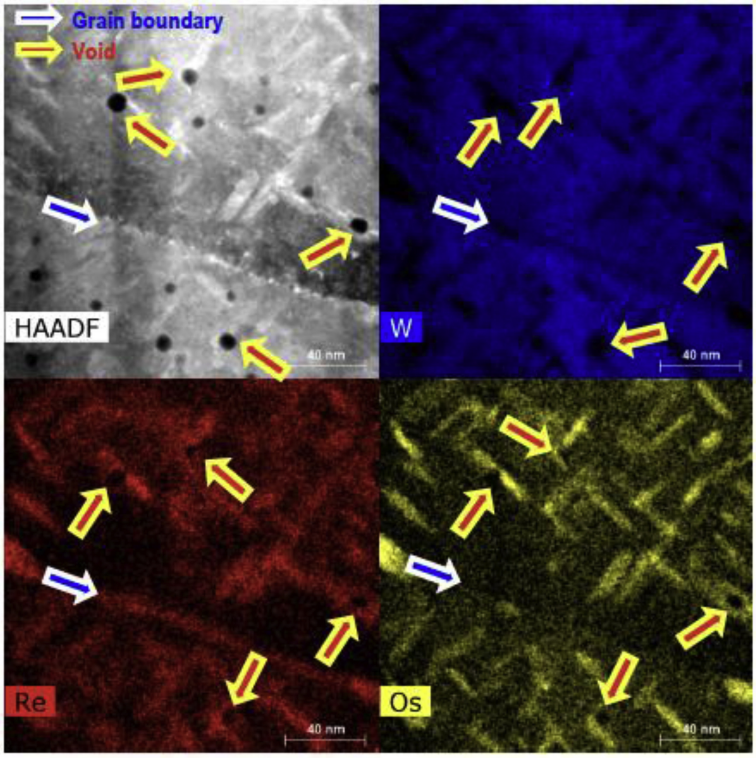


Figure 2.13: TEM imaging of voids, precipitates and grain boundaries in initially pure W sample, neutron irradiated at HFIR to 1.5dpa at 1073 K. The HAADF image with the location of the voids and grain boundary highlighted, and with the corresponding EDX maps for W, Re and Os. Reproduced from [116].

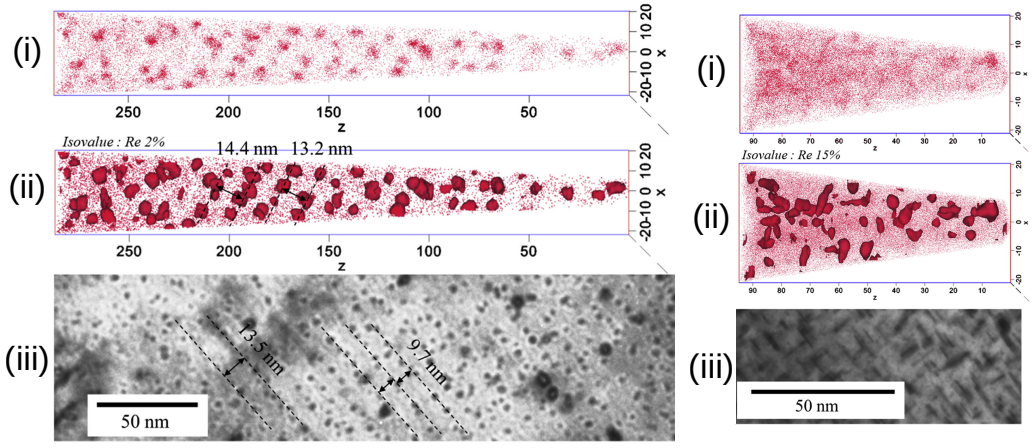
2.2.6.2 *Field-Ion Microscopy and APT*

χ-phase, rather than σ phase, precipitates were also observed in early atom-probe field-ion microscopy studies by Herschitz and Seidman in 1985. High dose (≈8.6dpa) and intermediate temperature (848-948 K) neutron irradiation of W-10Re and W-25Re confirmed that homogeneous precipitation in these alloys was possible, rather than at heterogeneous nucleation sites [117]. Voids were identified in several of these early studies [117–119] and no Re enrichment or depletion was observed [117]. As previously mentioned, studies of the effect of Os are more limited. However, Os segregation to dis-

locations in W was observed by Eaton and Nordén in 1983 using atom-probe field-ion microscopy, and attributed to the difference in atomic volumes [120] (see sections 2.1 and 2.2.3).

More recent APT studies of neutron irradiated W focus primarily on initially pure samples, rather than W-Re alloys in order to focus on transmutation effects [88, 89, 114]. APT of single crystal W samples, irradiated to 0.11dpa at 963 K was carried out by Katoh et. al. Roughly spherical precipitates were observed in the APT, and in STEM-EDX, but unlike previous studies, low dose irradiation resulted in the precipitation of coherent, Re rich precipitates (similar to α' precipitates formed in Fe-Cr), whereas at higher doses, the formation of Re rich intermetallic phases was observed [89]. The authors highlight the role of voids as sinks for point defects, as did Hu et. al, to act as potential nucleation sites, but the impact of these voids on the APT data is not clear (see section 2.2.7).

Hwang et. al analysed both initially pure, and pre-alloyed W-10Re, neutron irradiated to 0.96dpa at 811 K in Joyo, and 0.90dpa at 773 K in HFIR, using APT and TEM. Voids were observed using TEM in the initially pure-W sample and correlated with the spacing of the void lattice [114], though the spacing between features in APT is sensitive to the reconstruction methodology [121–123], and exact correlation is not possible without imaging of the tip directly with TEM prior to APT. In contrast, the pre-alloyed W-10Re sample showed no obvious signs of void formation in the TEM, as shown in figure 2.14, in agreement with Matolich et. al's



(a) Pure-W. **(b)** W-10Re.

Figure 2.14: Comparison between (i) Re atomic mapping from APT with (ii) Re isoconcentration surfaces and (iii) a TEM image of a different region of each sample. Shown in (a) is the data for initially pure W and (b) is the initially W-10Re alloy, both irradiated at Joyo to 0.96dpa at 811 K. Reproduced from [114].

findings in W-25Re [105].

Hwang et. al provide the first insight into Re/Os clusters in neutron irradiated W using APT, by plotting the average cluster compositions from APT on a ternary phase diagram for W-Re-Os. The clusters all lie within the bcc W, or σ+W region [114], rather than the high Re concentration χ phase seen by other neutron irradiations at HFIR [90, 111]. The average value for all of the clusters in the analysed data is provided, but not a measure of spread in the values. Furthermore, the clusters are identified using a maximum separation algorithm but not all of the parameters used in this method are provided, making direct comparison difficult. The composition of a single cluster is sensitive to where the interface between cluster and matrix is drawn. More information on this boundary layer is needed to better understand the clusters. No APT of neutron irradiated W to date

has found evidence of the σ or χ phases observed in TEM studies. More APT studies of samples from other fission reactors with known neutron energy spectra are needed to further understand the precipitation, particularly from samples in which the presence of σ or χ has been independently confirmed.

Hwang et. al. also emphasise that voids are not visible in APT, and discuss the potential for the introduction of artefacts by the voids. The effect of trajectory aberration on the atomic density in the reconstructed APT data was also discussed with respect to the HFR samples studied by Klimenkov et. al [88, 91]. High atomic density was reported in the cores of Re/Os precipitates formed under irradiation, indicating that these precipitates may be correlated with voids [88]. However, as Hu et. al, reported in their samples form HFIR [116], not all of the precipitates were associated with voids. Some of these precipitates were isolated, or associated with voids too small to observe using TEM. This is discussed further in section 2.2.7.

There are limited studies of samples with DEMO relevant doses but with lower Re and Os concentrations, as shown in figure 2.3. Os in particular has been shown to strongly precipitate even at concentrations as low as 0.1at.%Os [88]. Understanding the precipitation of Re and Os under DEMO neutron irradiation conditions requires further study, particularly of samples representative of the early stages of transmutation.

2.2.7 *Voids in APT*

Voids, bubbles and vacancy clusters are known to impact the process of APT. Figure 2.15 shows a sequence of FIM images taken through a void in neutron irradiated Mo, taken by Brenner and Seidman in 1975 [124]. Distortions around the void, in comparison to the perfect crystal underneath the void shown in image 18 of figure 2.15, are a result of local magnification of the emitted ions. Birdseye et. al. in 1974, show that this effect is a result of local field enhancement in the region of the void, or other surface features, that result in a non-uniform sample surface[125].

The same effect can be expected in APT where the emitted atoms, rather than deposited gas imaging ions, experience changes to their expected trajectory. In APT experiments, a perfectly hemispherical tip is assumed in order to reconstruct the atomic positions [126]. The impact of voids on APT data, however, is not fully understood. Some authors have reported an apparent decrease in the atomic density associated with the location of a void [127], but the majority see an increase in the apparent atomic density due to focusing of the ionic flight path [88, 126, 128]. The observed atomic density artefacts are likely to be influenced by the void size and the ratio of the void to specimen radius, though further study of this is needed.

An increase in the apparent atomic density associated with Re/Os precipitates, likely to have formed on voids in neutron irradiated W has been reported [88]. The effect has been modelled computationally by Fletcher et. al, and high atomic density regions have been found in the location of

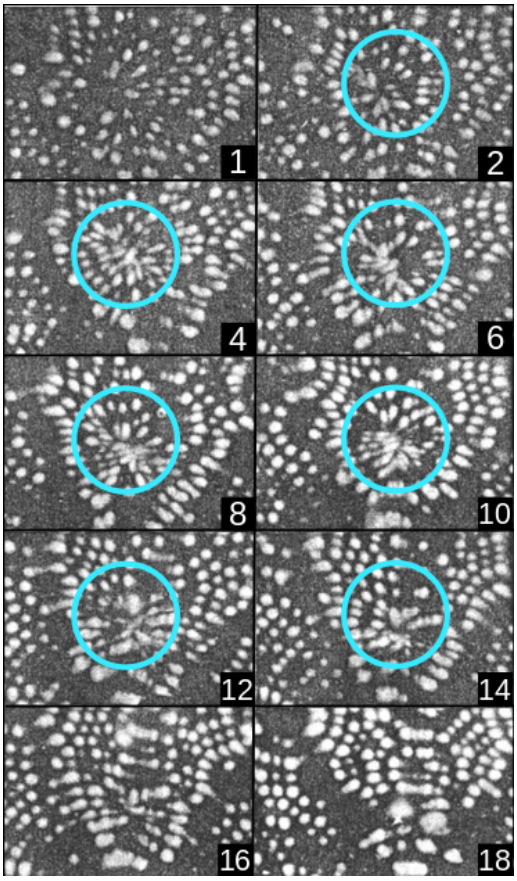


Figure 2.15: 10 FIM images from a sequence of 18 images taken through a controlled evaporation of a void in neutron irradiated Mo, adapted from [124]. Panel 18 shows the perfect crystal structure in the underlying material beneath the void. Position of the void highlighted with blue circle.

simulated voids [123].

Wang et. al, were able to use correlative APT and STEM-HAADF imaging to demonstrate the impact of voids experimentally, in Ni-based single-phase-concentrated solid solution alloys. A series of images of the APT samples prior to performing APT were taken, at different rotations. Figure 2.16 shows a subset of the images with the voids visible in TEM. Figure 2.16 e–h shows the corresponding APT data after reconstruction. By tracking the positions of the voids in the TEM and comparing to the APT, the locations of the voids can be pinpointed and correlated with the

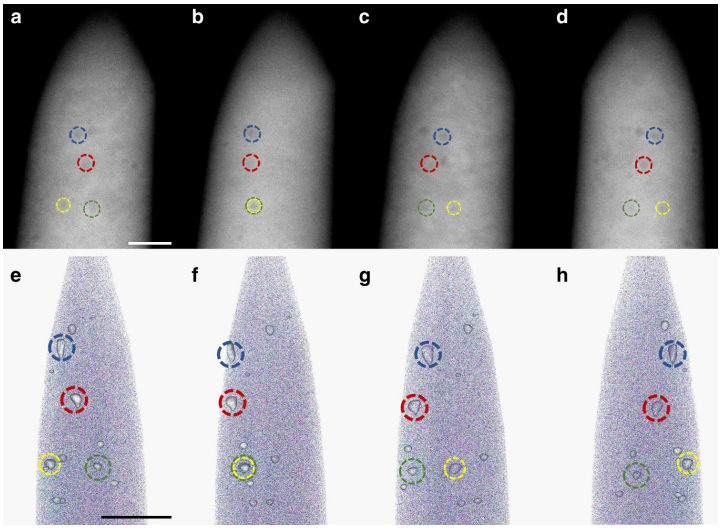


Figure 2.16: STEM HAADF and reconstructed APT data at various rotations. In the APT data, high density regions are highlighted using isodensity contour surfaces at 50 atoms/nm^3.

increased atomic density, highlighted by the isodensity contours in figure 2.16e–h [126].

The impact of voids on APT data has major implications for the study of materials expected to form voids or bubbles under irradiation. Understanding their impact is key to interpreting data on a range materials, including neutron irradiated W-Re-Os, and highlight the importance of using complementary techniques. In the W-Re-Os system, the presence of low-field evaporation threshold precipitates, not associated with voids, make interpretation more challenging, as these features will also introduce trajectory aberrations [123, 129].

2.2.8 *Ion Induced Microstructural Evolution*

As discussed in section 1.5.2, the costs and safety aspects of neutron irradiation, combined with the complexity of managing the transmutation rate

make neutron irradiation experiments difficult, time consuming and expensive. Ion irradiation has been used to study the expected property evolution in W from varying amounts of Re and Os. In this section, the microstructural evolution of ion implanted W, W-Re, W-Re-Os and W-Re-Ta will be discussed. Key differences in the microstructure produced by ions limit their practical applicability for the prediction of component performance in fusion.

2.2.8.1 *TEM*

Yi et. al analysed ion irradiated W and W-5Re using a range of temperatures and compositions, using both in-situ and ex-situ experimental setups. Self-ion irradiations at 773 K using 150 keV W^+ ions to a dose of 1dpa, led to the formation of both $\mathbf{b} = \langle 111 \rangle$, and $\mathbf{b} = \langle 100 \rangle$ dislocation loops [130], unlike in earlier studies in which only $\mathbf{b} = \langle 111 \rangle$ loops were found [130]. Compared to pure-W, smaller loops were found in the W-5Re, implying that Re acted to suppress loop growth. 1D migration of $\mathbf{b} = \langle 111 \rangle$ loops was observed during in situ irradiations at temperatures between 573 K and 1073 K, but not for $\mathbf{b} = \langle 100 \rangle$ loops [131]. Voids were not detected during these experiments indicating either that they did not form under ion irradiation or were too small to be detected using TEM.

Hwang et. al irradiated W and W-3Re to 5dpa with 18 MeV W^{6+} ions at 773 K and 1073 K. Small voids (1.3 nm–1.6 nm) were observed at both 1dpa and 5dpa [132], with a slightly smaller average void radius in the pre-alloyed W-3Re. Very small voids, such as those observed by Hwang et. al

are difficult to image, and the full focal series is not provided. It is possible that such features could be surface damage, given W can be sensitive to oxidation at the scale of a TEM foil or APT tip.

High temperature annealing studies of ion irradiated W by Ferroni et. al, found no observable voids or vacancy clusters prior to annealing, but after 1h at 1073 K, started to see visible voids in the TEM. Coarsening of these voids was observed upon annealing to 1673 K, alongside the removal of interstitial dislocation loops [133]. The impact of void decoration with Re and Os, observed under neutron irradiation [88, 91, 114, 116], on void growth under annealing is unknown, but is an important consideration for damage removal strategies in a fusion reactor.

Smaller voids in ion irradiated W are likely a result of a high dose rate, and the effect of pre-alloying with Re on the defect production and migration. There are no studies which measure the diffraction patterns produced by Re/Os rich precipitates formed under ion irradiation, and as such it is unclear whether ion irradiation produces χ or σ phase precipitates. The majority of literature on ion irradiated W uses APT to investigate the composition of precipitates and clusters, without diffraction pattern analysis from TEM.

2.2.8.2 *APT*

Xu et. al, carried out a comprehensive study of binary W-2Re and ternary W-1Re-1Os an W-1Re-1Ta, self-ion implanted to 33 dpa at temperatures of 573 K and 773 K. The precipitation in these experiments was found to

be highly dependent on the irradiation temperature. Figure 2.17 shows the microstructures observed using APT by Xu et. al for the W-2Re, W-2Re-1Ta and W-1Re-1Os samples. It is clear comparing the binary W-2Re sample in (a) and (b) that at 773 K, larger precipitates have formed [97], suggesting increased point defect diffusion could have been a contributory factor. In similar irradiation at varying doses to 573 K by Armstrong et. al, Re clustering in W-5Re was much less pronounced. Only the 33 dpa sample exhibited strong Re clustering, unlike the 1.2 and 13 dpa samples [75].

Xu et. al also demonstrated in (e) and (f), that Os had acted to suppress Re clustering, by preferentially forming small clusters of Os, when compared to (a) and (b) [134]. The clustering of Os in (e) and (f) also showed a strong dependence on the irradiation temperature, as clustering was much stronger in the 773 K sample. Unlike in neutron irradiated samples analysed with APT [88], no substantial increase in the atomic density (either from voids or second phase precipitates) was reported. Xu et. al measured a peak concentration of approximately 30at.%Re in the W-2Re and 20at.%Os in the W-1Re-1Os. This potentially puts the clusters within the bcc+σ phase region of the W-Re and W-Re-Os phase diagram (figures 2.5a and 2.6) however, this analysis is sensitive to the interface used to define the clusters [135]. More work is needed to understand the differences between ion and neutron irradiated material.

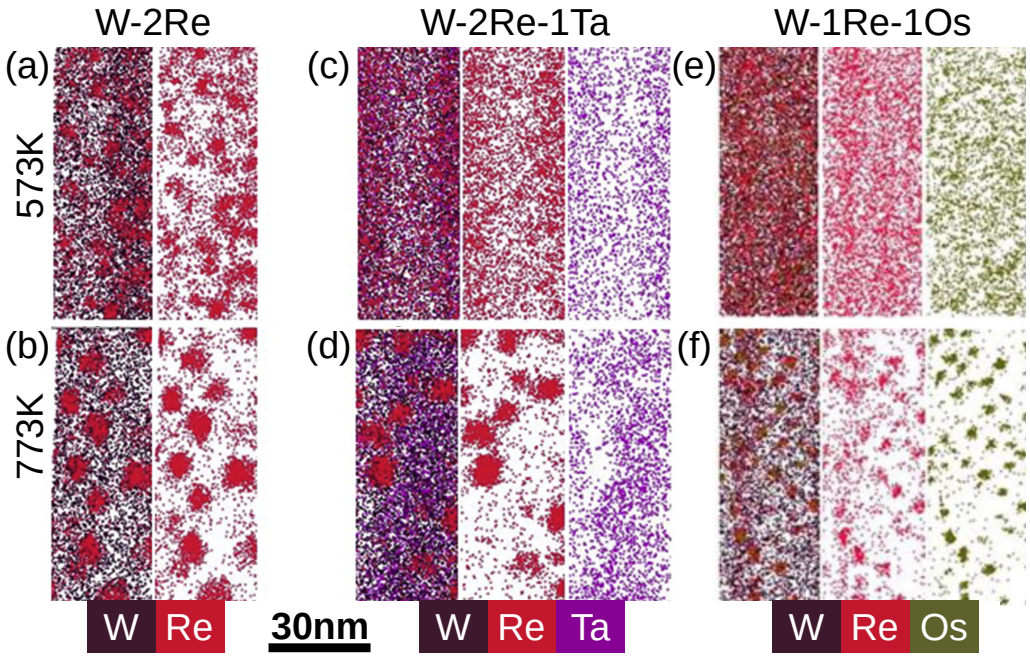


Figure 2.17: 4 nm slice through atom map of 6 samples, 3 irradiated at 573 K and 3 at 773 K. On the left most side in figures (a) and (b) are the W-2Re sample irradiated at 573 K and at 773 K respectively. (c) and (d) show the W-2Re-1Ta sample irradiated at 573 K and at 773 K respectively and (e) and (f) are the W-1Re-1Os sample irradiated at 573 K and at 773 K respectively. All are irradiated to a peak dose of 33 dpa calculated using the full-cascade model ($\approx$ 18 dpa under quick cascade mode).

2.2.9 *Summary of Irradiated Microstructures*

Neutron irradiation produces Re and Os decorated voids, and Re and Os rich precipitates, which are a mixture of χ or σ phase, depending on the neutron spectrum used. Ion irradiation produces smaller voids, and Re and Os rich clusters, with indicated compositions below the threshold for σ phase formation.

There are differences between neutron irradiated samples from different reactors (due to the transmutation to dose ratio) and between ion and neutron irradiation. There are also differences between ion irradiations carried

out at different facilities and using different methods to estimate the dose. Differences between ion and neutron irradiations are most likely linked to vastly different dose rates and the effect of pre-alloying with Re and Os. Re in neutron irradiations has been linked to the suppression of void formation by several studies. It is unclear whether this pre-alloying effect arises due to a change in defect mobility or due to a reduction in the surviving defect population after a cascade. It is unclear why no ion irradiation studies find evidence of σ or χ phase formation, but it is possible that this is coupled to the comparative lack of void formation.

There is a lack of samples with DEMO relevant Re and Os concentrations (either through transmutation or pre-alloying), both ion irradiated and neutron irradiated. In particular, more work is needed to study the effect of small quantities of Os, which appears to play a major role in the precipitation under neutron irradiation. Differences between ion irradiations and neutron irradiations can be addressed through computational modelling, but need to be validated against experimental data.

2.3 Modelling Microstructural Evolution in W

The occurrence of radiation induced phenomena is linked to the formation of point defects by radiation damage, which can be of vacancy type or interstitial type. Self-interstitial defects contain two atoms of the same type as the lattice and occupy a shared lattice site. Modelling the behaviour of these defects in W and alloys of W-(Re,Os) is key to understanding the

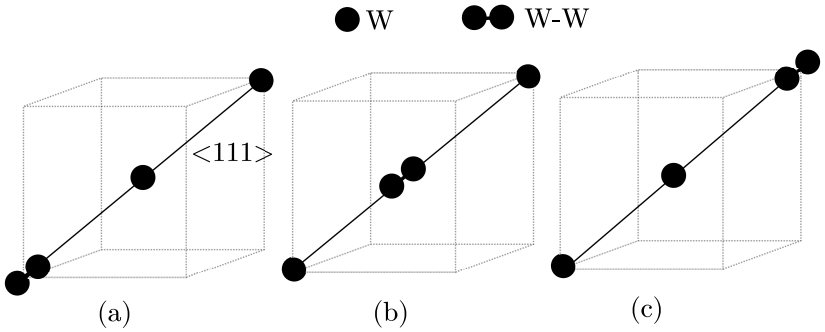


Figure 2.18: 1 Directional migration of a W-W interstitial dumbbell along the < 111 > direction. Reproduced from [140].

radiation induced phenomena outlined in the previous section.

2.3.1 *Defects in Pure W*

Self-interstitial defects in pure W form dumbbell configurations. Density Function Theory (DFT) studies by Nguyen-Manh et. al, have found that the most stable configuration of the W self-interstitial dumbbell is the ⟨111⟩, and that it undergoes rapid one dimensional motion [136, 137] with a low barrier to migration (0.05 eV [137], see figure 2.18). By comparison, previous interatomic potentials had predicted that the ⟨110⟩ would be the most stable in W.

Vacancy type defects in W exhibit unique properties. Wróbel et. al highlight that the di-vacancy interaction in W is repulsive. Typically the di-vacancy binding is attractive in materials such as Fe and acts as a nucleation point for larger vacancy clusters. Void formation in W is initiated by clusters of 3 or more vacancies, at which point the interaction becomes attractive [98, 138, 139]. This has ramifications for pair interaction models in which only the interactions between pairs of defects and atoms are considered.

2.3.2 *Defects in W-(Re,Os)*

The unique properties of the interstitial type point defects in W-Re and W-Os are thought to be the reason for the anomalous precipitation of Re and Os observed in neutron irradiation experiments. Becquart et. al calculated an attractive binding energy between both SIAs and vacancies in W, with impurity Re atoms (0.80 eV and 0.23 eV respectively [141]), indicating that both the vacancy and mixed W-Re interstitial (see figure 2.19) may contribute to the RIS. Suzudo et. al studied the behaviour of the W-Re and W-Os mixed interstitials further, investigating the migration pathways and calculating the binding energies for each defect type. Increased mobility of the W-Re dumbbell results in the enhanced recombination after a cascade, thus limiting the vacancy population and suppressing void formation [142].

The W-(Re/Os) mixed dumbbells have a very low migration barrier for rotation, E_R, suggesting that the mixed interstitial undergoes effective 3D motion through a series of rotation and translation events, rather than simple 1D motion as is the case for the self-interstitial. The 3D transport of solute through this mechanism leads to Re decoration of sinks of point defects [82, 142, 143]. Suzudo et. al also suggest the increased mobility of the mixed interstitial following the damage cascade could result in increased recombination, and thus a reduction in the vacancy population [82, 142]. This is a possible explanation for the suppression of void swelling in W-Re observed experimentally by Matolich et. al in 1974 [105], and in subsequent studies.

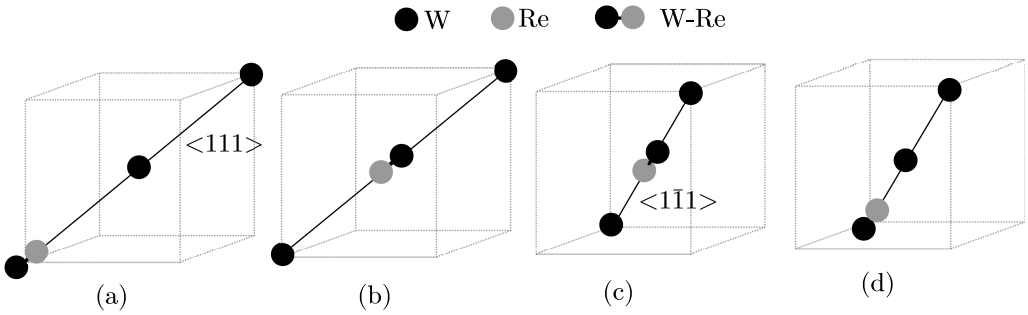


Figure 2.19: Migration of a mixed W-Re interstitial dumbbell via translation and migration. Reproduced from [140]. Mixed dumbbell migrates along $< 111 >$ direction and rotates to $< 1\bar{1}1 >$ direction. Following this process the dumbbell effectively migrates along the $< 100 >$ directions.

Wróbel et. al find that in dilute W-Re alloys, the lower energy configurations of defects are predominantly of Re-vacancy type. They observe that for the vacancy dominated alloy structure, the convex hull line has a maximum of 30 meV/atom [138], whereas it is about 10 times higher for the self-interstitial dominated alloys studied by Gharaee et. al [144]. Wróbel et. al simulate the formation of small voids, decorated with Re using a cluster expansion Hamiltonian, parameterised by a large DFT database [138].

Messina et. al, found that small vacancy clusters were stabilised by the presence of Re and Os, with Os having the strongest effect. They also found a significant reduction in vacancy mobility following the introduction of Os into their calculations [145], supporting the hypothesis that pre-alloyed W-Os would limit void formation compared to pure W. The reduction in vacancy mobility has important ramifications for the comparison between ion and neutron irradiated W.

Molecular dynamics simulations are used to study defect survival rates following cascades, and can be used to support the hypothesis that Re

and Os enhanced defect motion increases recombination rates. Recent MD simulation in W-Re by Fu et. al do not indicate significant changes to the defect survival probability by the introduction of 10-20at.%Re [146]. But MD simulations are dependent on accurate interatomic potentials. Accurate potentials for W-Re-Os alloys did not exist until recently [139].

2.3.3 *Kinetic Studies of Radiation Damage in W*

Kinetic Monte Carlo (KMC) is a subset of the Monte Carlo (MC) algorithm that is based on the generation of a distribution of random numbers, as is discussed further in chapter 5. A fixed lattice of points is created based on the crystal structure. Each point of the lattice is given a state i which determines the species of the atom at that point. The system evolves through the change of states, $i \rightarrow j$, at a rate based on the change of energy between states i and j [147, 148]. The use of KMC to study defect migration started in the 1960's and was applied to the study of vacancy motion in binary alloys [149]. A model of vacancy mediated diffusion of solute atoms in a bcc alloys was developed by Le Claire at Harwell in 1969, upon which many modern models are based [150].

The basis for the KMC technique is the calculation of the probability for events to occur, based on the change in energy between initial and final states. One commonly used technique for quantifying this change in energy between initial and final states is to use a *pair interaction model*, or *broken bond model*. Under the pair interaction model, constant interactions between pairs of atoms are defined, commonly using DFT calculations, and

summed over to build up an initial energy. This approach has been used for a range of alloy systems including Fe–MnNi [151] Fe–Cr [152, 153] and W–Re [138, 154]. Reuter and Scheffler first proposed combining DFT calculations and KMC simulations in 2004 to study the oxidation of RuO_2 [155, 156]. Recent extensions to the pair interaction model have included a local solute concentration dependence of the interactions. Martinez et. al introduce a local Cr concentration dependence on the Fe-Cr interaction [152], and Huang et. al use the fitting of the enthalpy of mixing to introduce a local Re concentration dependence for the W-Re pair interaction [154]. Soisson et. al implement a local solute dependence on the saddle point pair interactions in Fe-Cr [157].

Further extensions to the pair interaction model have introduced interstitial type defects as well as vacancies. Senninger et. al. implement self-interstitial defects into their model for Fe-Cr system in order to study RIS. This model successfully reproduced RIS in Fe–Cr and showed the enrichment of Cr at grain boundaries, modelled as an ideal planar points sink [153].

Huang et. al developed an on-lattice, KMC model, parameterised by DFT calculations in order to study the binary W-Re system [154, 158]. In simulations at 1800 K using a dose rate of 10^{-3} dpa/s in a simulation cell with 2at.%Re, Huang et. al predict the formation of Re precipitates, stabilising at a central concentration of 50at.%Re. These simulations, designed to compare with Xu et. al's ion irradiation studies [97, 134] suggest

that fast moving W-Re mixed interstitials become trapped in regions of increased Re concentration, or by binding with other mixed interstitials. The immobilised mixed interstitials allow sufficient time for vacancy migration to become significant. The vacancy eventually annihilates with the trapped mixed interstitial leading to an enrichment of Re over time. Vacancies act to dissolve the boundary of the precipitate, making the interface more diffuse over time [154]. Subsequent studies with this energy model only predicted cluster nucleation on ideal point defect sinks [159].

In both of these studies, the Re-Re dumbbell is not included due to the supposed low probability for its formation. With solute being transported via the mixed interstitial, it is not clear whether or not this would be the case. The application of a pair interaction model including both vacancies and interstitial type defects, with Re and Os solute elements in W is key to understanding RIS and anomalous precipitation in W.

There is not a complete study of interactions for a tertiary or quaternary W–Re–Os–Ta system at present. Huang et. al et al provide a list of W–Re interaction parameters including W-W and W-Re type dumbbell interactions [154]. W–Ta is described by Muzyk et. al [98], and several papers provide values for the interactions in W–Re–Os [82, 140].

Object KMC (OKMC) has been used by D. Mason et al to study the behaviour of point defects, voids and loops following a collision cascade in W. By using MD as an input, simulations can be extended to seconds from femto seconds as is the case with MD [21, 160]. In OKMC, multiple

atom objects such as loops and voids are assigned effective rates and states. As such, the motion of a cluster is treated as a whole rather than the individual atoms [147]. These simulations demonstrated the shrinking of large dislocation loops in W at low temperatures and the gliding motion of loops at high temperatures, which agreed with experimental studies of pure W [21, 160].

2.4 Properties after Irradiation

Understanding how the microstructural evolution discussed in sections 2.2 and 2.3 corresponds to changing material properties, is key to designing reliable components for a reactor. Mechanical property changes after irradiation are usually discussed in terms of the shift in the ductile to brittle transition temperature[6] (DBTT) and irradiation hardening (the measured difference between the hardness after irradiation and before irradiation) measured using either micro or nano indentation.

2.4.1 *Irradiation Hardening*

Vickers microindentation is a commonly used engineering method for measuring hardness, but techniques such as nanoindentation are also typically used for ion irradiated material, due to the shallow indentation depth. This

[6] the DBTT is a measure of the change from ductile to brittle behaviour in a material, typically measured using Charpy impact testing. As test temperature is reduced, the energy absorbed by the specimen progressively transitions from high energy absorption at higher temperatures, to reduced energy absorption at lower temperatures. The temperature at which this transition occurs can be defined in several ways, such as the half way point between upper and lower shelf energies, or by the temperature at which a specific impact energy is reached (typically 40J).

allows measurements to be taken within the implanted region of an ion implanted sample (see sections 1.3.2 and 1.5.2).

2.4.1.1 *Neutron Induced Hardening*

Neutron irradiation induced hardening of W is a well known phenomenon, and has been observed in samples from various reactors including the Japan Materials Test Reactor (JMTR) [90, 161], Joyo [90], and the High Flux Isotope Reactor (HFIR) [89, 90, 115]. Irradiation hardening is consistently observed in neutron irradiated samples from different reactors.

Hu et. al. observed hardening in samples from HFIR, measured using Vickers micro-indentation, and used the analysis of TEM images to split the hardening into different contributing factors. At low temperatures (<773 K) and low doses (<0.15dpa), the hardening was primarily attributed to dislocation loops, whereas at high doses (>1.5dpa), the hardening was mainly due to Re/Os precipitates, introduced through transmutation. At intermediate doses (between 0.15 and 1.5 dpa) and temperatures, the primary contributor to the hardening was voids, with a smaller contribution coming from loops [115]. This effect was also seen by A. Hasegawa et. al, where at low doses (<0.15dpa) hardening was caused by voids and loops, and with increasing doses a significant hardening developed, which the authors attribute to the formation of χ-phase precipitates.

Correlating these property changes is complex, because of the number of variables involved with an irradiation. Hu et. al. find precipitates are the primary contributor to hardening at high doses [115], but under a different

neutron spectrum the amount of Re and Os (as well as the ratio of Re to Os) will be different for a given dose. The hardness as a function of solute concentration in irradiations from various reactors is given in figure 2.20. There is a trend between increasing solute concentration and hardening, but in neutron irradiations the solute concentration is coupled to the dose. Figure 2.20 shows the hardening as a function of dose, with the marker size representing the total solute after irradiation in the sample.

Figure 2.20 also shows the lack of high dose, low transmutation rate neutron irradiation experiments. Sample from Joyo and HFR which use a fast neutron spectrum have an improved response. Irradiation temperature also plays a role, with increasing irradiation temperature correlated with increasing hardening as shown by figures 2.20 e and f. There is a lack of experiments at the highest temperatures, and at reactor relevant temperatures as high as 2000 K [31, 32]. There is also a lack of data at high doses at lower temperatures, which may be important for understanding damage in the strongly cooled section of components near to the coolant piping, though the temperature and transmutation rate in these sections needs clarification.

2.4.1.2 *Ion Induced Hardening*

Irradiation hardening has been measured using nanoindentation after self-ion irradiation in pure-W [75, 132, 162], W-Re [84, 97, 109, 134] W-Re-Ta [84, 97, 163] and W-Re-Os [84, 134].

Xu et. al measured 5.38 GPa hardening at 773 K but only 3.22 GPa

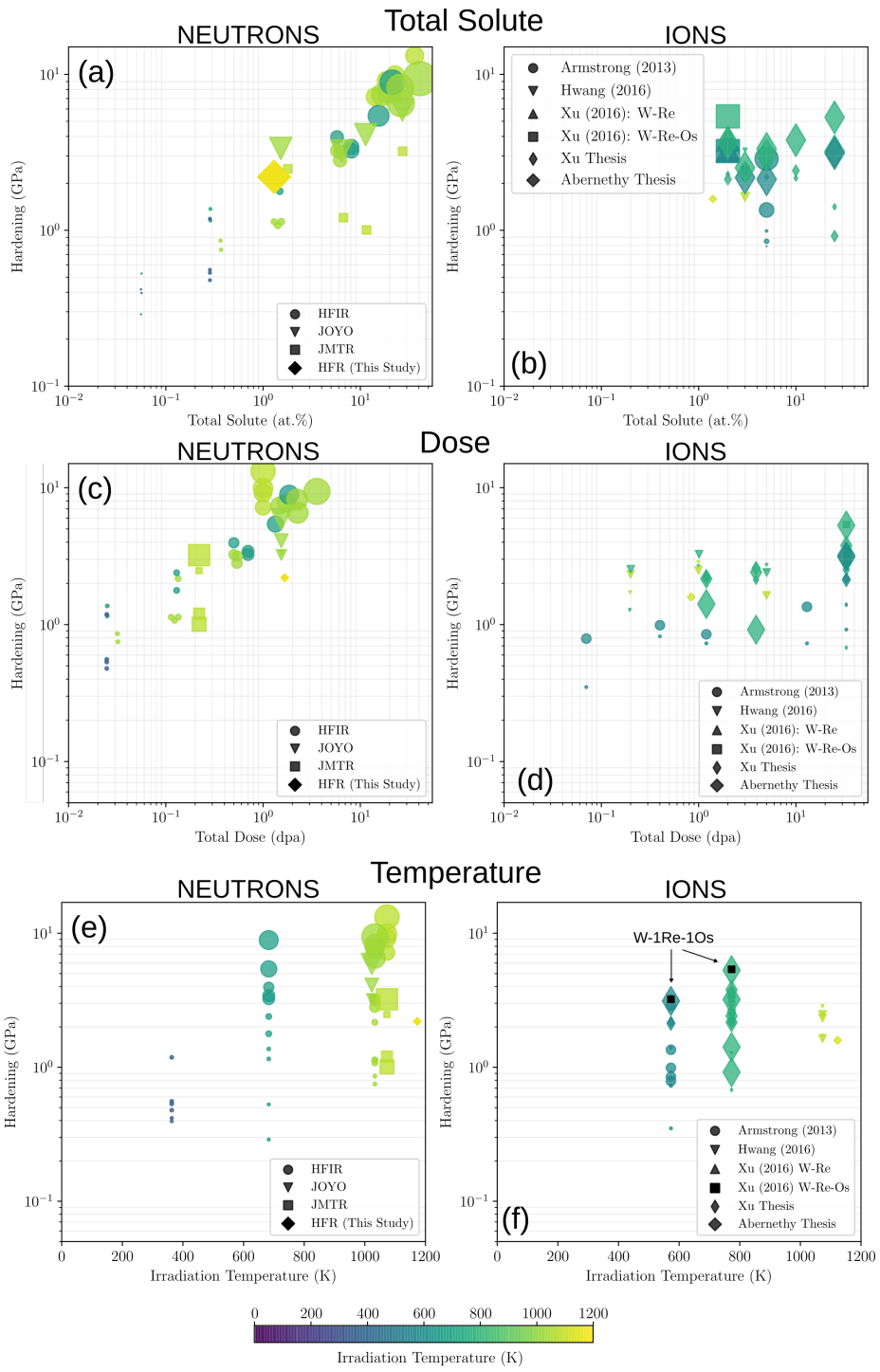


Figure 2.20: Comparison between irradiation induced hardening as a function of the (a) and (b) total solute concentration; (c) and (d) the total dose in dpa, and (e) and (f) the irradiation temperature. Solute concentration is Re + Os either from transmutation, pre-alloying or a combination of both. The marker size in both (a) and (b) is a measure of the dose, and otherwise a measure of the total solute concentration.

hardening at 573 K, for a W-1Re-1Os sample [134]. But as shown in figure 2.20 there is not a consistent trend between different studies, indicating that other factors such as sample processing may be important. Armstrong and Britton demonstrated a greater degree of hardening in annealed, ion implanted W-5Re compared to the same material in the as-rolled condition [164].

The use of SRIM to quantify dose in ion irradiation experiments is another source of uncertainty. The standard method outlined by Stoller et. al [43] for estimating the dose rate states that the *Quick Mode* method should be used, whereas Xu et. al use the *Full Cascade Model*. These two models can produce dramatic differences in the reported dose, as is discussed in section 4.2.

Another potential source of error is the value of the displacement threshold energy used. Xu et. al [84, 97, 134], Hofmann et. al [165], Abernethy [109] and Armstrong et. al [75, 163, 164] use 68 eV for the E_d however, Hwang et. al [132] and Zhang et. al [162] use the value in the ASTM standard listed by Stoller et. al [43] which is 90 eV [166]. The actual displacement threshold energy depends on the orientation of the crystal to the incident particle as well as the type of material: 42eV for (100), 44eV for (111) and 70eV for (110) in W [167]. The average of these gives an E_d of 55eV. It is not clear which value for the displacement threshold energy is the most accurate, but for comparison between different experiments, the ASTM standard value appears to be the most suitable value to use as it follows the currently

recommended standard.

Considering the irradiations of Xu et. al only, both Re and Os contributed to an increase in hardening under irradiation. Increasing the amount of Re in the alloys led to an increase in hardening after irradiation [84]. Alloying with 2at.%Re produced a hardening of 3.26 GPa (573 K) and 3.84 GPa (773 K), however, no reference sample with no alloying is provided. Alloying with 1at.%Re and 1at.%Os had a stronger effect at high temperature, producing a hardening of 3.22 GPa (573 K) and 5.38 GPa (773 K). Xu et. al link this large increase in hardening to the large volume fraction of small precipitates observed using APT (see section 2.2.8.2) [134]. Ta on the other hand had minimal effect on the irradiation hardening, slightly reducing the hardening by suppressing the formation of Re clusters at lower temperatures [97].

More systematic study of Re and Os content in ion irradiated samples is needed to consolidate Xu et. al's findings, as well as extending to reactor relevant temperatures. Furthermore, direct comparison between ion and neutron irradiated W-Re-Os is needed to understand difference in the resultant microstructure.

2.4.2 *Proton Irradiation*

Toloczko et. al irradiated high purity W to 23.3dpa using a beam of 800 MeV protons at between 50 and 270 °C. Unlike many other studies of radiation damage in W, the authors then carried out a series of conventional bending and compression tests, measuring an increase in yield stress by a factor

of 1.6 and a reduction in ductility [73]. The high energy of the proton beam used makes this possible as the stopping range is extended well into the sample, however, with such a high energy the effects of proton induced transmutation and (p,f) reactions may need to be considered. As no further chemical characterisation of the samples was carried out following the irradiation its not clear whether Re formation was significant, and the dose rate of the irradiation was not included.

2.4.2.1 *Comparing Ion and Neutron Induced Hardening*

Figure 2.20 shows the hardening due to irradiation in a number of literature sources for neutron irradiation in (a) and self-ion irradiations in (b). For the ion implanted samples, the hardening is taken with respect to the unimplanted alloyed material, rather than a pure W sample. The size of the plotted points shows the dose and the colour represents the irradiation temperature. There is a clear trend between increasing solute concentration and hardening in the neutron irradiated data, but also between the dose and hardening. This is because in the neutron irradiations, the solute concentration is linked to the dose because of transmutation.

In the ion irradiated data in figure 2.20(b), there is a less clear trend between increasing solute concentration and hardening. There is a lack of data at lower doses and more dilute solute concentrations. Generally however, figure 2.20(b) shows that there is a correlation between dose and hardening in self-ion implanted samples, but there is no clear correlation between the total solute concentration in the initial state and the hardening

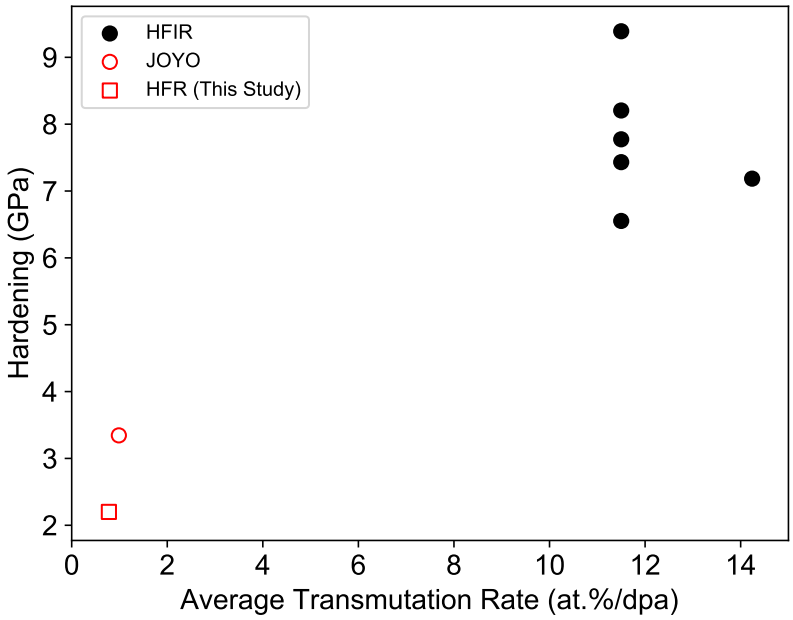


Figure 2.21: Hardening produced in initially pure W, neutron irradiated at JOYO, HFR and HFIR to doses of between 0.7 and 3dpa, at temperatures of between 1000 and 1200 K, plotted as a function of the rate of solute (Re + Os) production, per dpa in units of at.%/dpa.

observed after self-ion irradiation. This may be in part due to uncertainty in the dose arising from a range of factors which make comparison of different ion irradiations difficult.

There are few neutron irradiation studies with directly comparable conditions. Figure 2.21 shows a plot of hardening vs the average transmutation rate for irradiations in which the total dose is between 0.7 and 3dpa, and the irradiation temperature is between 1000 and 1200 K.

2.4.3 *Brittle to Ductile Transition*

The DBTT is a measure of the temperature at which a material undergoes a transition from ductile to brittle fracture, characterised by a reduction in the energy absorption under impact. Radiation damage is known to

increase this temperature, meaning that brittle behaviour is exhibited at higher temperatures.

There is at present limited data on the effect of neutron damage on the DBTT in W. Abernethy et. al characterised the DBTT in single crystal neutron irradiated W from HFR (characterised by Klimenkov et. al [91] and Lloyd et. al [88]) using four point bend testing. A shift in the DBTT of approximately 500K was observed after a dose of 1.7dpa and using a strain rate of $7 \times 10^{-6}\,\mathrm{s}^{-1}$, in agreement with earlier studies [66].

Understanding the underlying mechanism is key to developing design criteria. Abernethy et. al conclude that dislocation mobility near the crack tip is responsible for the their observations, despite the presence of small voids in the irradiated material. This study, however, focussed on a single dose only and prediction of component lifetimes will need more thorough investigation of the effects of multiple doses at appropriate rates of transmutation.

2.4.4 *Thermal Diffusivity*

Thermal diffusivity measurements were carried out by Fujitsuka et. al on 330 K neutron irradiated W and pre-alloyed W-Re from JMTR. They observed a consistent decrease in thermal diffusivity across all of the alloys irradiated [168]. The reason for this change in behaviour with increasing Re content is not clear, and the authors did not see evidence of precipitation using X-Ray diffraction. More studies in samples containing Re clustering are needed to understand the evolution of thermal conductivity with irra-

diation.

Similarly, Katoh et. al, observed a decrease in the RT thermal diffusivity from 66 $mm^2\,s^{-1}$ to 37 $mm^2\,s^{-1}$ following their irradiation of polycrystalline and single crystal W at HFIR [89]. Figure 2.22 shows the inverse of the thermal conductivity plotted as a function of solute concentration from transmutation, plotted with a summary of literature results [77, 168–170]. It shows that increasing solute concentration from transmutation is correlated with decreased thermal conductivity, however, in neutron irradiations the transmutation level is coupled to the dose.

Non-contact laser-induced transient grating techniques have been used by Hofmann et. al to study the impact of Re on the thermal diffusivity of self-ion and He-ion irradiated W and W-Re [165]. Figure 2.23 shows a trend of decreasing thermal conductivity with increasing Re content in the He ion implanted material. Reza et. al apply this technique to measure the decrease in diffusivity as a function of self-ion dose in pure W [171].

Degradation of the thermal conductivity has implications for component performance. It is not clear from current studies whether changes to mechanical or thermal properties will be the primary component life limiting factor.

2.4.5 *Oxidation*

W is resistant to oxidation at room temperature and is chemically inert, however, it will react in the presence of oxygen to form the volatile compound: tungsten-trioxide (WO_3) at elevated temperatures. Sublimation of

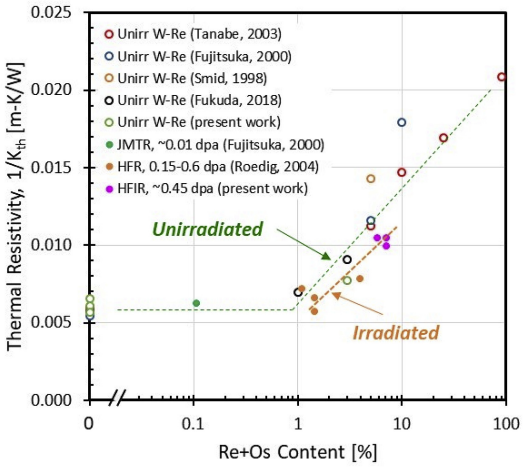


Figure 2.22: Thermal resistivity (1/thermal conductivity) as a function of total amount of solute produced from transmutation in different reactors and irradiations. Reproduced from [89].

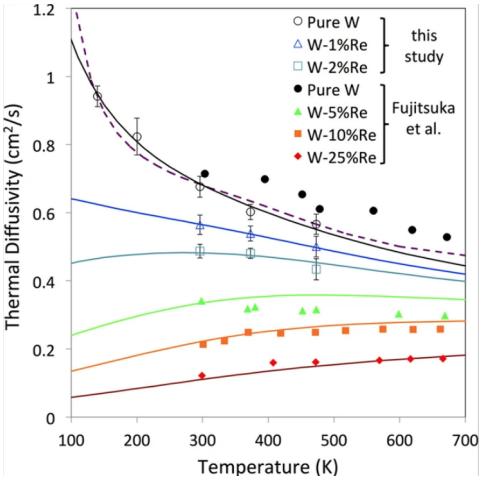


Figure 2.23: Thermal diffusivity of W-Re alloys with open symbols showing the transient grating measurements taken by Hofmann et. al [165].

WO_3 starts at 1023 K and becomes substantial above 1173 K, at a rate as high as 150 kg h^{-1} [172–176]. In a fusion power station, the W isotopes forming this oxide will also be active, posing a substantial safety risk in an accident scenario. The density of WO_3 is 7.16 g cm^{-3}, much lower than that of W, which makes it liable to cracking. At present, there is no systematic study of the impact of Re and Os alloying on the oxidation properties of W. The oxidation rate of pure Re is similar to that of W [177], undergoing linear weight loss with time.

Osmium forms the volatile oxide, osmium-tetroxide (OsO_4) under certain conditions, and is a highly toxic compound. Acute exposure to OsO_4 causes blindness and burning as well as breathing difficulties and death [178]. Experience processing Os containing metal is limited. Pure Os in powder form is dangerous because the high surface area results in an increased rate

of oxidation. There is less information on the oxidation behaviour of bulk Os metal. including at high temperatures, but it is reported that bulk Os metal forms OsO_4 at temperatures above 673 K. Even less is known about the safety of heating W alloys containing Os to temperatures above 673 K. Xu et. al did not report problems handling W-1Re-1Os, ion irradiated at 773K [134]. This suggests that at high vacuum conditions during ion irradiation, OsO_4 formation is not significant, however, more studies are needed to confirm this.

Self-passivating W alloys are under development to address the issue of oxidation in a LOVA. The problem is illustrated by Binner et. al, who have exposed TaC [179] and pure W [180] to an oxyacetylene torch. Studies have shown that coated tungsten-silicide materials perform much better under similar conditions [180]. New W *smart alloys* containing alloying additions such as Cr, and Y are also under development with the aim of producing a self-passivating film [174, 181, 182] which has been demonstrated to suppress WO_3 formation [182]. Other properties still need to be understood however, particularly the impact of neutron irradiation and activation. Studies of these materials at high temperatures (1473K) have however highlighted decreased oxidation suppression [181] and highlight the need for further development in this area, to account for a LOCA.

2.4.6 *He/H Plasma Exposure*

The exposure of a W surface to a He or mixed He–H plasma results in the formation of a diffuse, branching structure known as *fuzzy tungsten* [183].

The W fuzz forms when helium, within the surface of the tungsten, accumulates and forms bubbles [21, 184, 185]. The impact of this microstructure on the surface thermal diffusivity is yet to be understood, though it's thought that it could impact heat transfer, tritium retention erosion and embrittlement [21, 186, 187]. Studies have, however, indicated that W fuzz could in fact impede the sputtering of W into the plasma [184, 187], which should help to increase the performance of the reactor. This has been observed in a range of W grades and has been documented to occur at temperatures above 1000 K and above a flux of $10 \times 10^{24}\,\mathrm{m}^{-2}$ [21, 184, 186–188]. This fuzzy structure has also been observed in the divertor of the Alcator C–Mod tokamak at MIT [21, 186]. Further work is needed to understand the effects of transmutation and simultaneous oxidation on this phenomenon, as the temperature window for this phenomenon to occur could limit the operating conditions of tungsten components. A combination of X-ray diffraction, DFT modelling and SAW measurements have been used to analyse lattice swelling in helium implanted W by Hofmann et. al [183].

2.4.7 *Improving W Properties through Design*

Cyclic heat loading of mock ITER divertor tiles, coupled with Finite Element Modelling (FEM) has been linked to crack formation in macro scale thermal testing carried out by Nogami et. al. Based on examination of the crack surface, a combination of cleavage fracture and plastic deformation was attributed to the macroscale cracking [50]. Attempts to use novel fabrication methods to improve the mechanical performance of W have been

explored, but also require benchmarking with neutron irradiation to introduce transmutation effects.

Chemical Vapour Deposition (CVD) W exhibits a columnar microstructure which gives it improved fatigue resistance and thermal diffusivity. Studies undertaken by Xiaoou et. al. have investigated the neutron irradiation performance of these alloys and found a significant reduction in the initially improved thermal diffusivity, as well as hardening [189]. However, other studies of CVD grown W by Murphy et. al have shown brittle behaviour [190]. Other manufacturing methods under investigation include W fibre composites [191] and additive manufactured components [192].

2.5 Research Objectives

Based upon the research discussed in the previous chapters, the following 2 research goals have been identified for this thesis:

2.5.1 *Experimental Characterisation of Ion and Neutron Irradiated W*

In part I, APT is applied to the analysis of high temperature neutron irradiated material from HFR characterised mechanically by Abernethy et. al [66] and using TEM by Klimenkov et. al [91]. This sample is unique in that it has a reasonably high dose rate, without a significantly higher solute concentration. Though this is still not at the level expected in a DEMO, it is the most representative sample for fusion produced to date. APT will provide more information on the precipitation and clarify whether or not χ phase precipitation has occurred as was seen in HFIR [115].

Samples will be alloyed to the same composition as the HFR sample after neutron irradiation, and ion irradiated to the same dose and temperature to contrast the differences between ion and neutron irradiation. This will continue the work of Abernethy [109] and will include a microstructural comparison.

2.5.2 *Computational Study of Anomalous Re and Os Precipitation*

Understanding the anomalous precipitation of Re and Os in W requires the development of a new kinetic model, extended from the previous work of Huang et. al [154, 158]. In part II, an existing model used to study Cr precipitation in Fe-Cr, developed by Martinez et. al will be modified to include both self-interstitial and mixed interstitial dumbbells. The Huang energy model will be used to reproduce homogeneous precipitation of Re in binary W-Re.

A new parameterisation will then be used to create a unique pair interaction model of W-Re-Os with both vacancy and interstitial type defects. It is hoped that by developing this model, the short range repulsion, and long range binding of the vacancies can be reproduced within a pair interaction model. The results of this model will be used to interpret the experimental findings of part I.

Part I: Experimental Investigation

3 Neutron Irradiation

▶ Synopsis: In this chapter, the microstructure of high temperature, high dose neutron irradiated single and polycrystalline W, irradiated at HFR is investigated. Characterisation was carried out using a combination of APT and STEM-EDX, and found Re and Os decorated voids, precipitates and a small number of decorated loops.

STEM/EDX imaging was carried out by J.Haley and I. Griffiths. EELS thickness measurements were carried out by I. Griffiths. TEM imaging of APT samples was carried out by A.London. FISPACT-II simulations and data on the HFR neutron energy spectrum were provided by M. Gilbert. EDX measurements of bulk sample composition and gamma spectroscopy measurements were carried out by R. Abernethy.

3.1 Irradiation

In this study, single crystal and polycrystalline W samples, irradiated as part of the EXTREMAT-II campaign in 2008-2009, were characterised. Existing publications on this material are discussed the previous chapter. For full details of the irradiation and additional mechanical characterisation the reader is referred to [109].

3.1.1 *Pre-Irradiation Sample Preparation*

Samples of commercially pure single crystal and polycrystalline W were purchased from Metal Crystals and Oxides Limited, Cambridge UK (no longer trading). The samples were 100mm long rods, 10mm in diameter. The polycrystalline sample had a fine grained microstructure dominated by

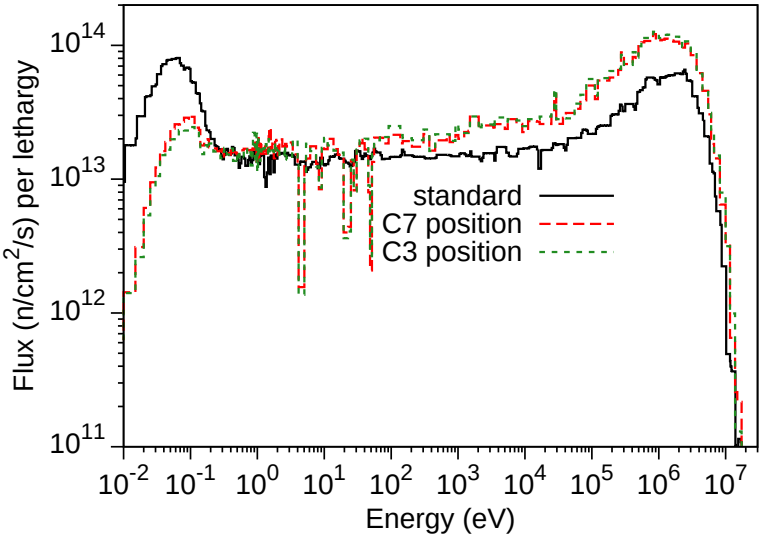


Figure 3.1: Local neutron energy spectrum received by samples, overlaid over the averaged spectrum for the HFR reactor.

elongated grains oriented along the rolling direction. Previous analysis of these samples showed that there was an average grain size of 100x10um with sub grains approximately 20x2um [109]. The samples were polished using a series of successively finer SiC grit papers, diamond suspension paste diluted with water (6um, 3um and 1um) and finally using colloidal silica. The samples were then annealed at 1673K for 24 hours.

3.1.2 *High Flux Reactor*

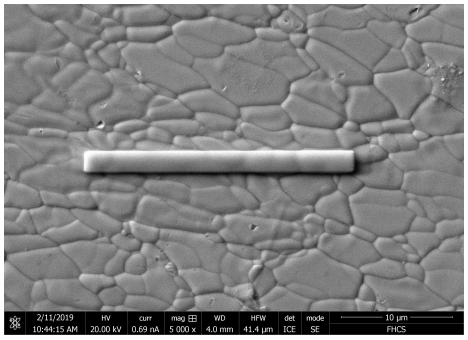
The samples underwent neutron irradiation at HFR, starting in 2008. Technical problems resulted in neutron irradiation being stopped in the summer of 2008, and resumed in the spring of 2009. Irradiation ended in April 2009. The samples were loaded alongside others into the HFR reactor and received a 208 full power day irradiation in 2 locations at 1173 K. The samples were located in positions C7 and C3 in drums 3 and 4. In total the samples received a neutron fluence of $1.21 \times 10^{26}\,\mathrm{m}^{-2}$ ($6.5 \times 10^{25}\,\mathrm{m}^{-2}$

at an energy above 0.1 MeV): $6.8 \times 10^{18}\,\mathrm{m^{-2}\,s^{-1}}$ in the first location and $6.6 \times 10^{18}\,\mathrm{m^{-2}\,s^{-1}}$ in the second location. The presence of an adjacent, strong thermal neutron absorber caused local modification of the neutron energy spectrum, reducing the thermal neutron population, as shown in figure 3.1. Following irradiation the samples had a specific activity of 8.2 $\mathrm{MBqkg^{-1}}$ after 5 years of cooling.

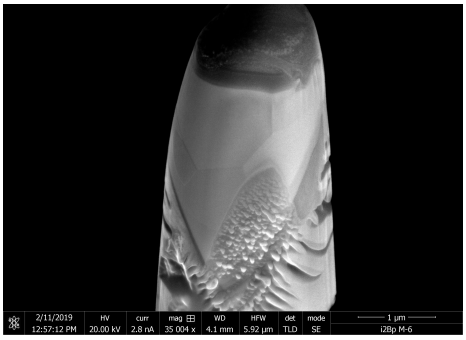
3.1.3 *Damage and Transmutation Quantification*

The dose in dpa received by the sample and the transmutation level were quantified using nuclear inventory modelling using FISPACT-II [15], in simulations carried out using a displacement threshold energy of 55 eV by Gilbert. The simulations accounted for self-shielding effects in the material, as well as the 2 locations within the reactor and the appropriate local energy spectrum. Transmutation in the material was also calculated accounting for 208 days of exposure and 6 years of decay following removal from the reactor.

A total dose of 1.67 dpa and a post-irradiation composition of 1.4at.%Re - 0.1at.%Os - 0.02 at.%Ta was predicted. This was confirmed by Abernethy et. al using γ–ray spectroscopy of the ^{186}Re decay and SEM-EDX measurements [66, 109]. EDX gave a measured transmutation level of 1.2at.%Re - 0.1at.%Os in agreement with FISPACT-II simulations. It was not possible to resolve Ta with EDX.



(a) Site location for the lift-out of the neutron irradiated polycrystalline material, showing the grain boundary etching and deposited platinum protective layer.



(b) Sectioned sample mounted onto Si pre sharp post following lift-out. Grain boundaries can be seen by the contrast of the image.

Figure 3.2: SEM images taken with the TLD detector during the lift-out of the polycrystalline neutron irradiated sample.

3.2 Post-Irradiation Sample Preparation

Chemical characterisation of the samples was performed using a combination of APT, TEM and STEM. APT and TEM samples were prepared for APT using a standard FIB-based lift–out and sharpening process, as described by Miller et. al [193]. An FEI Helios dual beam FIB-SEM system in the Materials Research Facility (MRF) was used to conduct the lift-out on the samples. The activity of the bulk sample required use of hot-cell facilities but the estimated activity from an individual lift-out was <1Bq meaning APT/TEM samples could be released as non-active.

3.2.1 *FIB Lift-out Procedure*

For APT a region of interest was identified and a protective layer of Pt was deposited. For site specific work this Pt protection was aligned with the feature of interest. An initial thin layer of Pt was deposited using the

electron beam to protect the surface during FIB imaging. A layer of Pt approximately 1.5 µm thick was then deposited using the ion beam. The material was undercut using a beam current of between 6 and 1.5 nA to produce a cantilever with triangular cross section.

The cantilever was removed from the sample surface using an Omniprobe micromanipulator and cross sections were mounted onto silicon posts on a 22 grid coupon, using Pt deposition. The samples were sharpened into needles using a series of successively smaller annular milling patterns and lower beam currents (1.5 nA - 40 pA) and an acceleration voltage of 30 kV. At a tip diameter of approximately 50-100 nm in diameter, a final polishing stage using an acceleration voltage of 2 kV and a beam current of 300 pA was used to remove approximately 500 nm of material from the top of the needles.

3.2.2 *Targeted Grain Boundary Sample Preparation*

For the polycrystalline sample, grain boundaries were targeted for analysis with APT. The same process of sharpening outlined in section 3.2.1 was used, however, the lift-out was made along a grain boundary in the sample. Figure 3.2a shows the sample surface with the deposited Pt protective layer prior to trenching. Figure 3.2a.

Initial thinning of the cross section mounted to the silicon post produced enough contrast for targeted milling, as shown in figure 3.2b. The GB was positioned so that it was within the top 100-300 nm of the tip. As the tip was sharpened, contrast became increasingly faint and exact positioning

was not possible. When GB was within approximately 500 nm of the apex, a 2 kV polishing stage was applied until the distance between the GB and the apex of the tip was removed from the sample.

3.3 Atom Probe Tomography

APT was carried out in a CAMECA LEAP 5000 XR at the University of Oxford in laser-assisted mode. Voltage mode was trialled in electropolished W and W-Re wire but produced a poor sample yield and was therefore not used in this study. Trials of samples at between 50 and 150pJ laser energies showed little variation in the resolution of the W and Re peaks in the mass spectrum. Parameters were chosen primarily to increase yield as a high sample fracture rate occurred in both single crystal and polycrystalline samples. For further detail on the technique the reader is referred to [194].

3.3.1 *Experimental Setup*

The electrode was aligned using sharpened silicon posts. The Si posts were first centred on the electrode visually using the live image. Voltage pulsing was then applied to the tip to centre it on the electrode more accurately using the ion detector hit map. The tip was positioned such that the emission was fully contained within the event histogram. Laser pulsing was then applied in order to align the laser on the tip apex. The laser was first positioned manually using the reflected laser spot to locate the tip. After manual positioning, a laser position scan and focal scan were used to calibrate the laser with the tip apex. Pulsing was then stopped and a focussing

dot was used to mark the position of the tip apex. The sample tip was then aligned with this point prior to starting analysis.

A sample temperature of 55K, a laser pulse energy of between 100pJ and 125pJ, and a pulse frequency of 100kHz was used to analyse the single crystal samples. Very poor ion yield in the GB targeted polycrystalline samples necessitated an increase in the laser energy to 150pJ. In total, 6 samples were obtained from the single crystal sample giving a total ion count of 16.26×10^6 ranged ions. For the polycrystalline sample, 2 samples containing a section of the grain boundary were obtained, and 4 without grain boundaries, with a total ion count of 13.71×10^6 ions. For mass spectrum analysis, a further 4 samples were added bringing the total ranged ions for the single crystal to 21.41×10^6. The data was reconstructed and visualised using IVAS 3.8.2, using a peak ranging method described in the following section. Reconstructions were carried out using a tip radius estimated by the voltage curve in IVAS as an input, unless specified otherwise.

3.3.2 *Mass Spectrum Analysis*

Figure 3.3 shows the averaged mass spectrum for all of the neutron irradiated samples obtained in this study. The emitted ions are primarily in the 3+ charge state with some signal also visible in the 2+ and 4+ for W. Fe impurities are visible, as is Ga from the FIB preparation, though both are low in concentration. Ranging the peaks in APT data relies on manual operator input to label peaks over a range defined by the user. It is therefore a process susceptible to human error. The standard approach to separate

the relative contributions of individual peaks in the mass spectrum is to use the heights of the adjacent non-overlapping peaks to determine the ratio of the elements in that peak. This is usually possible because the heights of the peaks in the mass spectrum follow the natural abundances for a given element.

However, the transmutation process does not produce isotopes in their natural abundances, and this method for mass peak identification is no longer valid. Figure 3.5 shows a comparison between the mass spectra obtained from (a) the single crystal neutron irradiated sample from HFR and (c) an ion irradiated sample with equivalent composition. The mass spectra shown in figure 3.5 are cropped to show a region between 58 and 65 Da. The positions and relative abundances of the different isotopes for each element are shown by the bars above the peaks. The mass resolution of the instrument allowed for the different elements, and individual isotopes to be separated, but it is clear from figure 3.5 (a) that the isotopes produced by transmutation cannot be identified by consideration of only the natural abundances. The peaks were therefore labelled using nuclear inventory modelling, as is discussed further in section 3.3.3.

To compare the ranging method used to nuclear inventory modelling, the uncertainty on the elemental concentrations also needs to be evaluated. Uncertainty in APT data comes from a number of different sources [195] but the counting error estimated by IVAS is the most commonly used. Studies by Haley et. al have found however, that mass peak misidentification, peak

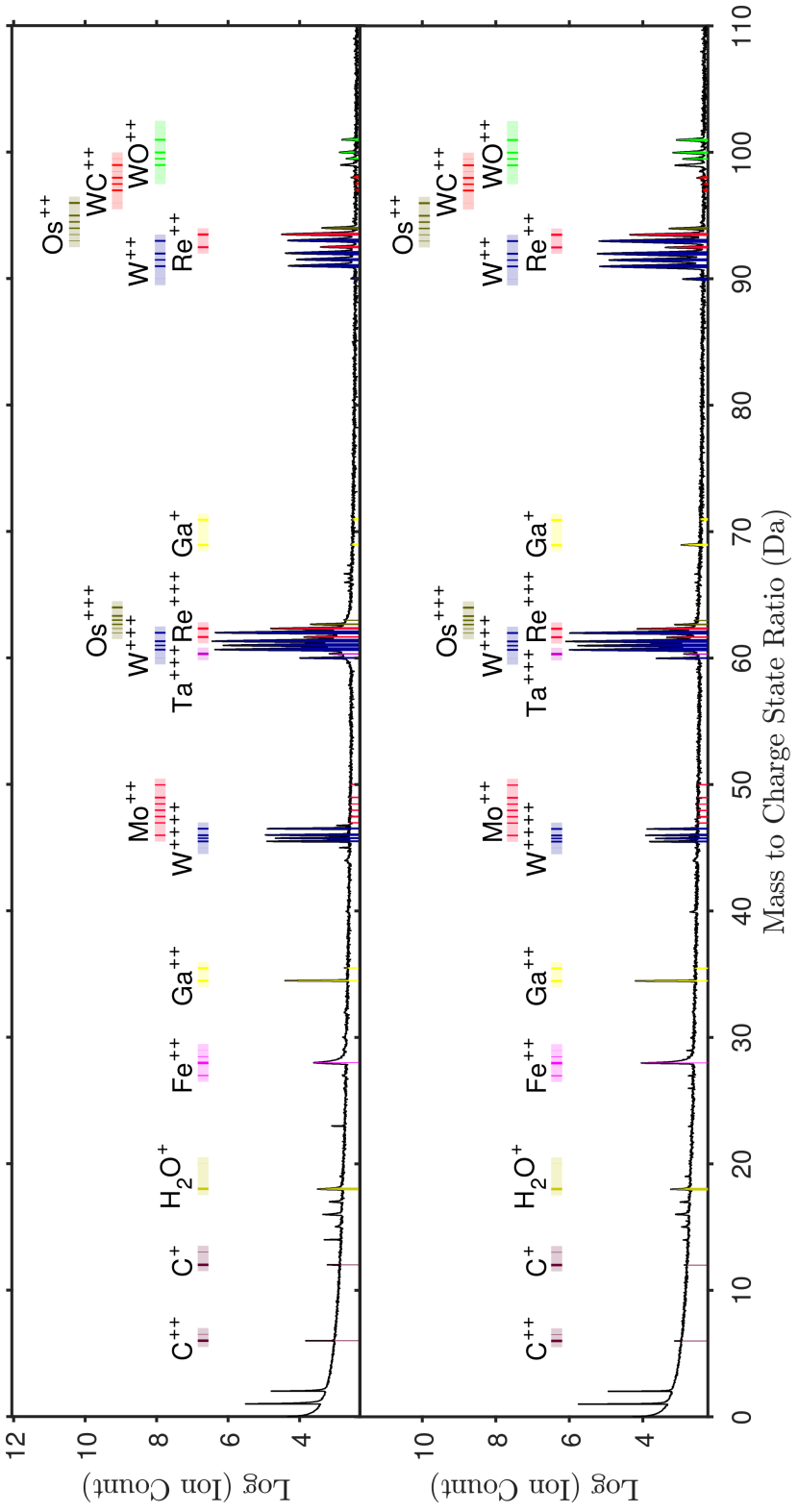


Figure 3.3: Averaged mass spectrum for (top) single crystal and (bottom) polycrystalline samples taken using APT.

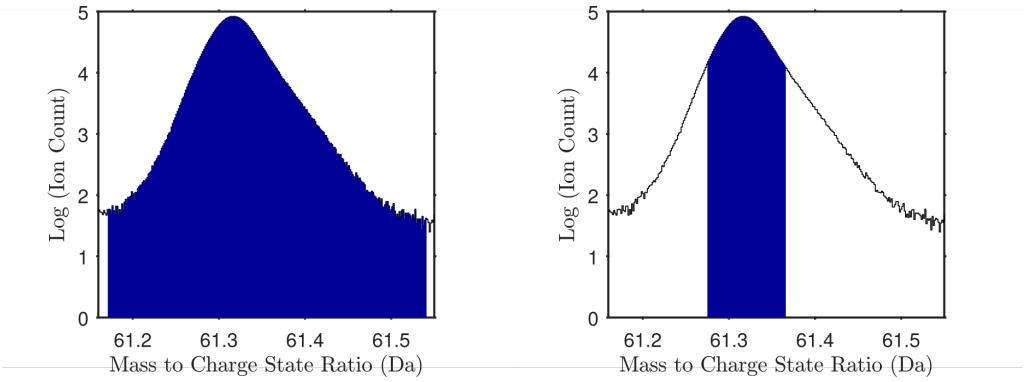


Figure 3.4: Summary of (left) over and (right) under ranging strategy used to estimate the uncertainty due to varying peak identification between different operators.

overlaps and varying ranging methodologies (ie the user defined extents of each peak) can be more important than the counting error [196]. This was demonstrated using randomised experimental trials, in which data sets were provided to multiple APT operators of varying experience levels.

To account for these additional sources of error in this study, two mass-peak ranging approaches were used to define the peak width, giving upper and lower bounds to the concentrations. Figure 3.4 shows the two approaches used to obtain the upper and lower bounds. The error on the concentration is reported as the range of possible values it is possible to produce using the two methods. The reported value for bulk concentration of solute component, x, in this study is therefore given by equation 3.1:

$$x = \frac{1}{N}\sum_{i}^{N} x_i \pm \frac{|x^i_{\text{over}} - x^i_{\text{under}}|}{2} \tag{3.1}$$

for an average of N individual data sets, where x_i is the solute concentration of sample i.

Figure 3.5 shows a portion of the mass spectrum between 58 and 65Da

containing the W^{3+}, Re^{3+} and Os^{3+} peaks. This section of the mass spectrum was plotted because it contains the W, Re and Os peaks with the most counts. Figure 3.5(a) shows the mass spectrum for the neutron irradiated sample, whereas figure 3.5(b) (c) and (d) show the spectra for W-1.4at%Re, W-1.4Re-0.1Os and W-1Re-1Os samples respectively, in which the Re and Os are present in their natural abundances. In particular, Figure 3.5(a) highlights the difference in the relative heights of Os peaks compared to those observed in the analyses of the pre-alloyed samples in figure 3.5(c) and (d). Whereas in the pre-alloyed samples, the Os isotopes follow the natural abundance of Os (plotted above the peaks as a bar), for the neutron irradiated sample, the Os has been introduced through the transmutation of Re and therefore does not follow the natural abundance. Figure 3.5(c) and (d) show that for the pre-alloyed sample, the majority of the Os counts come from the most common naturally occurring isotope, $^{192}Os^{3+}$, which accounts for 41% of naturally occurring Os. There are also differences in the detected Re signal, shown by figure 3.5(a) and (b). The pre-alloyed sample in figure 3.5(b) contains the natural ratio of ^{187}Re to ^{185}Re whereas in figure 3.5(a), the ratio is different due to the fact that the Re is produced through the transmutation of W isotopes. Figure 3.5(a) also shows the presence of a small Ta peak that was not detectable above the background signal in previous studies using EDX. Differences in the mass spectra under ion and neutron irradiation are discussed further in the next chapter, in section 4.5.1.

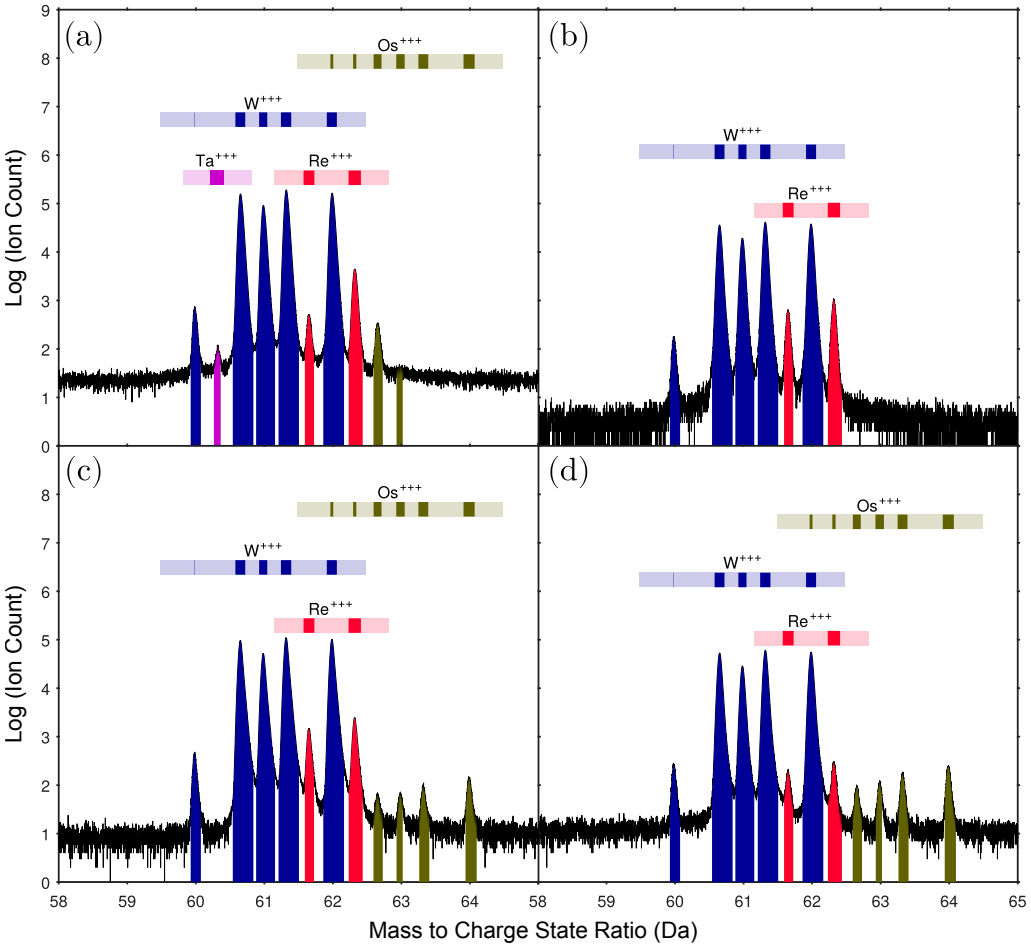


Figure 3.5: Portions of the mass spectra between 58 and 65Da, showing the 3+ charge state ions taken from (a) neutron irradiated (b)W-1.4Re Saclay ion irradiated (c) W-1.4Re-0.1Os SNL ion irradiated and (d) W-1Re-1Os SIBC ion irradiated samples.

3.3.3 *Validation of FISPACT-II*

Table 3.1 shows the isotopic abundances predicted by FISPACT-II modelling, for the 11 most abundant isotopes carried out by Gilbert (a further 60+ isotopes were predicted in lower concentrations). FISPACT-II calculations were performed accounting for self-shielding effects and using simulated local neutron spectra for the EXTREMAT-II experiment and using the TENDL-2015 nuclear data as input [91]. The simulations accounted for both locations in the reactor and the approximately 6 years of decay cooling

between the end of irradiation and APT/EDX measurements [88].

The modelling predicts that mass-to-charge-state overlaps for the irradiation conditions experienced by this sample were minimal due to the short half-lives of the other isotopes formed under irradiation. In pre-alloyed material the overlap is also minimal as the ^{185}W and ^{187}W isotopes have half-lives of 75.1 days and 23.72 hours respectively [18] and therefore are not naturally occurring in W and do not overlap with the ^{185}Re and ^{187}Re peaks. Any ^{185}W and ^{187}W produced in the neutron irradiated sample would also decay quickly and therefore not contribute to peak overlaps.

In pre-alloyed W-Re-Os there is a small overlap in the ^{187}Os and ^{187}Re peaks, however, ^{187}Os accounts for $<$2% of naturally occurring Os, and mass peak misidentification errors between these peaks is therefore minimal. In the neutron irradiated sample, FISPACT-II simulations predict that ^{187}Os should account for only 0.01% of the 187 mass peak, with the rest of the counts coming from ^{187}Re and zero contribution from ^{187}W. Again with the 185 peak, minimal overlap is predicted with only 3.54×10^{-6} % predicted to arise from isotopes other than ^{185}Re. ^{185}W is not a naturally occurring isotope and therefore has no impact on the peaks in the pre-alloyed material. Analysis of the mass spectra and comparison with FISPACT-II modelling gives confidence that the ranging approach used in this study is accurate and that significant errors due to incorrect mass peak labelling are not present. Bulk mass spectra averaged over the full range of samples were constructed using the CompositionFromPosList.m matlab script in the Atom Probe Lab

Table 3.1: Comparison between the calculated distribution of isotopes and the measured distribution from APT produced by transmutation from 208 day neutron irradiation at HFR and 6 years of cooling, as a percentage of the total number of atoms in the simulation and the total number of ranged ions in APT. The 11 most commonly occurring isotopes from the simulation are included, isotopes with lower concentration could not be separated from background using APT. Uncertainty on the concentration from APT is estimated by comparing different ranging approaches, background-to-background and at FWHM.

Nuclide	FISPACT-II (at.%)	APT (at.%)	
		Single Crystal	Polycrystalline
^{184}W	30.97	31.871 ± 0.898	31.862 ± 1.062
^{186}W	26.99	26.120 ± 0.778	26.632 ± 0.332
^{182}W	25.35	24.759 ± 0.619	24.142 ± 1.310
^{183}W	15.02	15.352 ± 0.567	14.984 ± 0.485
^{187}Re	1.34	1.246 ± 0.059	1.032 ± 0.045
^{188}Os	0.10	0.081 ± 0.016	0.074 ± 0.025
^{180}W	0.10	0.107 ± 0.003	0.080 ± 0.005
^{185}Re	0.09	0.110 ± 0.014	0.107 ± 0.014
^{181}Ta	0.02	0.0110 ± 0.002	0.010 ± 0.002
^{186}Os	0.01	Undetectable	Undetectable
^{189}Os	0.002	Undetectable	Undetectable

software package [197], the results of which are as summarised in table 3.1.

Table 3.2: Bulk sample solute concentration from transmutation measured using APT. Uncertainty quantified using under and over ranging approach. Compared to FISPACT-II results [88] and EDX measurements [66].

Sample	Re (at.%)	Os (at.%)	Ta (at.%)
Single Crystal	1.263±0.149	0.083±0.017	0.009±0.004
Polycrystalline	1.090±0.067	0.080±0.016	0.009±0.004
FISPACT-II	1.4	0.1	0.02
EDX [66]	1.2	0.1	Undetectable

The bulk transmutation product concentrations measured using APT are given in table 3.2 with the equivalent predicted elemental concentration from FISPACT-II. There is good agreement between the EDX measurements carried out by Abernethy [66], and the predicted composition. Some variation is expected due to the site-specific nature of APT. There is some deviation between FISPACT-II and APT in the ^{187}Re signal, that could indicate slight inaccuracies in the nuclear data or local neutron spectrum or because of artefacts in APT. A slightly lower Re concentration in the polycrystalline sample is also a result of the proximity of the clusters to the grain boundary.

The composition measurements carried out on the sample give confidence that the ranging method used is appropriate and that further spatial analysis of the samples can be applied. It also demonstrates that FISPACT-II is a reliable approach to simulating transmutation rates in these alloys and gives a robust description of post-irradiation composition.

3.4 Precipitation of Re and Os

Precipitation of Re and Os was observed in both single and polycrystalline samples, in agreement with the findings of numerous studies (see section 2.2.6). SEM-EDX mapping of the sample at various voltages was not able to resolve clusters or grain boundary decoration.

3.4.1 *Single Crystal*

Large clusters of Re and Os were observed in all of the 6 single crystal samples analysed. Figure 3.6 shows reconstructions of the 6 successful needles taken from the single crystal sample, with between 5 and 20 at.% W atoms in blue shown for visual clarity, 100 at.% of Os atoms in green, and with 5 at.%Re isoconcentration surfaces shown in red to highlight the location of the clusters. Ta was present in very small concentrations and was not shown to be correlated with the clusters and therefore is not shown in figure 3.6. Clear segregation of Re has therefore occurred from the matrix.

Figure 3.10 shows one of the APT reconstructions with 5 at.%Re isoconcentration surfaces in red, and 1.5 at.%Os isoconcentration surfaces in green. The Os isoconcentration surfaces show that precipitation of Os has also occurred, despite the much lower nominal concentration ($\approx$ 0.1 at.%Os). The majority of the clusters shown in figure 3.6 exhibited this core shell structure of Os, surrounded by Re, as highlighted in the magnified image shown in figure 3.10. This effect has only been reported previously in neutron irradiated high Re pre-alloyed samples in which transmutation likely occurs within existing Re precipitates.

3.4.2 *Polycrystalline*

Reconstruction of the needles taken from the polycrystalline samples show a similar structure to the single crystal sample. Figure 3.8 shows the reconstructed samples with between 5 and 20 at.% W atoms in blue shows for

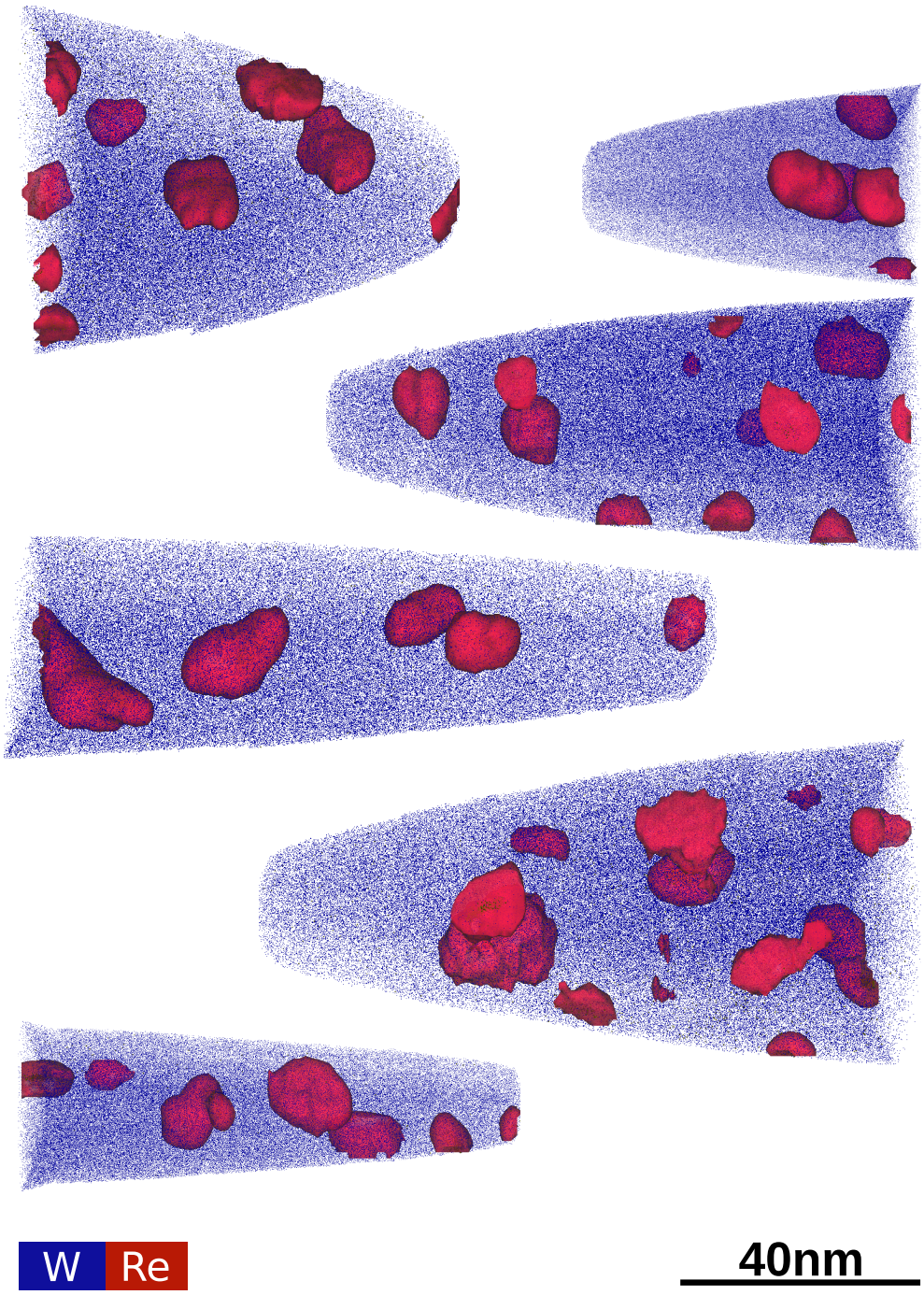


Figure 3.6: Summary of the 6 reconstructed APT data sets, taken from the single crystal neutron irradiated sample. W atoms are plotted in blue, with between 5 and 20% of atoms shown for visual clarity. Re isoconcentration surfaces at 5at.%Re are shown in red to highlight the positions of the precipitates. 100% of Os atoms are plotted in green but are not strongly visible because they are located primarily within the Re clusters. Each atom map shows a different sample analysed using APT.

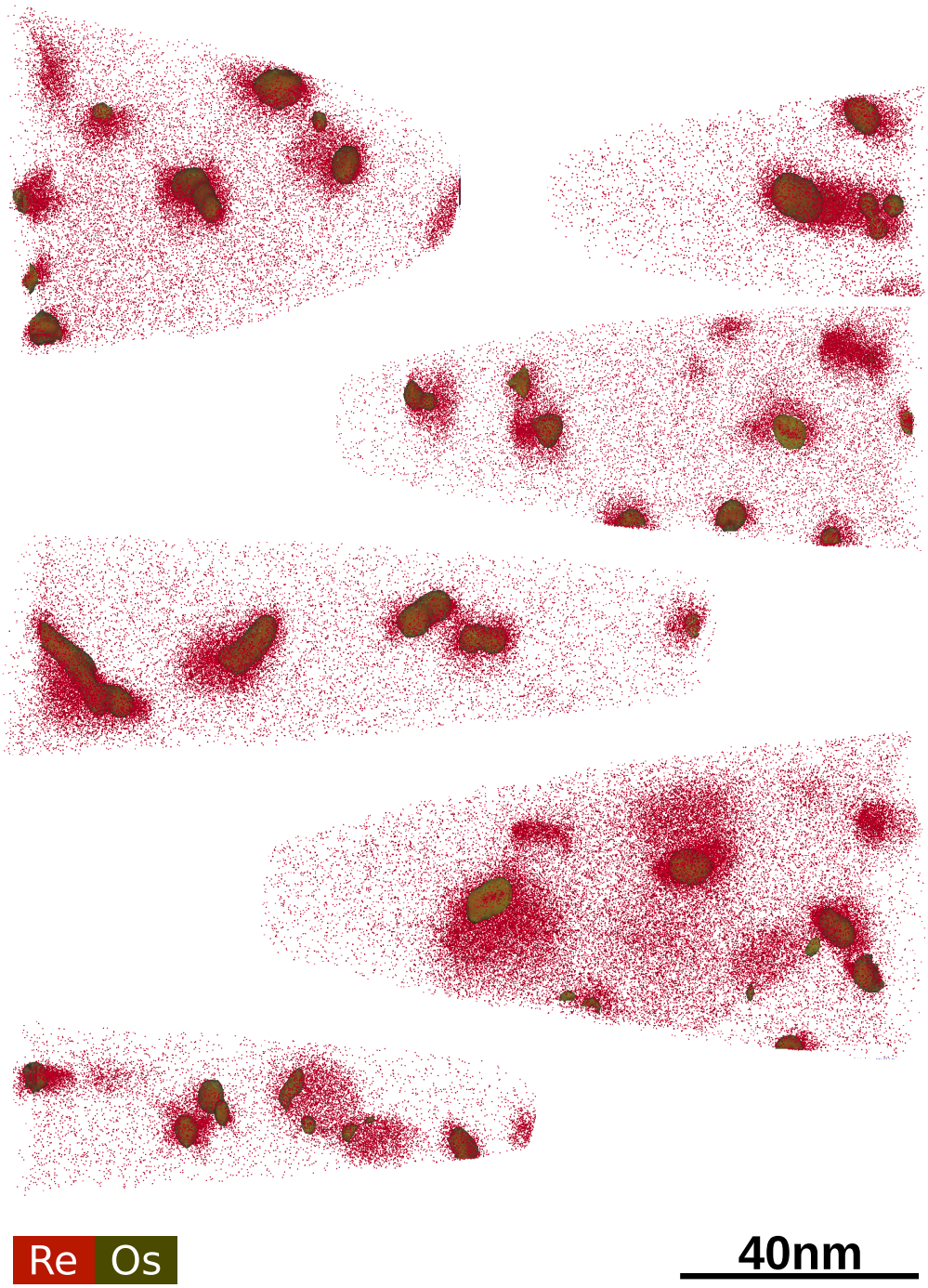


Figure 3.7: Summary of the 6 reconstructed samples shown in figure 3.6 with all of the W atoms removed, and 100% of Re atoms plotted as red spheres of diameter 0.1 nm. Os isoconcentration surfaces at 1.5at.%Os are shown in green and highlight the position of the Os within the Re rich clusters. Each atom map shows a different sample analysed using APT.

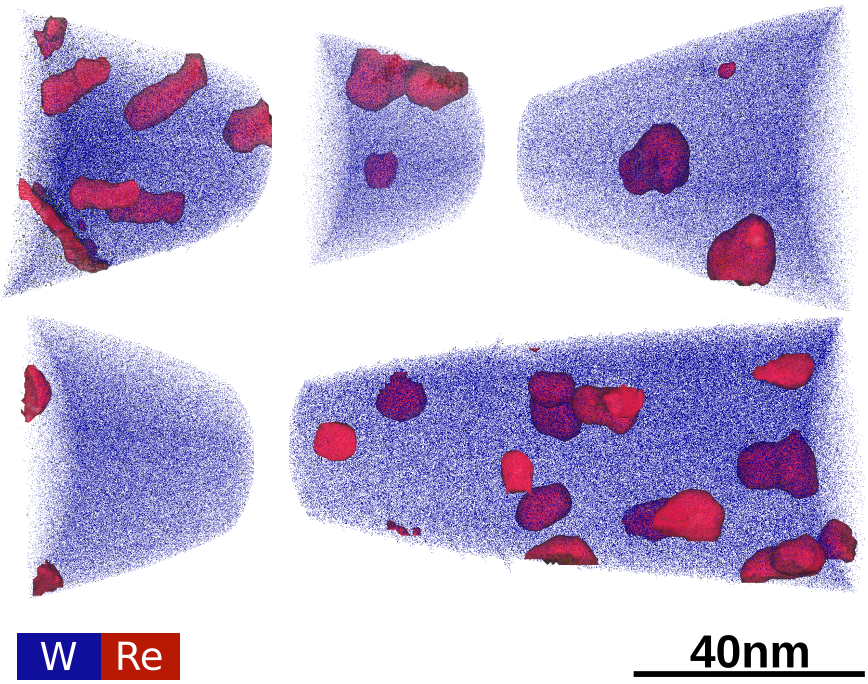


Figure 3.8: Summary of the 5 reconstructed APT data sets taken from the polycrystalline neutron irradiated sample. W atoms are plotted in blue, with between 5 and 20% of atoms shown for visual clarity. Re isoconcentration surfaces at 5at.%Re are shown in red to highlight the positions of the precipitates. 100% of Os atoms are plotted in green but are not strongly visible because they are located primarily within the Re clusters. Each atom map shows a different sample analysed using APT.

visual clarity, and 100at.% of Os atoms in green, and with 5at.%Re isoconcentration surfaces shown in red to highlight the location of the clusters. Large Re clusters were detected with a central shell of Os.

Figure 3.11 shows a higher magnification section of the one of the reconstructions from figure 3.8, showing the location of the Os atoms using a 1.5at.%Os isoconcentration surface. As in the single crystal samples, the Os is located primarily within the Re precipitates. The majority of the clusters in the polycrystalline samples have a central Os core shell surrounded by Re.

As shown in figures 3.6 and 3.8, some of the precipitates are elongated

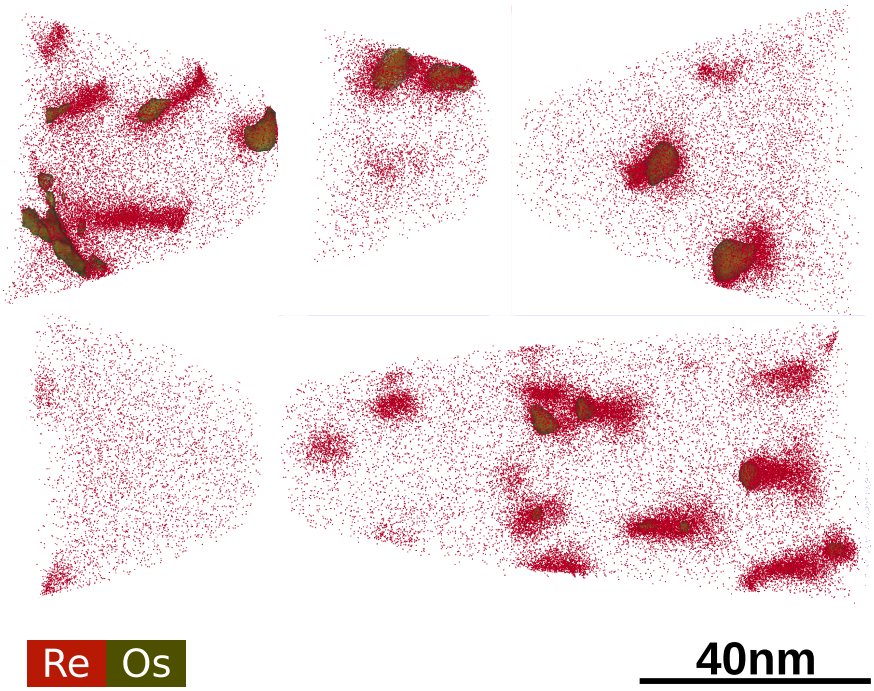


Figure 3.9: Summary of the 5 reconstructed samples shown in figure 3.8 with all of the W atoms removed, and 100% of Re atoms plotted as red spheres of diameter 0.1 nm. Os isoconcentration surfaces at 1.5at.%Os are shown in green and highlight the position of the Os within the Re rich clusters. Each atom map shows a different sample analysed using APT.

in one direction. These rod shaped precipitates are consistent with the shapes observed in higher transmutation level samples from HFIR [116], as discussed in section 2.2.6.

3.4.3 *Cluster Composition Analysis from APT*

To investigate the composition of the clusters quantitatively, a cluster analysis was performed using a maximum separation algorithm implemented in the posgen program within the APTTools software package [198]. The method is discussed further in section 4.5.3, as the parameters used were optimised for small clusters in the ion implanted samples. A maximum separation distance d_{max} of 1 nm, an envelope parameter, L of 0.7 nm, an

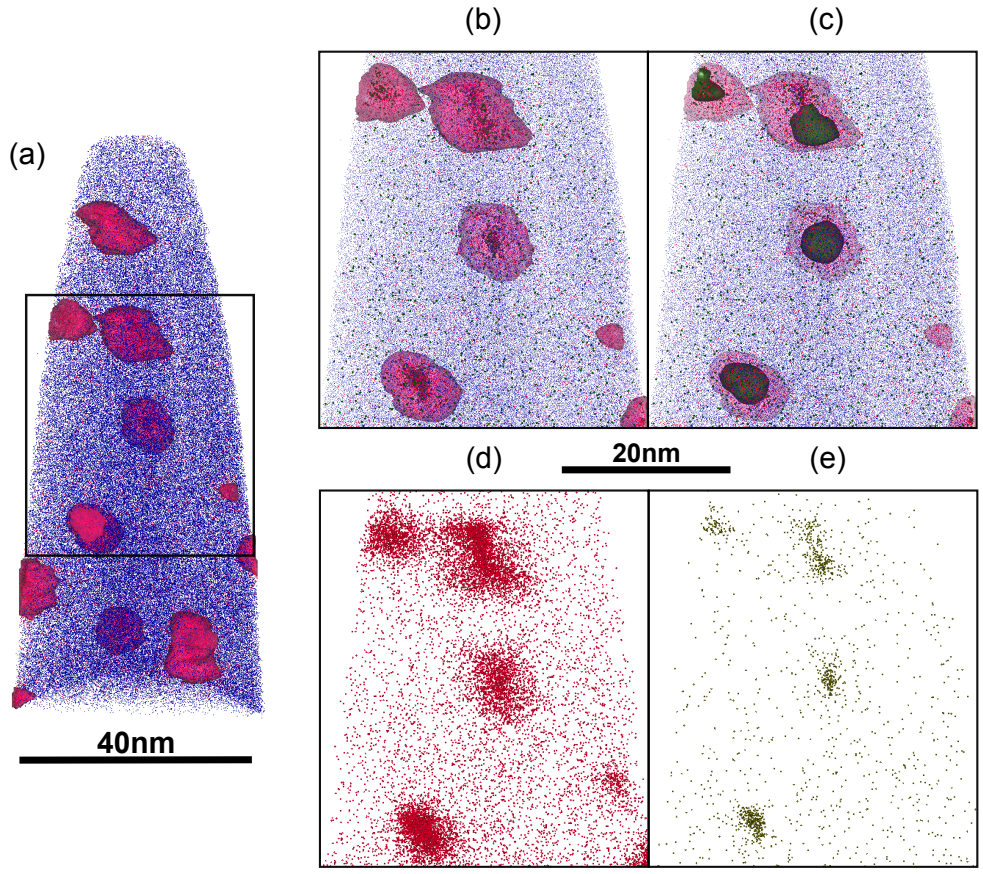


Figure 3.10: APT reconstruction of single crystal neutron irradiated sample. (a) For visual clarity, only 1.3% of total detected W ions are shown in blue, all detected Re and Os ions are shown in red and green respectively. Red surfaces represent Re isoconcentration surfaces plotted at 5at.%Re. (b) Higher magnification of the region of interest showing Re isoconcentration surfaces at 5at.%Re and individual Os atoms as green squares. (c) Region of interest showing transparent Re isoconcentration surfaces and green Os isoconcentration surfaces at 1.5at.%Os.The positions of the Re and Os atoms are shown separately in (d) and (e) respectively.

erosion distance of 0.25 nm and a minimum cluster size of 20 ions was used, assuming a cluster core comprised of Re and Os atoms and a matrix of W.

The cluster search returns a total number of ranged ions and the number of Re, Os and W ions within the cluster. The Re and Os concentrations were taken as $x_{\mathrm{Re}} = N_{\mathrm{Re}}/N_T$ and $x_{\mathrm{Os}} = N_{\mathrm{Os}}/N_T$ respectively, where N_{X} is the number of ions of type X in the cluster and N_T is the total number of ions in the cluster. The concentration of W was taken as $1 - x_{\mathrm{Re}} - x_{\mathrm{Os}}$.

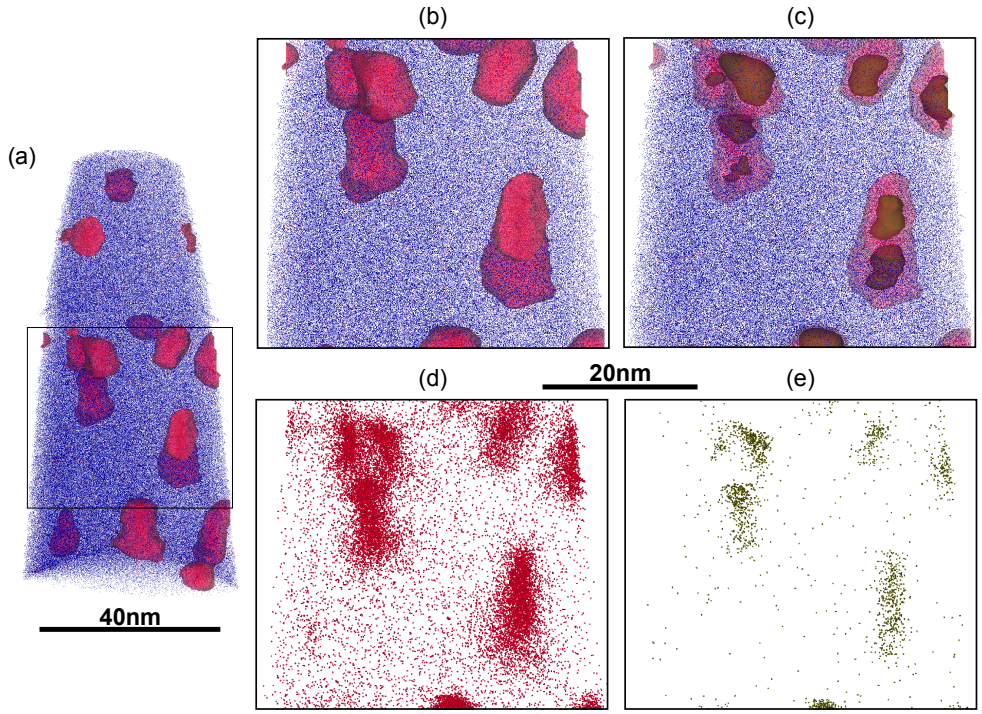


Figure 3.11: APT reconstruction of polycrystalline neutron irradiated sample. (a) For visual clarity, 11% of total detected W ions are shown in blue, all detected Re and Os ions are shown in red and green respectively. Red surfaces represent Re isoconcentration surfaces plotted at 5at.%Re. (b) Higher magnification of the region of interest showing Re isoconcentration surfaces at 5at.%Re and individual Os atoms as green squares. (c) Region of interest showing transparent Re isoconcentration surfaces and green Os isoconcentration surfaces at 1.5at.%Os.The positions of the Re and Os atoms are shown separately in (d) and (e) respectively.

The average cluster composition for the single and polycrystalline samples are shown in table 3.3, with results from experiments at JOYO and HFIR [114, 199] which have a similar dose. The samples have a similar average cluster composition to the pure-W samples irradiated at JOYO, which, as shown in figure 2.3, have a similar transmutation rate to HFR. The HFIR reactor has a much higher transmutation rate which produces a higher nominal post-irradiation composition. Therefore the clusters in HFIR samples have a higher average Re and Os concentration.

As shown in table 3.3, the composition of individual clusters in the HFR

Table 3.3: Average cluster compositions in the single crystal and polycrystalline neutron irradiated samples, measured using a maximum separation algorithm. The average compositions measured in the sample from JOYO and HFIR were also calculated on APT data using a maximum separation algorithm, details of which are given in [114]. The samples irradiated at JOYO and HFIR are polycrystalline pure-W and pre-alloyed W-10at.%Re [199]. The standard deviation of the Re and Os concentration around the average, σ_x, for the concentration of x is also given.

Reactor	Sample	dpa	Re (at.%)	σ_{Re}	Os (at.%)	σ_{Os}
HFR	Pure-W (Single Crystal)	1.67	8.6	3.4	0.6	0.6
HFR	Pure-W (Polycrystalline)	1.67	6.9	3.6	0.6	0.5
JOYO	Pure-W [114]	0.96	7.6	-	0.2	-
JOYO	W-10Re [114]	0.96	20.9	-	3.0	-
HFIR	Pure-W [114]	0.90	13.4	-	2.6	-
HFIR	W-10Re [114]	0.90	16.6	-	7.7	-

samples vary significantly with respect to the mean value. The spread in cluster compositions is also shown in figure 3.12, with each point representing a single cluster in the HFR samples. The Re concentration in the clusters varies between around 5 and 20 at.%Re, with Os varying between 0 and 5at.%. There is a linear trend between increasing Os and Re. This could be a result of Os forming from transmutation within the clusters, rather than forming elsewhere and migrating to the clusters, as is discussed in section 4.5. On average, the clusters in the polycrystalline material have a lower Re and Os concentration, likely because of their proximity to the grain boundary which is enriched with both Re and Os.

The composition of the clusters measured using this approach is not con-

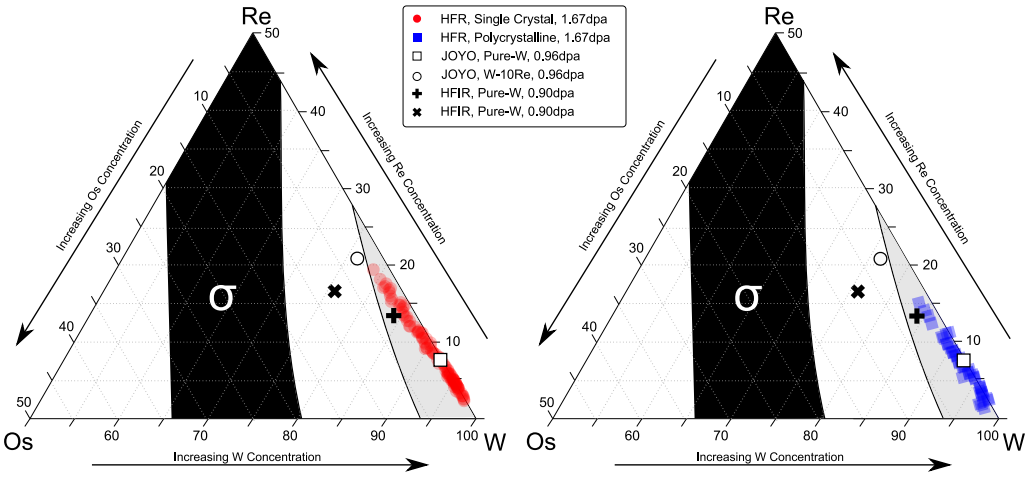


Figure 3.12: Cluster compositions in neutron irradiated single and polycrystalline W samples from HFR, plotted on the equilibrium ternary W-Re-Os phase diagram at 1873 K, with average cluster compositions from experiments at HFIR and Joyo [114, 199].

sistent with the formation of σ (shown as the black region in figure 3.12) or χ phase (see figures 2.4 and 2.5a). This is also true of the initially pure, Joyo samples [114, 199]. For a few clusters the measured concentration is close to the boundary with the bcc + σ phase region. However, the reported cluster composition is highly sensitive to the user-defined cluster search parameters, which are not always reported. Here a standard approach was used, similar to that performed by Hwang et. al in order to allow comparison.

Some of the clusters in the APT data showed an elongated rod shaped topography, with a central Re and Os rich region surrounded by a more diffuse cloud of Re. This is shown most clearly by figures 3.7 and 3.9. In cases where the clusters exhibit a rod shaped morphology, the Os atoms are found within this central region, as shown in the example plotted in figure

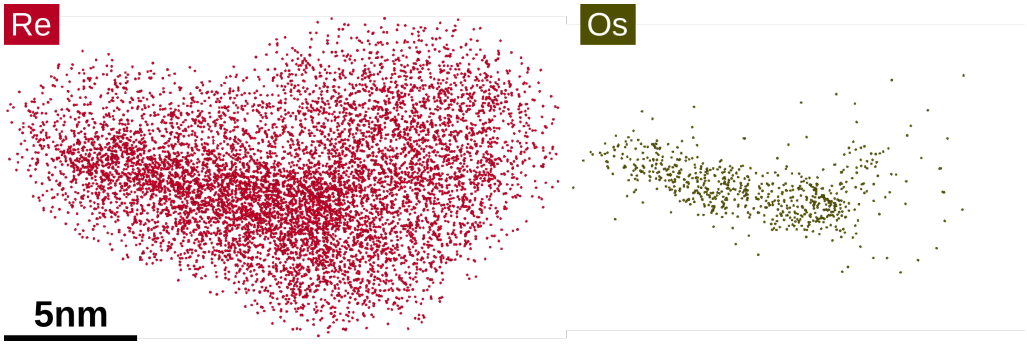


Figure 3.13: High magnification image of the Re and Os atoms in the precipitate analysed in figure 3.14, plotted as spheres of radius 0.05nm. 100% of Re and Os atoms are shown respectively with all other atoms hidden for visual clarity. The boundary of the cluster was defined using a 5at.%Re isoconcentration surface.

3.13. Re isoconcetration surfaces indicate that the central region of this precipitate had a concentration higher than 25 at.%Re.

To investigate this core region further, a line profile was taken through the core of the cluster shown in figure 3.13. A cylindrical ROI was centred on a 5at.%Re isoconcentration surface, and then manually aligned to the Re and Os rich rod in the centre of the cluster. The ROI diameter was defined such that it mostly contained the core atoms. Figure 3.14 shows the binned concentration as a function of the distance from the start of the ROI (which is illustrated by the inset figure). The central concentration rises to approximately 50 at.%Re and between 5 and 10at.%Os. This Re concentration is consistent with the σ phase predicted in other neutron irradiation studies.

Diffraction pattern analysis using TEM is needed to confirm the presence of σ phase conclusively, however, neither σ or χ phase was detected in TEM analysis performed on this sample by Klimenkov et. al [91]. The

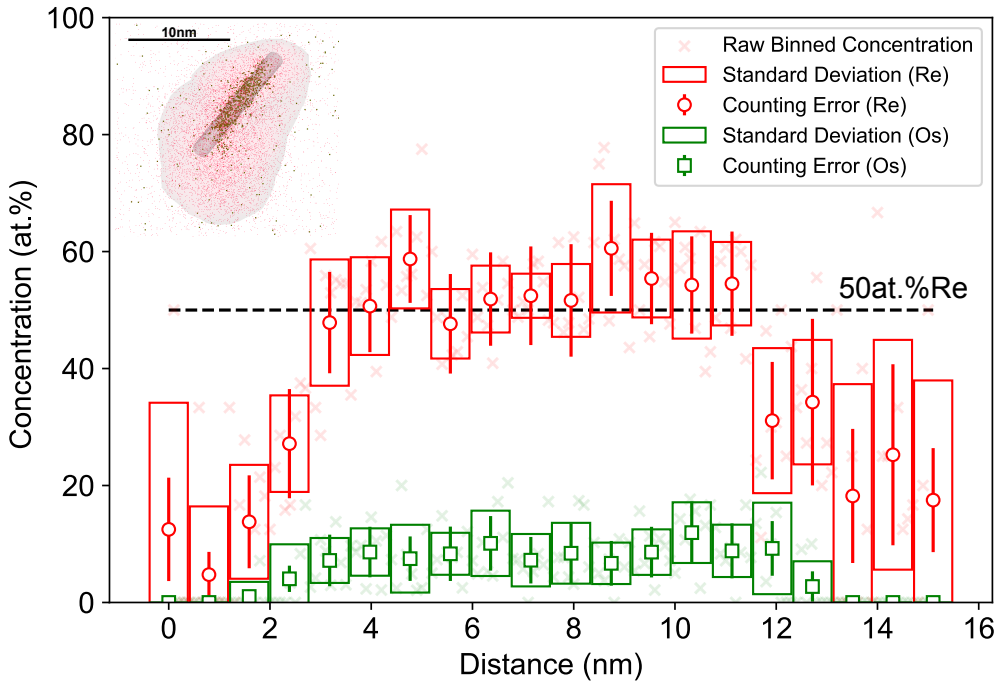


Figure 3.14: Line profile taken through rod-shaped cluster in APT data, centred on a 25at.%Re isoconcentration surface. Cylindrical ROI of dimensions 1.64 nm radius, 15 nm long, binned into 152 bins along the z-direction of width 0.1 nm in IVAS, rebinned into 20 bins using Python. Errors plotted are both counting error from IVAS and the standard deviation on each bin. Inset image shows the ROI centred on the cluster core. An isoconcentration surface at 5at.%Re is shown with Os atoms plotted as green squares to highlight the central rod shape.

results from the cluster analysis are in line with previous studies at similar doses and transmutation levels [114, 199], with the majority of cluster compositions within the solid solution bcc region. However, line profile analysis suggests that in the centre of some of the clusters which exhibit an elongated rod shaped morphology, the concentration is consistent with σ phase. The combination of spherical and elongated clusters suggests that a mixture of coherent bcc, and less coherent σ phase precipitates are present following neutron irradiation. It is possible therefore that the signal produced by this small region was insufficient to allow detection using TEM. There is no

indication from either TEM or APT analysis that any of the clusters were consistent with χ phase. It is unclear from these results why χ phase is typically observed elsewhere. It is likely that the cluster compositions are highly sensitive to the transmutation rate and the overall level.

3.4.4 *Grain Boundary Decoration*

Figure 3.15 shows a reconstruction of an APT sample obtained using a targeted GB lift-out from the polycrystalline sample. The GB runs through the centre of the reconstruction and is clearly decorated with Re and Os transmutation products. There are two Re and Os rich precipitates near the the GB as well. The light green atom map shows the signal from WO, which is present in the precipitates but not at the GB. This could indicate the presence of voids in these clusters to which Oxygen has segregated. Re clusters further from the boundary were not typically associated with an increase in the WO signal, which could indicate a higher concentration of oxygen near to the grain boundary. Fe is present along the GB but not in the precipitates. Fe is not produced through transmutation reactions and is likely present as a result of impurities introduced during manufacture. This agrees with the findings of Uray and Menyhárd who investigated the grain boundaries of unirradiated W wires doped with 40appm Fe in 1984. It was shown that Fe segregation to GBs upon heat treatment had occurred by using electrical resistivity measurements and analysis of fracture surfaces using Auger Electron Spectroscopy (AES) [200].

The lines of enriched solute elements, shown in figure 3.15, indicate that

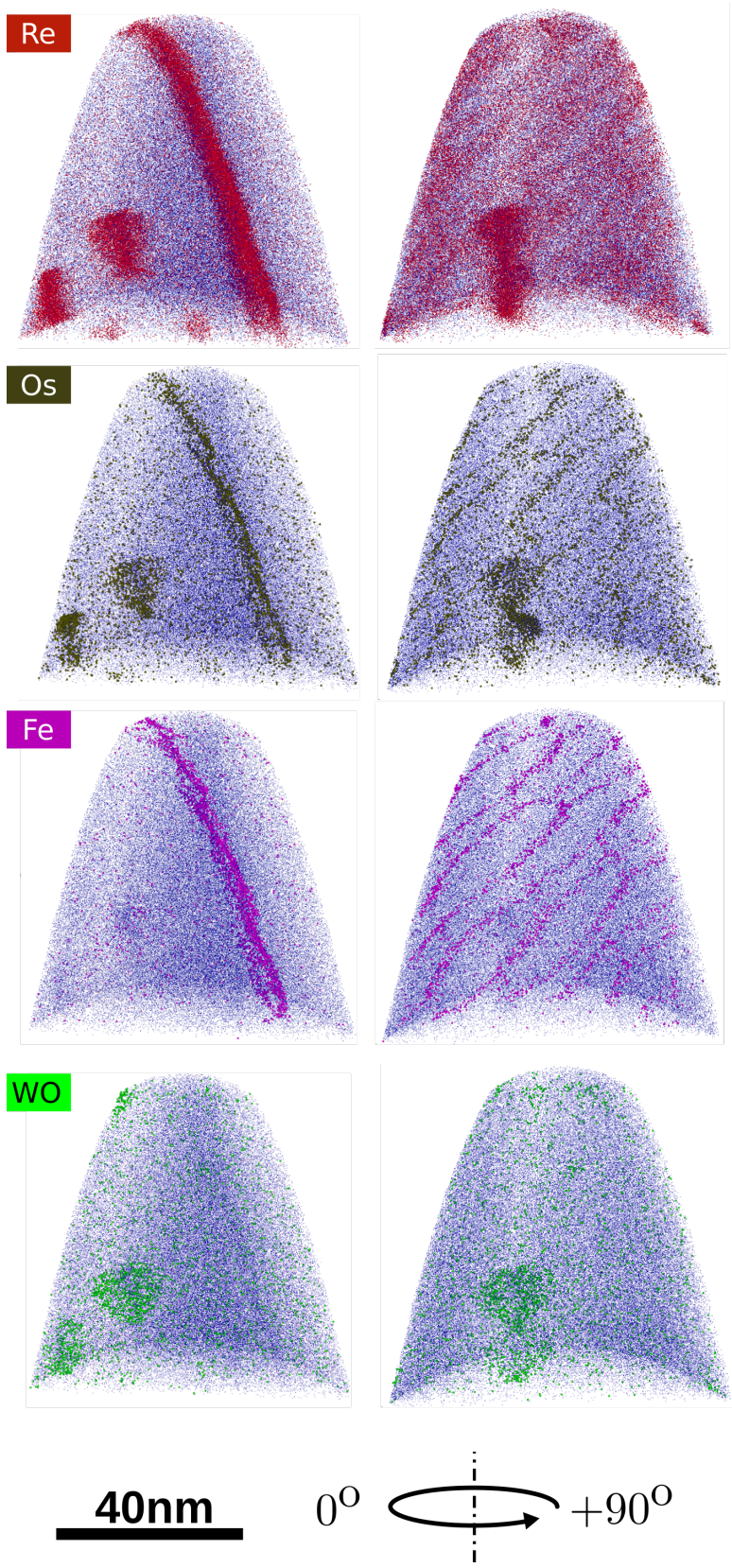


Figure 3.15: Reconstruction of sample taken from polycrystalline neutron irradiated sample showing the decoration of the central GB with solute Re, Os and Fe atoms.

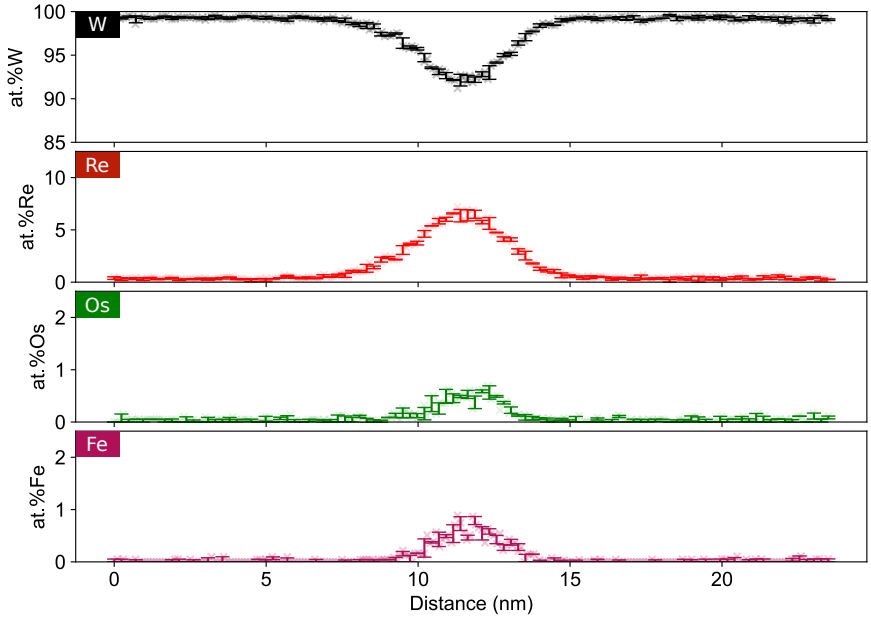


Figure 3.16: Line profile of concentration taken in the z-direction along a cylindrical ROI across the grain boundary showing enriched Re, Os and Fe concentration.

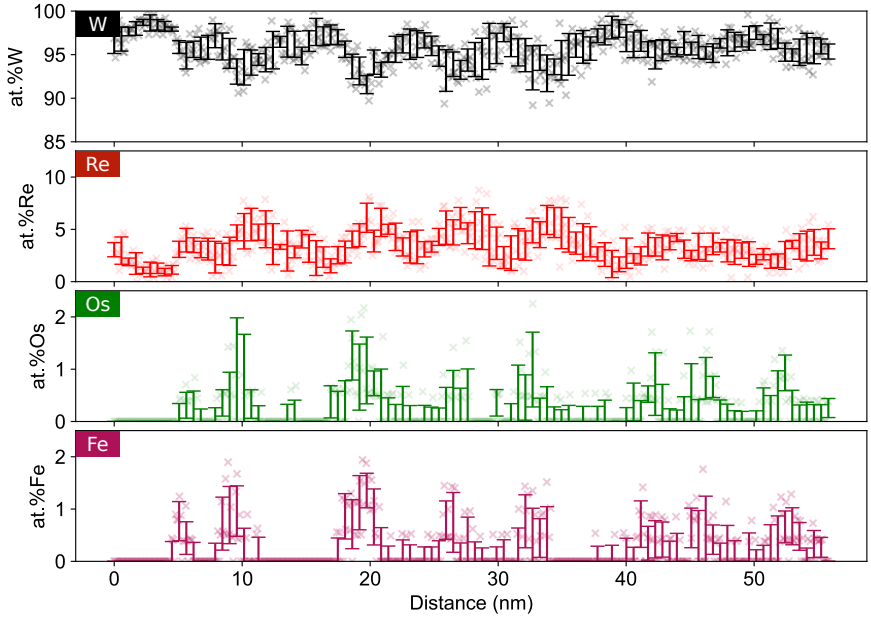


Figure 3.17: Line profile of concentration taken in the z-direction along a cylindrical ROI along the direction of the grain boundary, showing variation in the Re, Fe and Fe concentration.

this is likely a low angle GB made up of individual dislocations. Figure 3.2a suggests that this is likely a subgrain boundary, as the grain sizes are consistent with the average subgrain size reported prior to irradiation. There is insufficient spatial resolution in the APT data to analyse the orientation of the grains, due to the high laser energy and temperature needed to run the sample without fracture, so the actual misorientation angle is unknown. Figures 3.16 and 3.17 show 1D line profiles taken across and along the GB respectively. Figure 3.16 shows the overall segregation of Re, Os and Fe to the GB, up to a maximum of 5-6at.%Re, 0.5-1at.%Os and 0.5-1at.%Fe. Despite the low nominal concentration of Os in the sample, the segregation is significant. The Os is enriched by a factor of 5-10, whereas Re is only enriched by a factor of approximately 4. Figure 3.17 shows the variation along the direction of the GB, highlighting the decoration of individual dislocations within the GB with Re, Os and Fe.

3.4.5 *Dislocation Decoration*

Os in the samples analysed was primarily located within the cores of Re clusters and on the GB, however, other features were observed that were decorated with mostly Os. Figures 3.18 (a) and (b) show a line of Os highlighted with a 0.5at.%Os iso concentration surface which separates regions of nominal and slightly increased Re concentration. Because this APT tip was taken from the single crystal sample, the feature is likely to be a dislocation. Figure 3.18 (c) shows a 1D concentration profile of a cuboidal ROI of dimensions 10 nmx32 nmx13 nm, centred on the 0.5at.%Os iso concentra-

tion surface. The ROI was binned into 122 bins along the z-direction, with bin widths of 0.1 nm. The data were re-binned in Python to quantify the spatial variation in solute concentration, and measure the variation of the solute concentration.

Comparing figure 3.18 (c) with the dislocations in the suspected low angle grain boundary shown in figure 3.17, a similar level of Os segregation is detected, to around 1-2at.%. The Re concentration on one side of the dislocation is consistent with the Re segregation to the dislocations in figure 3.17 at between 4 and 5at.%Re. In figure 3.18 (a) the Re peaks behind the peak in the Os concentration. The fact that Os has been shown to decorate features independently of Re supports the hypothesis that Os was formed in the bulk of the material and then migrated to these features, rather than forming in Re concentrated areas. Transmutation in these regions would be higher than elsewhere but not all of the Re would undergo transmutation reactions.

Figure 3.19 shows a spherical region enriched in Re, which is less dense than the adjacent clusters. A map of the Os atoms shows a ring around the edge of this feature. The enrichment of Os suggests that this is a small dislocation loop around 15 nm in diameter. Os segregation to dislocation was also observed by by Eaton and Nordén in unirradiated W [120], but this has not been observed previously in W-Re-Os alloys.

Os in W is more strongly bound to point defects, as is analysed in chapter 6. The distribution of Re suggests that point defect mediated transport of

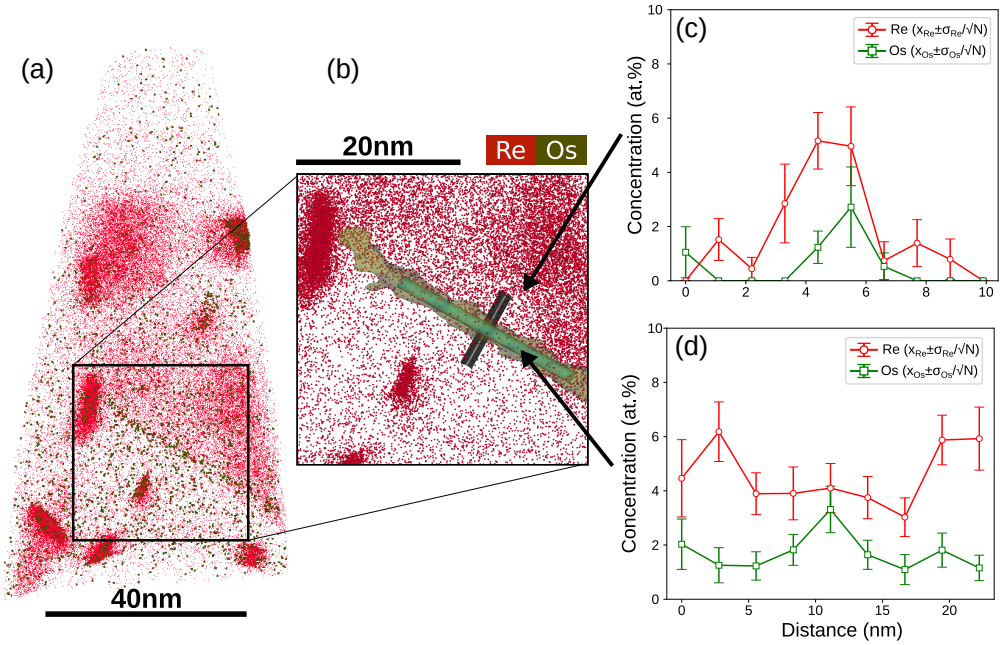


Figure 3.18: Segregation of Re and Os transmutation products to a line dislocation in W-1.4Re-0.1Os irradiated to 1.67dpa at 1173K, measured using APT. Shown in (a) is the full data set with Re atoms plotted in red and Os atoms in green, with (b) a higher magnification section of the sample with the line dislocation highlighted with a 0.5at.%Os isoconcentration surface. Plotted in (b) are the ROIs used to analyse the segregation of Re and Os to the dislocation. The plots shown in (c) and (d) show the line profile concentrations from the ROIs shown in (b) for the transverse and in-line directions respectively. In (c) and (d), the circular red points represent Re and the square green points represent Os. The error bar is given by the standard error, $\sigma_{\bar{x}}$ for each of the bins, calculated using $\sigma_{\bar{x}} = \sigma/\sqrt{N}$ where N is the number of points in each bin, and σ is the standard deviation of the bin concentration.

Re to the loop, in addition to Os has occurred but that it is not as strongly bound to this location.

3.5 Voids

APT analysis detected the presence of Re and Os rich precipitates, and Os decorated dislocation loops. A number of previous studies of neutron implanted W, including analysis by Klimenkov et. al of this material have detected the presence of voids using TEM. APT cannot directly image voids,

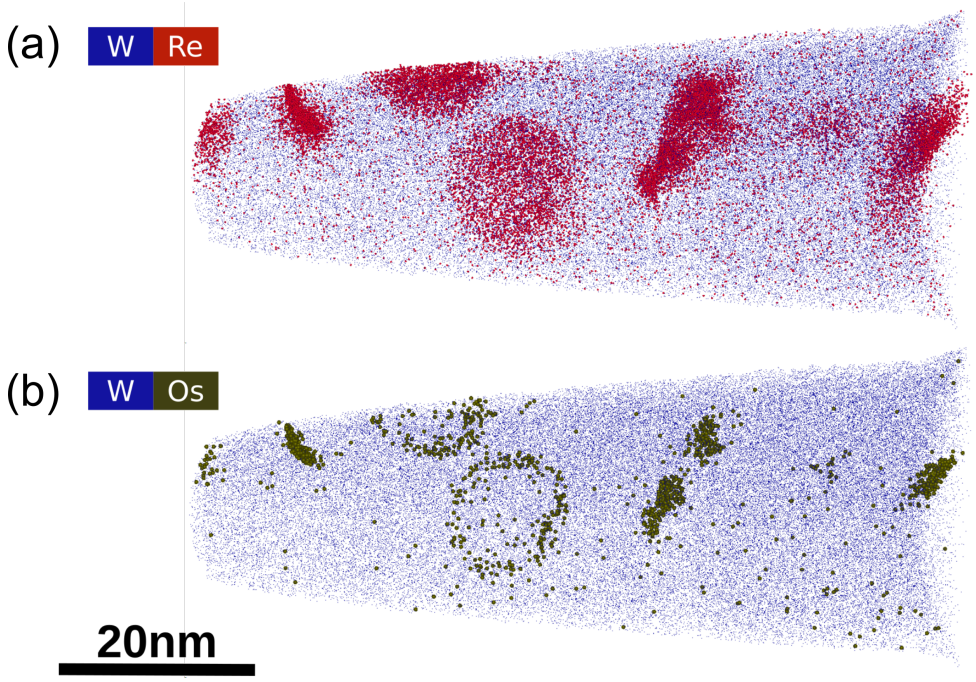


Figure 3.19: Segregation of Re and Os transmutation products to a dislocation loop in W-1.4Re-0.1Os irradiated to 1.67dpa at 1173K, measured using APT, showing 8% of W atoms for visual clarity in addition to (a) Re atoms and (b) Os atoms.

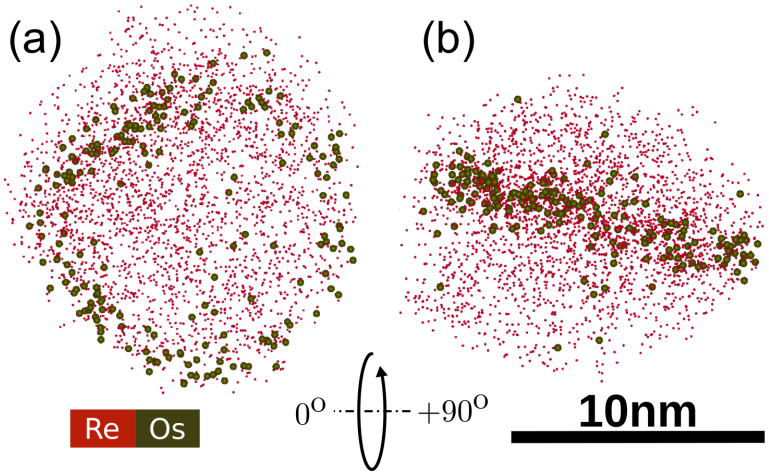


Figure 3.20: Higher magnification image of the loop shown in figure 3.19, obtained by extracting a volume defined by a Re isoconcentration surface, showing two different orientations which are rotated 90° with respect to one another, with all W atoms removed. The Os atoms are plotted as larger spheres compared to the Re atoms.

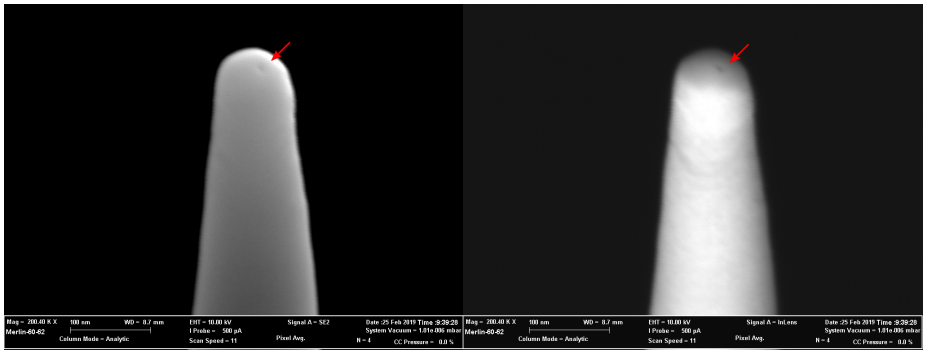


Figure 3.21: SEM image of tip number M-21 imaged using both secondary electron and in lens detectors showing the presence of a small region of contrast corresponding to a void.

but as described by Wang et. al [126], atomic density artefacts due to voids can be observed. In this section the effect of voids on APT analyses will be discussed as well as STEM imaging of voids.

3.5.1 *Density Artefacts in APT*

While performing APT, high density regions were observed on the detector ion hit map during evaporation through a Re rich area. This indicated that field induced trajectory aberrations had been introduced during evaporation. On one sample, laser pulsing was stopped during evaporation through a Re rich region in which a high density region was observed on the detector ion hit map. The tip was then removed and imaged using a Zeiss Merlin SEM. As shown in figure 3.21, there was a faint contrast caused by a feature on the surface of the tip, in both secondary electron and in-lens detectors. This indicated that the Re rich features seen in the APT data may be correlated with voids and motivated further investigation.

Analysis of the reconstructed APT data also supported the hypothesis that voids were correlated with the Re and Os rich features observed in

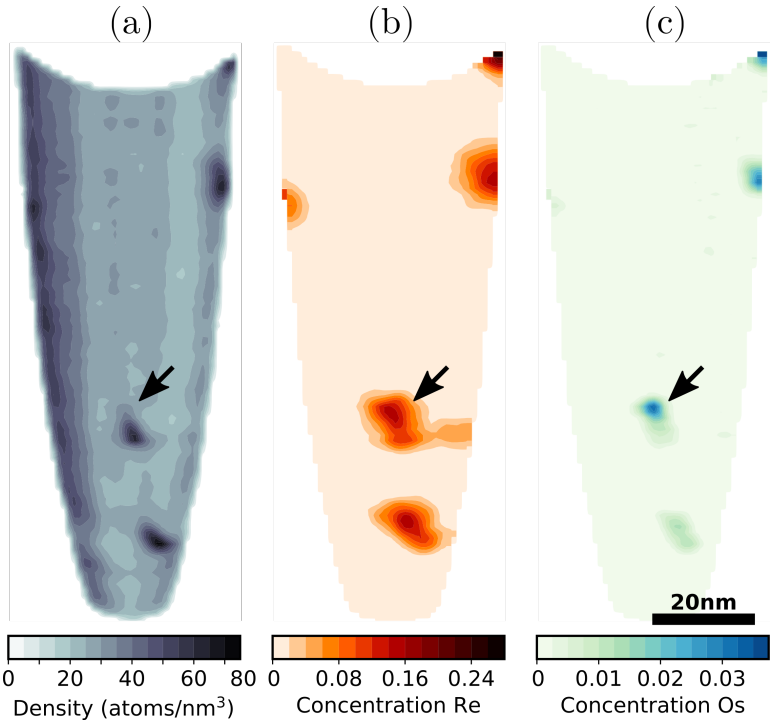


Figure 3.22: 5nm cross section of the atom map shown in figure 3.10. (a) Density contour in number of atoms per cubic nm (b) Re concentration contour (c) Os concentration contour. Arrow indicates central precipitate with Os rich zone offset from higher density region.

section 3.4.3. To investigate the density aberrations typically associated with voids, a 5 nm slice was taken through a reconstructed sample from the single crystal material. A 2D density plot was then produced using the binned atomic density data from this slice, as shown in figure 3.22. High density regions with atomic density above 60 atoms/nm^3 are correlated with the Re and Os rich clusters. At the centre of the Re clusters in figure 3.22, the measured atomic density from APT is ≈80 nm^{-3}, whereas on average the bulk density is ≈30-40 nm^{-3}. Bulk density measurements from APT are significantly lower than the theoretical atomic density as APT does not detect 100% of the atoms. Despite this, the measured core density of the clusters is above the theoretical maximum atomic density of W 62.84 nm^{-3}

[1]. Accounting for a detection efficiency of around 50% [201] for the LEAP 5000 XR gives a bulk density for W of around $30\,\mathrm{nm}^{-3}$, in agreement with figure 3.22.

The presence of these high density regions in the APT data does not conclusively prove that all of the clusters are associated with voids, as other features such as phases with low field evaporation thresholds could also introduce these artefacts [194]. Wang et. al outline a method for correlating isodensity surfaces with voids using correlative TEM [126], but this was performed for samples without the presence of solute rich clusters. Re has a lower evaporation field threshold and therefore local curvature effects at the specimen surface due to the preferential evaporation of Re could contribute to an increase in the observed density. In small clusters in ion implanted data this effect was lower than was measured in figure 3.22, but the effect of large Re and Os rich clusters is unknown. Fully understanding the post-irradiation microstructure therefore required the use of additional characterisation techniques.

3.5.2 *STEM Imaging of Single Crystal Sample*

To investigate the voids further STEM analysis was carried out on TEM foils prepared by Abernethy, details of which can be found in [109]. A combination of STEM High Angle Annular Dark Field (HAADF) imaging and EDX mapping was carried out using a JEOL 200F ARM TEM, operating

[1]The theoretical maximum density was calculated as $\mu = N/V$, where N is the number of atoms in the unit cell, which is 2 for the bcc structure, and V is the unit cell volume given by $V = a_0^3$ where a_0 is the lattice parameter (3.169 Å for bcc W)

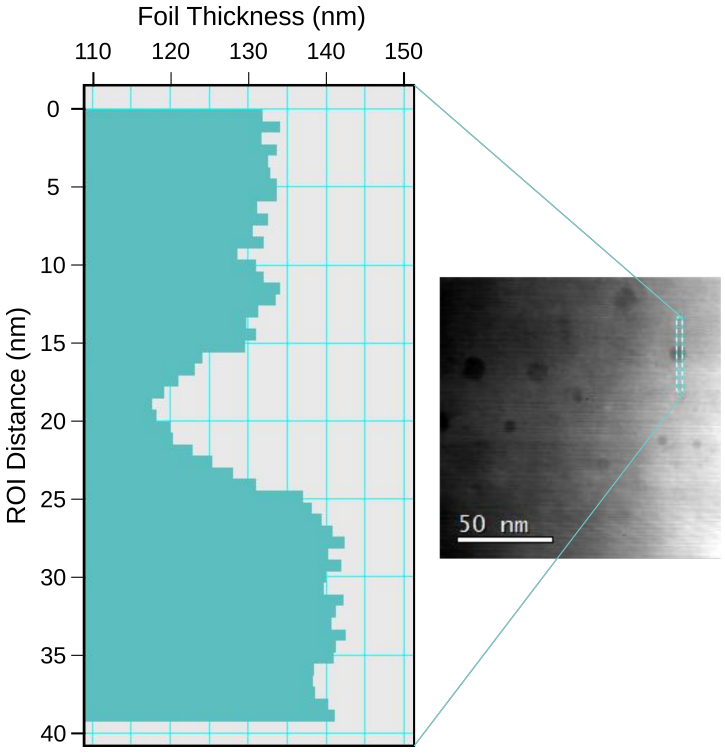


Figure 3.23: EELS thickness measurement across a suspected void in STEM image (right), showing the drop in thickness in the darker region.

at 200 kV and equipped with a JEOL Centurion EDX detector and a Gatan GIF.

High Angle Annular Dark Field (HAADF) imaging of the foil found a large number of dark circular features, which is indicative of voids. This was confirmed using Electron Energy Loss Spectroscopy (EELS) thickness line scan measurements across the dark regions, as shown in figure 3.23. TEM imaging of the APT samples prior to analysis supported this, with under and over focus images showing a clear change in contrast, thus confirming the presence of voids[2]. Figure 3.24 shows a higher magnification image of a void in the single crystal sample, in which atomic planes are visible. The

[2]These samples were prepared for correlative TEM/APT analysis as is discussed in section 3.6, however, this study was not completed due to the impact of the Covid-19 pandemic

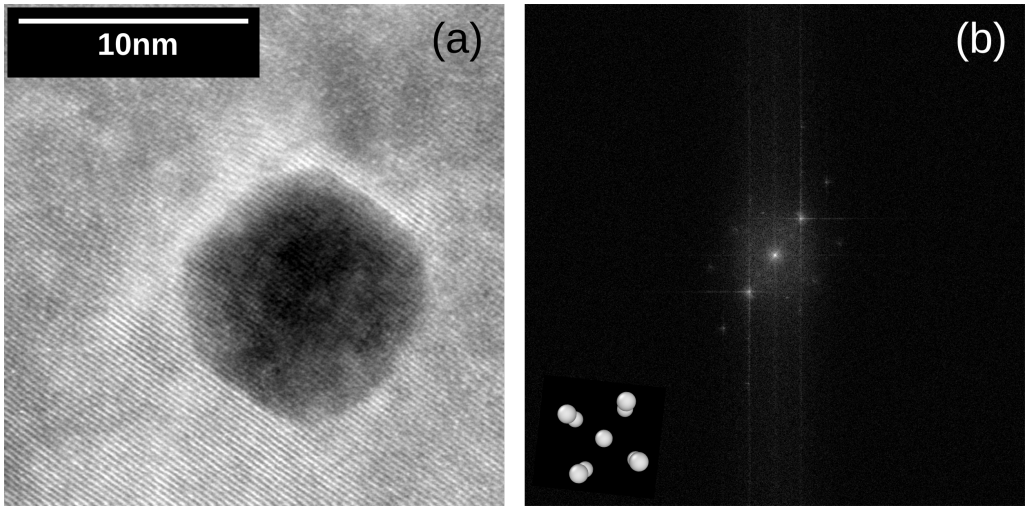


Figure 3.24: (a) High magnification HAADF image of a void in the single crystal neutron irradiated sample with (b) corresponding Fast-Fourier Transform (FFT) image showing the orientation of the void facets, which are aligned along the (110) directions.

void has faceted surfaces aligned along the (110) planes, confirmed using a Fast Fourier Transform of the left hand image. Figure 3.25 shows lower magnification HAADF images from two sites in the single crystal sample, which clearly shows the voids. In addition to the voids a number of small bright features can also be seen in figure 3.25a.

EDX mapping was performed using the Lα peaks of Re, Os and W at 8.651 eV, 8.910 eV and 8.396 eV respectively, to identify the atomic species. To reduce drift artefacts, EDX was performed using multiple scans and a fast acquisition time. EDX mapping of a single large void identified a Re rich shell around the void with a precipitate offset to one side, as shown in figure 3.26. The smaller isolated precipitates were also shown to be associated with a Re and Os signal, indicating that both precipitates and decorated voids were present in the material. The apparently isolated precipitates could be associated with small vacancy clusters that could not be resolved.

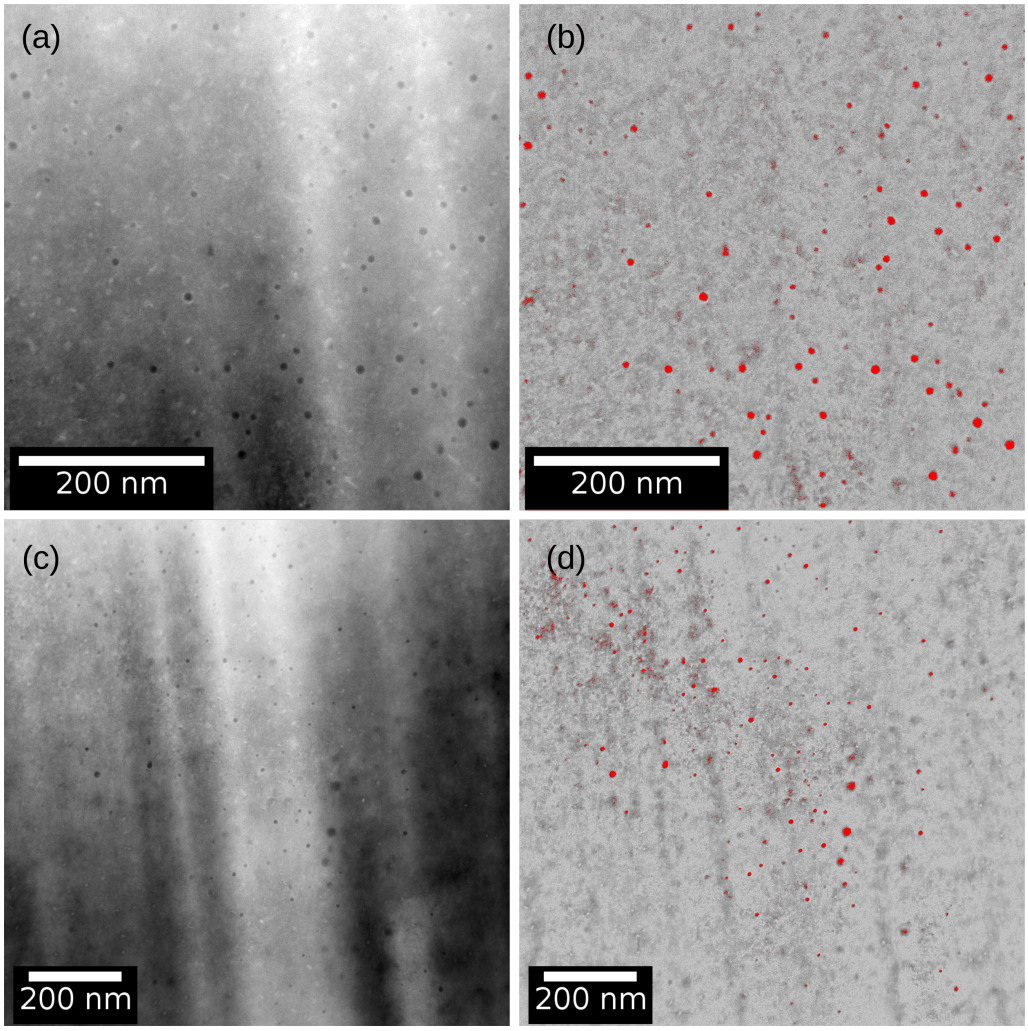


Figure 3.25: Low magnification STEM-HAADF images of voids and precipitates in single crystal neutron irradiated sample. Raw images from two sites are shown in (a) and (b) and after background subtraction in ImageJ in (c) and (d). Voids are shown as regions of dark contrast. Voids are highlighted in (b) and (c) in red using a contrast threshold.

3.5.3 *STEM Imaging of Polycrystalline Sample*

Similar analysis was performed on a foil taken from the polycrystalline sample. The foil investigated by Abernethy [109] was polished further in an FEI HELIOS FIB-SEM at the MRF to reduce the thickness and remove FIB damage and surface oxidation. Figure 3.27 shows 3 HAADF images taken from the polycrystalline foil with corresponding W, Re and Os EDX map-

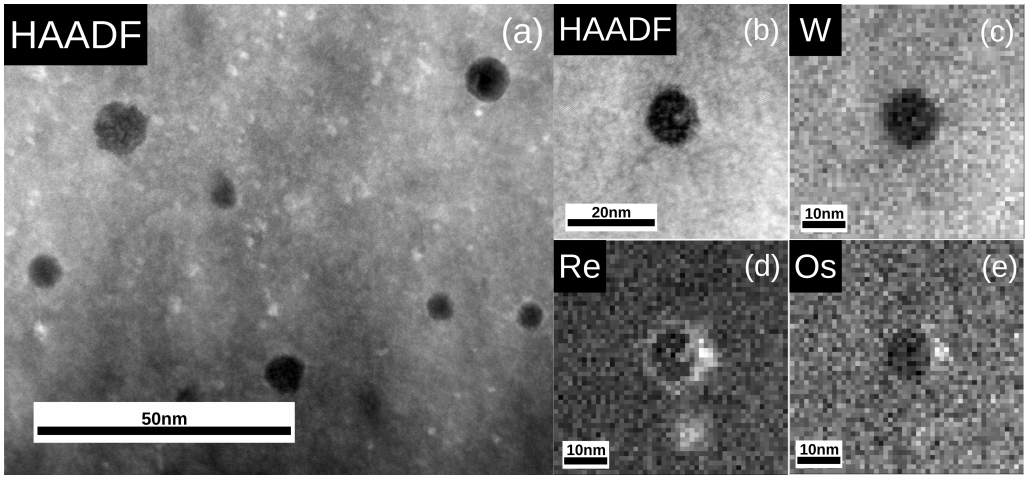
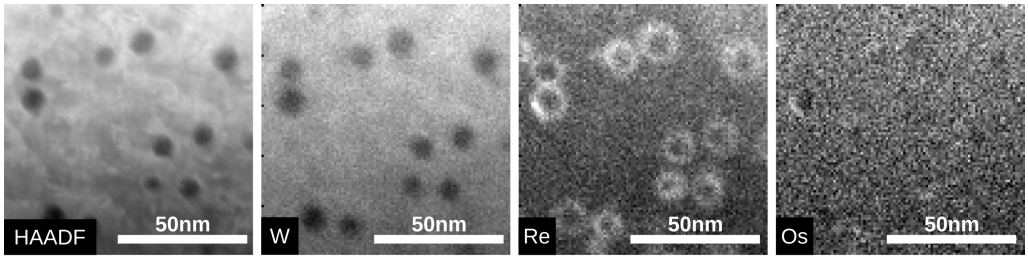


Figure 3.26: (a) Lower magnification and (b) high magnification High Angle Annular Dark Field (HAADF) images of voids in neutron irradiated single crystal W. EDX Maps of (c) W (d) Re and (e) Os showing the decoration of the central void.

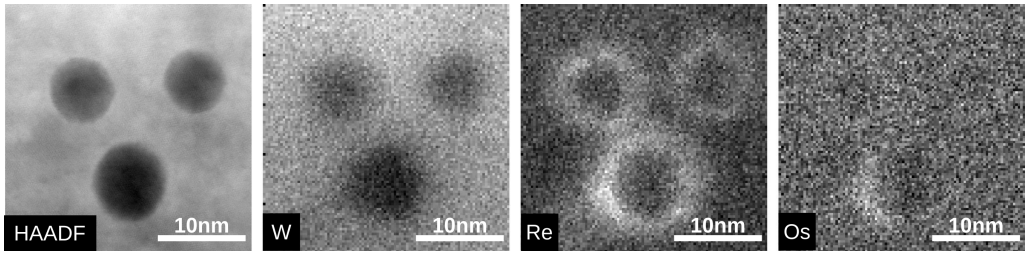
ping. As with the single crystal sample, the EDX mapping shows that the voids are decorated with Re and Os. The signal from Os is much lower and therefore an Os shell is not visible on all of the voids. Figure 3.27b shows a strong Os signal on one side of the void, corresponding to the region where the Re signal is also maximum.

Figure 3.27c shows that in addition to the decorated voids, the small rod shaped features are rich in Re and Os, confirming they are small precipitates. Diffraction pattern analysis of the small features was unable to detect the presence of σ or χ phases, however, the size of the rod is consistent with the centre of the precipitate shown in figure 3.13.

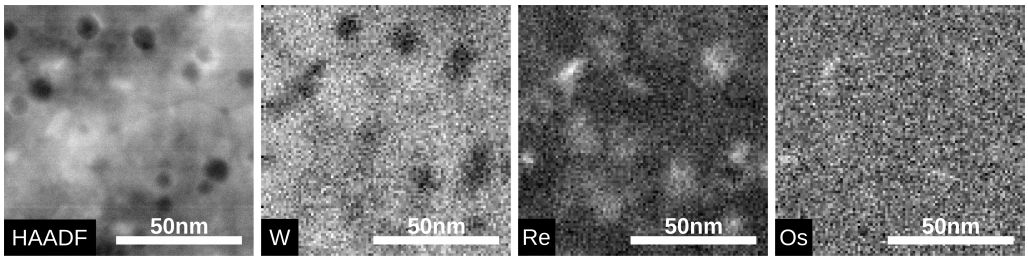
HAADF imaging of the sample close to GBs showed that the microstructure was strongly affected. Figures 3.28 and 3.29 show HAADF images taken of the sample at low magnification showing multiple grain boundaries, and at a higher magnification at a grain boundary triple point respectively.



(a) Lower magnification.



(b) Higher magnification.



(c) Voids and Precipitates.

Figure 3.27: (a) Low and (b) high magnification STEM-HAADF images of voids and (c) voids and precipitates in the polycrystalline neutron irradiated sample, with corresponding EDX maps of W, Re and Os.

As highlighted in the inset image in figure 3.28, close to the GB there is a void denuded zone followed by a region of large voids. The void size trends downwards further away from the boundary. Voids are still present far away from the boundary as shown in figure 3.28.

To illustrate this effect further, figure 3.30 shows the variation in void size as a function of distance from the GB in a 600x600nm ROI taken from the image shown in figure 3.28, with the approximate location of void denuded zone highlighted in blue. The void sizes in nm^2 were extracted using a contrast thresholding method in ImageJ. Each region of dark contrast cor-

responding to an individual void is approximated by a circle of equivalent area in figure 3.30a which shows the trend of increasing void size close to the boundary. Figure 3.30b shows the mean of the binned area associated with a void in the HAADF as a function of distance from the centre of the void denuded zone. The error bar is given by the standard error for each bin. Close to the boundary at 0 the error bar is larger because of the small number of voids at that position. There is a clear declining trend in void size away from the GB.

EDX analysis of the GBs confirmed the presence of Re and Os decoration, as was observed using APT as shown in figure 3.15. Figure 3.31 shows HAADF imaging of a GB with corresponding W, Re and Os mapping.

3.6 Correlative TEM/APT

A combined TEM/APT analysis was started for these samples, using a similar method to that outlined by Wang et. al [126], however, this was not completed due to the impact of the Covid-19 pandemic. Samples were imaged using TEM prior to APT using different rotation angles to show the void positions using under and over focus (as shown in figure 3.32), however, correlation with the APT data was not possible with the data obtained. Comparison of the TEM and APT data did confirm that a higher number of Re rich clusters were present in the APT data than there were voids in the corresponding TEM image.

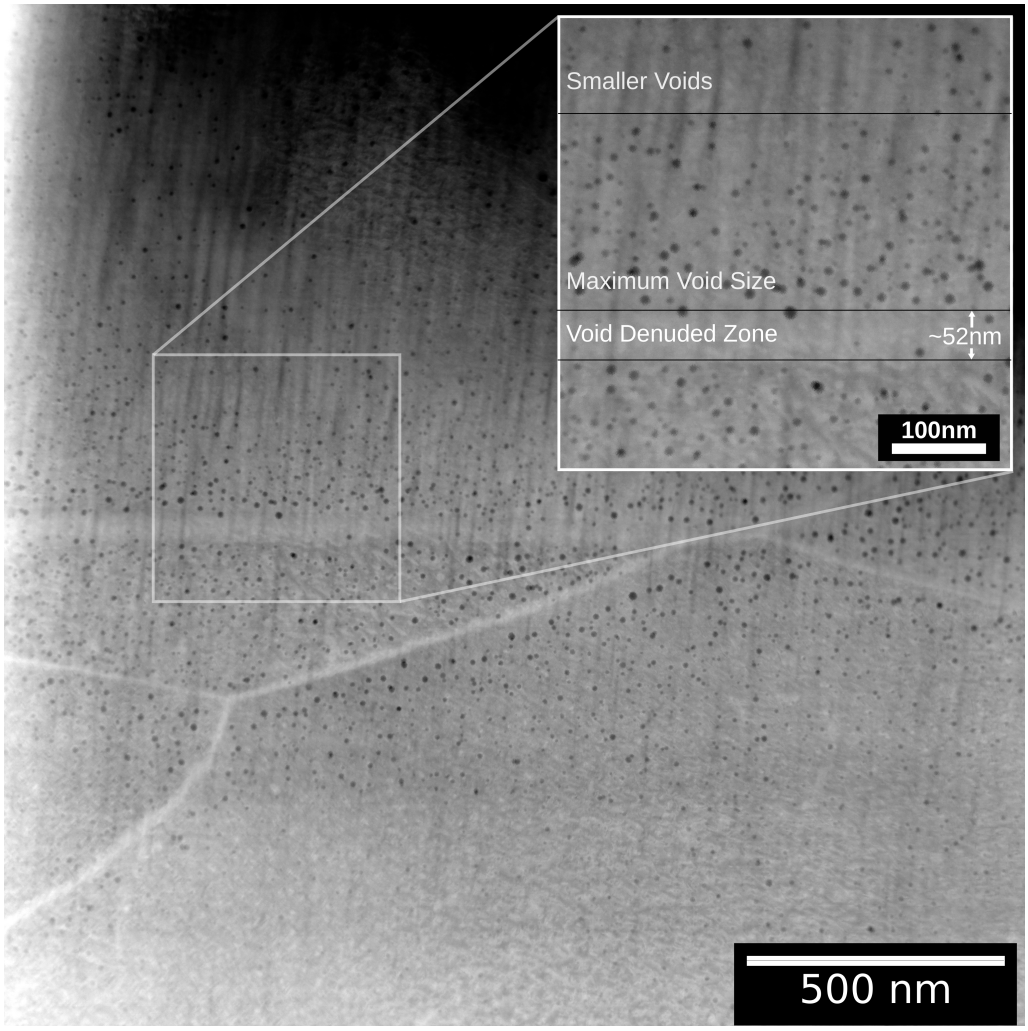


Figure 3.28: Low magnification HAADF images of the neutron irradiated polycrystalline sample, showing voids as dark regions and grain boundaries as bright lines. Inset is a higher magnification image of a region containing a GB showing the void denuded zone and maximum void size region.

3.7 Summary of Neutron Irradiation

In this chapter, single and polycrystalline samples were neutron irradiated at high temperature and with a lower transmutation rate that typical fission spectrum neutron irradiations. Post-irradiation characterisation found a combination of Re and Os decorated voids, small dislocation loops and Re and Os rich precipitates. A mixture of spherical and rod/plate like pre-

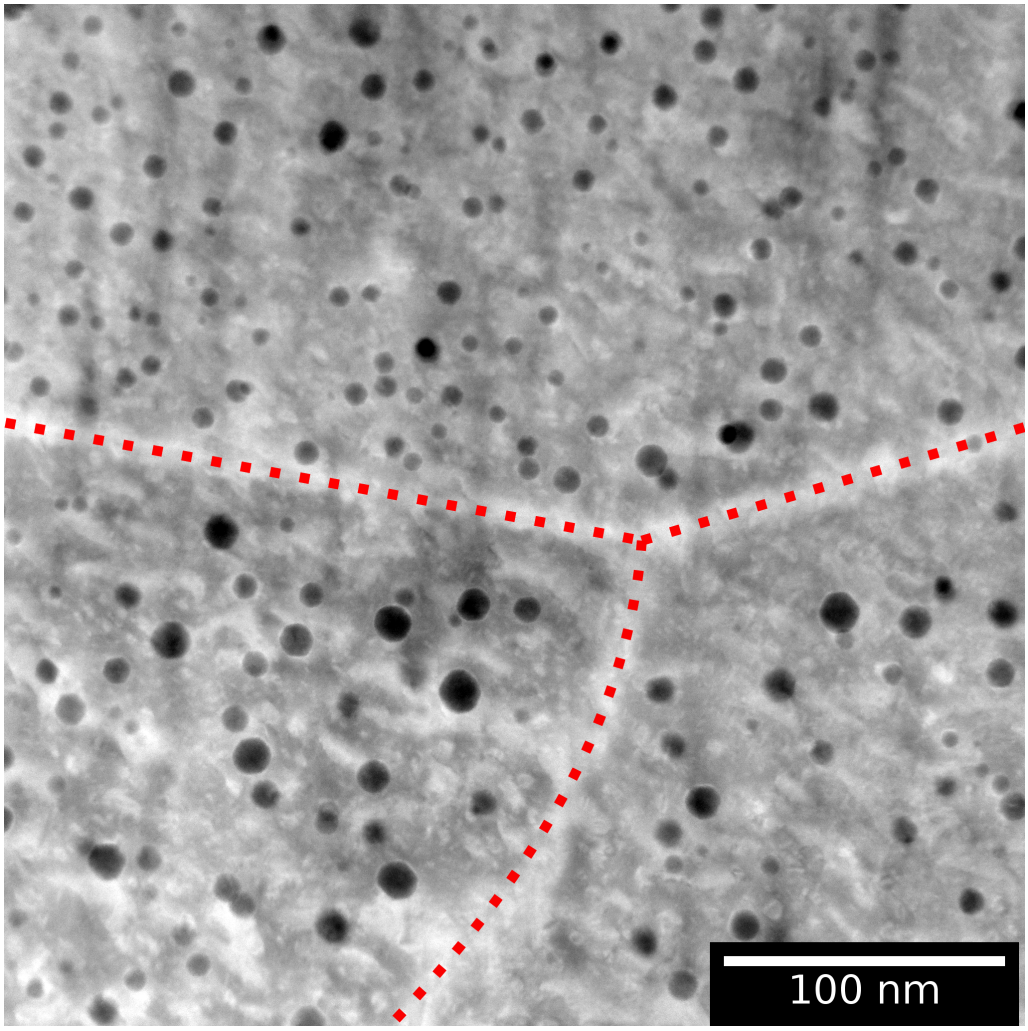
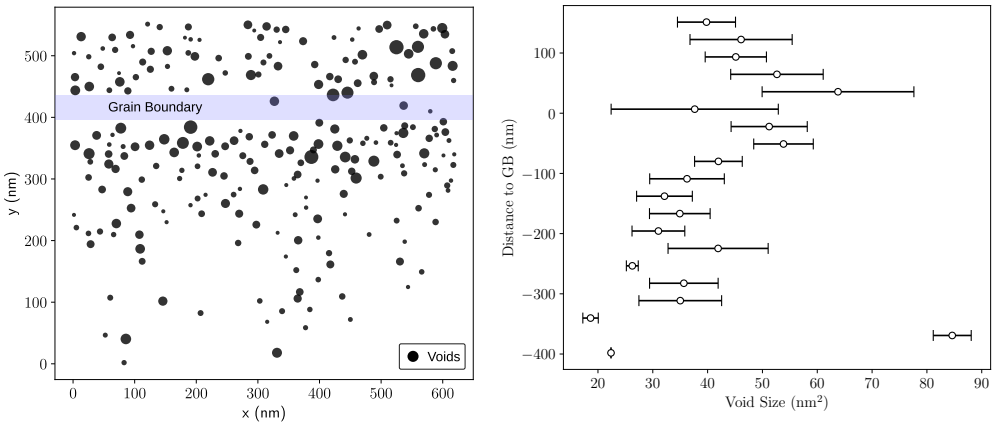


Figure 3.29: High magnification HAADF images of the neutron irradiated polycrystalline sample, showing voids as dark regions and grain boundaries highlighted in red.

cipitates were observed, suggesting that a combination of coherent bcc, and less coherent precipitates were present. Despite the low nominal concentration of Os (0.1at.%), strong precipitation was observed to voids, dislocation loops and precipitates. Precipitates analysed using APT typically showed a central Os and Re rich core surrounded by a cloud of more diffuse Re. Cluster analysis found that on average these clusters had a composition consistent with the solid solution region of the ternary phase diagram, however, line profile analysis showed that in the centres of some of these precipitates,



(a) Void Size Distribution. **(b)** Distance to GB.

Figure 3.30: Spatial distribution of voids near to the GB, showing (a) a graphical representation of voids as black spheres of area corresponding to the area obtained by contrast thresholding of the original image and the grain boundary highlighted in blue. Shown in (b) is the binned void size in nm^2 as a function of distance from the GB.

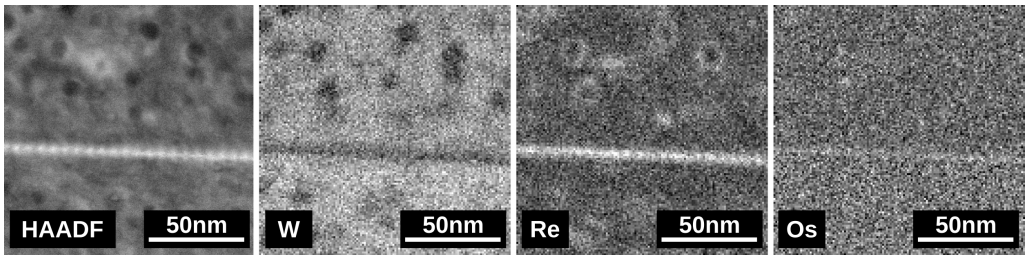


Figure 3.31: HAADF image of GB with adjacent voids with corresponding EDX maps of W, Re and Os respectively showing GB decoration with Re and Os.

the concentration had reached 50at.%Re and around 8at.%Os which is consistent with the σ phase region of the ternary phase diagram. Diffraction pattern analysis from TEM and FFT of STEM images was unable to detect the presence of σ phase independently of APT. In both analyses there was no indication of χ phase. In the polycrystalline sample, GBs were decorated with Re and Os. Adjacent to the GBs was a void denuded zone, followed by a distribution of void sizes which was maximum adjacent to the void denuded zone and decreased further from the boundary.

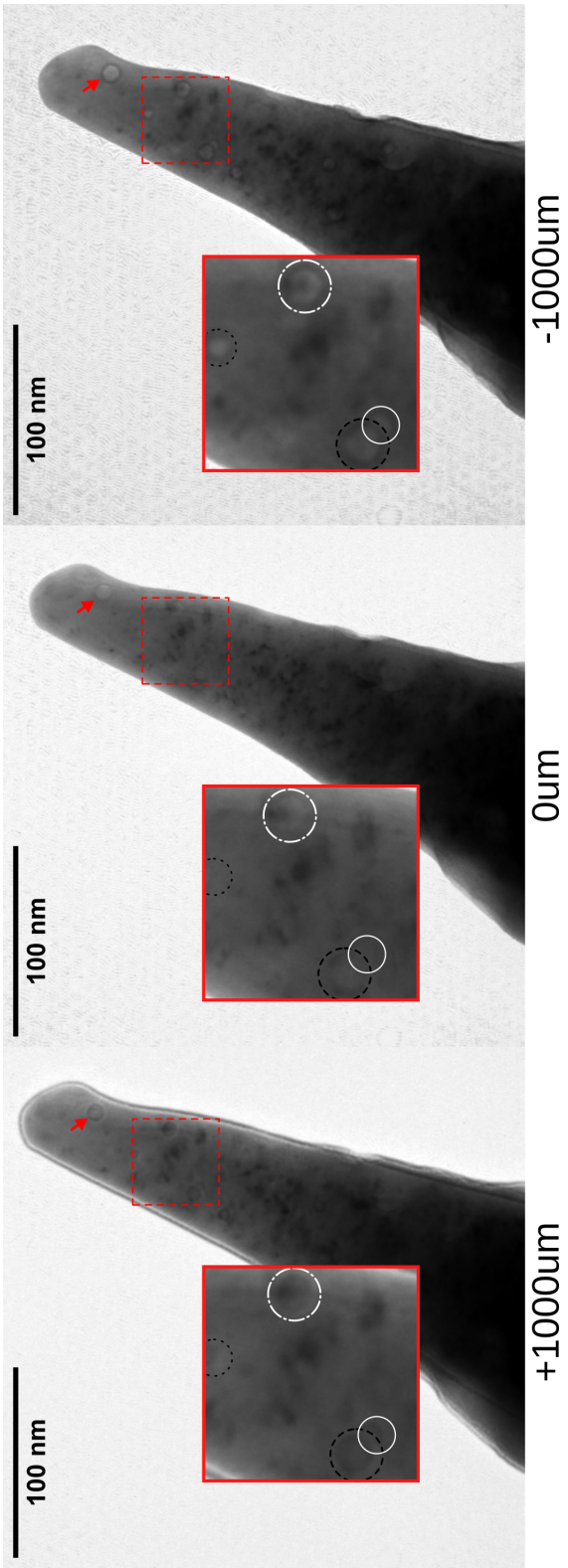


Figure 3.32: Under and over focus conditions used to confirm the presence of voids. Images shown for one rotation condition at ±1000 µm from the in focus condition. Arrow shows presence of one void to illustrate the change from bright to dark contrast.

The number of Re precipitates in APT, compared to the number of voids observed using TEM confirms that not all of the features in the APT data are associated with voids. Density artefacts suggest that some of these features are voids but without correlative TEM it is not possible to confirm this. The features observed in the APT data in figure 3.6-3.9 are therefore a mixture of decorated voids and isolated precipitates, both of which appear to exhibit an Os and Re rich core surrounded by Re.

The cluster analysis shows that the precipitates have a similar composition to other studies of samples with similar transmutation levels, but that this approach may not account for the region at the core of the precipitates in which the Re and Os concentration is consistent with σ phase. The reason for the lack of χ phase when compared to other studies is unclear but could be a result of different transmutation levels.

Re and Os introduced via transmutation, undergo point defect mediated transport, including rapid movement via mixed interstitials. Voids are formed by the clustering of vacancies introduced via radiation damage. Precipitates nucleate on voids which act as sinks for point defects leading to decoration, at other sinks of point defects such as dislocations, or via mixed interstitial clustering. As transmutation proceeds, more solute transport to these features occurs as well as localised transmutation leading to Os production (though the comparative importance of these two mechanisms on the Os concentration is currently unknown). Os transport would be preferential to Re because of its higher binding to point defects. It is likely

that in samples with higher levels/rates of transmutation, this transport is accelerated thus further increasing the central Re and Os concentration to the extent that χ phase formation is favoured.

At grain boundaries, decoration with Re and Os occurs due to point defect mediated transport. Close to the boundary, the vacancy concentration is lower, because they are annihilated at the GB. But due to the higher concentration of Re and Os adjacent to the GB, which is more strongly bound to vacancies in W, it would be energetically favourable for the vacancies to migrate to this region compared to the bulk of the grain where the concentration of solute is lower. This could explain the void denuded zone and region of maximum void size region observed in figure 3.28. Modelling could be used to test this hypothesis but depends on an accurate description of the vacancy, Os and Re interactions in W.

4 Ion Irradiation

▶ Synopsis: In this chapter, the post-irradiation characterisation of high temperature, heavy-ion implanted alloys of W-Re-Os-Ta is presented. Characterisation was performed using APT and STEM and the microstructure is compared to that produced by neutron irradiation.

Ion irradiation was carried out at SNL with the help of Osman El Atwani (Los Alamos National Laboratory, USA), Khalid Hattar and Trevor Clark. Some additional analysis was performed on samples irradiated by Alan Xu at the Surrey Ion Beam Centre and by Robbie Abernethy at Saclay. TEM imaging was performed by Jack Haley on the SNL samples. Heat treatments were performed by Tony Wheeler and the W-2Re sample from SNL was prepared and analysed using APT by Hazel Gardener.

4.1 Sample Production

As discussed in the previous chapter, neutron irradiation under a DEMO fusion neutron spectrum results in comparatively small quantities of Re and Os per dpa when compared to a fission reactor irradiation. In the samples discussed in section 2.2.1 the transmutation rate was lower than usual, but still considerably higher than in DEMO as shown in figure 2.3. Heavy-ion irradiation, as a means of simulating neutron damage, has many advantages over neutron irradiation (as discussed in section 1.5.2). Heavy-ion irradiation does not produce transmutation reactions, and the sample composition is kept constant during irradiation. This is advantageous for the study of transmutation induced phenomena because it allows for fusion relevant dose to solute ratios to be studied systematically. However, neutron

and heavy-ion irradiation are known to produce different microstructures. Understanding these differences is key to accelerating component design with ion irradiation.

In this study samples were designed with compositions corresponding to the predicted transmutation level under a DEMO FW neutron spectrum. Additional samples were prepared with the same composition as the neutron irradiated sample from the previous section. Characterisation of the complete set of these samples was not carried out due to the impact of the Covid-19 pandemic.

4.1.1 *Simulated Transmutation Samples*

A matrix of alloys with compositions representing points along the predicted transmutation pathway (shown in figure 4.1) for W were produced commercially by ACI Alloys. The alloys purchased are summarised in table 4.1, and the chemical analyses provided by the supplier are given for two samples in Appendix E. All of the compositions were quoted by the manufacturer as accurate to within ± 0.01 at %. The composition was achieved by mixing metallic powders and then arc melting oversized billets (at least 4x larger than the final sample). After melting and solidification the samples were then turned using a lathe to create bars, 10 mm in diameter and 25 mm long.

The bars were sectioned into circular discs, 10 mm in diameters and between 1 and 2 mm thick. Electrical discharge machining (EDM) was possible in non-Os containing samples but not for those containing Os.

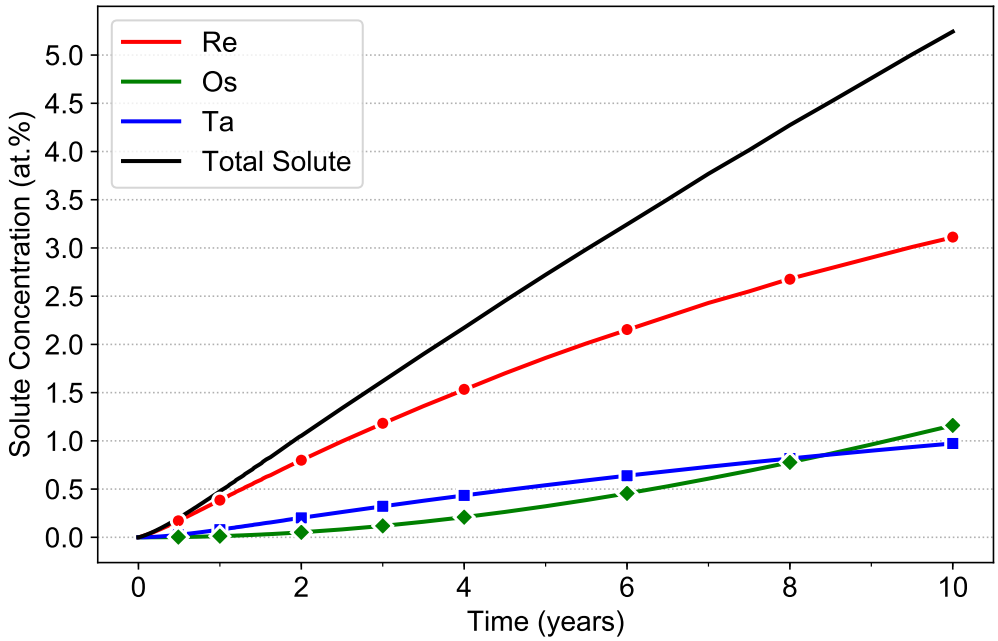


Figure 4.1: Simulated solute concentrations as a function of irradiation time for pure W tiles under a DEMO first wall neutron spectrum. Points show the transmutation concentrations at which pre-alloyed samples were made.

Potential oxidation and formation of OsO_4 was prevented by using an oil bath, however, the resistance of the samples to spark erosion led to depletion of the electrodes rather than the sample. A Beuhler IsoMet low speed saw equipped with a diamond tipped wafering blade was therefore used to section the Os containing alloys. The resistance of the alloyed samples to cutting compared to the pure W was notable and the alloyed samples typically took between 4 and 6 hours for a single cross sectional cut to be made, compared to <1 hour for a pure W sample.

For irradiation at SNL, a subset of 9 samples was chosen, indicated in table 4.1 by an asterisk. Grinding and polishing was carried out on a maximum of 5 samples at a time, mounted using Crystalbond onto a heavy sample holder. All of the samples were ground manually, using SiC grit

Table 4.1: List of samples used in this study. Samples irradiated at SNL are indicated by a * symbol. Samples irradiated at Saclay by R. Abernethy are indicated by a † [109]. Samples marked with a ' were made in reference to [134].

ID	Re (at.%)	Os (at.%)	Ta (at.%)	Description
WP1*	0.00	0.00	0.00	Ref.
WP2	0.00	0.00	0.00	Ref.
WB1'*	2.00	0.00	0.00	
WB2*	5.00	0.00	0.00	
WB3'	0.00	1.00	0.00	
WB4*	0.00	0.00	1.00	
WB5	1.00	0.00	0.00	
WT2'	2.00	1.00	0.00	
WT3'	2.00	0.00	1.00	
WQ1*	0.38	0.01	0.08	0.5 years DEMO
WQ2*	1.18	0.12	0.32	3 years DEMO
WQ3	1.9	0.32	0.54	5 years DEMO
WQ4*	2.68	0.78	0.82	8 years DEMO
WQ5	3.10	1.20	1.00	10 years DEMO
WQ6	5.00	3.00	3.00	
WQ7	10.0	5.00	5.00	
WB6†	1.40	0.00	0.00	208 days HFR (Re)
WT1**	1.40	0.10	0.00	208 days HFR (Re+Os)
WT4	1.00	2.00	0.00	Xu et. al. [134]

papers, of successively finer grades from 125 to 2000. The samples were then polished using diamond suspension paste from 6 µm to 1 µm followed by a final stage of colloidal silica. Each polishing and grinding stage lasted between 10 min and 30 min. Following polishing the samples were removed from the holder using acetone and an ultrasonic bath. Each sample was then cleaned in the ultrasonic bath and then using a cotton wool bud and isopropanol.

4.1.2 *Other Samples used in this Study*

In addition to the samples irradiated in this study, other previously irradiated samples were characterised. An arc melted W-1.4Re sample fabricated by Abernethy and irradiated at JANNuS (Joint Accelerators for Nanosciences and NUclear Simulation), Saclay was used. Full details of the production of this material are available from [109]. A W-1Re-1Os sample made by Xu, and ion irradiated at the Surrey Ion Beam Centre to a reported dose of 33 dpa[1], was also analysed, full details of which are available in [84]. In the following section, a brief description of the ion irradiation carried out in each study is given.

4.2 Ion Irradiation

The main focus of the ion irradiation carried out in this project was to produce the same dose (1.67dpa), at the same temperature (1173 K) as the neutron irradiated samples from HFR studied in the previous chapter. In this section the ion irradiation experiment at SNL is outlined, as well as a brief description of the irradiations carried out elsewhere at JANNuS and the Surrey Ion Beam Centre.

4.2.1 *Procedure for Estimating Damage Profile*

The dose as a function of depth was estimated using the Stopping Range of Ion in Matter (SRIM) program, following the standardised procedure out-

[1] using the SRIM full-cascade mode, see section 4.2.1 for further details on the calculation of the peak dose level in these samples

lined by Stoller et. al [43]. SRIM simulations were performed in *Quick Kinchin and Pease* mode using a displacement threshold energy, E_d of between 55–90eV and with the lattice binding energy set to 0 eV. After calculating the displacements as a function of depth[2], the ion fluence needed to generate a peak dose at the required dpa was approximated using equation 4.1.

$$\mathrm{dpa}(z) = \frac{\Phi N(z)}{\mu} \tag{4.1}$$

where Φ is the ion fluence, $N(z)$ is the number of collision events per penetrating atom, per unit depth z, and μ is the atomic density of matrix atoms. For the purposes of comparison, the damage received by the samples studied here are discussed in terms of their peak dose in dpa, taken at the Bragg peak in the profile estimated by SRIM. The dose profiles for the samples studied here are given as a function of three displacement threshold energies: 55 eV, 68 eV and 90 eV to cover the range of values used in literature and the standard recommended by Stoller et. al [43] (ASTM standard, ASTM E521, Standard Practice for Neutron Radiation Damage Simulation by Charged-Particle Irradiation, Annual Book of ASTM Standards, Vol. 12.02, ASTM International, West Conshohocken, PA, 2009 [166]).

4.2.2 *Sandia National Laboratory*

The W-1.4Re-0.1Os (WT1) and W-2Re (WB1) samples were irradiated at the HVE 6MV tandem accelerator at Sandia National Laboratory's Ion

[2]provided in the VACANCY.txt SRIM output file in units of Å/ion

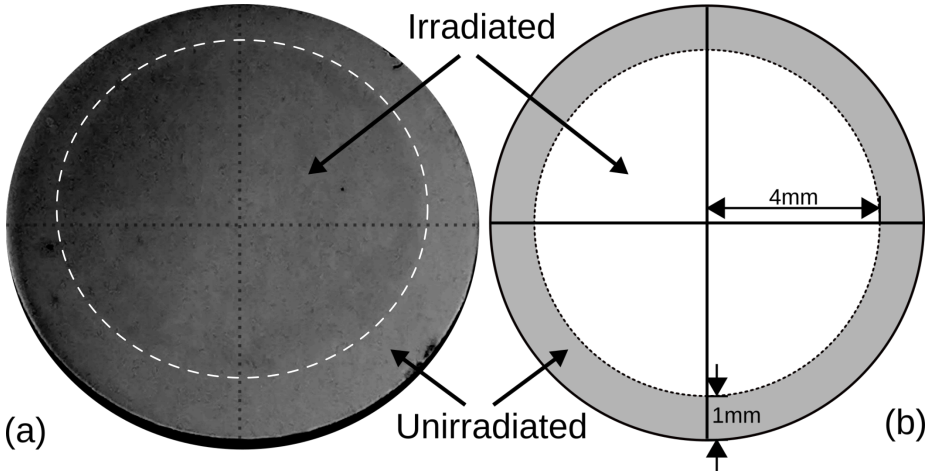


Figure 4.2: Ion irradiated sample from SNL showing (a) an enhanced contrast photograph showing the darker contrast from the central irradiated region and (b) a schematic illustration of the irradiated area shown in (a). The dashed line on (a) highlights the boundary between dark and light contrast on the sample surface, marking the boundary between irradiated and unirradiated material.

Beam Lab, capable of using an acceleration voltage of between 2 and 6MV. A 4MV voltage was used to accelerate W^{2+} ions to an energy of 8.0 MeV and these were implanted into each sample separately. A non-rastered beam with a Gaussian flux profile, approximately centred on the sample was used, covering an area of 0.58 cm^2 and producing an overall fluence of 2.8×10^{14} ions/cm^2. As shown in figure 4.2, each sample was 10 mm in diameter and therefore the irradiation left a circular ring of unirradiated material around the edge of the samples, approximately 1.0 mm thick.

The sample was irradiated at a temperature of 1173 K, monitored using a thermocouple welded to a ring shaped cap that covered the outer edge of the sample surface. High temperature was achieved using a button heater mounted to the underside of the sample. The thermal history of the sample during the irradiation is shown in figure 4.3. The irradiation conditions are

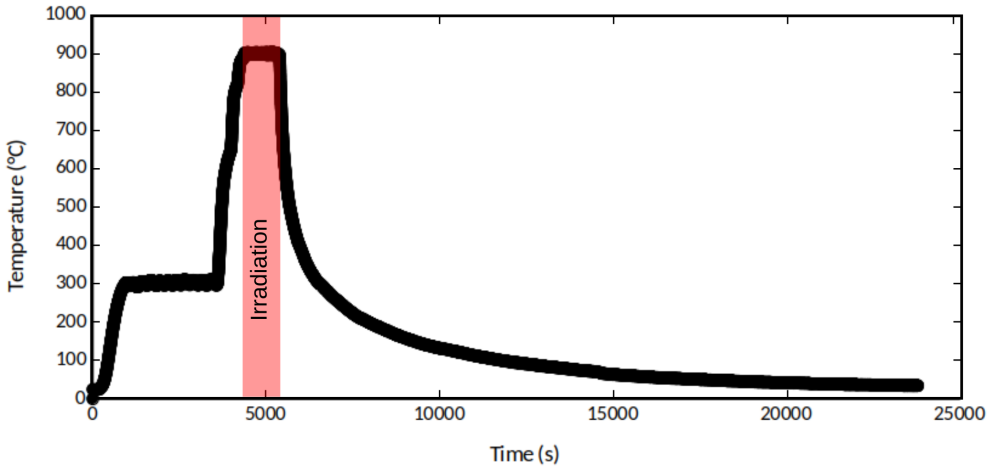


Figure 4.3: Thermal history of the sample during irradiation at SNL.

summarised in table 4.3 along with the JANNuS and Surrey samples.

The predicted damage as a function of depth into the sample surface estimated by SRIM is shown in figure 4.4a. A damage level at the Bragg peak of approximately 1.70dpa was achieved, calculated using $E_d = 55\text{eV}$ (equivalent to the E_d used in the prediction of damage for the HFR sample).

4.2.3 *JANNuS, Saclay*

A W-1.4Re sample (WB6† table 4.1) was irradiated at the JANNuS Saclay facility using W^{9+} ions, accelerated to 24MeV using a 3MV Pelletron accelerator (Épiméthée). Aluminium degrader foils of varying thickness were used to flatten out the irradiation profile and provide a damage plateau at approximately 1.7dpa, as shown in figure 4.4c. The peak damage in the Saclay sample was calculated as 1.7dpa using a displacement threshold energy of 68 eV in quick cascade mode. Irradiation was carried out at a temperature of 1073 K with an ion flux of $7.0 \times 10^{14}\,\text{m}^{-2}\,\text{s}^{-1}$, lasting an overall time of 11 580 s. The irradiation conditions are also summarised in table

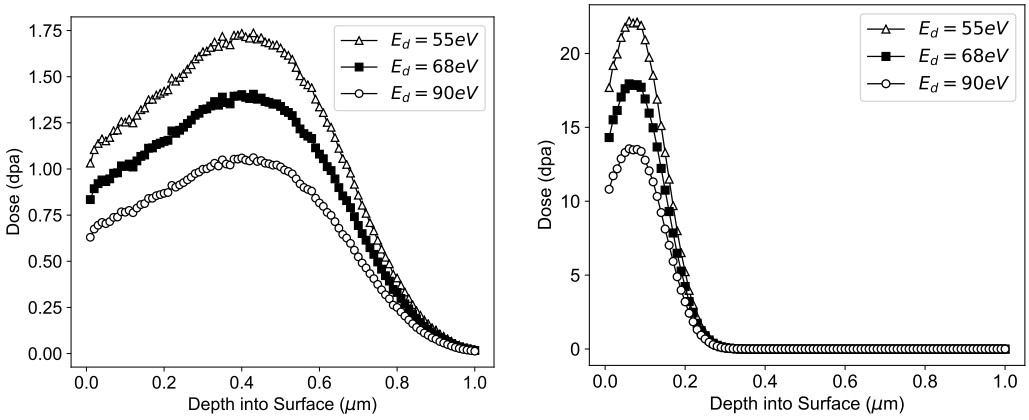
4.3. Full details are available from [109].

4.2.4 *Surrey Ion Beam Centre*

Arc-melted W-25at.%Re, and W-1Re-1Os samples were irradiated by Xu in a previous study at the Surrey Ion Beam Centre (SIBC) to a peak reported dose of 33 dpa at 773 K [84, 97, 134]. These samples were implanted using single charge, W^+ ions, accelerated using a 2 MV tandem accelerator to an energy of 2 MeV. The comparatively low energy of the ions and the high stopping power of W resulted in a Bragg peak at approximately 100 nm into the sample surface, extending to a maximum depth of between 250-300 nm. The reported Bragg peak dose in these samples was calculated using the full-cascade mode of SRIM, and were therefore recalculated here, as discussed in the next section.

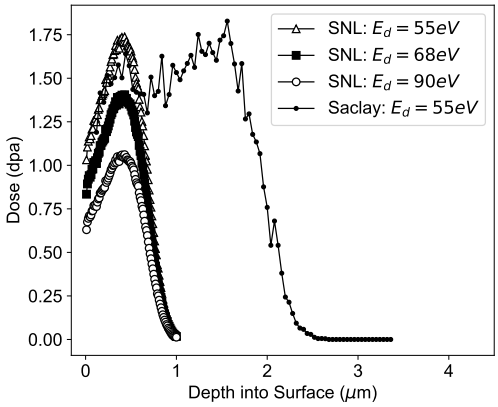
4.2.5 *Comparison of Depth Profiles*

The SRIM program, utilises the binary collision approximation to estimate the number of vacancies produced in a collision cascade. Standard practice is to use the displacement threshold energy listed in the ASTM standard [166], which is 90 eV for W. In studies of W, the value used varies between 55 and 90eV, with many using 68eV. Discrepancy also arises as a result of using the *Full Collision Mode* of SRIM, which overestimates the dose and results in an over-reporting of the peak dose and is not standard practice.



(a) SNL.

(b) Surrey Ion Beam Centre.



(c) Comparison between SNL and Saclay.

Figure 4.4: Dose as a function of depth into the sample surface estimated for the different self-ion irradiations conducted as part of this study and in previous work, estimated using SRIM with 3 displacement threshold energies: $E_d = 55$eV,$E_d = 68$eV and $E_d = 90$eV.

Table 4.2: Comparison of doses in dpa measured at the Bragg peak in the W-1.4Re-0.1Os sample irradiated at SNL using 3 different displacement threshold energies.

Displacement Threshold Energy (E_d)	Dose at Bragg Peak (dpa)
55	1.70
68	1.40
90	1.06

Table 4.3: Summary of irradiation conditions used in this study. Dose for ion implanted samples taken at the Bragg peak. For the SIBC and Saclay samples, the dose is taken at the Bragg peak simulated using an E_d of 68eV, whereas for the neutron irradiated sample and the SNL ion irradiation, the Bragg peak dose is taken from the simulation using E_d=55eV. Sample composition for the neutron irradiated samples is the predicted post-irradiation composition predicted by FISPACT-II and measured experimentally in this study using APT. Approximate irradiation times for SIBC irradiation calculated form the flux and fluence.

Irradiation Facility	Sample	Ion	Ion Energy (MeV)	Dose (dpa)	Flux ($m^{-2}\,s^{-1}$)	Fluence (m^{-2})	Temperature (K)	Time (s)
SIBC	W-1Re-1Os	W^{+}	2.0	18	3.06×10^{14}	2.5×10^{19}	773	81699
	W-25Re	W^{+}	2.0	18	3.06×10^{14}	2.5×10^{19}	773	81699
JaNNUS	W-1.4Re	W^{9+}	24	1.70	7.0×10^{14}	8.1×10^{18}	1073	11580
SNL	W-1.4Re-0.1Os	W^{2+}	8	1.70	2.8×10^{14}	3.0×10^{17}	1173	1071
	W-2Re	W^{2+}	8	1.70	2.8×10^{14}	3.0×10^{17}	1173	1071
HFR	W-1.4Re-0.1Os	n	N/A	1.67	$6.6–6.8 \times 10^{18}$		1173	1.8×10^{7}
Measured	W-1.2Re-0.1Os	n	N/A					

For the ion irradiation carried out in this research, SRIM simulations were carried out at 55, 68 and 90eV as shown in figure 4.4a. The variation between these simulations is significant: changing E_d from 55 to 90 eV, results in a peak dose of 1.70 and 1.06dpa respectively for the SNL irradiation, as shown in table 4.2. A value of 55eV was used as this was the value used in FISPACT-II simulations in the neutron irradiated material. The dose at the Bragg peak calculated using $E_d = 55$eV will be used from this point onward when discussing the SNL samples with respect to the previous chapter.

Xu et. al reported the value estimated using the full cascade model which is known to result in an overestimation of the peak dose compared to the standard quick mode. Equivalent SRIM simulations following the method outlined by Stoller [43] are shown in figure 4.4b. Using a E_d=68eV[3] gives a dose of approximately 18 dpa, rather than 33 dpa reported using the full cascade model. From this point onward, discussion of the samples reported in [84, 97, 134] will use a damage level of 18 dpa.

The range of peak doses given by the currently accepted values of the displacement threshold energy for W show the importance of this parameter in the setup of a SRIM calculation and the need for detailed reporting of the method of estimating the dose profile. Use of the full-cascade mode can also result in significant discrepancies, and highlights the need for a standardised approach.

[3]The E_d used by Xu et. al for the prediction of dose profiles in W-Re, W-Re-Os and W-Re-Ta [97, 134]. For comparison, quick Kinchen Pease simulations using E_d=55eV gives a peak damage at $\approx$ 125nm of 22dpa.

4.3 APT Sample Preparation

4.3.1 *FIB Lift-Out*

The ion implanted samples were prepared using a FIB lift–out procedure using a dual beam Zeiss NVision FIB-SEM. The SNL samples were taken from the centre of the disc at the point of maximum ion flux, where the dose received by the sample was 1.70dpa. Samples were also taken from the outer ring of the disc, where no ions were implanted but the same thermal cycle was applied (shown in figure 4.3).

A protective layer of C was first deposited on the surface of the samples, between 1-1.5 µm thick, in order to provide maximum contrast during thinning. W deposition was trialled with an electron beam deposited carbon interlayer, however, this did not provide sufficient contrast during tip sharpening. A triangular cross sectioned cantilever was made by milling trenches with an acceleration voltage of 30 keV and a beam current of 3 nA. The cantilever was then undercut using these same conditions. Lift-out was carried out using a Kleindeik Nanotechnik W manipulator.

The cantilever was joined to a Cameca 22post silicon micropost array, using GIS deposited W as a binding material, and then sectioned to leave a triangular cross section attached to the post. This resulted in between 6 and 10 APT tips per lift-out. The samples were then shaped using a range of successively lower beam currents between 700 pA and 10 pA until a tip diameter of 100 nm was achieved at the contrast boundary between

the carbon protective layer and W sample. A 2 keV, 300 pA beam was then used to polish the carbon protective layer away from the surface and remove a depth of the sample which depends on the implantation condition. In each of the ion irradiated samples, the samples were polished such that the Bragg peak was contained within the first 100-200 nm of the sample. The samples were transferred from the FIB to a vacuum chamber within 12 hours to prevent any oxidation. For targeted grain boundary APT, samples were made according to the procedure discussed in section 3.2.2.

4.3.2 *APT Analysis Parameters and Reconstruction*

APT was carried out using a Cameca LEAP 5000 XR. Samples were loaded into the load lock chamber within 12 hours of removal from the FIB and were left for >12 hours before proceeding to the higher vacuum buffer chamber. Samples were analysed in laser mode using a laser beam energy of 100 pJ, a specimen temperature of 55K and a pulse frequency of 100kHz for consistency with the previous chapter. The detection rate was varied between 1% and 0.1% depending on the tip. The tip alignment process described in section 3.3.1 was used to limit specimen fracture during setup.

A total of 6.38×10^6, 18.84×10^6 and 12.58×10^6 ranged ions were obtained for the Saclay, SNL and SIBC samples respectively. These ions were obtained in 3 APT data sets for the Saclay sample, 2 data sets for the SNL sample and 1 data set for the SIBC centre sample. The data was reconstructed using IVAS version 3.8.4, with a voltage mode reconstruction and an initial tip radius predicted by the software. The tip radius evolution was

also estimated using the voltage curve.

4.4 Re and Os Clustering

The following section will outline the APT results from the ion implanted material. Initial samples were taken from the concentrated W-25Re sample irradiated to 18 dpa by Xu et. al [84]. APT of the dilute W-1.4Re irradiated by Abernethy et. al to 1.7dpa is presented, followed by studies of ternary W-Re-Os. The primary focus of the ternary alloy study is to compare the results from neutron irradiated HFR samples discussed in the previous section.

4.4.1 *Solute Clustering in Concentrated Alloy*

Clustering/precipitation in the ion implanted W-25Re was expected to be strong as the Re concentration is closer to the phase boundary in the equilibrium phase diagram (see figure 2.5a). APT was carried out using a laser energy of 150 pJ for this sample to increase ion yield.

Figure 4.5 shows a 10 nm slice of the reconstructed sample, with Re

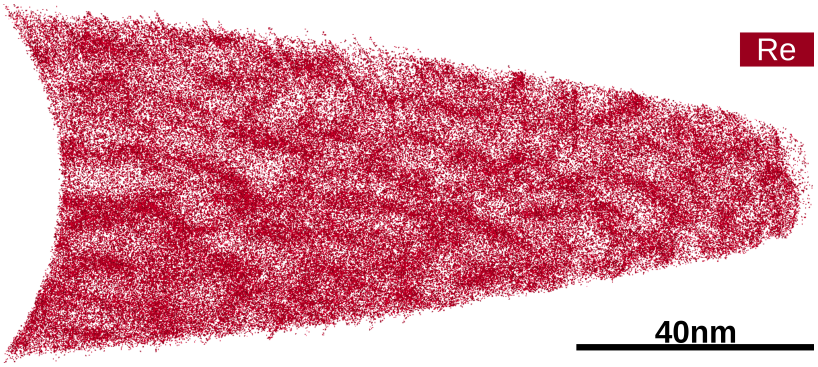


Figure 4.5: APT atom map of W-25Re ion implanted to 18 dpa at 773 K, showing 60% of Re atoms as red spheres of radius 0.1 nm.

atoms shown as red spheres of radius 0.1 nm. Only 60% of the Re atoms are shown for visual clarity and all of the W atoms are removed. Unlike the clusters formed in dilute Re and Os alloys at the same temperature, investigated by Xu et. al [84, 134], the concentrated alloy shows elongated rod shaped precipitates instead of spherical clusters, which are consistent with the morphology of σ phase precipitates observed under neutron irradiation [116]. To analyse the cluster composition, precipitates were defined using a 30at.%Re isoconcentration surface. One of these was chosen at random and a cylindrical ROI was placed along the long-direction of the precipitate. Figure 4.6 shows the line profile analysis along the precipitate. As with the neutron irradiated sample, there is a central concentration of 50at.%Re, consistent with the σ phase region of the binary W-Re phase diagram. No TEM analysis was performed on this sample which means the presence of σ phase cannot be confirmed.

4.4.2 *Solute Clustering in Dilute Binary and Ternary Alloys*

Figure 4.7 shows the APT analysis of needles taken from the 18 dpa, W-1Re-1Os sample previously irradiated by Xu et. al. The entire Bragg peak is captured within the APT sample and there is a clear decline in Os clustering correlated with the end of the dose profile. Visually there is no Re segregation to these clusters, unlike in previous studies [134], shown in figure 2.17 of the same material. This is highlighted by figure 4.8 which shows a higher magnification region of the sample shown in figure 4.7. The atom maps show clusters primarily comprised of Os, which could be a result of dif-

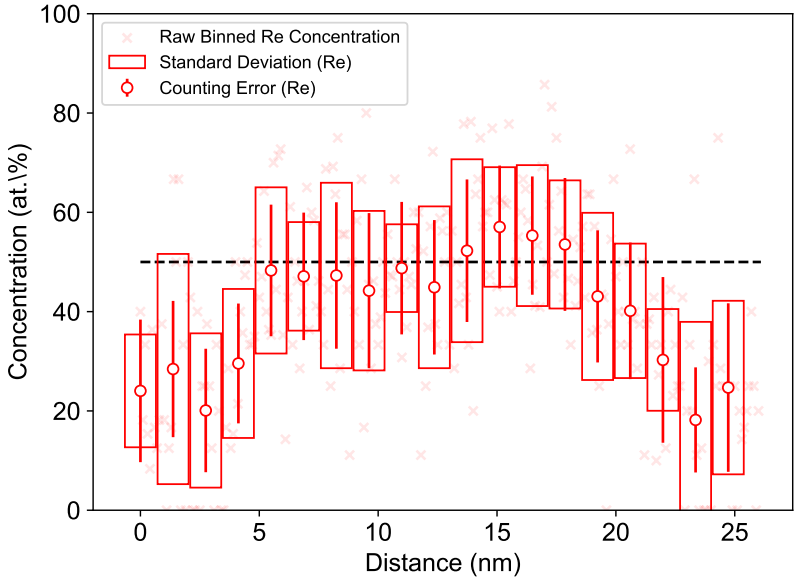


Figure 4.6: Re-binned line profile taken along the direction of a rod shaped precipitate in the 18 dpa ion irradiated W-25Re sample. Cylindrical ROI of diameter 1.85 nm, length 26 nm, initially split into 262 bins of width 0.1 nm. Rebinned into 20 concentration bins.

ferent ranging between studies or site specific variation in the bulk sample.

Analysis of the W-1.4Re-0.1Os sample (WT1), irradiated at SNL to 1.7dpa at 1173 K also showed that Os had clustered preferentially to Re. Figure 4.9 shows a comparison between the irradiated and unirradiated regions of the sample. There is no clustering in the unirradiated material, but clear Os clustering after irradiation. The clusters are primarily Os, with no visible segregation of Re in either the sample shown in figure 4.9, or the 5 nm slice shown in figure 4.8. The sample shown in figure 4.9 was taken at the approximate depth of the Bragg peak, however there is uncertainty in this position due to poor contrast during FIB milling. An APT sample starting at the sample surface, shown in figure 4.16(c), shows less strong clustering close to the surface.

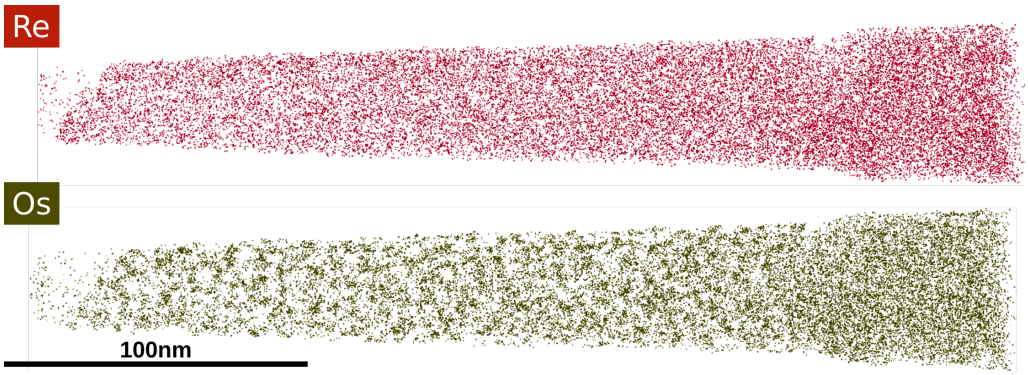


Figure 4.7: Re and Os atom maps, showing 100% of Os atoms, and ≈10% of Re atoms, rendered as spheres of radius 0.22 nm, taken from a sample ion implanted by Xu et. al [134] to a peak dose of 18 dpa, at 773 K at the Surrey Ion Beam Centre. The sample surface is located on the left of the image and the underlying unirradiated material is on the right side of image.

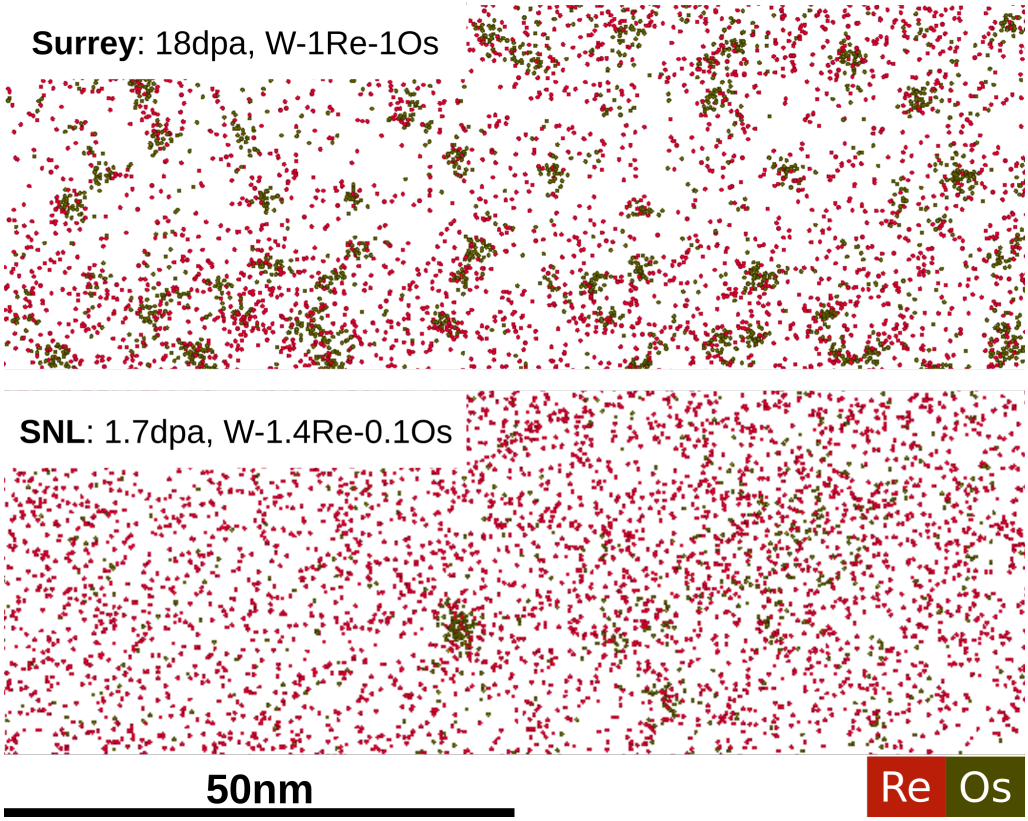


Figure 4.8: Re and Os atom maps, showing 100% of Os atoms, and 100% of Re atoms, rendered as spheres of radius 0.22 nm, taken from a 5 nm slice through the centre of samples ion implanted by Xu et. al [134] and as part of this study to different irradiation conditions to illustrate the position of Re atoms with respect to Os clusters.

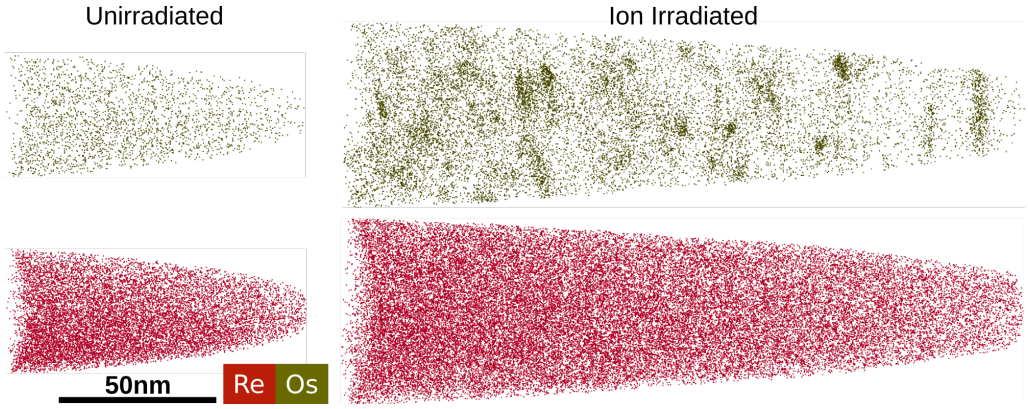


Figure 4.9: Re and Os atom maps, showing 100% of Os atoms, and 50% of Re atoms for 2 samples taken from the W-1.4Re-0.1Os sample irradiated at SNL, one from the unimplanted edge of the sample and one from the centre which received a peak dose of 1.7dpa.

Figure 4.16 shows the difference between ion irradiations at Saclay and SNL, as well as differences to the neutron irradiated samples discussed in chapter 3. The differences between the ion and neutron irradiated samples will be discussed in section 4.5.

Figure 4.16(a) shows the W-1.4Re sample, ion irradiated at Saclay to 1.7dpa at 1073 K. Figures 4.16(b), (c) and (d) show samples irradiated to 1.7dpa, at 1123 K in the SNL irradiation. Figure 4.16(b) shows the W-2Re sample, whereas (c) and (d) show the W-1.4Re-0.1Os sample. Figure 4.16(c) was taken just below the original sample surface whereas 4.16(d) was taken at the Bragg peak. The dose rates for each experiment are given in table 4.3 but are similar.

A similar diffuse Re cluster morphology is present in the Saclay and SNL samples shown in figure 4.16(a) and (b). Comparing figures 4.16(a) and (b) to 4.16(c) and (d) however shows that the addition of 0.1at.%Os has significantly changed the clustering behaviour. This confirms the hypothesis

that Os acts to suppress Re clustering, because of a stronger interaction between Os and point defects [134]. This is also supported by the modelling work of Messina [145] that shows Os clusters more strongly, and suppresses Re migration to defect sinks. Messina also show that Re mobility is reduced by the presence of Os in W, further supporting the observations in this study. These findings are unique in that they demonstrate even at very low nominal concentrations, Os is the dominant species controlling the structure of the clusters. This highlights that binary W-Re alloys cannot be used to understand reactor component degradation, and the introduction of small amounts of Os may be significant during the early stages of component service in a DEMO reactor.

4.4.3 *Grain Boundary Decoration*

Targeted grain boundary sample preparation in the ion implanted W-1.4Re sample irradiated at Saclay showed strong Re segregation. Figure 4.10 shows Re and W atom maps with a clear decoration of the GB with Re. The decoration of the GB was measured using an ROI taken across the GB and is plotted in figure 4.11. There is a maximum concentration of around 5at.%Re on the GB, with a depletion below the nominal concentration of around 1at.% either side. The effect of Os on the GB is unknown as samples taken from the SNL W-1.4Re-0.1Os material were unsuccessful. Unlike the neutron irradiated sample shown in figure 3.15, clear Re depleted zone is visible next to the decorated boundary.

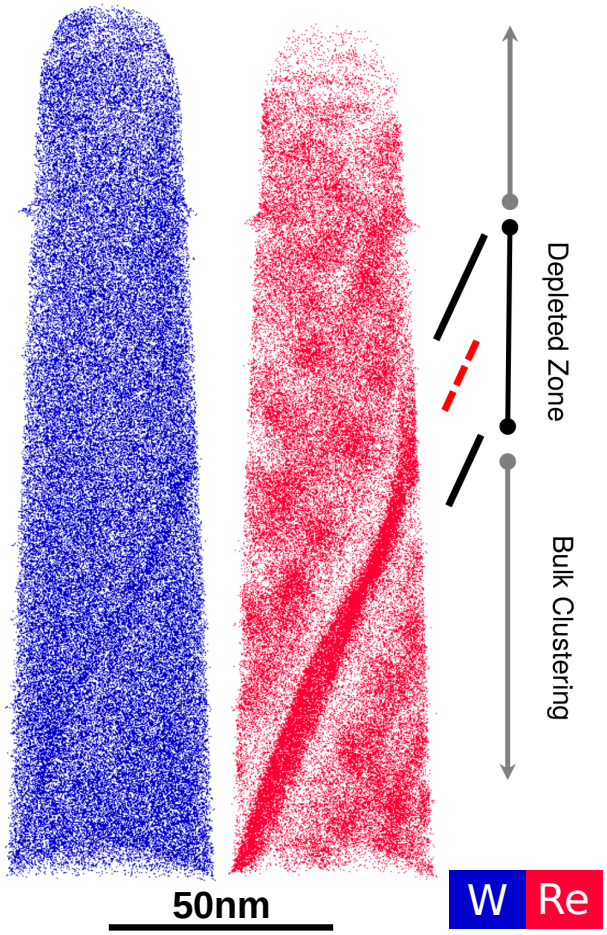


Figure 4.10: APT reconstruction of W-1.4Re sample ion irradiated to 1.67dpa at 1073K. Re atoms shown in Red, all other atoms hidden. Grain boundary visible decorated with Re surrounded by a region depleted in Re compared to the bulk. An increase in the W signal also highlights the GB and is a result of artefacts from the APT process.

4.4.4 *Thermal Stability of Re Clusters*

The thermal stability of the clusters observed under both ion and neutron irradiation is an important consideration for reactor designers. Annealing of the PFCs could reduce damage if Re precipitate growth can be minimised. Activation of the neutron irradiated material discussed in chapter 3 makes annealing studies difficult. Ion implantation therefore could provide insight into the behaviour of Re rich clusters under annealing, without the radiolo-

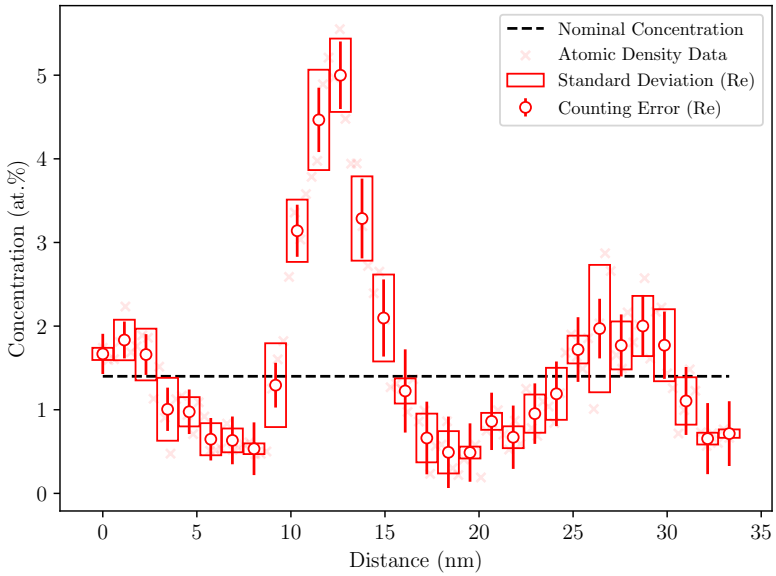
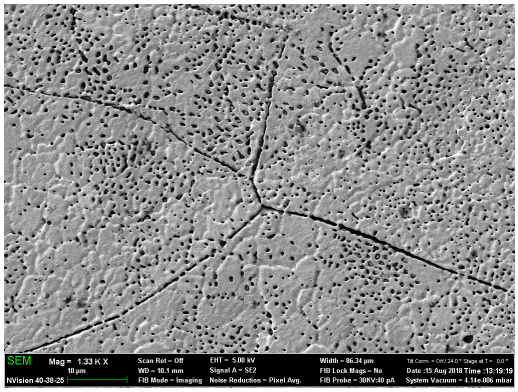


Figure 4.11: Re concentration across GB in Saclay ion implanted W-1.4Re sample.

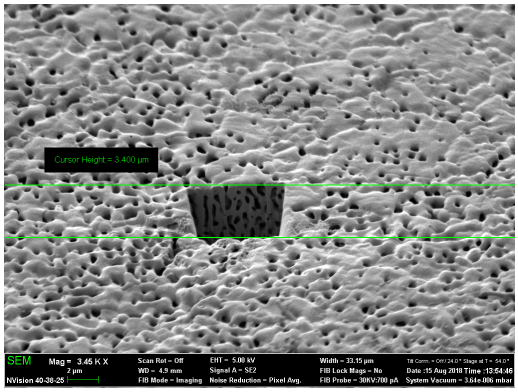
gical risks associated with activated material. Annealing of ion implanted samples however, requires adequate protection of the surface, due to the shallow implanted layer in W.

4.4.4.1 *Heat Treatment*

Heat treatment was applied to the W-1.4Re sample, ion irradiated to 1.7dpa at Saclay at 1073 K by Abernethy. All heat treatments were conducted between 700 and 1500 C for between 24 and 72 hours to ensure that sufficient time was given for diffusion. A sealed silica tube was used to protect the sample from oxidation in the vacuum furnace. Previous trials using 1) an Argon backfilled furnace chamber and 2) a higher vacuum furnace (without the use of a protective tube) showed visible oxidation on the sample surface. Heat treatment under Argon for 12 hours at 1400 K led to a spongy surface



(a) Low magnification SEM image of oxidised GBs.



(b) Higher magnification SEM image of FIB milled Trench.

Figure 4.12: SEM images showing the surface topography of ion implanted sample annealed for 12 hours under an Argon atmosphere.

topography, as shown in figure 4.12 despite the apparent lack of oxygen inside the chamber. The reason for this surface topography is unclear. The surface most likely oxidised due to residual oxygen in the chamber or Argon supply, and is the reason for the enhanced pitting at the GB in figure 4.12a. The cavities formed are likely a result of the sublimation of tungsten-oxide formed due to oxygen impurities in the furnace. Other attempts using a higher vacuum furnace also showed more oxidation than the initial tube method and at higher temperatures the oxidation was more pronounced. EDX analysis showed increased Re content at the surface, either due to the preferential loss of W through sublimation or because of point defect transport and solute drag to the free surface. Deposition of a Pt protective coating prior to heat treatment prevented oxidation but led to significant diffusion between the protective coating and the implanted layer, preventing further analysis.

The sample was placed inside the tube and evacuated to for approxim-

ately 12 hours until the reading on the pump hit its minimum reading of 10^{-6} mbar. The tube was sealed and heated in the furnace to 1273 K for 24 hours. A temperature of 1273 K was used as it was the maximum operating temperature of the silica tubes. The furnace was ramped down to room temperature and the sample was allowed to cool inside the tube to room temperature. The tube was broken to release the sample which was then cleaned and analysed.

The sample was still reflective and had not transitioned to a dull grey colour as was the case in previous attempts. Optical images showed that there was some etching at the GBs and that the microstructure consisted of many small grains, indicating that some degree of recovery had occurred without full recrystallisation. Overall the sample surface was smooth with little roughness induced by oxidation and subsequent W loss. The surface had many smaller scratches which were a result of pre annealing sample preparation and removal from the silica tube. APT was carried out according to the procedure described in section 4.3, without further sample polishing, using a lift-out from the centre of a larger grain approximately 25 µm in diameter.

4.4.4.2 *Re Cluster Dissolution*

APT analysis of this sample suggested that Re had dissolved back into solution, in agreement with the experimental findings of Hu et. al in sample after neutron irradiation [116]. Figure 4.13 shows samples taken from the sample before and after annealing. Re isoconcentration surfaces did not

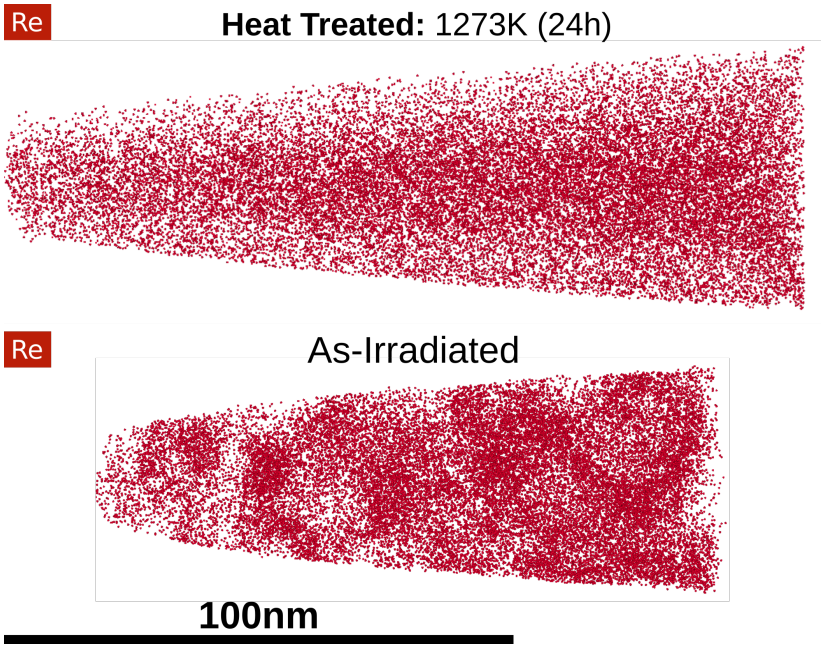


Figure 4.13: Comparison of ion irradiated W-1.4Re sample from Saclay (bottom) before and (top) after annealing at 1273 K for 24 hours.

reveal any regions of increased Re concentration. The dissolution of the clusters implies that continued defect transport to point defect sinks is required to produce clustering behaviour. There was no indication prior to annealing that the clusters in the as-irradiated material had reached the threshold for σ phase formation.

This is a positive result for the use of W in a reactor, but requires further study. It is unclear whether or not the dense Re and Os clusters formed under neutron irradiation would dissolve in a similar way. It is also unclear whether the smaller Os rich precipitates would also dissolve.

4.4.5 *Void Formation in Dilute Alloys*

STEM focal series images, taken between −2000 nm to 2000 nm under and over focus conditions, detected the presence of small voids, between 1-2 nm

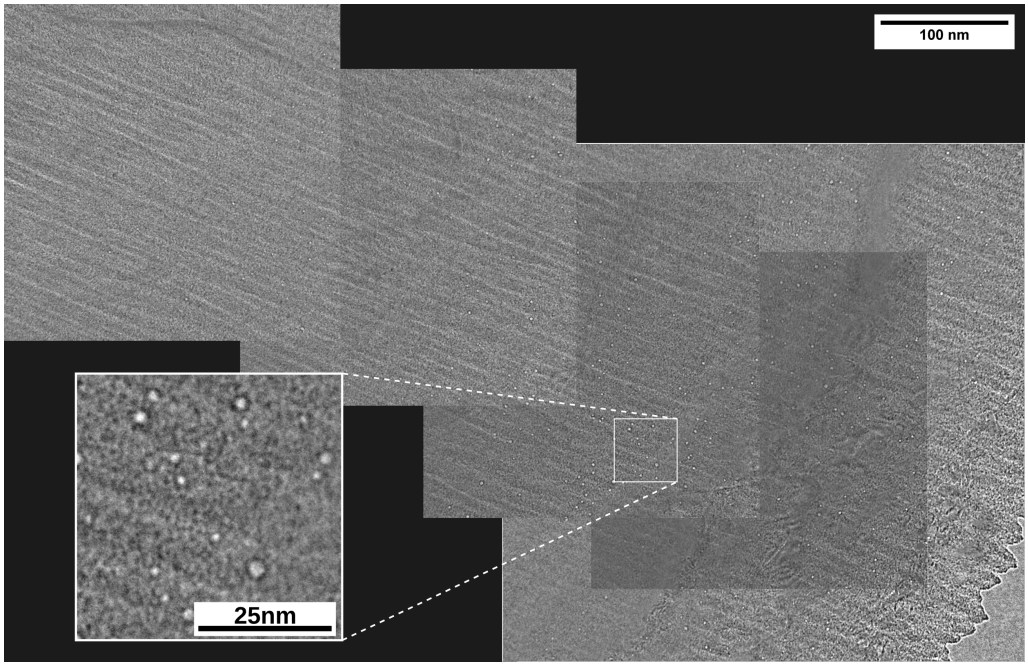


Figure 4.14: Stitched STEM image of voids in the ion implanted W-1.4Re-0.1Os sample from SNL. The bottom right of the image is located approximately 300nm from the original sample surface. The top left of the image is the underlying unirradiated material.

in diameter within the ion implanted range. A stitched image of voids which appear as bright contrast is shown in figure 4.14. Void formation in ion implanted alloys of W-Re has not been observed prior to this.

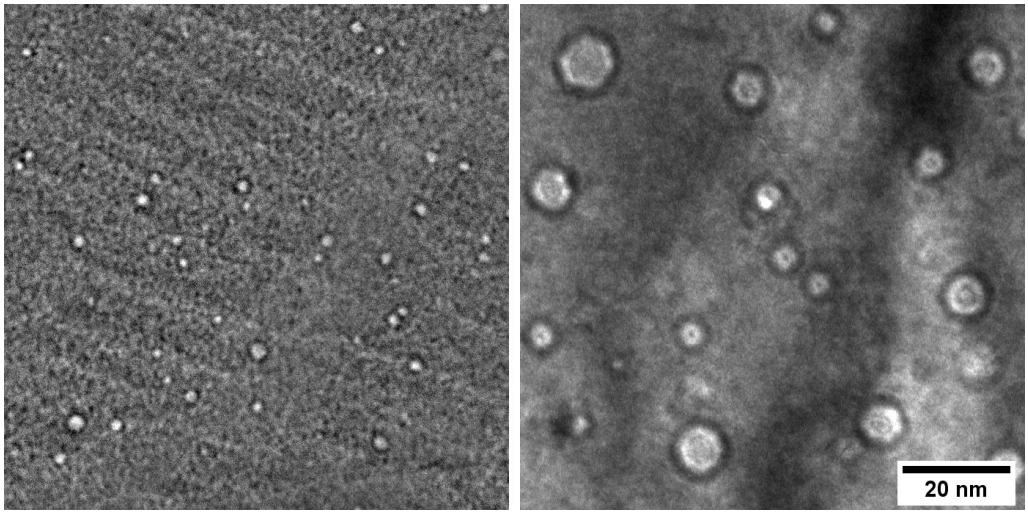


Figure 4.15: Comparison between voids observed under ion and neutron irradiation showing voids in (left) the ion implanted W-1.4Re-0.1Os sample and (right) the polycrystalline neutron irradiated material.

Small voids have been observed previously in ion irradiated W, however, suppression of void formation is expected in W-Re alloys [142]. The fast dose rate used for the ion irradiation may also have acted to suppress void growth, in comparison to the HFR samples from chapter 3. As shown in figure 4.15 the void size is smaller for the ion implanted material than for neutron irradiation.

There was no indication from the APT data that voids had contributed to atomic density artefacts in the ion implanted material, but the number density of voids shown in figure 4.14 would suggest that some voids were likely present in the data. This suggests that smaller voids may have a negligible effect on the reconstruction. More work is needed to ascertain whether the voids observed in figure 4.14 are decorated with Re and Os as in the neutron implanted samples discussed in chapter 3. It is possible, however, that small voids in the ion irradiated material acted as point defect sinks, around which enrichment of Os occurred. The presence of voids in the ion irradiated material is a positive indication that it might be possible to use ion irradiation to study a range of W-alloy compositions, if the effects of pre-alloying and different dose rates can be understood and accounted for. In the following section, the differences between the precipitate structure between neutron and ion irradiation are explored further.

4.5 Comparison to Neutron Irradiation

In this section, the ion and neutron irradiated samples (listed in table 4.4) with the same post-irradiation composition and same dose will be compared.

The composition of the clusters found in both will be analysed in further detail. Table 4.4 shows the primary differences between the samples are the different incident radiation, the difference in dose rate and the pre-irradiation composition.

Table 4.4: Samples used to compare between ion and neutron irradiations at equivalent temperatures. The Saclay sample was implanted at 1073 K. The uncertainty in the dose is a measure of the spread of values calculating with SRIM for different displacement threshold energies.

Sample	Pre-Irradiation Composition	Post-Irradiation Composition	Dose (dpa)	Dose Rate (dpa s^{-1})
Saclay	W-1.4Re	W-1.4Re	1.70 ± 0.5	1.4×10^{-4}
SNL	W-1.4Re-0.1Os	W-1.4Re-0.1Os	1.70 ± 0.5	1.6×10^{-3}
HFR	Pure-W	W-1.2Re-0.1Os	1.67	9.5×10^{-8}

4.5.1 *Mass Spectrum Analysis*

The differences in pre-irradiation composition are present in the mass spectrum of the ion and neutron irradiated samples. As discussed in section 3.3.2, differences in the isotopic distributions compared to the natural abundances arise as a result of transmutation under neutron irradiation. Figure 3.5 shows the differences between (a) the neutron irradiated single crystal W sample, and (c) the ion irradiated Saclay sample, both of which have approximately the same composition post-irradiation. In the ion irradiated material, the abundances follow the natural distribution of isotopes, but this is not the case for the neutron.

The problem of ranging approaches for the neutron irradiated sample is discussed in further detail in section 3.3.2. The natural abundances given

Table 4.5: Comparison between isotopic abundances in ion irradiated W-1.4Re-0.1Os from SNL and polycrystalline neutron irradiated sample from HFR (W-1.2Re-0.1Os) compared to the natural abundance of each element [18, 65]. Isotopic abundances are calculated as the number of ions ranged per isotope, as a percentage of the total number of atoms ranged as that element. Uncertainty on the concentration from APT is estimated by comparing different ranging approaches, background-to-background and at FWHM.

Nuclide	Natural Abundance (%)	APT (%)	
		SNL	HFR
^{180}W	0.12	0.12 ± 0.003	0.11 ± 0.002
^{182}W	26.50	27.13 ± 0.558	26.38 ± 0.379
^{183}W	14.31	14.13 ± 0.212	14.46 ± 0.363
^{184}W	30.64	31.96 ± 1.360	33.07 ± 1.569
^{186}W	28.43	26.66 ± 1.708	25.99 ± 1.586
^{185}Re	37.40	37.10 ± 0.234	9.33 ± 0.718
^{187}Re	62.20	62.90 ± 0.234	90.67 ± 0.718
^{184}Os	0.02	Undetectable	Undetectable
^{186}Os	1.59	Undetectable	Undetectable
^{187}Os	1.60	Undetectable	Undetectable
^{188}Os	13.29	15.27 ± 4.621	92.24 ± 0.862
^{189}Os	16.21	18.96 ± 0.214	5.48 ± 0.274
^{190}Os	26.36	25.07 ± 1.246	0.57 ± 0.137
^{192}Os	40.93	40.70 ± 3.161	1.71 ± 0.726

in table 2.2 shows that for alloys of W-(Re,Os,Ta) there are no mass peak overlaps that need to be deconvoluted.

The isotopic distribution produced by the chosen ranging approach is summarised in table 4.5, with the natural abundances of the different elements. For each isotope, the abundance was measured as the percentage of the total number of ranged ions for that element. For the SNL sample in which transmutation did not occur, the measured abundances are in agree-

ment with the expected natural abundances. A small amount of overlap between the ^{187}Os and ^{187}Re peaks is expected, but due to the low nominal concentration of these samples, the effect is negligible. For the HFR samples in which transmutation has occurred, the abundances of the W isotopes are largely consistent with the natural abundances, with some depletion of ^{186}W detectable. For the Re, 90% of the atoms are ^{187}Re, whereas in the ion implanted samples this is only 60%. For the Os, 92% of the atoms are ^{188}Os whereas in its natural state, only 13.3% of the atoms are this isotope. The other Os peaks, which are present in the SNL sample are very small for the HFR sample, as shown in figure 3.5. The measured bulk composition of the SNL sample is also consistent with the chemical analysis from the sample supplier, with a measured composition from APT of W-1.338Re-0.0966Os.

4.5.2 *Precipitate Structure*

Comparing the ion and neutron irradiated microstructure shows differences in the Re and Os precipitate structure. Figure 4.16 shows two APT samples taken from the SNL sample in (b) and (c) and a sample taken from the neutron irradiated single crystal sample in (d). In the neutron irradiated material, the clusters are comprised of both Re and Os, typically with a central core of Os and Re, surrounded by Re. In the ion irradiated material, the clusters are primarily Os despite the lower nominal concentration compared to Re. In the atom maps of the ion implanted material in figure 4.16 (b) and (c), there is no clear segregation of Re to these precipitates. Comparison between the SNL and Saclay sample shown in figure 4.16, dis-

cussed in section 4.4.2, shows that Os has suppressed Re cluster formation. Neither of the ion irradiated samples exhibit similar clustering to the neutron irradiated sample.

Initial analysis of the response of the Saclay and single crystal HFR to irradiation samples showed a similar level of hardening [109]. Despite this, comparison of the Re clusters in these samples shows that the clusters are very different. Figure 4.17 shows Re isoconcentration surfaces at 3, 5 and 10at.%Re for each sample. Despite the similar overall size, the Re in the neutron irradiated samples is more dense in the core of the precipitates. In the ion irradiated material there is a more diffuse interface. There is a higher concentration of Re in the centre of the clusters in the neutron irradiated material (>10at.%Re) whereas the maximum concentration for the ion is ≈5at.%Re.

The SNL and HFR samples, which have the same post-irradiation composition, have very different cluster structures. The HFR samples have a dense core of Os and Re surrounded by Re. In the ion implanted sample, the Os clusters are less well defined, with a fairly diffuse interface, and are visibly smaller than in the HFR sample. Density in the APT reconstruction may be increased in the neutron irradiated material due to the presence of voids. Voids were observed in the ion irradiated sample but were much smaller than those observed after neutron irradiation (1-2nm for the ion compared to 5-6nm for the HFR sample [91]). It is possible therefore that the central cluster atomic density in the ion implanted material is lower

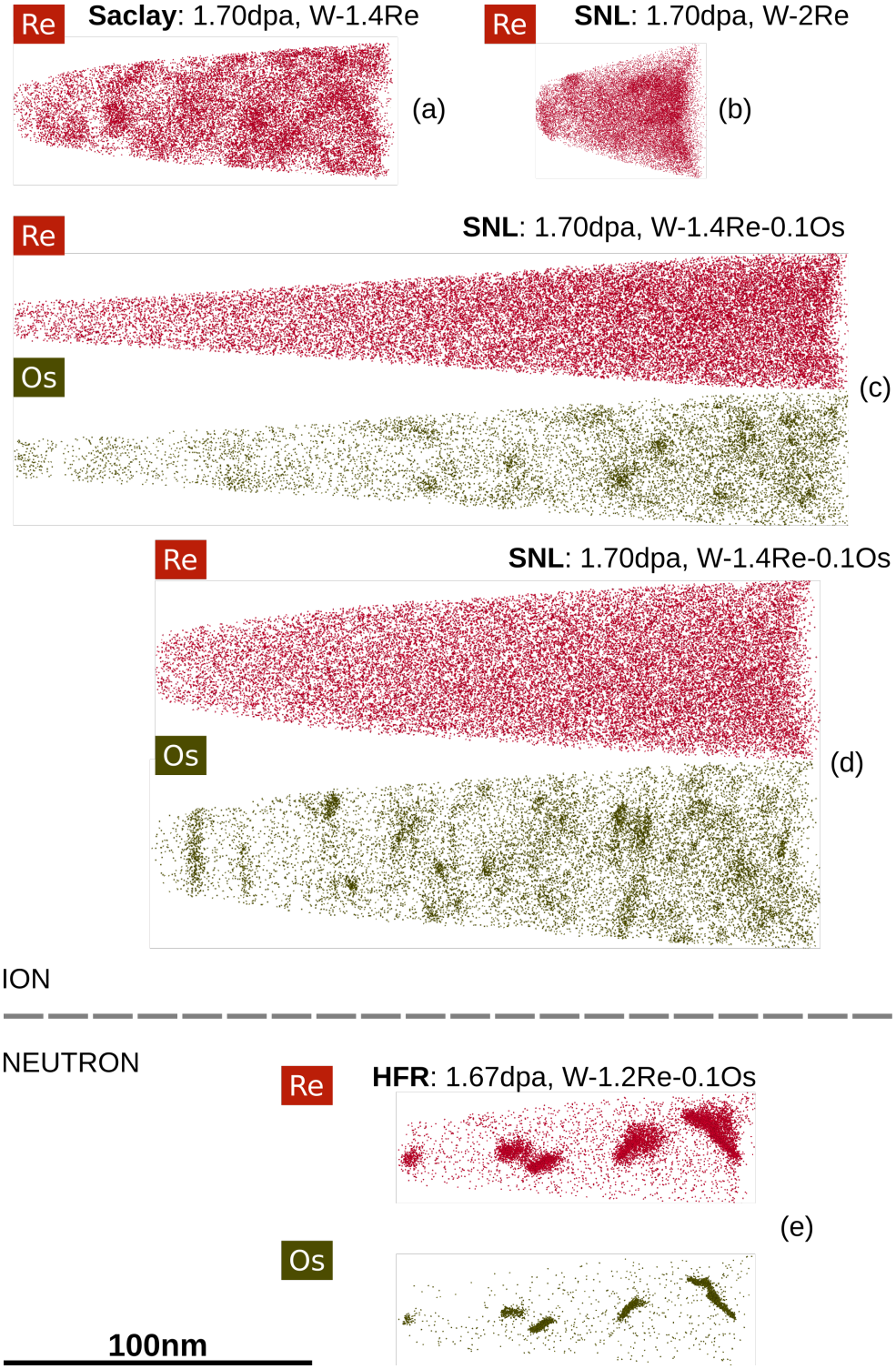


Figure 4.16: Re and Os atom maps from APT reconstructions of samples taken from (a) Saclay irradiated W-1.4Re (b) near surface region of SNL irradiated W-1.4Re-0.1Os (c)subsurface region of SNL irradiated W-1.4Re-0.1Os and (d) the single crystal neutron irradiated sample from HFR. The tip shown in (b) starts from just below the original sample surface below the protective layer, but (c) had more material removed. The exact amount of material removed is not accurate but is between 200 and 500 nm.

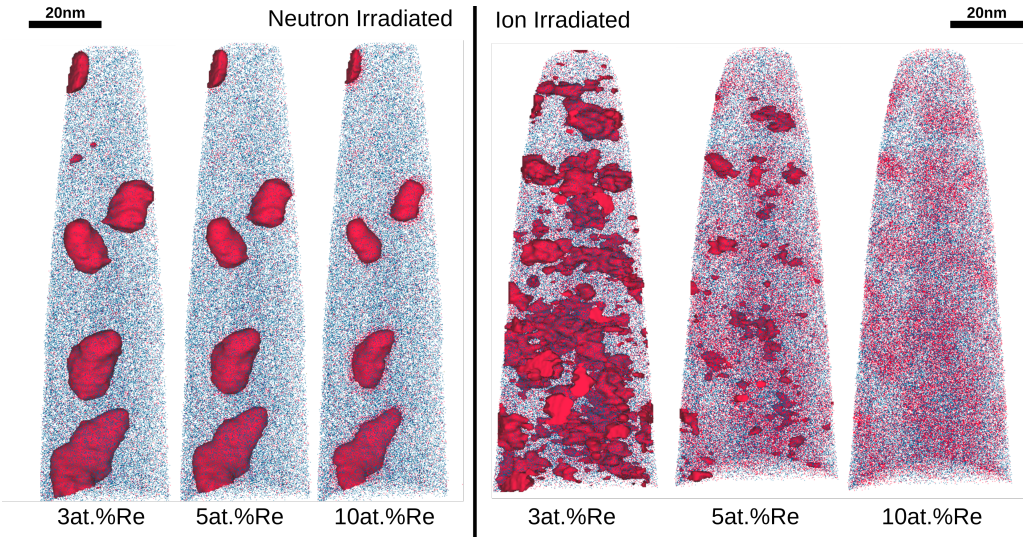


Figure 4.17: Re isoconcentration surface analysis for single crystal neutron irradiated sample and ion irradiated W-1.4Re Saclay sample.

because smaller voids which acted as nucleation sites did not introduce significant artefacts. Analysis of the number densities shows that not all of the precipitates in the HFR sample could be from voids. Some contribution to the density may come from the formation of a second phase, such as σ which was suggested by the line profiles in figure 3.14.

4.5.3 *Cluster Composition Comparison*

In order to compare the ion and neutron irradiated samples further, the compositions of the clusters were calculated. There are several methods for determining the composition of clusters within APT data, however, it is not clear which of these is most appropriate. The definition of the boundary between a cluster and the matrix can be subjective, especially when the interface between the cluster and matrix is diffuse. The most common approach to defining clusters is to use a cluster search algorithm (either using IVAS's built in tools or using posgen [197]).

Line profile analyses carried out in chapter 3 highlighted that in the precipitate cores, the Re and Os concentration was significantly higher than the average cluster compositions reported by maximum separation methods. The small clusters in the SNL sample shown in figure 4.16 make a line profile analysis impractical. Previous studies by Hwang et. al employed a cluster search method to study cluster compositions in neutron irradiated W from HFIR and Joyo. Their findings are interpreted with respect to the ternary W-Re-Os phase diagram [114]. Xu et. al also utilised this method for the study of ion implanted W-Re-Os [97, 134]. A cluster search method was therefore used to investigate the composition of the clusters detected in the material studied here.

The maximum separation method uses an algorithm to determine which atoms are within a cluster, based on a number of adjustable parameters. The maximum separation distance, d_{max}, was estimated using a nearest neighbour distribution of the Os atoms from IVAS. This gives a distribution of the average distance between solute atoms in the data set as a function of d_{max}. This was compared to the randomised data set and the d_{max} value was chosen at the point of maximum difference. The nearest neighbour distribution was then applied to the cluster subtracted data in order to check whether any residual clustering remains.

A minimum cluster size in atoms, N_{min}, was estimated by comparison to the randomised data set in IVAS using the cluster size comparison tools. Finally, values for the erosion parameter d_e and the envelope distance, L,

Table 4.6: Cluster search parameters used for various samples in this analysis. A range of values for the SNL sample were used to capture the impact of different approaches on the cluster composition. Where applicable the exact value of each parameter used is given in future analyses in this section.

Sample	d_{max} (nm)	N_{min}	L (nm)	d_e (nm)
HFR	1	20	0.7	0.25
SNL	1-2	13	0.5-1	0.25-0.5
Surrey	1.1	20	0.7	0.3

were defined. The envelope distance distance, L was set to $d_{max}/2$ and the erosion parameter d_e to $L/2$. The erosion parameter, d_e, defines a distance from the matrix atoms around the cluster. If ions within the cluster are within this erosion distance they are removed from the cluster. This optimisation was applied to each sample individually, and parameters were obtained accordingly. The parameters used are summarised for each sample in table 4.6

The parameters listed in table 4.6 were applied to multiple data sets from both HFR and SNL samples, using an approach outlined in section 4.5.1. For each cluster identified using this method, the ranged ions were exported and the Re and Os concentration of each cluster, i was taken as $x^i_X = N_X/N_T$, where N_X is the number of atoms of type X in the cluster, and N_T is the total number of ranged ions in the cluster. The W concentration in each cluster, i, was then calculated as $x^i_W = 1 - x^i_{Re} - x^i_{Os}$.

Figure 4.18 shows the composition of the clusters from the HFR and SNL samples shown in figure 4.16, as well as the clusters observed by Xu et. al in high dose (18 dpa) W-1Re-1Os [134], shown in figure 4.7. Average

Table 4.7: Average cluster compositions, $\bar{x}_i$, and size in number of atoms, N, and radius of gyration, $\bar{r}_g$, for ion and neutron irradiated samples. The variation in average cluster compositions is represented by the standard deviation, σ_i.

Sample	$\bar{x}_{\mathrm{Re}} \pm \sigma_{\mathrm{Re}}$	$\bar{x}_{\mathrm{Os}} \pm \sigma_{\mathrm{Os}}$	N	$\bar{r}_g$
SNL	2.32 ± 0.72	9.28 ± 1.52	473	1.6
Surrey	1.18 ± 0.51	5.12 ± 1.18	828	1.6
HFR (Single)	7.23 ± 4.42	0.36 ± 0.498	26979	4.3
HFR (Polycrystalline)	6.81 ± 3.38	0.64 ± 0.44	20605	3.9
Joyo (Pure-W)	7.6	0.2		
Joyo (W-10Re)	20.9	3.0		
HFIR (Pure-W)	13.4	2.6		
HFIR (W-10Re)	16.6	7.7		

cluster compositions in samples from Joyo and HFIR by Hwang et. al and Edmondson et. al are plotted as hollow markers [114, 202]. A portion of the ternary phase diagram at low solute concentrations is overlaid to show the predicted phase regions at equilibrium at 1873 K, as discussed in section 2.2.3. Each solid data point represents an individual cluster, and the colour represents the sample from which the APT needle was taken. The average compositions are summarised in table 4.7.

The blue data points from the neutron irradiated single crystal and polycrystalline samples in figure 3.12, are fully contained within the region in which solid solution is predicted. Some of the points are approaching the boundary at which a mixture of solid solution and σ phase is predicted. As discussed in section 3.4.3, the concentration is not constant across all of the clusters, and to take an average, as has been done here, reduces the overall concentration depending on where the interface is drawn. Figure 3.14

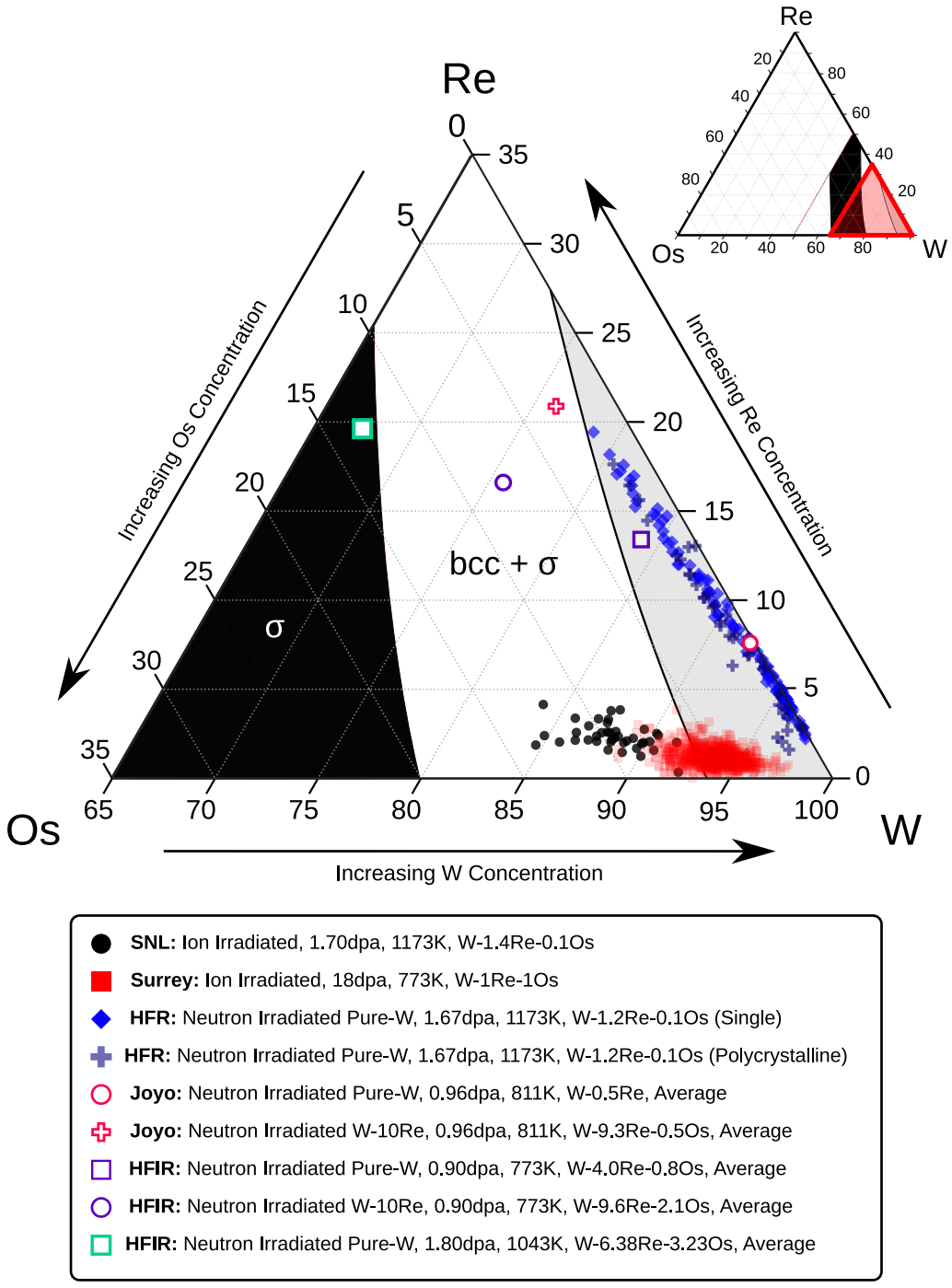


Figure 4.18: Comparison of cluster concentration determined using the maximum separation algorithm, in ion and neutron irradiated W and W-(Re/Os). Overlaid is a section of the W-Re-Os ternary equilibrium phase diagram at a 1873 K isotherm, between 0 and 30at.% solute. Shown in black is the region of solute concentration within which σ phase is predicted to form. Hollow markers represent the average cluster compositions obtained by Hwang et. al and Edmondson et. al [114, 202] using APT, from neutron irradiated samples from HFIR and Joyo.

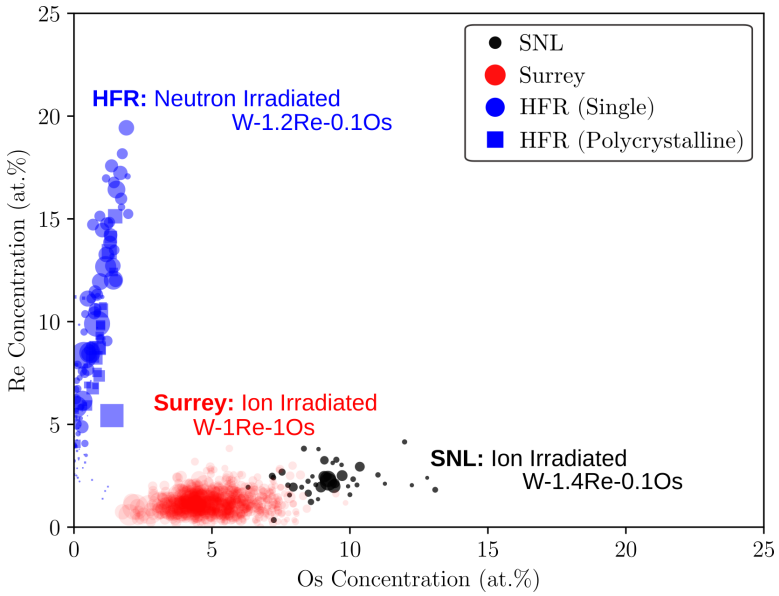


Figure 4.19: Re to Os ratio for clusters in ion and neutron irradiated W. The red points represent the W-1Re-1Os samples ion irradiated to 18 dpa by Xu et. al [134]. The black points represent clusters in the SNL ion irradiated W-1.4Re-0.1Os sample, irradiated to 1.70dpa. The blue points represent clusters in the neutron irradiated single and polycrystalline samples which have a post-irradiation composition of W-1.2Re-0.1Os, and a damage level of 1.67dpa.

shows that in the centres of the clusters formed under neutron irradiation, the concentration is consistent with σ phase. There is a large spread in the HFR data, with an average cluster concentrations of 7.23Re, 0.36Os and 6.81Re, 0.64Os for the single and polycrystalline samples respectively. On average the cluster compositions measured here are similar to the Joyo irradiation.

Comparing the neutron irradiated samples, it is clear that the clusters formed are very different in terms of composition. The ratio of Re to Os in the clusters is shown in figure 4.19. In the neutron irradiated samples, there is a much greater number of Re atoms per Os atom. As shown in the atom maps in figure 4.16, the clusters in the SNL sample are primarily comprised

of Os atoms. The cluster analysis shown in figures 4.18 and 4.19 show that Re is weakly associated with the clusters in the ion implanted samples in both the SNL sample and Surrey implanted sample studies by Xu et. al. As shown in table 4.7, the average Os content in the ion irradiated samples is higher than in any of the neutron irradiated samples, but the average cluster size is much smaller. There is also less spread in the data, relative to the mean value than in the neutron irradiated samples, shown also in the range of cluster values plotted in figure 4.18.

The linear trend between Re and Os in the neutron irradiated samples could be a result of transmutation effects producing Os in the cores of pre-existing Re clusters. However, there is no trend between increasing cluster size and Os concentration which implies that the Os transport to these regions may be dominant. Comparison between the two ion implanted samples plotted in figure 4.18, is difficult because of the large difference in dose rate (18 dpa, compared to 1.7dpa) as well as a different temperature and pre-alloy composition. Figure 4.18 shows however, that despite the higher dose and higher pre-alloy Os content in the Surrey sample; the clusters formed in the SNL sample are smaller but more highly concentrated in Os. This is despite the lower nominal concentration of Os (0.1at.%), further reinforcing the importance of considering low Os containing alloys to understand the early stages of transmutation in a DEMO reactor.

Differences between the cluster size and compositions in the ion and neutron irradiated W-1.4Re-0.1Os and W-1.2Re-0.1Os, suggest that either

the different dose rate, the effect of pre-alloying with Os and Re or ballistic mixing under ion irradiation have had an impact. Smaller clusters formed under ion irradiation because the faster dose rate suppresses the diffusion of point defects. Pre-alloying with Re is known to prevent void formation under neutron irradiation by increasing defect recombination. Increased recombination in the ion irradiated pre-alloyed sample, combined with the faster dose rate, limited void formation, as shown in figure 4.14, and might have reduced the number of defect sinks for cluster formation. While in the neutron irradiated material the clusters may have reached the threshold for σ phase in the centre, there is no indication that this has occurred under ion irradiation. The concentration of Os in the centres of the clusters in the SNL sample is consistent with the bcc+σ region of the ternary phase diagram. It is possible that with a slower dose rate, and more time for diffusion to occur, a similar core structure as seen in the HFR samples could be formed, by the transport of Re to the pre-existing Os clusters. Both Re and Os have an attractive binding to point defects, and diffuse to point defect sinks due to solute drag. There is a competing effect due to the differences in binding energy between Os and Re. Os has the strongest binding and therefore forms clusters first. As the bulk concentration of Os is reduced, transport of Re may begin to be favoured, and the core shell structure seen in the HFR samples may form.

There is also the balance between diffusive transport and ballistic mixing to consider. The low flux rate of the neutron irradiation experiments

promotes the diffusion of Re and Os atoms to defect sinks and clusters. In the ion irradiation, however, where the flux rate is several orders of magnitude higher, the role of ballistic mixing becomes more substantial. Some ballistic effects occur under neutron irradiation, either in cascades caused by neutron impacts, or due to the recoil of atoms which have undergone decay. In the high flux rate ion irradiation experiments, ballistic mixing acts to dissolve fine scale features and to promote erosion of the clusters in cascade events. This could explain the diffuse Os cluster boundaries that are seen in figure 4.16. However, compared to the SNL samples, the Surrey samples studied by Xu et. al. have a higher dose, similar dose rate and lower irradiation temperature, which should further promote ballistic effects over diffusive transport, but strong Re and Os clustering is observed. This further highlights the challenge to using ions as a surrogate for neutron damage, and shows that more work is needed.

To investigate this hypothesis experimentally, low dose rate ion irradiation studies are needed. The effect of pre-alloying on this process is still unknown and would be difficult to study experimentally. Computational modelling can provide access to these phenomena and may provide insight into these processes. Current kinetic modelling efforts have focussed primarily on W-Re, but as shown in figure 4.16, even low nominal concentrations of Os can disrupt the usual behaviour of W-Re. New computational models of the W-Re-Os system, complemented by these experimental findings, are needed to understand the effects of dose rate and pre-alloying. In the second

part of this thesis, a new energy model developed for the W-Re-Os system is outlined, as well as the expansion of a KMC model to study these effects.

Summary of Experiments

Neutron irradiation of pure-W at 1173 K led to the formation of Re and Os rich precipitates, formed by transmutation. Voids decorated with Re and Os formed as well as smaller isolated Re and Os rich precipitates. Cluster analysis performed using the maximum separation algorithm showed that clusters had Re and Os concentrations within the bcc solid solution phase regions. Line profile analysis suggests that in the centres of some of the precipitates, the concentration could be as high as 50at.%Re, which is consistent with σ phase. The clusters in which this occurred had a rod shaped morphology. Diffraction pattern analysis with TEM is needed to confirm this hypothesis. None of the samples studied had clusters with a composition consistent with the anomalous χ phase observed in previous studies. Adjacent to the GB which was decorated with Re and Os, a void denuded zone formed followed by a zone of larger than average voids.

Ion irradiation at the same dose and temperature supported the findings from the neutron irradiated material. Pre-alloying with Re and a combination of Re and Os confirmed the results from point defect transport modelling that Os clusters preferentially to Re, due to its stronger association with point defects, and also reduces the mobility of Re. The effect of Os was significant, with a nominal concentration as low as 0.1at.%Os leading to the formation of primarily Os clusters, in agreement with the previous

experimental findings of Xu et. al [134]. This was also found in the neutron irradiated samples, in which strong enrichment of Os was seen in the clusters. It is possible that Os segregated first, followed by Re when the bulk concentration of Os decreased sufficiently. In the ion irradiated material, Re segregation was not observed but may occur at longer time scales than studied here.

Comparing the ion and neutron irradiated material, the ion irradiation led to smaller clusters which contained a higher concentration of Os, and a weakly enriched Re content. Smaller voids were formed under ion irradiation but were detected for the first time in ion irradiated alloys of W-(Re,Os). In the neutron irradiation, a central core of Re and Os, surrounded by Re was observed. Differences between the two are likely a result of differences in the dose rate, the effects of pre-alloying with Re and Os, and the action of ballistic mixing to promote cluster dissolution under ion irradiation. The differences are most likely caused by a combination of these effects. The formation of voids under ion irradiation is a positive result for its viability as a surrogate for neutron damage as it demonstrates that it may be feasible to use produce similar microstructural features if irradiation parameters can be adjusted to account for differences in the damage produced.

Part II: Computational Investigation

5 Introduction to Modelling

▶ Synopsis: In this chapter, an overview of multiscale materials modelling and its application to the study of radiation damage and transmutation is provided. An overview of the various algorithms used in the Monte Carlo simulations discussed in the following chapters is given.

5.1 Outstanding Questions and Modelling

The aim of the computational study presented in part II of this thesis is to address some of the outstanding questions raised by the experimental findings of chapters 3 and 4. A key result of these chapters was the strong influence of Os on the clustering behaviour. The analysis presented in section 4.5 showed that the presence of Os in the alloys acted to suppress Re segregation to the clusters, in agreement with the findings of Xu et. al in W-1Re-1Os. The key finding of section 4.5 is that this effect was observed even at nominal concentrations as low as 0.1at.%Os. APT ultimately only can provide analysis of the material following irradiation. But computational modelling can provide insight into the active processes and help to address the outstanding questions.

This chapter will outline the algorithms used by the MC methods that are applied in this study. The effect of Os on the microstructure means that binary energy models of W-Re alone are insufficient to understand damage evolution in a DEMO reactor. Because of this, a new energy model

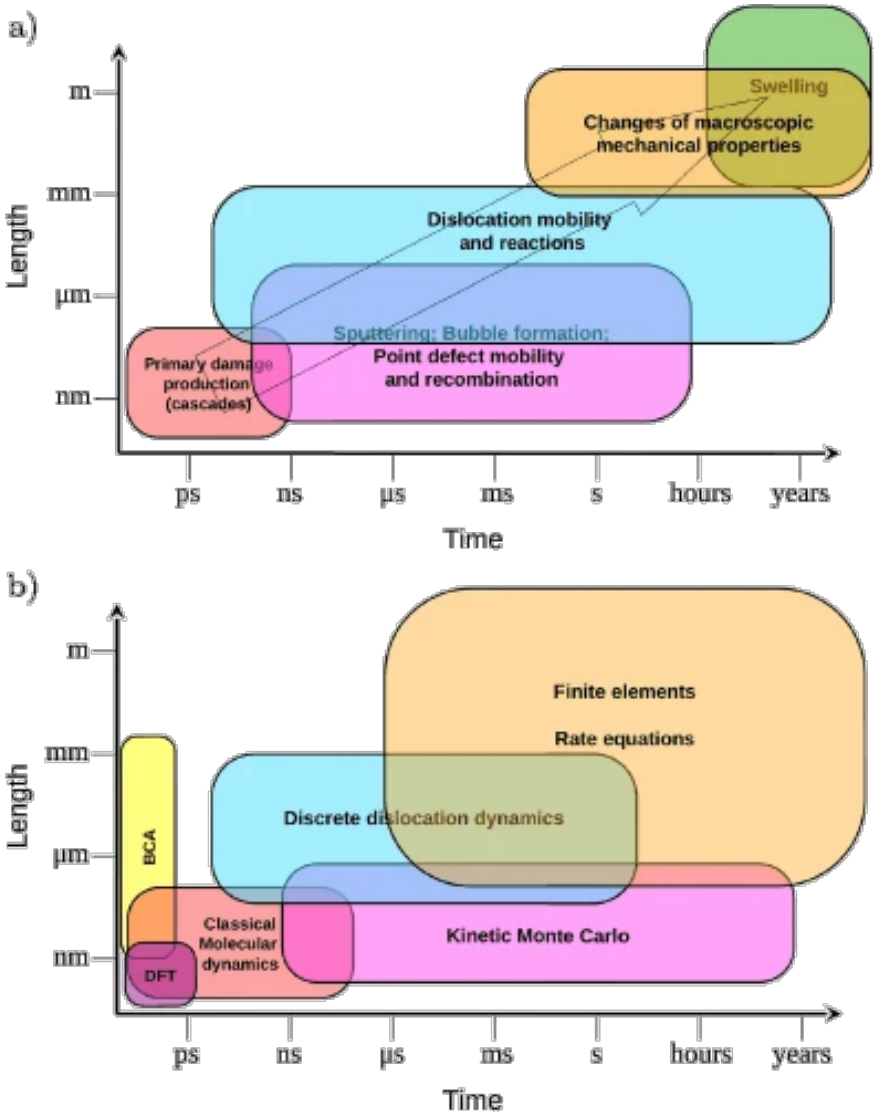


Figure 5.1: Schematic diagram showing time and length scales associated with (a) radiation induced phenomena and (b) multiscale materials modelling techniques, adapted from [203].

for the W-Re-Os system, including both vacancies and interstitial defects was developed, and is discussed in chapter 6. Finally, the results of the simulations carried out in this study are presented in chapter 7.

Computational models are extremely valuable tools for understanding radiation induced clustering but must be validated against experiments. Radiation damage and transmutation are inherently difficult to model com-

putationally because of the wide range of time and length scales involved, as shown in figure 5.1. A displacement cascade occurs when an atom is displaced from its original lattice site, and produces a cascade of subsequent displacements which occurs over pico-second time scales. But the surviving point defects from a cascade cause macro scale changes to material properties over years of time in service. Different simulation methods are inherently required to capture these effects [203].

Electronic structure calculation methods such as DFT, are used to study the ground state behaviour of a system of atoms or molecules. The interactions between different atoms can be investigated by solving the quantum mechanical wave function equations, using a series of approximations. Because of the complexity of these calculations, computational cells in DFT are usually limited, typically with a hundred or so atoms. This typically prevents realistic defect concentrations from being simulated and is not large enough for cascade events to be simulated directly, but DFT calculations provide reliable inputs for other modelling methods such as Molecular dynamics (MD), KMC and Finite Element Analysis (FEA).

MD techniques treat atoms as spheres which interact according to an interatomic potential. This simplification allows cascade events to be analysed directly and for longer time scales to be studied, but is still limited to very small fractions of a second. To extend simulations to greater time scales, atomistic MC methods which further simplify the interatomic interaction are often used. Atomistic KMC methods (AKMC) can extend the

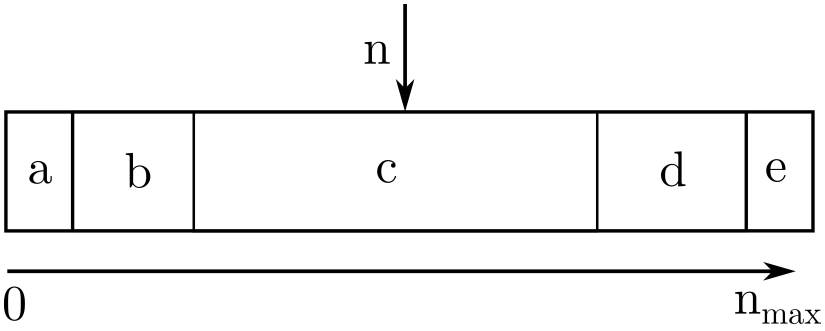


Figure 5.2: Event selection in KMC, adapted from [147, 148].

simulated time to years, allowing larger scale phenomena such as precipitation and void formation to be studied, provided that the rates of individual processes are known. These models can use a rigid lattice of atoms or more complex models employ an off-lattice approach where atomic positions are flexible. AKMC is clearly a very powerful simulation tool, but is dependent on a complete understanding of the possible processes and an accurate quantification of these rates.

5.2 Atomistic Monte Carlo

Atomistic MC models use an algorithm based on the generation of a distribution of random numbers. For on-lattice applications, a fixed lattice of points is created based on the crystal structure of the material. Each point of the lattice is given a state, i, which represents the atomic species occupying that point. For each site in the lattice a full list of the possible processes is required to describe how the state can change. The probability or rate for the change from state, i, to state, j, for example, depends on the change in energy between these states, ΔE_{ij}.

An event is selected from the list of possible processes, based on the

probability of that event occurring, and executed accordingly. A pseudo-random number, n, between 0 and n_{max} is generated and used to select an event from the list, as is shown schematically in figure 5.2. Each event between a and e is assigned a portion of the range between 0 and n_{max} depending on its relative probability of occurrence. Event c is the most likely to occur and so covers the largest range [147, 148].

Rejection KMC simulations either accept an event if a threshold probability is reached or reject it if the rate falls below that threshold. In a Rejection-free KMC simulation (rfKMC), an event is carried out during every sampling of the distribution. The model presented in this study uses a rejection free implementation.

The MC method used determines the processes which can be used to build up the list of possible processes for each site. For example, in Metropolis MC simulations, atom-defect exchanges are considered which allows the system to evolve to an equilibrium state. In simulations with canonical and semi-grand canonical ensembles, atoms can be exchanged with neighbouring atoms, and a reservoir of solute atoms respectively.

In KMC simulations, atom–defect exchanges are considered, but a rate λ_{ij}, rather than a probability for each event is considered by multiplying the probability by an attempt frequency, ν, which depends on the defect type. By considering the rate of an event, the time associated with different phenomena can be investigated. The time, δt, associated with each event in a rfKMC algorithm is calculated using the Residence Time Algorithm

(RTA) which was derived by Young and Elcock in 1966 [149], and is given by equation 5.1 where u is a random number between 0 and 1, and Γ_i is the frequency associated with event i [149, 204]. The total time in the simulation is given by the sum of the time associated with successive accepted events.

$$\delta t = \frac{-ln(u)}{\sum_i \Gamma_i} \tag{5.1}$$

Regardless of the algorithm used to evolve the system, the change in the energy for each rate or probability must first be calculated. A simple method for computing this energy is by using a pair-interaction model, which considers the interaction strength between individual pairs of atoms, or pairs of atoms and defects. In section 5.3, the basis of the pair interaction energy model is outlined.

5.3 Pair Interaction Energy Model

To construct the change in energy, ΔE_{ij}, between states, a pair interaction model uses the sum of individual interaction energies between pairs of atoms, ε. This interaction depends on the atom or defect types occupying the two sites i and j, and the interatomic distance. The Hamiltonian, $\mathscr{H}$, for the pair interaction model can therefore be expressed as equation 6.1, where (i) is the index of the neighbour shell, α and β are the atom types of the two sites being considered and n is the number of bonds between α and β.

$$\mathscr{H} = \sum_{i} \sum_{\alpha,\beta} n^{(i)}_{\alpha-\beta} \varepsilon^{(i)}_{\alpha-\beta} \tag{5.2}$$

Simulating material systems with this method therefore depends on an accurate description of the pair interaction energies, which have to be determined for each possible pair of atoms and defects. Soisson et. al applied a pair interaction model to study the kinetics of copper precipitation in steels. In this study, the pair interactions were obtained using experimentally derived values for the cohesive energies for Fe and Cu. The cohesive energy, E_A, of material, A, is the energy required to break all of the bonds associated with one of the atoms. Soisson et. al estimate the value of the Fe-Cu interaction by considering the mixing energy, ω, and the solubility limit of Cu [205]. More recent models have been developed which use DFT calculations to determine the pair interaction energies. Levesque et. al published a pair interaction model for the Fe-Cr system in 2011, which included concentration dependant Fe-Cr interactions. These interactions were obtained by fitting the enthalpy of mixing for Fe-Cr, a method which was also applied by Huang et. al for the W-Re system [154, 206].

In this study we apply the Huang parameterisation for the W-Re system, as well as developing a new energy model for the W-Re-Os system in chapter 6. This new energy parameterisation accounts for vacancy interactions by considering the local vacancy concentration. The energy model published by Huang et. al is summarised in appendix A, and will be referred to as the Huang energy model from this point onwards. For further information the

reader is directed to the following published works using this energy model [154, 158, 159].

5.4 SPPARKS Implementation

In this section, an overview of the model is given and the implementation of the various MC methods used in this study are summarised. The code is based on a custom variant of the Stochastic Parallel PARticle Kinetic Simulator (SPPARKS) software, originally developed by SNL [152, 207]. In general, the model considers the transition from a less stable to a more stable state, lowering the overall free energy of the system.

Defects are introduced into the simulation cell and move into lower energy configurations. During irradiation there is also a driving force to increase the free energy of the system, and this is not accounted for in this model. As discussed in section 4.5, high flux irradiation leads to ballistic mixing effects which oppose the diffusion of point defects and transmutation products to lower energy configurations. Experimentally this leads to the erosion of precipitates, as well as the diffusion of solute atoms to these features.

In this study, self-interstitial and mixed, W-Re interstitial migration and creation was included, in addition to the existing vacancy interactions. Interactions and local concentrations are considered at first and second nearest neighbour positions of the two sites which are being exchanged.

5.4.1 *Metropolis Monte Carlo*

Equilibrium simulations such as Metropolis MC algorithm (MMC) can be run with a fixed defect concentration. In the MMC model used here, defects can exchange with a neighbouring atom in the first nearest neighbour positions. The event probability, $\prod_{i\to j}$, is calculated according to equation 5.3.

$$\prod_{i\to j} = \min\left\{1,\ \exp\left(-\frac{\Delta\mathscr{H}_{i\to j}}{k_{\mathrm{B}}T}\right)\right\} \tag{5.3}$$

where $\Delta\mathscr{H}_{i\to j}$ is the change in energy between initial and final states i and j, given by equation 5.4, where the initial state of the sites are α and δ with neighbours β and γ respectively.

$$\Delta\mathscr{H}_{i\to j} = \left(\sum_{\delta}\varepsilon^{(n)}_{\delta-\beta} + \sum_{\gamma\neq\alpha}\varepsilon^{(n)}_{\alpha-\gamma}\right) - \left(\sum_{\beta}\varepsilon^{(n)}_{\alpha-\beta} + \sum_{\gamma\neq\alpha}\varepsilon^{(n)}_{\delta-\gamma}\right) + \Delta E^{x}_{i\to j} \tag{5.4}$$

The second term is therefore the sum over the pair interactions for the atom and defect in their initial positions, whilst the first term is the equivalent sum with the atom and defect in their exchanged positions. The final term is the change in energy due to non-broken bonds, and is a result of the movement of an atom affecting the local concentration terms in some of the nearby atoms. This algorithm can be applied to both vacancy and interstitial defects, and can be run in conjunction with SGMC events, as will be discussed in section 5.4.2.

5.4.2 *Semi-Grand Canonical Algorithm*

In the semi-grand canonical ensemble, the average behaviour of the atoms is considered as a function of external conditions, with a fixed temperature T, number of particles N_T, volume, V and chemical potential, μ given by equation 5.5[1]. In the equivalent grand-canonical ensemble the number of particles would not be fixed [154].

$$\mu_X = \left(\frac{\partial G}{\partial N_X}\right)_{T,p} \tag{5.5}$$

In the SGMC model, atoms are selected at random from the simulation cell and exchanged with a reservoir in which the particles do not interact. The probability, $\prod_{i\to j}$, for this exchange is calculated using equation 5.6, where $\Delta E_{i\to j}$ is the change in energy before and after the swap, ΔN_{B} is the change in the number of solute atoms of type B, and $\Delta\mu$ is the change in chemical potential given by $\Delta\mu = \mu_A - \mu_B$ for elements A and B, and T is the temperature [154, 208, 209].

$$\prod_{i\to j} = \min\left\{1,\ \exp\left(\frac{-\Delta E_{i\to j} - \Delta\mu\Delta N_{\mathrm{B}}}{k_{\mathrm{B}}T}\right)\right\} \tag{5.6}$$

For calculations using this method, the change in the chemical potential $\Delta\mu$ and the temperature T are used as input parameters. The simulation cell is initiated and after a threshold number of events are executed (which

[1] where ∂G is the change in Gibbs free energy, T is the temperature, p is pressure and N is the number of atoms. Obtained from the derivative of the function $dG = -SdT + Vdp + \sum_{i=1}^{k}\mu_i dn_i$ at constant temperature and pressure.

in this case is set to 100 events per atom in the simulation cell), $\Delta\mu$ is incremented. At the end of the defined $\Delta\mu$ range, T is incremented and $\Delta\mu$ is reset to its original value but the configuration of the simulation cell remains unchanged. At each increment, the solute concentration, X_B, is obtained after the threshold number of events is exceeded.

Simulation cells can also be initiated with a fixed number of defects. Defect migration events can be executed alongside atomic exchanges, with a probability given by equation 5.3, where the change in energy, $\Delta\mathscr{H}_{ij}$, is given by equation 5.4. By evolving the system with a fixed concentration of defects the equilibrium configurations can be obtained.

5.4.3 *Canonical Algorithm*

In the canonical ensemble, the number of atoms, N, the temperature, T and the volume, V are kept constant. MC simulations within this ensemble allow for systems with fixed defect and solute concentrations to be studied, whereas in SGMC simulations the solute concentration varies via reservoir exchange. Exchange events are allowed between an atom and its neighbours in the 1NN shell. These events are accepted with a probability given by equation 5.7, where $\Delta\mathscr{H}_{i\to j}$ is the change in energy between the initial and final states in an exchange.

$$\prod_{i\to j} = \min\left\{1,\ \exp\left(-\frac{\Delta\mathscr{H}_{i\to j}}{k_{\mathrm{B}}T}\right)\right\} \tag{5.7}$$

5.4.4 *Kinetic Monte Carlo*

Events in KMC simulations involve the exchange of defects with neighbouring atoms. The full list of possible events in the KMC model are summarised in table 5.1. The probability, p_{ij} is converted to a event rate, λ_{ij}, using the attempt frequency ν which depends on the type of defect and the material[2], according to harmonic transition state theory (TST), as shown in equation 5.8, where ΔE_{ij} is the activation energy for the event.

$$\lambda_{ij} = \nu \exp\left(-\frac{\Delta E_{ij}}{k_B T}\right) \tag{5.8}$$

Events in the code are calculated from the perspective of the migrating atom - exchange events are calculated if the atom under consideration is neighbouring a defect. The rate calculation depends whether the defect is a vacancy or an interstitial, the calculation of which is discussed in sections 5.4.5 and 5.4.6 respectively.

5.4.5 *Vacancy Migration*

Vacancies migrate via first nearest neighbour exchanges. The energy,$\Delta E^V_{i\to j}$, between the initial configuration and at the saddle point between the initial and final states is calculated using equation 5.9. The first term on the RHS of equation 5.9 is the sum of the pairwise interactions at the saddle point, α, over the neighbours of the atom at the saddle point, θ, where s is the

[2]In this study, the following defect attempt frequencies were used for W: $\nu_V = 6.5 \times 10^{12}$Hz for vacancies and $\nu_I = 1.5 \times 10^{12}$Hz for interstitials [154]

index of the neighbour shell.

$$\Delta E^{V}_{i\to j} = \sum_{\theta} \varepsilon^{(s)}_{\alpha-\theta} - \left(\sum_{\beta} \varepsilon^{(n)}_{\alpha-\beta} + \sum_{\gamma\neq\alpha} \varepsilon^{(n)}_{\delta-\gamma} \right) + \Delta E^{x}_{i\to j} \tag{5.9}$$

The second term is the energy of the original state, i, and is made up of two sums over the pair interactions: between the atom, α, at its original position and its neighbours, β , and between the defect, δ at its original position with its neighbours, γ. For the vacancy, δ, the sum does not include the bond that was already counted in the first sum, where $\gamma = \alpha$. The final term in equation 5.9, $\Delta E^{x}_{i\to j}$ is the change in energy from non-broken bonds, due to the change in the local concentration. Atoms in the vicinity of the moving defect or solute atom can have pair interactions which depend on the local solute concentration within this model, and this change must be accounted for even if the bond is not broken directly during the exchange.

5.4.6 *Interstitial Migration*

For self and mixed-interstitial defects, the activation energy for migration is calculated between the initial and final positions, following the implementation of Huang et. al [154]. The overall change in energy between states i and j for an interstitial jump, $\Delta E_{i\to j}$ is given by equation 5.10, where E_m is a constant barrier which depends on the interstitial type and $\Delta\mathscr{H}_{i\to j}$ is the change in energy calculated using the broken-bonds.

$$\Delta E_{i\to j} = \begin{cases} E_m + \Delta\mathscr{H}_{i\to j} & \text{if } \Delta\mathscr{H}_{i\to j} > 0 \\ E_m & \text{if } \Delta\mathscr{H}_{i\to j} < 0 \end{cases} \tag{5.10}$$

If $\Delta\mathscr{H}_{i\to j} < 0$, the overall change in energy used to calculate the rate, $\Delta E_{i\to j}$ is simply set to E_m^{SIA} or E_m^{MI} for the self-interstitial or mixed interstitial respectively[3]. For the self interstitial, which migrates via a series of translation events, the migration energy when $\Delta\mathscr{H}_{i\to j} > 0$ is therefore given by equation 5.11 for the atom α and its neighbours β and for the interstitial δ and its neighbours γ excluding the case where $\delta = \gamma$.

$$\begin{aligned} \Delta\mathscr{H}_{i\to j} = E_m^{\text{SIA}} &- \left(\sum_{\beta} \varepsilon^{(n)}_{\alpha-\beta} + \sum_{\gamma\neq\alpha} \varepsilon^{(n)}_{\delta-\gamma}\right) \\ &- \left(\sum_{\beta} \varepsilon^{(n)}_{\delta-\beta} + \sum_{\gamma\neq\delta} \varepsilon^{(n)}_{\alpha-\gamma}\right) + \Delta E^{x}_{i\to j} \end{aligned} \tag{5.11}$$

Interstitial migration is directional, so interstitial jumps are only calculated and added to the possible event list if the direction of exchange is consistent with the previous jump. Self interstitial defects migrate in the $\langle 111\rangle$ directions in W. A direction is chosen at random when it is inserted into the simulation cell and is stored for that defect. SIA defects undergo rotation events which change their direction of travel to a new $\langle 111\rangle$ direction, with a rate, λ_R given by equation 5.8. A fixed activation energy for rotation, E_R, is used which also depends on the interstitial defect type. For

[3] $E_m^{\text{MI}} = 0.12\text{eV}$, $E_m^{\text{SIA}} = 0.003\text{eV}$ [154]

the W self-interstitial, a rotation barrier $E_R^{\mathrm{SIA}} = 0.43$ is used [154].

For mixed-interstitial defects, migration occurs through a combined series of $\langle 111 \rangle$ translation and rotation events [140], as shown in figure 2.19. This is implemented into SPPARKS as an effective migration to a randomly assigned $\langle 100 \rangle$ direction. The activation energy for this event is calculated in 3 components: an initial translation in the $\langle 111 \rangle$ direction, followed by a rotation and a second $\langle 111 \rangle$ translation. The total migration rate, λ_T, is calculated using equation 5.12, where the time associated with a process, t^i, is given by $1/\lambda^i$. The total time of the process, $t^{a\to d}_{\langle 100 \rangle}$, is given by the sums of the times associated with each translation and the rotation, as shown in equation 5.12.

$$t^{a\to d}_{\langle 100 \rangle} = t^{a\to b}_{\langle 111 \rangle} + t^{b\to c}_{r} + t^{c\to d}_{\langle 111 \rangle} \tag{5.12}$$

The total rate, λ_T, is the inverse of the total time and is given by equation 5.13. The rate of each translation can be calculated using equation 5.8, where the change in energy for each translation in the process is calculated using equation 5.11 using the migration barrier for the mixed interstitial $E_m^{\mathrm{MI}} = 0.12\mathrm{eV}$ [154].

$$\lambda^{a\to c}_{T,\langle 100 \rangle} = \frac{1}{\left(1/\lambda^{a\to b}_{\langle 111 \rangle}\right) + (1/\lambda_r) + \left(1/\lambda^{b\to c}_{\langle 111 \rangle}\right)} \tag{5.13}$$

For the rotation of the mixed interstitial dumbbell, a fixed activation energy, $E_R^{\mathrm{MI}} = 0.03\mathrm{eV}$, is used. The interstitial and vacancy migration

processes implemented into the SPPARKS model are summarised in table 5.1.

5.4.7 *Instantaneous Process and Deposition*

Other events that can occur within the KMC and Metropolis simulations are the recombination of defects, either with each other or at a point defect sink[4], and the insertion of defects into the simulation box. When a vacancy and an interstitial come within third nearest neighbours (3NN) of each other, we assume that they recombine instantaneously leaving behind either two solvent atoms or a solvent and a solute atom depending on the interstitial type (self-interstitial or mixed-interstitial respectively). The strong attractive binding energy between a SIA and a Re atom in W means that W-Re mixed interstitial formation is likely in the event that a self-interstitial moves nearby to a Re atom. This is implemented in SPPARKS as an instantaneous transition of a SIA to MI dumbbell, if a SIA and Re atoms are separated by a distance corresponding to the 3NN shell following a prior defect migration event. The global number of solute atoms within the cell is therefore conserved.

Defects are inserted into the simulation cell in vacancy-interstitial pairs at a global rate, λ_D, per second. If an insertion event is selected, a site in the simulation cell is chosen at random. If the site is a solvent atom, it is replaced by a self-interstitial defect. If it is a solute atom it is replaced

[4]sinks of points defects are implemented as a new lattice type. If a defect exchanges with an atom that is within the third nearest neighbour shell of the sink site, it is instantaneously removed from the simulation cell

by a MI. A second site, located within a separation distance $< 10a$, where a is the lattice parameter of the first defect, is chosen and replaced with a vacancy. If the defects are within 3NN range, they are instantaneously recombined.

Transmutation events are implemented using a fixed global transmutation rate, λ_{Tr}. If a transmutation event is selected, an atom chosen at random from the simulation cell is converted from a solvent to a solute. If a solute atom is selected, and the simulation is being run with a ternary element, it is converted to the second solute species.

5.4.8 *Summary*

In summary, The SPPARKS model contains both vacancy and interstitial defects. Metropolis and KMC algorithms in SPPARKS allow both of these defect species to migrate by exchange with atoms. For the vacancies and self-interstitials, diffusion occurs through exchange processes with atoms in the 1NN shell of the defect, provided that the direction of motion is preserved in the case of the SIA. Mixed interstitial diffusion occurs in the $\langle 100 \rangle$ directions to 2NN positions from the defect, in a 3 step process. Both defect insertion and transmutation events are also implemented within the model. Defect recombination and conversion from SIA to MI is approximated by an instantaneous process that occurs if the defects are within 3NN of one another. The full description of possible events within the different algorithms are summarised in table 5.1.

Table 5.1: Possible events within the KMC and SGMC models. Lattice sites are designated as follows: V=Vacancy, A,B = Atoms, AA = SIA, AB = Mixed Interstitial, S = Sink Site.

	Vacancies	Interstitials	Instantaneous	Deposition	Transmutation	Exchange
KMC	V+A $\rightarrow$ A+V	AA+A $\rightarrow$ A+AA	AA+V $\rightarrow$ A+A	A $\rightarrow$ AA+V	A $\rightarrow$ B	
	V+B $\rightarrow$ B+V	AB+A $\rightarrow$ A+AB	AB+V $\rightarrow$ A+B	B $\rightarrow$ AB+V	B $\rightarrow$ C	
		AB+B $\rightarrow$ B+AB	AA+B $\rightarrow$ AB+A			
		AA$\langle 111\rangle \rightarrow$ AA$\langle 111\rangle$	AA+S $\rightarrow$ A+S			
		AB$\langle 111\rangle \rightarrow$ AB$\langle 111\rangle$	V+S $\rightarrow$ A+S			
			AB+S $\rightarrow$ B+S			
SGMC	V+A $\rightarrow$ A+V	AA+A $\rightarrow$ A+AA		A $\rightarrow$ B		
	V+B $\rightarrow$ B+V	AB+A $\rightarrow$ A+AB		B $\rightarrow$ A		
		AB+B $\rightarrow$ B+AB				
Canonical	V+A $\rightarrow$ A+V	AA+A $\rightarrow$ A+AA		A $\rightarrow$ B		A + B $\rightarrow$ B + A
	V+B $\rightarrow$ B+V	AB+A $\rightarrow$ A+AB		B $\rightarrow$ A		A + C $\rightarrow$ C + A
		AB+B $\rightarrow$ B+AB				C + B $\rightarrow$ B + C

6 W-Re-Os-Vac Energy Model

▶ Synopsis: In this chapter, a new energy parameterisation for the W-Re-Os system with vacancy defects is presented. The new pair-interaction coefficients are obtained by fitting enthalpy of mixing data from DFT simulations including Re, Os and vacancies. A new method of including both local solute and defect concentrations was used to generate void formation within a pair interaction model.

DFT simulations were carried out by D. Nguyen–Manh. Simulations were carried out in a custom application originally developed by E. Martinez within the SPPARKS KMC simulator, developed by S. Plimpton and A. Thompson and A. Slepo. Vacancy-solute cluster configurations used to assess binding energies were generated by L. Messina.

6.1 Outline of Fitting Methodology

The experimental results of chapters 3 and 4 highlight the importance of Os on the precipitation of transmutation products in W. Furthermore, the decoration of voids shows that an accurate description of the vacancy interactions is required to fully simulate the evolution of these materials under irradiation. This is the motivation for the development of a new pair interaction model for the W-Re-Os system, with both vacancy and interstitial type defects, the derivation of which is described in this chapter.

The energy model is based on a pair interaction Hamiltonian, that considers the interactions between individual pairs of atoms and point defects. The Hamiltonian for a basic pair interaction model can be expressed as a sum of interaction coefficients between pairs of atoms, ε, according to equa-

Table 6.1: Local solute and defect dependencies of the pair interactions parameterised in this study.

Interaction	W-Re	W-Os	Re-Os	W-Vac	Re-Vac	Os-Vac
Local Dependence	Re	Os	Os	Vac	Vac	Vac

tion 6.1, where (i) is the nearest neighbour shell, α and β are the atom types of the two sites being considered and n is the number of bonds between α and β.

$$\mathscr{H} = \sum_{i} \sum_{\alpha,\beta} n^{(i)}_{\alpha-\beta} \varepsilon^{(i)}_{\alpha-\beta} \tag{6.1}$$

In the presented model, interactions are considered between the first nearest neighbour atoms (1NN) and the second nearest neighbour atoms (2NN). For a bcc system such as W, the total number of atoms in the first and second nearest neighbour shells are $n^{(1)}_T = 8$, and $n^{(2)}_T = 6$. In this study, new interaction coefficients are derived from analysis of DFT calculations for the W-Re-Os system. Solute and defect concentration dependencies (summarised in table 6.1) were introduced to the coefficients in order to reproduce effects observed between larger clusters of defects, such as the attractive binding between clusters containing 3 or more vacancies.

To introduce these interactions, we consider the enthalpy of mixing for the quaternary W-Re-Os-Vacancy system, calculated using DFT. The enthalpy of mixing, ΔH_{mix}, for a 4 component alloy containing constituents A, B, C and D, is given by equation 6.2, where Ω is the heat of solution and x_A is the concentration of element A.

Table 6.2: DFT energies used to fit the atom-atom interactions.

Configuration	Description	DFT Value [eV]	Reference
$E_{\mathrm{W}}^{\mathrm{coh}}$	Cohesive Energy	-8.4117	[138]
$E_{\mathrm{Re}}^{\mathrm{coh}}$	Cohesive Energy	-7.4935	[138]
$E_{\mathrm{Os}}^{\mathrm{coh}}$	Cohesive Energy	-7.4283	This Study
$E_{\mathrm{V}}^{\mathrm{f}}$	Formation Energy	-3.6190	[138]
$E_{\mathrm{V\text{-}V}}^{\mathrm{b(1)}}$	Binding Energy	-0.048	[139]
$E_{\mathrm{V\text{-}V}}^{\mathrm{b(2)}}$	Binding Energy	0.2860	[139]

$$\Delta H_{\mathrm{mix}} = \sum_{\mathrm{pairs}} \Omega^{p} x_{A}^{p} x_{B}^{p} + \sum_{\mathrm{ternary}} \Omega^{t} x_{A}^{t} x_{B}^{t} x_{C}^{t} + \sum_{\mathrm{quaternary}} \Omega^{q} x_{A}^{q} x_{B}^{q} x_{C}^{q} x_{D}^{q} \tag{6.2}$$

In this approach we fit the enthalpy of mixing for each of the 6 binary systems: W-Re, W-Os, Re-Os, W-Vacancy, Re-Vacancy and Os-Vacancy, in the whole concentration range in order to obtain the concentration-dependent interaction coefficients, ε. With these parameters, we reproduce the quaternary enthalpy of mixing, ΔH_{mix} given by equation 6.2, using the binary components only. We then compare the result of this to the quaternary DFT data and evaluate the accuracy of the enthalpy of mixing produced by this parameterisation. In sections 6.2.1 and 6.2.2, the binary W-atom interactions are obtained. The fitting for the atom-vacancy systems is discussed in section 6.3.

6.2 Fitting Interatomic Interactions

6.2.1 *Atom-Atom Interactions*

The interactions between two identical elements (ie AA, BB, or CC) can be obtained from the cohesive energies, $E_{X,coh}$, for each system, which are calculated using DFT and are summarised in table 6.2. The cohesive energy of element A, $E_{A,coh}$, can be approximated by the sum of the AA pair interactions, $\varepsilon_{AA}^{1,2}$ over z_1 1NN and z_2 2NN as shown in equation 6.3.

$$E_{A,coh} = -\frac{z_1}{2}\varepsilon_{AA}^{1} - \frac{z_1}{2}\varepsilon_{AA}^{2} \tag{6.3}$$

In the case of Re and Os, which have hcp crystal structures, the cohesive energy is calculated using simulations where these elements are constrained onto a bcc lattice. To obtain the values of the pair interactions from equation 6.3, a scaling relation between the first and second nearest neighbour interactions is used, as shown in equation 6.4. For the bcc system, the scaling factor has a value of $\theta = 0.421875$ [154, 210].

$$\frac{\varepsilon_{AA}^{2}}{\varepsilon_{AA}^{1}} = \theta \tag{6.4}$$

Using this method, the interactions between W-W, Re-Re and Os-Os atoms are calculated. The calculated interaction coefficients are summarised in Appendix B.

6.2.2 *Cross Atom-Atom Interactions*

To obtain the cross interactions between pairs of dissimilar atoms, the enthalpy of mixing, ΔH_{mix}, for the W-Re, W-Os and Re-Os binary systems are used. Figure 6.1 shows the DFT data as hollow points. The convex hull of the data was extracted (as shown in figure 6.1) and was used to fit a function $f(x)$ to the data using a least squares method employing the Levenberg-Marquardt algorithm [211].

The enthalpy of mixing can be expressed in terms of the heat of solution, Ω_s, as shown in equation 6.5.

$$\Delta H_{\text{mix}} = x(1-x)\Omega_s \tag{6.5}$$

The convex hull was fit using the function $f(x) = \delta + \gamma x$ shown in equation 6.6, where δ and γ are the variables used to optimise the fitting, and x is the solute concentration. This function was chosen as the lowest order polynomial that provided an acceptable visual fit to the DFT data shown in figure 6.1, without visibly over fitting the data. These optimised fitting variables were then used to obtain the value of the respective pair interaction coefficients, which were assumed to have the same functional form as the heat of solution, Ω_s.

$$\Delta H_{\text{mix}} = x(1-x)(\delta + \gamma x) \tag{6.6}$$

The heat of solution can be expressed in terms of the 1NN and 2NN

contributions according to equation 6.7, where z_1 and z_2 are the number of 1NN and 2NN and $\Omega_s^{(1)}$ and $\Omega_s^{(2)}$ are the respective heats of mixing for the first and second nearest neighbours.

$$\Omega_s = z_1\Omega_s^{(1)} + z_2\Omega_s^{(2)} \tag{6.7}$$

They can be written as a function of the pair interactions, ε, as shown in equations 6.8 and 6.9, where $\varepsilon_{\text{A-B}}^{(1)}$ is the cross-atom pair interaction between two atoms of type A and B. The pair interactions, $\varepsilon_{\text{A-A}}^{(1)}$ and $\varepsilon_{\text{B-B}}^{(1)}$ are obtained from the cohesive energy for each system.

$$\Omega_s^{(1)} = \varepsilon_{\text{A-B}}^{(1)} - \frac{1}{2}\left(\varepsilon_{\text{A-A}}^{(1)} + \varepsilon_{\text{B-B}}^{(1)}\right) \tag{6.8}$$

$$\Omega_s^{(2)} = \varepsilon_{\text{A-B}}^{(2)} - \frac{1}{2}\left(\varepsilon_{\text{A-A}}^{(2)} + \varepsilon_{\text{B-B}}^{(2)}\right) \tag{6.9}$$

Combining equation 6.7 with equations 6.8 and 6.9 and using the relation between the first and second nearest neighbours given in equation 6.4, the heat of solution, Ω can be written as a function of the 1NN interaction between the cross A-B interaction, as shown in equation 6.10.

$$\begin{aligned}\Omega = \varepsilon_{\text{A-B}}^{(1)}(z_1 + \theta z_2) - \frac{z_1}{2}\left(\varepsilon_{\text{A-A}}^{(1)} + \varepsilon_{\text{B-B}}^{(1)}\right) \\ - \frac{z_2}{2}\left(\varepsilon_{\text{A-A}}^{(2)} + \varepsilon_{\text{B-B}}^{(2)}\right)\end{aligned} \tag{6.10}$$

We assume that the cross atom-atom interactions, $\varepsilon^{(1)}_{\text{A-B}}$, follow the same form as the fitted function in equation 6.6: ($\varepsilon^{(1)}_{\text{A-B}} = d + cx$). The unknown components of $\varepsilon^{(1)}_{\text{A-B}}$, c and d can therefore be expressed in terms of the fitting variables, γ and δ, as shown in equations 6.11 and 6.12.

$$d = \frac{\delta + \frac{z_1}{2}\left(\varepsilon^{(1)}_{\text{A-A}} + \varepsilon^{(1)}_{\text{B-B}}\right) + \frac{z_2}{2}\left(\varepsilon^{(2)}_{\text{A-A}} + \varepsilon^{(2)}_{\text{B-B}}\right)}{(z_1 + \theta z_2)} \tag{6.11}$$

$$c = \frac{\gamma}{(z_1 + \theta z_2)} \tag{6.12}$$

Using equations 6.11 and 6.12 and the fitting variables γ and δ obtained from the fitting of the data shown in figure 6.1, the values of the pair interaction coefficients $\varepsilon^{(1,2)}_{\text{W-Re}}$, $\varepsilon^{(1,2)}_{\text{W-Os}}$ and $\varepsilon^{(1,2)}_{\text{Re-Os}}$ were calculated and are shown in Appendix B.

6.3 Fitting Defective Interactions

6.3.1 *Atom-Vacancy Interactions*

A similar approach is used to obtain the defect-atom interaction coefficients. The enthalpy of mixing for the atom-vacancy systems was calculated using DFT simulations for the full range of vacancy concentrations, constrained to a bcc lattice, as shown in figure 6.2. Higher order polynomials were required to generate an acceptable fit to the data for each of the atom-vacancy binary systems as this was shown to improve the fit quality.

The heat of mixing for the binary atom-vacancy interaction is given by

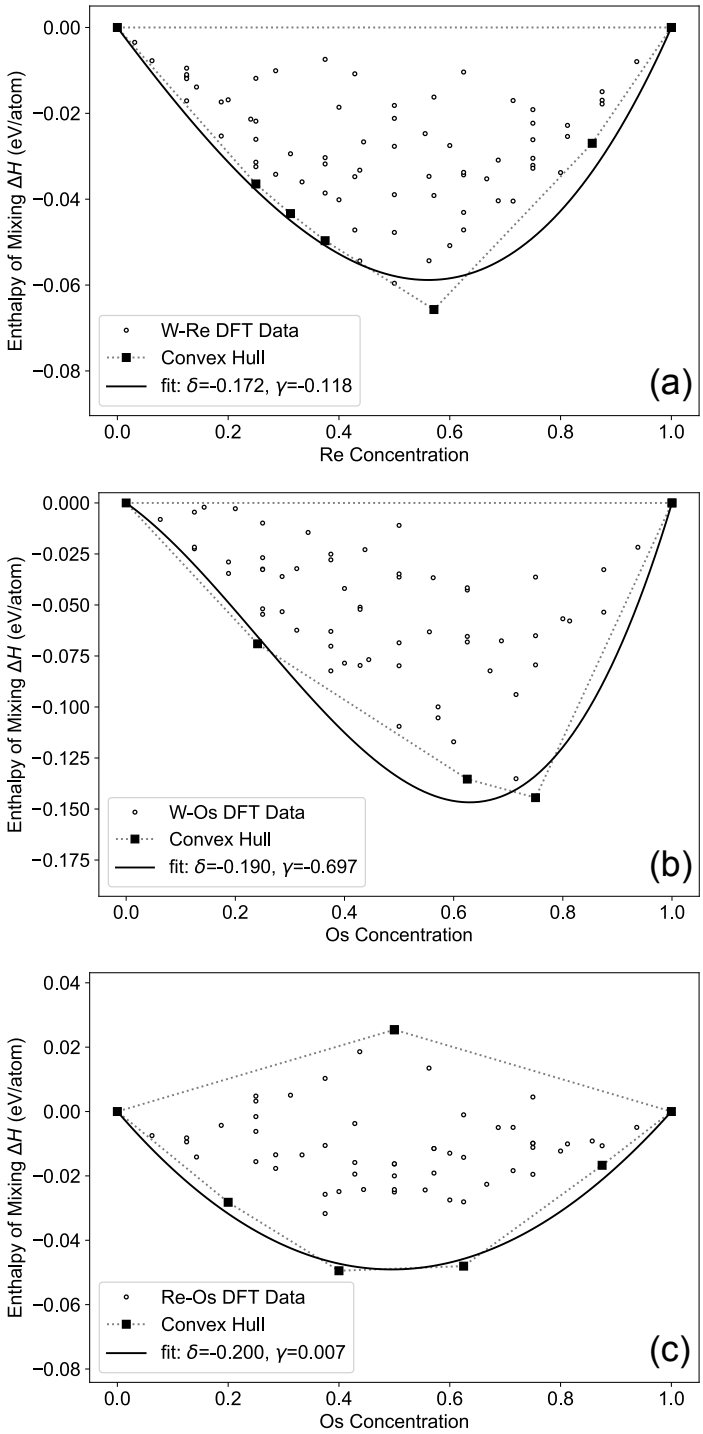


Figure 6.1: Enthalpy of mixing data from DFT calculations for the (a) W-Re (b) W-Os and (c) Re-Os binary systems, showing the convex hull and fitted polynomial function. Each hollow data point refers to a DFT calculation of a specific configuration of atoms.

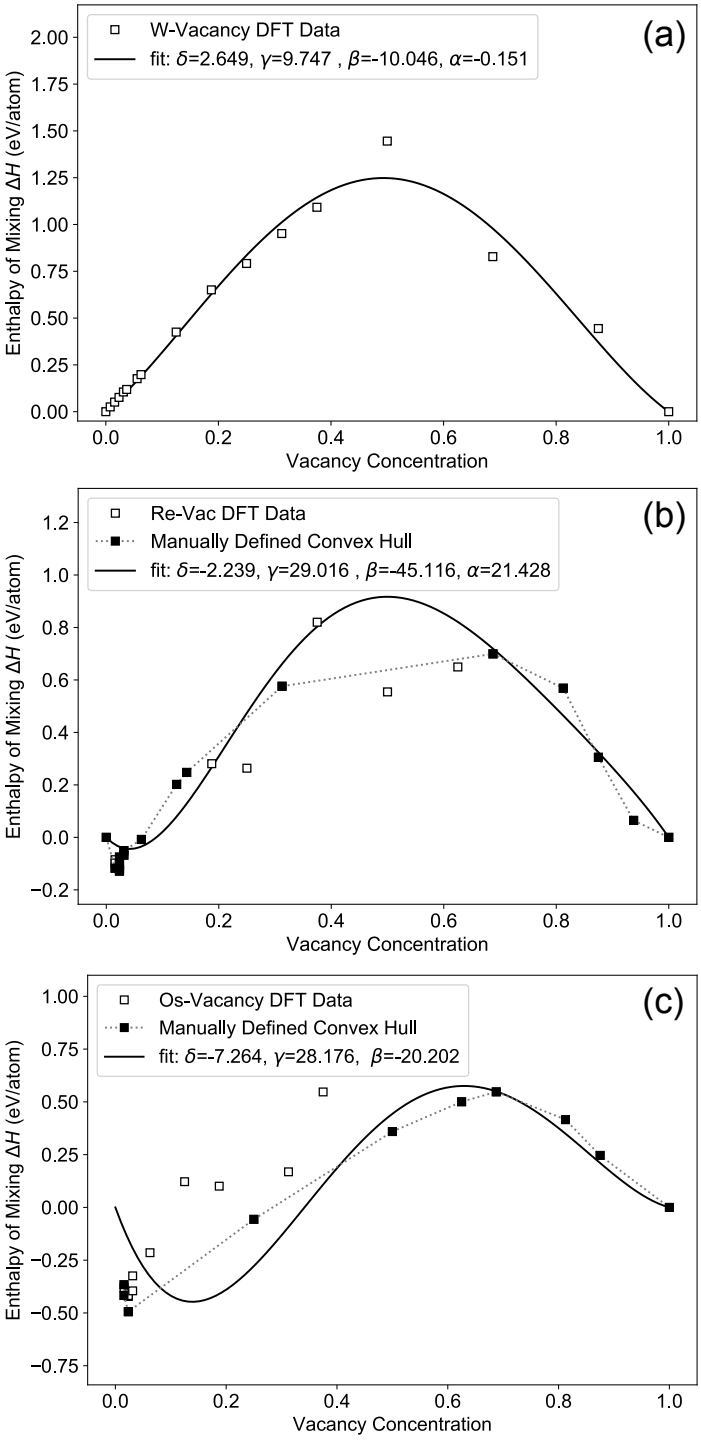


Figure 6.2: Enthalpy of mixing data from DFT calculations for the (a) W-Vacancy, (b) Re-Vacancy and (c) Os-Vacancy binary systems constrained to a bcc lattice, showing the convex hull and fitted polynomial function. Each hollow data point refers to a DFT calculation of a specific configuration of atoms and vacancies.

equation 6.13, where A is the atom type and $\varepsilon^{(i)}_{\text{V-V}}$ is the pair interaction between two vacancies at the ith nearest neighbour distance.

$$\Omega(x) = \varepsilon(x)^{(1)}_{\text{A-V}}(z_1 + \theta z_2) - \frac{z_1}{2}\left(\varepsilon^{(1)}_{\text{A-A}} + \varepsilon^{(1)}_{\text{V-V}}\right) - \frac{z_2}{2}\left(\varepsilon^{(2)}_{\text{A-A}} + \varepsilon^{(2)}_{\text{V-V}}\right) \tag{6.13}$$

The vacancy-vacancy pair interaction coefficient, $\varepsilon^{(i)}_{\text{V-V}}$, is set to zero as there is no vacancy-vacancy interaction within the voids. The interaction occurs between the atoms on the periphery of the void with the surrounding atoms in the matrix. The reference energy for the vacancies in the DFT simulations is also taken as zero [138], which is the equivalent of the cohesive energy for the pure systems. By setting $\varepsilon^{(i)}_{\text{V-V}} = 0$, equation 6.13 can be reduced to equation 6.14.

$$\Omega(x) = \varepsilon(x)^{(1)}_{\text{A-V}}(z_1 + \theta z_2) - \frac{\varepsilon^{(1)}_{\text{A-A}}}{2}(z_1 + \theta z_2) \tag{6.14}$$

The convex hull of the enthalpy of mixing DFT data was fit using the function given in equation 6.15, where δ, γ, β and α are the variables optimised during the fitting and x is the vacancy concentration.

$$\Delta H_{\text{mix}} = x(1-x)(\delta + \gamma x + \beta x^2 + \alpha x^3) \tag{6.15}$$

We assume that the atom-defect pair interactions, $\varepsilon^{(1)}_{\text{A-V}}$, follow the same form as the fitted function in equation 6.15: $(\varepsilon^{(1)}_{\text{A-V}} = d + cx + bx^2 + ax^3)$,

where a, b, c and d are the pair interaction components that need to be obtained. Comparing the variables obtained during the fitting, the results of which are shown in figure 6.2 for the W-vacancy, Re-vacancy and Os-vacancy systems, with the heat of solution given by equation 6.14 allows for the following expressions to be defined for the unknown variables in the atom-vacancy pair interaction coefficient:

$$a = \frac{\alpha}{(z_1 + \theta z_2)} \tag{6.16}$$

$$b = \frac{\beta}{(z_1 + \theta z_2)} \tag{6.17}$$

$$c = \frac{\gamma}{(z_1 + \theta z_2)} \tag{6.18}$$

$$d = \frac{\delta + \frac{z_1}{2}\left(\varepsilon^{(1)}_{\text{A-A}} + \varepsilon^{(1)}_{\text{V-V}}\right) + \frac{z_2}{2}\left(\varepsilon^{(2)}_{\text{A-A}} + \varepsilon^{(2)}_{\text{V-V}}\right)}{(z_1 + \theta z_2)} \tag{6.19}$$

As the value of the vacancy-vacancy pair interaction coefficient, $\varepsilon^{(i)}_{\text{V-V}}$, is set to zero for this parameterisation, equation 6.19 can be reduced to equation 6.20

$$d = \frac{\delta + \frac{z_1}{2}\varepsilon^{(1)}_{\text{A-A}} + \frac{z_2}{2}\varepsilon^{(2)}_{\text{A-A}}}{(z_1 + \theta z_2)} \tag{6.20}$$

Using equations 6.16, 6.17, 6.18 and 6.20 and the fitting variables α, β, γ and δ obtained from the fitting of the data shown in figure 6.2, the values of the pair interaction coefficients $\varepsilon^{(1,2)}_{\text{W-Vac}}$, $\varepsilon^{(1,2)}_{\text{Re-Vac}}$ and $\varepsilon^{(1,2)}_{\text{Os-Vac}}$ were calculated and are summarised in Appendix B. For the Os-vacancy system in which a 3rd order polynomial is applied, the same approach is used, however, $\alpha = 0$

for the fitted function so equation 6.16 can be ignored.

6.4 Evaluating Fit Accuracy

The enthalpy of mixing, ΔH_{mix}, for a quaternary system is given by equation 6.2, and consists of the sums over the contributions for pairs of atoms, and clusters containing 3 or more atoms. In this study, the pair interactions were derived by assuming that the ΔH_{mix} described by equation 6.2 could be approximated by considering only the sum over the pair interactions. In this section, the validity of this assumption is tested by comparing the enthalpy of mixing approximated by the derived pair interactions, summarised in table B.1, with the ternary and quaternary DFT data for the W-Re-Os, W-Re-Vacancy, W-Os-Vacancy and , Re-Os-Vacancy systems.

$$\Delta H_{\text{mix}} \approx \sum \Omega_s x_A x_B \tag{6.21}$$

For a ternary system of A, B and C atoms types, ΔH_{mix} can therefore be written as a function of the concentrations, x_A, x_B and x_C and the heat of solution, Ω_s, for each binary system, as shown in equation 6.22.

$$\begin{aligned}\Delta H_{\text{mix}} \approx \Omega_s^{AB}(1-x_B)x_B + \Omega_s^{AC}(1-x_C)x_C \\ +\Omega_s^{BC}x_B x_C\end{aligned} \tag{6.22}$$

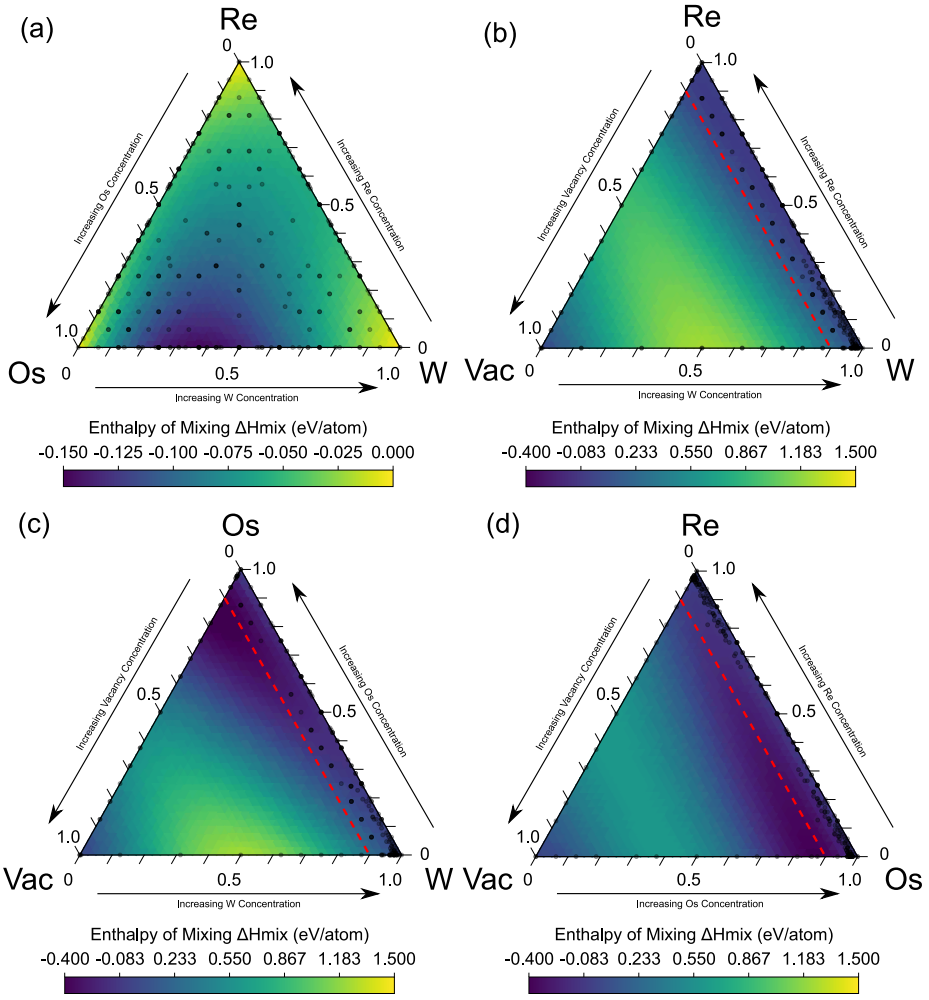


Figure 6.3: Enthalpy of mixing, ΔH_{mix}, of the ternary W-Re-Os system, described by equation 6.22 as a function of Re, Os and W concentration. Overlaid in black are the enthalpy of mixing points for various concentrations. The opacity of the DFT points is a function of the number of configurations at that concentration point.

Figure 6.3 (a) shows a plot of ΔH_{mix} given by equation 6.22 using the derived parameters for the W-Re, W-Os and Os-Re interactions, summarised in table B.1. Multiple stacked points show the locations of DFT simulations at that concentration. The DFT data was binned into concentration bins of dimensions, 0.1x0.1x0.1, and the minimum value from each concentration bin was obtained. The difference between the ΔH_{mix} produced by the pair interaction model, $\Delta H_{\text{mix}}^{\text{pred}}$, and the value calculated using DFT, $\Delta H_{\text{mix}}^{\text{DFT}}$,

Table 6.3: Loss function for each of the ternary systems studied in this project.

System	$\ell(x)$ (eV)
W-Re-Os	0.0250
W-Re-Vacancy	0.0257
W-Os-Vacancy	0.0914
Re-Os-Vacancy	0.2000
W-Re-Os-Vacancy	0.1376

was derived using the loss function $\ell(x)$ given by equation 6.23.

$$\ell(x) = \frac{1}{N_i} \sum_i |\Delta H_{\text{pred}} - \Delta H_{\text{DFT}}| \tag{6.23}$$

This gives a measure of the average deviation between the predicted surface given by equation 6.22 and the minima of the binned DFT data. The calculated differences are summarised in table 6.3 for each of the ternary and quaternary systems. The difference for the W-Re-Os system was small and no further dependencies need to be included into the W-Re, W-Os and Re-Os interactions.

The value of the loss function for the W-Re-Os system using the estimated surface was $\ell(x) = 0.0195$eV, which was deemed acceptable. The ternary W-Re-Os DFT data can be appropriately reconstructed using the binary W-Re, W-Os and Re-Os fittings and no additional concentration dependencies need to be introduced.

As summarised in table 6.3, the same process was applied to the W-Re-Vacancy, W-Os-Vacancy and Re-Os-Vacancy ternary systems as well as

the W-Re-Os-Vacancy quaternary. The ΔH_{mix} produced by the parameters are shown in figures 6.3 (b), (c) and (d) respectively, with the regions in which DFT data was available shown in black. Acceptable values of $\ell(x)$ were obtained indicating that no further dependencies on the W-Vac, Re-Vac or Os-Vac interactions were required. A larger $\ell(x)$ was measured for the vacancy containing systems, and is related to the quality of the fitting shown in figure 6.2.

6.5 Binding Energies

6.5.1 *Calculation of Binding Energy*

The binding energies of various vacancy and solute-vacancy clusters were analysed to understand the capabilities of the new parameterisation. The formation energy, E_f of a vacancy-solute cluster is given by equation 6.24 where $E^{(i)}_{\text{box}}(n\text{V}; m\text{B}; k\text{C})$ is the box energy of a simulation cell of N atoms containing n vacancies, m B type solute atoms and k C type solute atoms. $E_{\text{box}}(\text{A})$ is the box energy of the simulation cell containing only solvent A atoms. The total box energies of the non-defective simulation cell was calculated as the sum of the pair interaction energies for all of the atoms within the simulation cell.

$$E_f = E^{(i)}_{\text{box}}(n\text{A}; m\text{B}; k\text{C}) - n_A E_{coh}(A) - n_B E_{coh}(B) - k_C E_{coh}(C) \quad (6.24)$$

For a cluster configuration i, in a box of element A, with n vacancies,

m, type B solute atoms and k type C solute atoms, the cluster binding energy, $E_{\text{bind}}^{(i)}$ is given by equation 6.25, where $E_{\text{box}}(1\text{B})$ is the energy of a simulation cell containing a single atom of type B; $E_{\text{box}}(\text{A})$ is the energy of a simulation cell containing no solute atoms, and $E_{\text{box}}^{(i)}(n\text{v}; m\text{B}; k\text{C})$ is the energy of the box containing the cluster, i, as defined by Wróbel et. al [138]. Equation 6.25 can be used to calculate the binding energy of both vacancies or a mixture of vacancy and solute atoms. In this form, a positive value of the binding energy results in an attractive interaction.

$$E_{\text{bind}}^{(i)} = \overbrace{nE_{\text{box}}(1\text{V}) + mE_{\text{box}}(1\text{B}) + kE_{\text{box}}(1\text{C})}^{\text{Single Solute/Vacancy Box Energy}} - \underbrace{E_{\text{box}}^{(i)}(n\text{V}; m\text{B}; k\text{C})}_{\text{Cluster } i \text{ Box Energy}} - \underbrace{(n+m+k-1)E_{\text{box}}(\text{A})}_{\text{Pure A Box}} \tag{6.25}$$

6.5.2 *Vacancy Clusters*

The binding energy of vacancy clusters, ranging from the di-vacancy to clusters of 15 vacancies, was evaluated using equation 6.25 (see figure 6.4). Cluster configurations provided by L. Messina were read from a database [145] and converted into input files for SPPARKS. The input file then placed vacancies in different configurations and recalculated the total box energy.

Figure 6.4 shows the results from the binding energy calculations. Void formation is predicted at clusters of 3 or more vacancies. There is a negative binding between pairs of vacancies in all of the configurations simulated, corresponding to a repulsive interaction. In the clusters containing

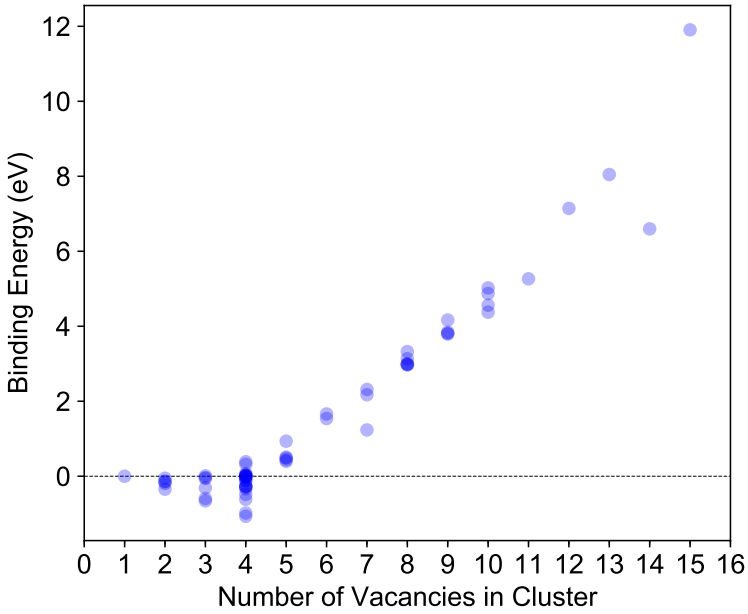


Figure 6.4: Comparison of binding energies of different vacancy clusters up to 15 vacancies calculated with new pair interaction model. Configurations taken from [138, 139] and a comparison of the formation energy of a 4 vacancy cluster as a function of box size.

4 vacancies, the majority of the configurations are also negative, indicating a repulsion exists, but in some configurations the binding energy is positive, indicating an attractive interaction. This trend continues, with larger vacancy clusters experiencing an increasing attractive binding energy. This suggests that larger voids should form, as seen experimentally, something that was not observed in previous simulations using a constant vacancy pair interaction [159].

Unlike previous pair interaction models for W, it is clear from figure 6.4 that under the new parameterisation, void formation is now possible. The repulsive nature of the di-vacancy is also correctly captured. The trend of the calculated binding energies shown in figure 6.4 agree with data from the literature which show that in small vacancy clusters including the di-

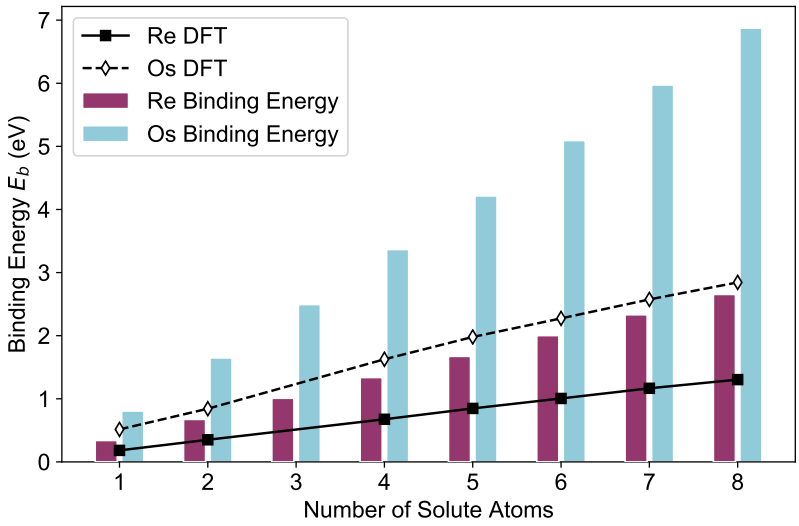


Figure 6.5: Cluster binding energies for a single vacancy surrounded with Re and Os solute calculated using the new W-Re-Os-Vac energy model.

vacancy, and some configurations of the 3 and 4 vacancy clusters, there is a slight repulsion. However, after a certain size of vacancy cluster these begin to become attractive, suggesting that larger voids should form under this parameterisation, as seen experimentally.

6.5.3 *Vacancy Solute Clusters*

To study the effect of Re and Os solute atoms on the stability of vacancy clusters, the binding energy of a single vacancy surrounded by an increasing number of solute atoms was calculated. A central vacancy surrounded by Re or Os atoms in the 1NN shell was studied until the vacancy was fully surrounded by solute atoms. The calculated binding energies for the single vacancy - solute clusters are shown in figure 6.5.

Figure 6.5 shows an increasingly attractive binding energy as the number of Re and Os atoms surrounding the vacancy increases. The equivalent

DFT data provided by D. Nguyen-Manh is also plotted in figure 6.5, showing a similarly increasing trend with increasing solute atoms. Os had a greater stabilisation effect than the Re, with the binding energy of the 8 atom cluster being more than double for Os than Re. Although trends are similar, the pair interaction model significantly overestimates the binding energy, and therefore a weaker void decoration to that shown below should be expected. The variation between DFT data and the binding energies calculated using the pair interaction model are a result of imperfect fitting of the enthalpy of mixing, shown in figure 6.2. Despite these variations, the trend in the data still shows good agreement with the DFT simulations, and indicates that both Re and Os should bind to vacancies or voids, as observed experimentally in chapter 3.

The binding energies of a randomised set of cluster configurations were calculated for a database of Vacancy - (Re,Os) cluster configurations, according to equation 6.25 [145]. The calculated binding energies are shown in figure 6.6, with each point on the x-axis representing a different cluster composition, marked in the label for each x axis bin. The colour of each bin represents the number of vacancies in the cluster, as shown in the legend. The first axis segment shows only vacancy clusters, up to a maximum of 4. The central two axis segments are clusters of vacancies and Re, and vacancies and Os respectively. The final axis segment shows a mixture of vacancies, Re and Os. All of the clusters considered here contain a maximum of 4 solute atoms and vacancies. Figure 6.6 shows clearly that both

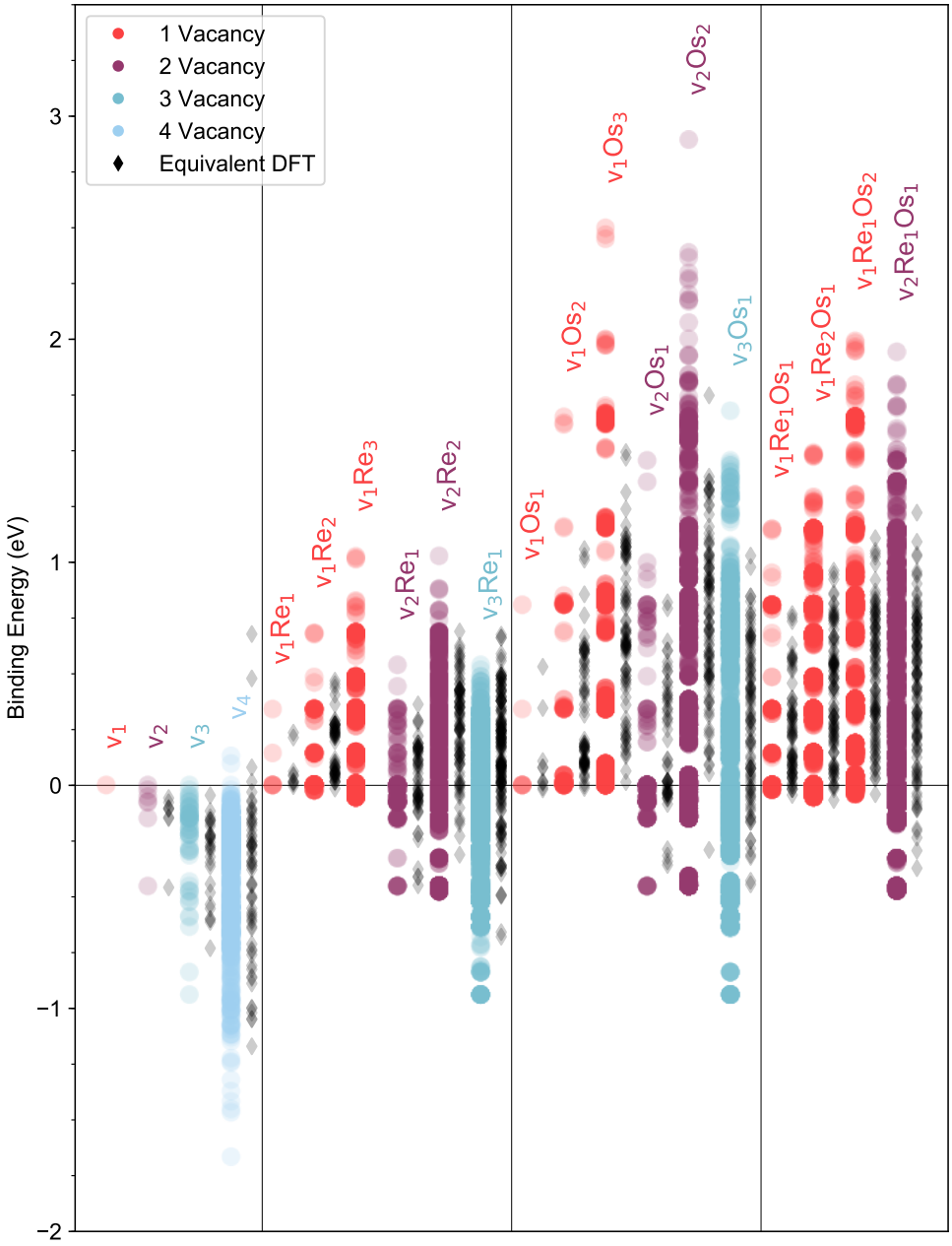


Figure 6.6: Vacancy solute cluster binding energies, calculated using new W-Re-Os energy parameterisation. Labels indicate the composition of the each cluster, with each point on the x-axis representing a different cluster composition. The first axis segment is comprised of vacancy clusters only. The second and third are vacancy-Re and vacancy-Os clusters respectively and the final axis segment is for mixed clusters of vacancy-Re-Os. The colour represents the number of vacancies in a cluster, as shown in the legend. The black points represent DFT data provided by Messina [145].

Re and Os stabilise small vacancy clusters including di-vacancies. Os has the strongest effect on stabilisation, with vacancy-Os clusters having the strongest attractive binding energies.

6.6 Phase Analysis

In this section, the phases produced by the new energy model are investigated using a combination of SGMC and Canonical MC simulations. For the defective systems, a mean field approach is used due to the low equilibrium concentration of vacancies.

6.6.1 *W-(Re/Os)*

To investigate the W-Re and W-Os systems, SGMC simulations were carried out (see section 5.4.2) in which the change in chemical potential, $\Delta\mu$, was incremented and the effect on the solute concentration in the box was measured. Figure 6.7 shows a plot of $\Delta\mu$ against Re concentration. At low temperatures (<300K) there is a sharp increase in the Re concentration up to a plateau at 50at.%Re which is consistent with the intermetallic σ phase (see figure 2.4). This jump is indicative of a miscibility gap in which a range of solute concentrations is predicted. This is consistent with the Huang energy model in which a 50at.%Re phase was observed at low temperatures [154].

Canonical simulations at 200K with a concentration of 50at.%Re show an alternating system of Re and W atoms. These simulations were run for a minimum of 100 MC per atom. The phase transition to 50 at.%Re shown in

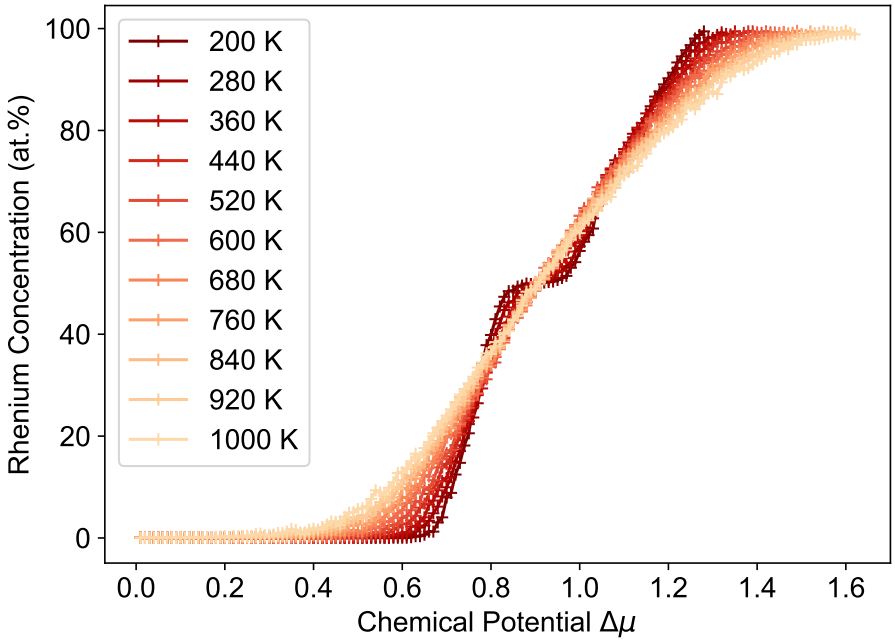


Figure 6.7: Plot of chemical potential for Re atom exchange with solute reservoir as a function of Re concentration, calculated for the W-Re-Os energy parameterisation using the method outlined in section 5.4.2.

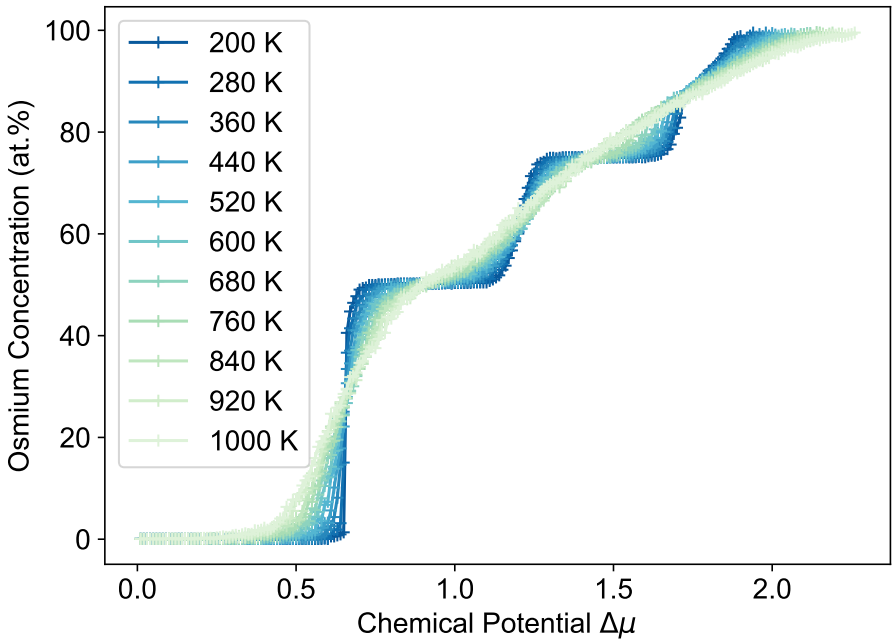


Figure 6.8: Plot of chemical potential for Os atom exchange with solute reservoir as a function of Os concentration, calculated for the W-Re-Os energy parameterisation using the method outlined in section 5.4.2.

figure 6.7 is not associated with a change in crystal structure to σ phase. The model is based on a rigid lattice approximation and the crystal structure has a fixed bcc structure. But the plateau at 50 at.%Re indicates that a coherent metastable bcc phase is present at this concentration. This supports the experimental findings of Chapter 3 in which a mixture of spherical, coherent clusters, and elongated σ phase precipitates were observed following neutron irradiation.

SGMC simulations of the W-Os system, shown in figure 6.8, show the presence of jumps from 0 to 50at.%Os and from 50 to 75at.%Os. The temperature at which the miscibility gap occurs is higher than in the case of W-Re. As with the W-Re binary, the solute concentrations of the two phases is consistent with the intermetallic phases in W-Os (see figure 2.5b).

Canonical simulations at 200K were carried out with various W-Os compositions. At 50at.%Os the simulations predicted an alternating B2 structure, similar to that which was observed in the W-50at.%Re.

6.6.2 *W-Vacancy*

For the W-vacancy system, the equilibrium concentration of vacancies, C_{eq}, can be calculated using equation 6.26, where E_f is the vacancy formation energy, k_B is the Boltzmann constant and T is the temperature. Using a temperature of 1000K, and the mono vacancy formation energy predicted by the new parameterisation, $E_f^V = 3.2\text{eV}$, the equilibrium vacancy concentration given by equation 6.26 is $C_{\text{eq}}^V = 7.45 \times 10^{-17}$.

$$C_{\text{eq}} = e^{-E_f/k_B T} \tag{6.26}$$

The very low vacancy concentration means that for SGMC a prohibitively large simulation cell is required. We therefore use a combination of mean field calculations and canonical simulations to study the equilibrium phases in the W-vacancy system. The Helmholtz free energy, ΔF [1] can be expressed in terms of the heat of solution, Ω, and the solute concentration, x, as shown in equation 6.27.

$$\Delta F = x(1-x)\Omega(x) - T\Delta S \tag{6.27}$$

The entropy of mixing contribution, ΔS can be approximated by assuming a random distribution of solute as $nR(x_1 \ln(x_1) + x_2 \ln(x_2))$, where x_1 is the concentration of solvent and x_2 is the concentration of solute (which in this case refers specifically to vacancies). Substituting this into equation 6.27, the Helmholtz free energy ΔF can be expressed in terms of temperature, T, and the solute concentration x, where $x_1 + x_2 = 1$ for a binary alloy, as shown in equation 6.28.

$$\Delta F = x(1-x)\Omega(x) - k_B T(x \ln(x) + (1-x)\ln(1-x)) \tag{6.28}$$

The heat of solution, $\Omega(x)$ can be expressed in terms of the pair inter-

[1] which is a function of the internal energy, U and the entropy, S such that, $\Delta F = \Delta U - T\Delta S$. Under the pair interaction model, the internal energy, U, can be written as a function of the heat of solution

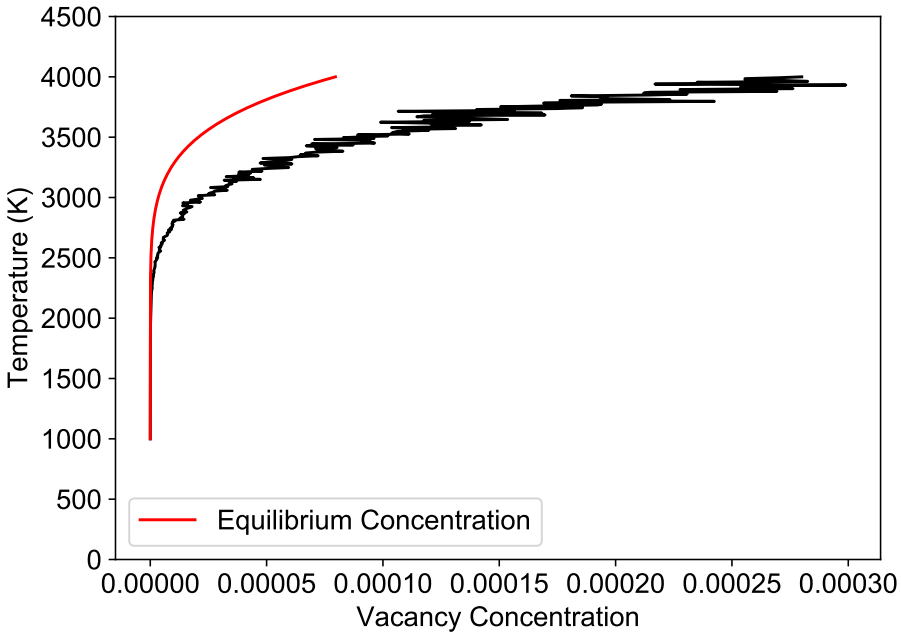


Figure 6.9: Low vacancy concentration section of the W-Vacancy phase diagram predicted by new parameterisation.

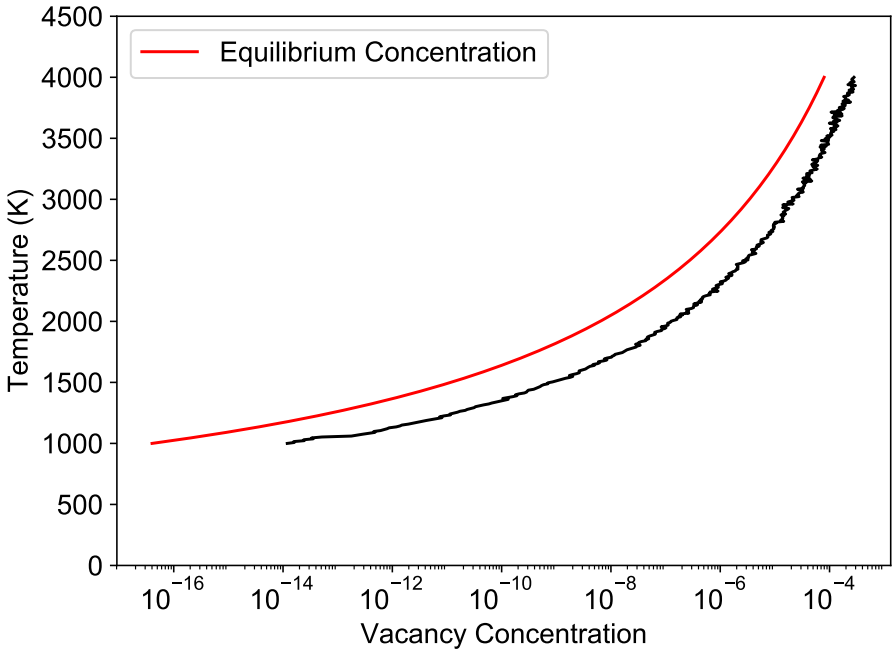


Figure 6.10: Low vacancy concentration section of the W-Vacancy phase diagram predicted by new parameterisation, plotted on a log scale of vacancy concentration.

actions according to equation 6.10. A plot of equation 6.28 against x shows two minima, one at low solute concentrations and one at high solute concentrations. The points at which the common tangent between these two curves gives the bounds of the phase region in which vacancy clustering is predicted. The common tangent can be obtained for multiple temperatures and a phase diagram constructed. To determine the common tangent, the gradient of ΔF is calculated at increasing solute concentrations. The data for each temperature was cut off between 0 and the cross over point at which $\Delta F > 0$. The reverse was also carried out at the high concentration range between $x = 1$ and the point at which $\Delta F > 0$. The points at which the gradient of the lower range, $(dF/dx)_{lower}$, were equal to the gradient of the upper range, $(dF/dx)_{upper}$ were averaged and the values of x at those points taken as the upper and lower concentration limits at that temperature.

Figures 6.9 and 6.10 show the W-vacancy phase diagram over the lower concentration region, on a normal and log scale respectively. Plotted in red is the equilibrium concentration of vacancies given by equation 6.26 as a function of temperature. The phase boundary determined by the common tangent method is higher in concentration than the equilibrium concentration across the whole range of temperature. This implies that a very small concentration of vacancies is possible before void formation is predicted. The difference in the curves is due to the repulsive interaction between pairs of vacancies which prevents di-vacancy formation. The concentration at the boundary is very low, indicating that under typical irradiation conditions

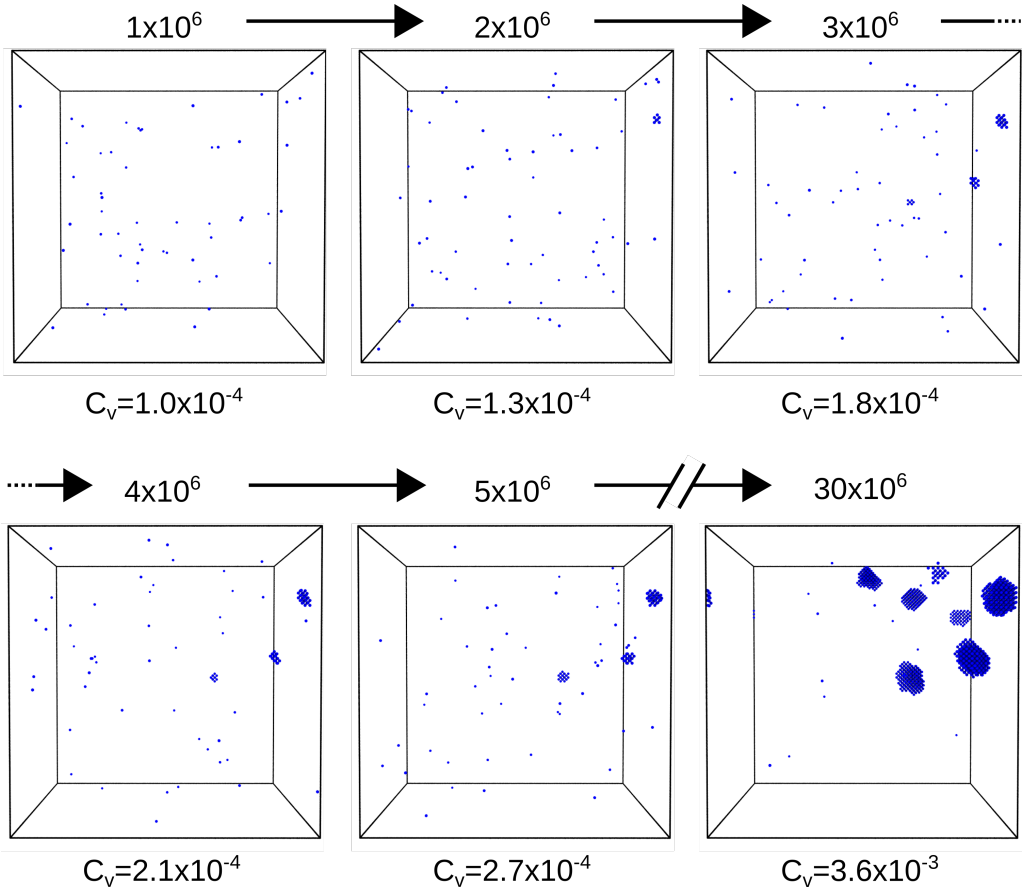


Figure 6.11: Void nucleation under new energy parameterisation, in a 64x64x64 W atom box, simulated using a metropolis algorithm (see section 5.4.1), with number of MC steps and vacancy concentration highlighted. Individual vacancies are shown in blue and are introduced with a dose rate of 1×10^{-2} per MC step.

the material will be in a saturated state and will form vacancy clusters.

6.7 Void Nucleation

The attractive binding of vacancy clusters calculated in sections 6.5.2 and 6.5.3 suggest that void formation will occur under this parameterisation. Metropolis simulations were carried out at 1800 K in a 64x64x64 atom simulation cell with an initial vacancy concentration of 0. The vacancy concentration was incrementally increased at a rate of 1×10^{-2} per MC step.

As outlined in section 5.4.1, in these metropolis simulations, vacancies can exchange with their neighbouring atoms, and the solute and defect concentrations are kept constant. Figure 6.11 shows snapshots of the simulations at various points in the simulation. After 2×10^6 MC steps, small vacancy clusters containing 3 or more vacancies begin to form. These small clusters grow larger between 3×10^6 and 3×10^7 MC steps. In section 7.2 the formation of voids is investigated further and compared to the Huang parameterisation for W-Re.

6.8 Summary

The generalised Hamiltonian for the new energy model can be redefined from equation 6.1 to equation 6.29 in order to reflect that the pair interactions now depend on the local concentration of solute atoms or vacancies.

$$\mathscr{H} = \sum_{i,j,\alpha,\beta} n^{i,j}_{\alpha,\beta}(x^i_\alpha, x^j_\beta)\varepsilon^{i,j}_{\alpha,\beta}(x_1 \dots x^i_\alpha, x^j_\beta, \dots) \tag{6.29}$$

where $n^i_{\alpha,\beta}$ is the number of bonds at site i, between atoms of type α and β; $\varepsilon^{i,j}_{\alpha,\beta}$, is the bond energy between atoms of type α and β; and x_α is the local concentration of α. The pair interactions can be split into three groups according to their local solute dependence. The interactions depend on either the Re, Os and vacancy concentration.

Metropolis simulations confirm that void formation is now possible within the new parameterisation and that small voids can nucleate due to the

attractive binding energy of clusters containing 3 or more vacancies. In chapter 7 simulations are carried out with the W-Re interaction model developed by Huang et. al, and the new parameterisation presented in this chapter. In section 7.2 the decoration of voids with Re and Os is explored further using a combination of SGMC and Canonical simulations.

7 Radiation Damage Simulations

▶ Synopsis: In this chapter, simulations of radiation damage in W, modelled using SPPARKS are presented. Initial studies using the Huang parameterisation for W-Re were carried out and compared to APT data from W-1.4Re samples from Saclay. Studies of the neutron and ion irradiated W-1.4Re-0.1Os were carried out using the new pair interaction model for W-Re-Os-Vacancies discussed in the previous chapter.

DFT simulations were carried out by D. Nguyen–Manh. Simulations were carried out in a custom application originally developed by E. Martinez within the SPPARKS KMC simulator, developed by S. Plimpton and A. Thompson and A. Slepo. The energy model for W-Re was developed by C.–H. Huang, L. Gharaee, Y. Zhao, P, Erhart and J. Marian and for more information the reader is directed to [154].

7.1 Simulations of Binary W-Re

Initial studies were carried out on the W-Re binary system to test the implementation of interstitial defects in SPPARKS and to benchmark against existing studies. The treatment of interstitial defects within the model is discussed in section 5.4.6. Simulations with the new energy model discussed in chapter 6 are also discussed in this chapter.

7.1.1 *SGMC Simulations of W-Re*

SGMC simulations were carried out using the method outlined in section 5.4.2, as was applied to W-Re and W-Os for the new parameterisation in section 6.6.1. Figure 7.1 shows the equilibrated Re content as a function of the change in chemical potential, $\Delta\mu$. There is a clear jump in the Re content at temperatures lower than 200K, suggesting the presence of a

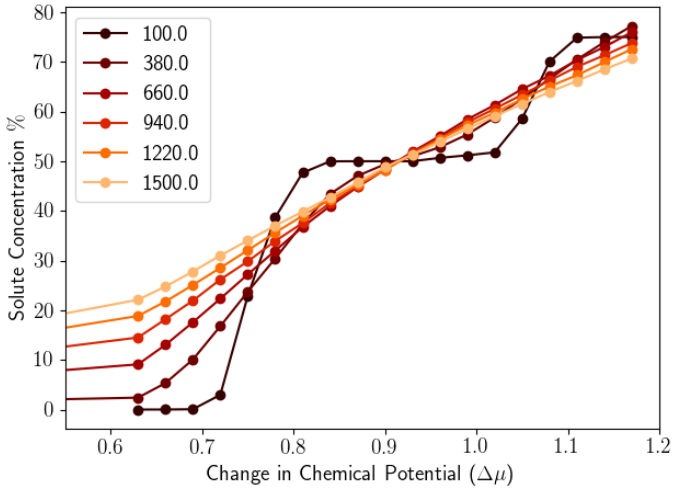


Figure 7.1: Plot of equilibrated solute concentration in % as a function of the change in chemical potential $\Delta\mu$ for a range of temperatures.

phase transition at this point. As was observed in section 6.6.1, a plateau at 50at.%Re can be seen, which is consistent with the concentration of the σ phase intermetallic. Canonical simulations for 50at.%Re alloys showed that this phase had an alternating W-Re B2 type structure, as was observed by Huang et. al [154]. Extending $\Delta\mu$ to a higher range shows the presence of another plateau at 75at.%Re which was not observed in the new pair interaction parameterisation.

SGMC simulations were also carried out with a fixed initial defect concentration. Figure 7.2 shows the final configuration of these simulations, which were carried out in a 30x30x30 atom box, at 600K using a fixed defect concentration of 0.5% Vacancies and 0.1% Mixed interstitials. The change in chemical potential $\Delta\mu$ was set such that the Re concentration shown in figure 7.2 was 4%Re and 0.5%Re respectively.

Figure 7.2 shows that mixed interstitials cluster as a result of their strong

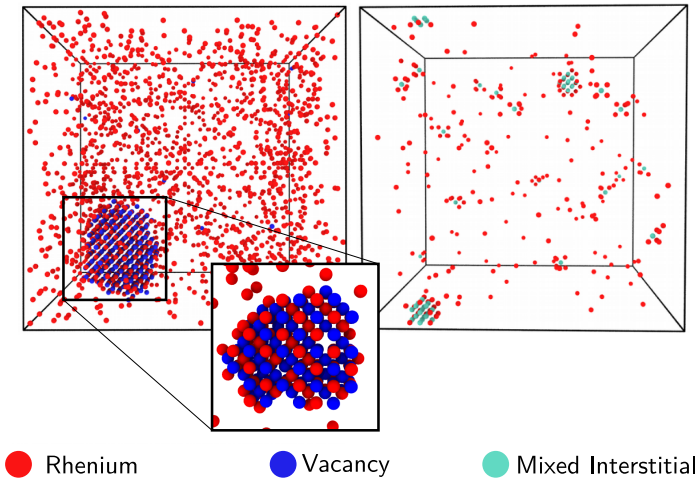


Figure 7.2: Equilibriated configurations of W-Re-Vacancy and W-Re-Interstitial for a fixed starting defect concentration and change in chemical potential, $\Delta\mu$.

attractive binding energy to one another (-3.2eV [154][1]). Re atoms also decorate these clusters due to their attractive binding (-0.53eV[154]).

SGMC simulations of the W-Re-Vacancy system, shown in figure 7.2, shows the formation of an alternating structure of Re and vacancies. Vacancies are only weakly bound to one another within this parameterisation, and, as will be discussed in section 7.2.1, are not predicted to form voids or vacancy clusters. In figure 7.2, the binding of Re and vacancies occurs due to the slightly attractive binding between vacancies and Re atoms (-0.2096eV [154]). This is larger than the di-vacancy binding in this model (-0.0146eV [154]).

These results compare well with previously published work [154] and give confidence in the implementation of interstitial defects.

[1]Note that a negative sign implies an attractive binding energy in the Huang model whereas in chapter 6 a negative binding energy implied repulsion

7.1.2 *Kinetic Monte Carlo*

In this section, a summary of the KMC simulations carried out in W-Re is given. These simulations were carried out with the algorithm outlined in section 5.4.4.

7.1.3 *Calculation of Diffusion Coefficients*

The diffusion coefficient for defects can be expressed as an Arrhenius equation as shown in equation 7.1, where E_A is the activation energy for migration, D_0 is the diffusion prefactor and T is the temperature.

$$D = D_0 \exp\left(-\frac{E_A}{kT}\right) \tag{7.1}$$

Local variations in the solute concentration can limit the migration of defects by trapping. The extent to which this occurs depends on the binding energy of vacancies with the solute atoms, which for Re and vacancies is relatively weak. To quantify the effect that this has on the migration of defects within the model, the diffusion coefficient was calculated and plotted as a function of Re concentration within the simulation box.

The diffusion coefficient, D can also be given by equation 7.2, where $\langle \Delta r^2 \rangle$ is the mean-squared-displacement and Δt is the time. To calculate the value of the diffusion coefficient, the position of a defect or solute atom is tracked in the simulation and output as a function of time.

$$\langle \Delta r^2 \rangle = 6D\Delta t \tag{7.2}$$

Table 7.1: Diffusion coefficient, D_0 and activation energy, E_A for vacancy diffusion as a function of solute concentration, x.

$x_{\mathrm{Re}}(\%)$	D_0 ($\mathrm{m^2 s^{-1}}$)	E_A (eV)
0.0	1.4×10^{-7}	1.64
0.5	2.61×10^{-7}	1.78
1.0	3.59×10^{-7}	1.84
5.0	2.56×10^{-7}	1.86

Table 7.2: Diffusion coefficient, D_0 and activation energy, E_A for solute diffusion as a function of solute concentration, x.

$x_{\mathrm{Re}}(\%)$	D_0 ($\mathrm{m^2 s^{-1}}$)	E_A (eV)
Self-diffusion Eq.7.1	6.49×10^{-7}	4.79
0.0	3.03×10^{-7}	4.79
5.0	2.20×10^{-7}	4.61
25.0	1.27×10^{-7}	4.08

The trajectory is subdivided into different time steps, $\Delta t^{(i)}$ and the displacement that occurred during this time step, $\Delta r^{(i)}$ is measured. The gradient of a linear fit of the square displacement vs time steps, $\Delta t^{(i)}$ divided by 6 gives the value of the diffusion coefficient.

The time step in the KMC simulation, Δt_{kmc} is rescaled by the equilibrium vacancy concentration, C_{eq}, for simulations of solute diffusion. Typical vacancy concentrations are many orders of magnitude lower than can be simulated in a cell and so the time step has to be rescaled for simulations of solute or self diffusion. The rescaled time step, Δt, is given by equation 7.3.

$$\Delta t = \Delta t \frac{C_{\mathrm{V}}}{C_{\mathrm{eq}}} \tag{7.3}$$

The vacancy concentration in the simulation cell, C_{V} is simply given by $1/N$ for simulations containing a single vacancy, where N is the number of atoms in the simulation cell. The equilibrium vacancy concentration, C_{eq}, is calculated using equation 7.4, where the formation energy of the vacancy, E_F^V.

$$C_{\mathrm{eq}} = \exp\left(-\frac{E_F^V}{kT}\right) \tag{7.4}$$

The instantaneous vacancy formation energy, E_F^V, is given by equation 7.5 and depends on the local environment of the defect. The sum of the first two terms on the RHS of equation 7.5 gives the cohesive energy of pure W. The sum of the third and fourth terms on the RHS of equation 7.5 are the local binding of the vacancy to its neighbours, and is the sum over the z_1 first nearest and z_2 second nearest neighbours multiplied by the pairwise energies, ε, which depend on the local solute environment. The subtraction of these two gives the vacancy formation energy as a function of the local alloy and can be used to estimate the equilibrium vacancy concentration, C_{eq}.

$$E_F^V = -\frac{z_1}{2}\varepsilon^{(i)} - \frac{z_2}{2}\varepsilon^{(i)} - z_1\varepsilon^{(i)} - z_2\varepsilon^{(i)} \tag{7.5}$$

Figure 7.3 shows the vacancy diffusivity as a function of temperature and the solute concentration. Table 7.1 shows the diffusion coefficient, D_0 and the activation energy, E_A for each of the fitted lines. Figure 7.3 shows that

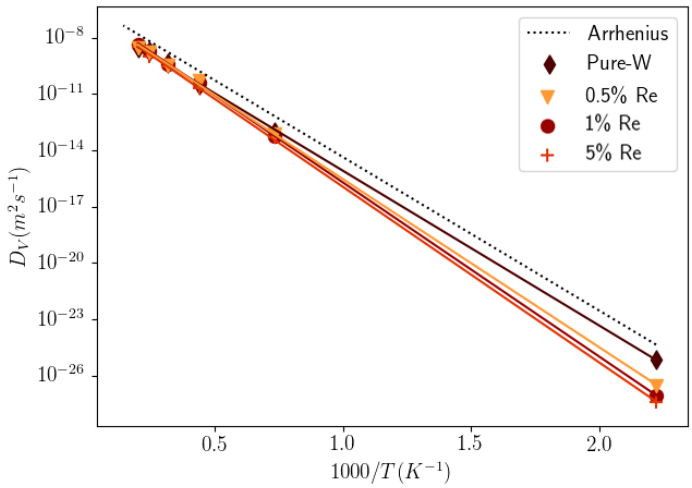


Figure 7.3: Vacancy diffusivity, D_v, as a function of temperature and Re concentration. Dashed line shows the Arrhenius relationship described by equation 7.1.

the motion of the vacancies is slowed by the presence of Re in the simulation cell. Vacancies have an attractive binding to Re [154] and therefore are slowed by Re that they encounter in the box. This supports the hypothesis from chapter 4 that pre-alloying with Re, in addition to dose rate differences may reduce cluster sizes in ion irradiation experiments. In section 7.1.6 the effect of Re on cluster growth and nucleation is discussed further.

Figure 7.4 shows the average solute diffusivity, D_s as a function of temperature and solute concentration as well as the self-diffusion of W in W. The dashed line on figure 7.4 represents the Arrhenius relationship described by equation 7.1 using an activation energy of 4.79eV [154]. The hollow circles represent experimental data points taken by Mundy et al. [212] for the self-diffusion of W. The diamond shaped markers represent the self diffusion calculated from our simulations. The other markers show the diffusivity of the solute atoms. The values for the solute diffusivity are in

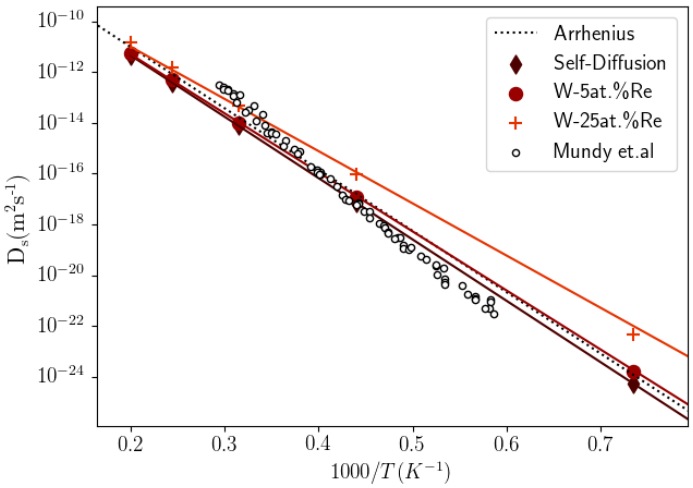


Figure 7.4: Solute and self-diffusivity, D_s, as a function of temperature and Re concentration. Dashed line shows the Arrhenius relationship described by equation 7.1 using an activation energy of 4.79eV. The black points represent experimental values for the self-diffusion of W in W taken from [212].

good agreement with both the experimental data points and that predicted by equation 7.1. The introduction of 5%Re slightly decreases the solute migration activation energy as shown in table 7.2 which becomes more pronounced at 25%Re. This also agrees well with previous modelling work with this parameterisation [154].

7.1.4 *Precipitation in W-Re*

In this section, precipitation of Re in a binary W-2Re alloys is simulated to allow comparison with the experimental work of Xu et. al [97, 134] and computational results from Huang et. al [154]. A simulation cell $30 \times 30 \times 30$ atoms in size was filled with a random distribution of Re atoms, at a concentration of 2at.%. A dose rate of 1×10^{-3} dpa/s was used to insert defects into the simulation cell, the same dose rate as in Xu. et. al's ions

irradiation experiments.

A high temperature of 1800K, compared to 773K in the experiments, was used in order to accelerate diffusion and reduce computational expenditure. This was the same temperature used by Huang et. al in their study of W-2Re. The simulations were run for a total duration of 100s, over which time a dose of 0.1dpa was received.

Simulations without a sink of point defects did not predict the formation of a Re cluster under equivalent starting conditions. In previous simulations, Re cluster formation occurs due to the immobilisation of mixed interstitial defects by Re or by other mixed interstitials, which provides the vacancy sufficient time to migrate to the trapped interstitials and recombine [154]. Simulations containing a central Re cluster showed that the cluster dissolved completely back into solution without a point defect sink. Simulations with considerably higher dose rates also showed that mixed interstitial clustering is predicted to occur.

Figure 7.5 shows the result of a simulation containing a central ideal point defect sink. The position of Re atoms at 0s, 10s and 100s is plotted. In the case where the sink is included, Re cluster formation is now predicted. In this model the interstitial, upon reaching a Re rich area, is trapped in this region but then acts to dissolve the cluster over time through many exchange events. In the time it takes the vacancy to reach the immobilised interstitial, it has sufficient time to dissolve the cluster slightly, reducing the central Re concentration and reducing the effectiveness of the cluster

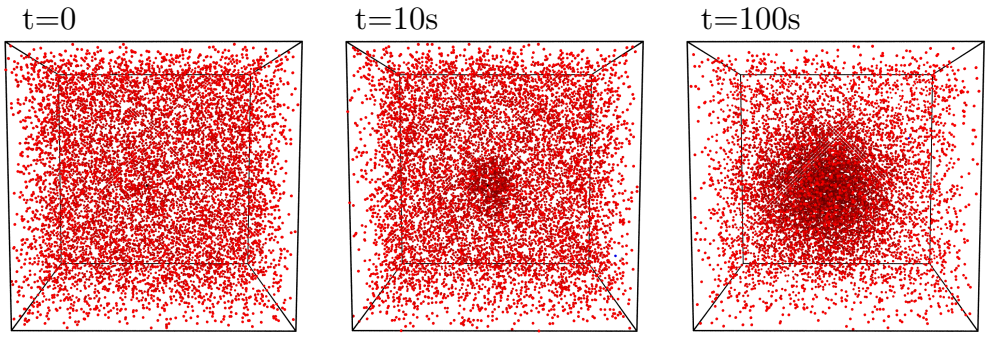


Figure 7.5: Precipitation of Re around a point sink at 10 and 100s of irradiation in a W-2at.%Re alloy. A dose rate of 1×10^{-3} dpa/s was used at an irradiation temperature of 1800K which ensures that vacancies are mobile within our simulation.

to trap further interstitials, by spreading out the interface between W and Re. Over many of these events the cluster reaches a point at which it is too diffuse to act as a trapping site and it is dissolved back into the matrix.

Figure 7.6 shows the Re concentration in the cluster shown in figure 7.5 as a function of radius from the point sink. The concentration is estimated using a series of progressively smaller concentric spherical shells. Plotted as hollow squares is the radial concentration profile seen by Xu et al. using APT of a W-2Re alloy, irradiated to 18 dpa (reported 33 dpa, see section 4.2) at 773K using self ion implantation [134]. The experimental and computational results are not directly comparable, due to the different total dose and temperature used, but suggest a similar Re profile.

As seen in figure 7.6, when a sink is artificially introduced into the box, there is strong Re segregation. After 100s of irradiation the maximum concentration of Re at the sink is between 25 and 30 at.%. This agrees well with experimental data from A. Xu et al's ion implantation which shows a maximum concentration of around 30at.% [134] in the centre of the cluster.

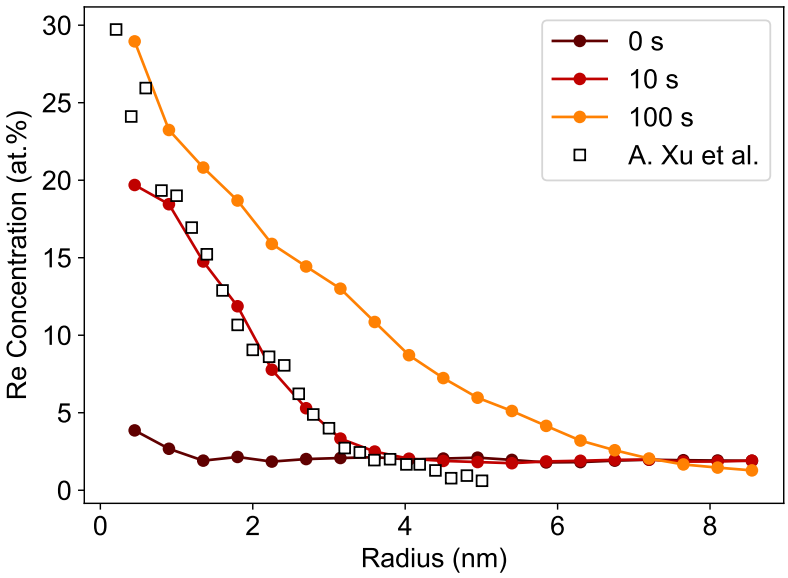


Figure 7.6: Re concentration as a function of radius from an ideal point sink, in a W-2%Re alloy irradiated with a dose rate of 1×10^{-3} dpa/s and an irradiation temperature of 1800K.

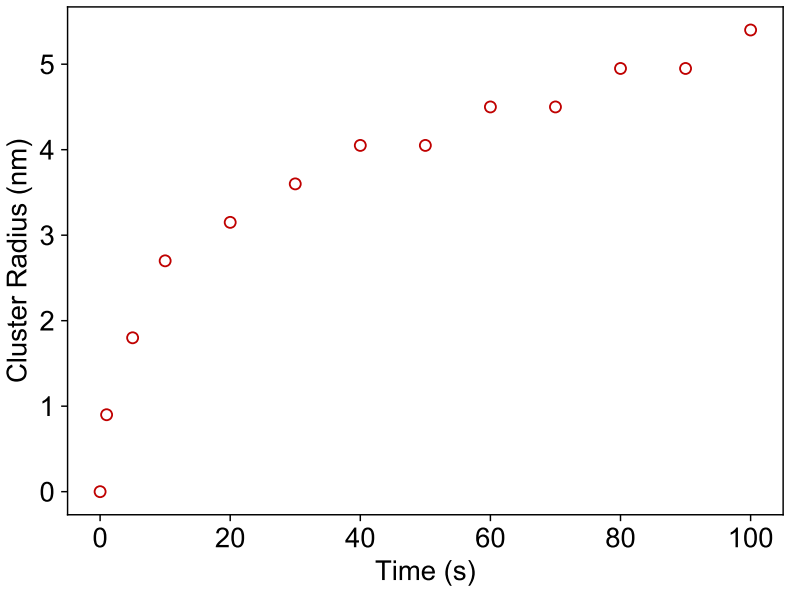


Figure 7.7: Growth of cluster in terms of the number of atoms in the cluster as a function of irradiation time for the simulation shown in figure 7.5.

Figure 7.7 shows the growth of the cluster shown in figure 7.5 as a function of time. A cluster is defined as the region within which the Re concentration is above 5% which we approximate as spherical. Plotted in figure 7.7 is the radius beyond which the concentration drops below 5% as a function of the irradiation time in seconds.

We see the continuous growth of the cluster from the moment the sink is introduced at time t=0. As time progresses up to 100s, there is a slight decrease in the growth rate as more Re from the bulk is contained within the cluster and some degree of dissolution occurs. Overall the growth of the cluster is slower than observed previously [154], but approaches a similar size after 100s. The Re concentration after this time is lower in our simulations, reaching between 25 and 30 at.% compared to 50at.% in the simulations of Huang et. al [154]. Compared to Xu et. al's experiments we see similarly sized Re clusters to the ion implantations conducted at 773K [134], however, direct comparison requires further study using equivalent conditions. This is dependent on further improvement of the computational efficiency of the model.

In summary, our results indicate that there is competition between the transport of Re to the sink and the thermodynamic driving force for dissolution. Without a flux of defects to the sink, our model predicts the dissolution of the Re cluster back into solution, in agreement with the phase diagram. This would imply that if an irradiated W-Re sample were to be annealed, the clusters would dissolve back into solution, as observed experimentally in

section 4.4.4. Both mixed interstitials and vacancies bind to Re but simulations of transport properties indicate a reverse coupling of vacancies and Re [154]. The mixed interstitial transports Re to the point defect sink via rapid migration due to its low activation energy. Clustering of these defects only occurred in our model at very high dose rates. As was discussed in chapter 6, the underestimation of the vacancy interactions in this parameterisation limits the formation of voids, which can also act as point defect sinks. If voids form in the material initially, they may then act as sinks for point defects, having Re transported to them by mixed interstitial diffusion.

7.1.5 *Grain Boundary Decoration in W-Re*

Grain boundary decoration with Re was observed in both neutron and ion irradiation experiments, as discussed in sections 3.4.4 and 4.4.3. To study non-equilibrium GB segregation in W, a simple model was constructed in which the GB was modelled as a planar ideal defect sink. No additional binding energy between the solute atoms and the boundary was included. There is no crystallographic variation on either side of the sink. The planar defect sink acts in a similar way to the point sink in the previous section, removing defects instantaneously if they come with the recombination range of the sink (3NN).

To compare with the experimental findings in section 4.4.3, a simulation cell 64x64x256 atoms in size, containing a random distribution of 1.4at.%Re was used, with a central GB perpendicular to the long direction of the simulation cell. Defects were introduced at a rate of 1.19×10^{-3} dpa/s

and using a temperature of 1800K to accelerate diffusion. Computational expenditure limited the total simulated time to 5s, in which a total dose of 5.96×10^{-3} dpa was received by the cell.

Segregation of Re to the GB was observed even after only 5 seconds of exposure, as shown in figure 7.8. The Re atoms in the simulation cell in red with the other atoms hidden. The maximum Re concentration at the GB was approximately 8 at.%Re after 5 seconds of irradiation. Most ion irradiation experiments are limited to temperatures below around 1200 K. As with the point sink simulations, lower temperatures significantly increase computational expenditure as individual defects become trapped or slowed by Re atoms[2]. At higher temperatures the detrapping of these defects is enhanced and the defects reach the sink more quickly. At lower temperatures however, this detrapping is unlikely, and a significant amount of time is spent simulating the defects diffusing within the potential well.

Figure 7.9 shows a comparison between the GB shown in figure 7.8, and the experimentally observed GB decoration shown in figure 4.11. The experimental concentration was measured using a 1D fixed bin width concentration profile, as described in section 4.4.3. The computational concentration peaks at a higher value (around 8at.%) than the experimental data, however, the two are not directly comparable due to differences in the dose rate, total dose and temperature. The shape of the profile is similar but no depletion of the surrounding region is observed computationally. This may require longer simulation times and a more complete description of the

[2]The results shown in figure 7.8 took several days to simulate on a single processor

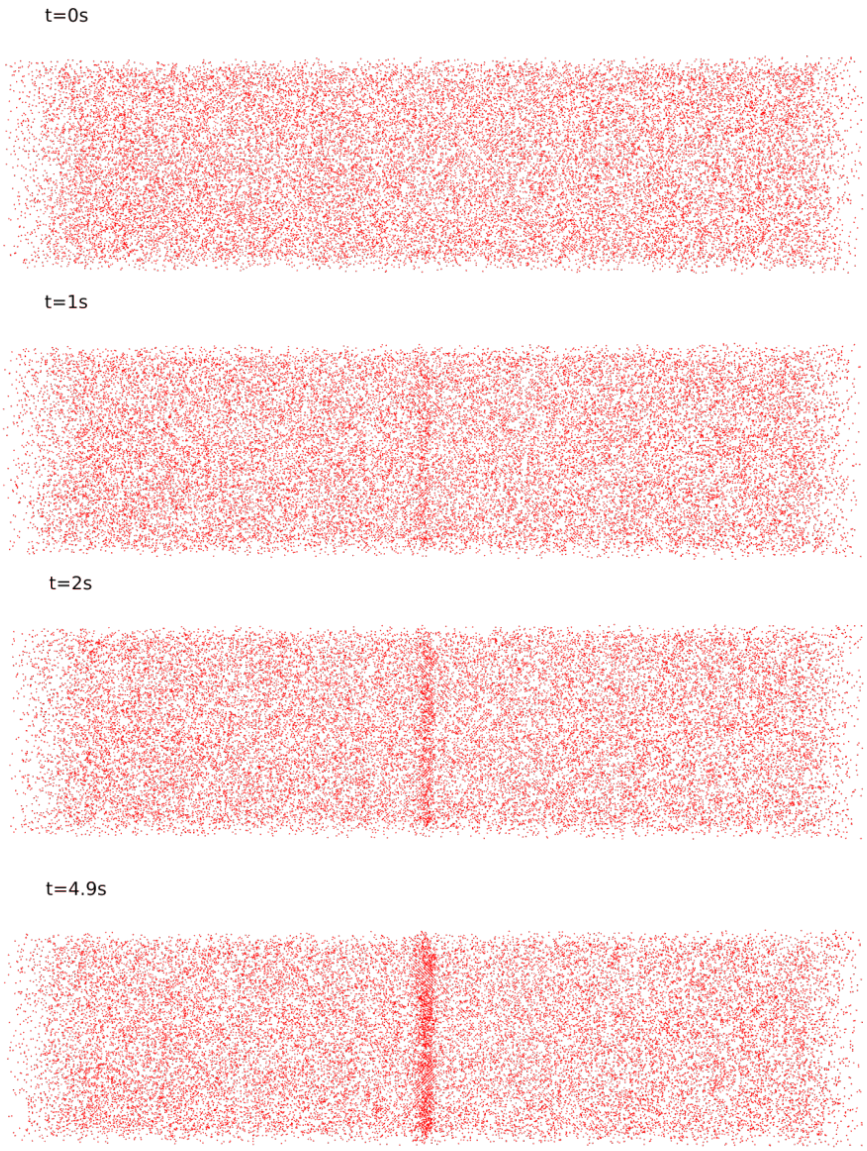


Figure 7.8: Segregation of Re in a 1.4at.%Re alloy to a planar ideal sink at 1800K after a total dose of 5.96×10^{-3}dpa with a dose rate of 1.19×10^{-3}dpa/s.

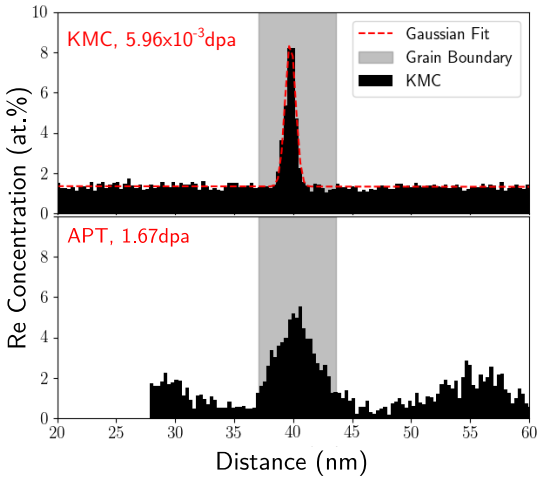


Figure 7.9: (top) Segregation of Re in a W-1.4at.%Re alloy to a planar ideal sink at 1800K after a total dose of 5.96×10^{-3}dpa with a dose rate of 1.19×10^{-3}dpa/s. (bottom) Segregation on GB in a W-1.4at.%Re alloy, observed experimentally using APT - as shown in figure 4.11.

grain boundary environment than the simple approximation used here.

7.1.6 *Effect of Re Pre-Alloying on Precipitation*

Differences between the ion and neutron irradiated W-1.4Re-0.Os discussed in chapter 4, are a result of different dose rates and the effect of pre-alloying in the ion irradiated material. Because ion irradiation does not introduce transmutation effects, Re and Os must be studied in ion irradiation by alloying samples prior to irradiation. Alloying W with Re is known to suppress void formation compared to pure W [90, 105, 111] and is thought to be the result of increased interstitial mobility following the cascade, promoting recombination and thus reducing the surviving vacancy population [82, 142].

Both dose rate differences and pre-alloying were thought to reduce the overall cluster size observed in ion and neutron irradiated W, as discussed in chapter 4. Literature studies of neutron irradiated W and W-10Re have

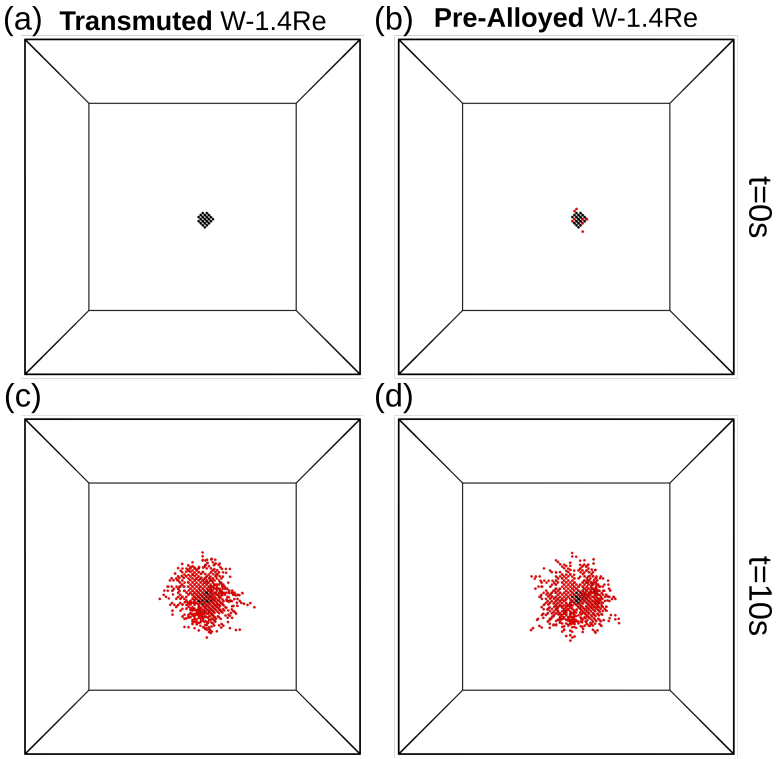


Figure 7.10: Comparison before and after KMC for two samples containing pre-alloyed W-1.4Re and one in which W-1.4Re was introduced continuously with a fixed transmutation rate. All atoms are hidden apart from those contained within the largest cluster in the simulation cell which forms around an ideal sink shown in black.

also shown a smaller average cluster size in the pre-alloyed material, despite equivalent and equivalent dose rate [114].

In section 7.1.3, Re was shown to decrease the mobility of vacancies but here the interstitials are primarily responsible for the transport of Re to point defect sinks. To investigate the effects of Re on the transport of Re to clusters, two KMC simulations were carried out at 1800K in a simulation cell of dimensions $30 \times 30 \times 30$ atoms, with a central spherical point sink, as shown in figure 7.10. One simulation had an initial random distribution of 1.4at.%Re atoms whereas the other started with pure-W. In the pure-W box, transmutation was introduced at a rate of 760 Re atoms per second.

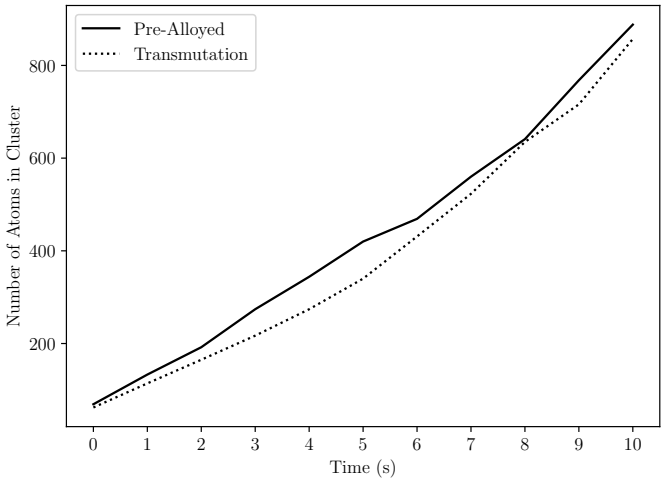


Figure 7.11: Plot of maximum precipitate size in transmuted and pre-alloyed simulations, in terms of the total number of Re atoms contained within the cluster, defined by the cluster search function in Ovito using a cutoff distance of 5.5 Å.

Figure 7.10 shows an image of both simulation cells at 10s, with all atoms except for those contained within the cluster removed. The atoms within the cluster were defined using the cluster search function in Ovito with a cutoff distance of 5.5 Å.

There is little impact on the size of the cluster on the overall concentration at the final time step. There is also little effect on the growth rate of the cluster, as shown in figure 7.11. Both clusters grow at approximately the same rate throughout the simulation. This implies that even though the mixed interstitial, which is responsible for the growth of Re clusters in these simulations, is attracted by solute Re atoms and therefore slowed, the effect on the overall transport is low. The mixed interstitial moves with such a low barrier to migration that the trapping by Re atoms does not majorly reduce the time taken by the interstitial to reach the sink of point defects.

More work is needed to understand the effects of Os on this process and to correctly simulate vacancy interactions.

7.1.7 *Summary of W-Re Study*

In summary, it was found that mixed interstitial mediated Re diffusion led to the precipitation of Re at point defect sinks. Unlike previous studies using the same energy model, homogeneous clustering due to mixed interstitial binding or trapping in sites of enriched Re was not possible at low dose rates, with clustering in this case only facilitated by the presence of an ideal point sink or grain boundary. This highlights the importance of the mixed interstitial for solute transport. Pre-alloying with 1.4Re has no observable effect on the precipitate formation time, indicating that trapping by isolated Re atoms had little effect overall. Void formation was not predicted and Os was not included in this parameterisation. The experimental findings of chapter 3 found voids decorated with Re and Os shells, whereas in chapter 4, small Os clusters formed preferentially to Re. This led to the development of W-Re-Os-Vac model discussed in the previous chapter.

7.2 Simulations of Ternary W-Re-Os

7.2.1 *Metropolis Simulations of W-Vac*

Preliminary analysis of the behaviour of vacancies under the new parameterisation, shown in figure 6.11, indicated that at high temperatures void formation was now possible. To compare this with the previous W-Re

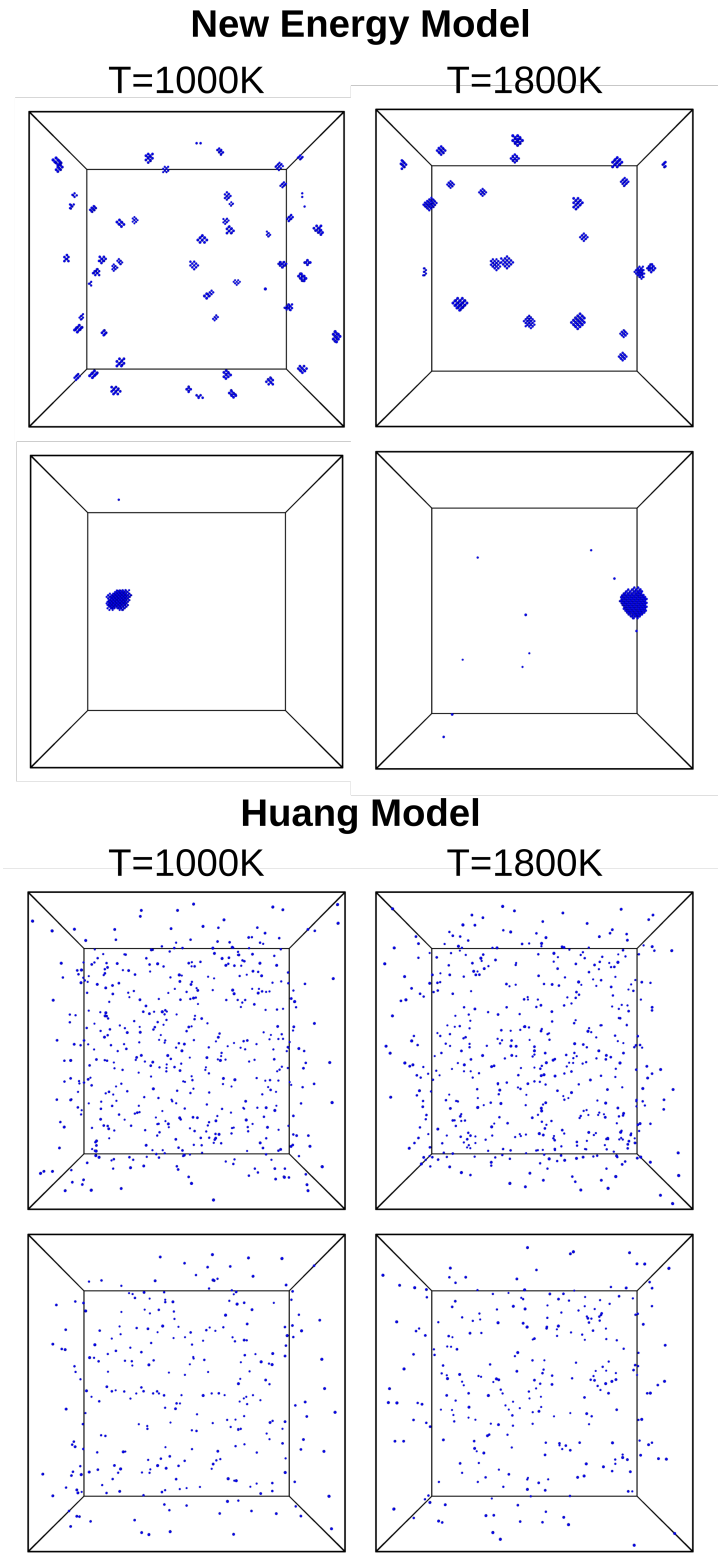


Figure 7.12: Metropolis simulations at 1000K and 1800K, shown at 3×10^7 MC steps with vacancies shown in blue. Simulations were carried out using an initial vacancy concentration $C_V^i = 0.1$at.% and using a vacancy insertion rate corresponding to a final vacancy concentration of 0.1at.%.

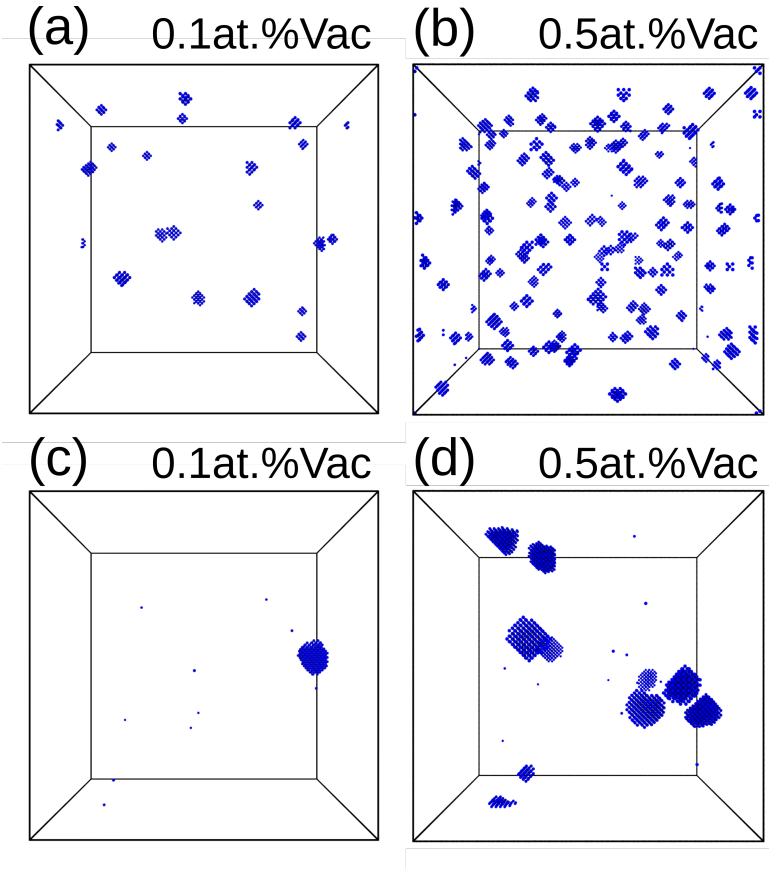


Figure 7.13: Metropolis simulations with a vacancy concentration of 0.1 and 0.5at.% at 1800K. (a) and (b) show simulations carried out with an initial vacancy concentration of 0.1 and 0.5 at.% at respectively, whereas in (c) and (d), vacancies were inserted at a rate that resulted in a final vacancy concentration of 0.1 and 0.5 at.% at 3×10^7 MC steps respectively.

model, metropolis simulations of W-Vac systems were carried out at 1000K and 1800K using both energy models. Figure 7.12 shows the differences between the two models at both temperatures. Simulations were carried out using the algorithm described in section 5.4.1, using both an initial concentration of 0.1at.%Vac and using a continuous defect insertion, until a maximum of 0.1at.%Vac was reached in the simulation cell. Simulations were run in a box 64x64x64 atoms in size, containing a total of 524288 atoms, for a total of 3×10^7 MC steps or 57 steps per atom.

Figure 7.12 shows that using the previous energy model developed by

Huang et. al [154], void formation is not predicted under any of the conditions simulated. Under the new energy model, void formation is predicted under all simulation conditions. In the simulations containing an initial concentration of 0.1at.%Vac, a population of small voids is visible. In the vacancy insertion simulations, a single large void is formed which grows larger as more defects are inserted into the box, as also shown by figure 6.11. Higher temperatures increase the mobility of the defects and allow larger voids to be formed. Figure 7.13 shows that at higher vacancy concentrations, a number of large voids were formed.

7.2.2 *Canonical Simulations of Void Decoration*

To study the interaction between voids and Re and Os solute atoms, canonical simulations were carried out using void structures formed using the metropolis algorithm as a starting point. A simulation cell, 64x64x64 atoms in size, containing a total of 524288 atoms was evolved for 3×10^7 steps, containing 0.5at.%Vac, and used as a starting point for this study, as shown in figure 7.14(a). Solute atoms were randomly distributed in the simulation cell and a canonical algorithm, described in section 5.4.3, was used to allow the atoms to migrate. Simulations were run for W-1.4Re, W-1.4Os and W-1.4Re-0.1Os, for a further total of 3×10^7 MC steps, the results of which are shown in figure 7.14.

Figures 7.14(b) and (c) show the decoration of the voids with both Re and Os in the binary alloys. This is in agreement with the findings summarised in figure 6.6 which shows an attractive binding in Vac-(Re/Os) clusters.

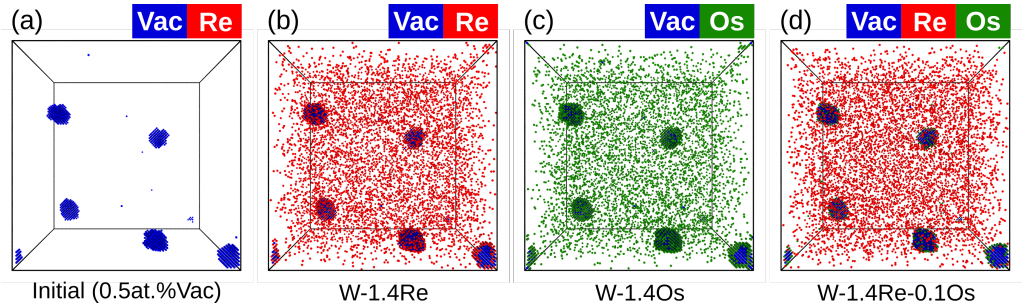


Figure 7.14: Canonical simulations for a W box containing 0.5at.%vacancies, evolved with metropolis to form voids as shown in (a). Canonical simulations were carried out for (b) W-1.4Re (c) W-1.4Os and (d) W-1.4Re-0.1Os, randomly distributed through the initial simulation cell shown in (a) at a temperature of 1800K.

Figure 6.5 suggests that Os binds more strongly to vacancies that Re in this parameterisation. This is shown by figure 7.14(d) which contains both Re and Os, and in which Os has more strongly segregated to the voids.

Figure 7.16 shows the proportion of Re and Os atoms contained with clusters of Re, Os and vacancies, in the simulation cells shown in figures 7.14 (b) and (c) respectively, as a function of MC steps. Clusters were defined using the *Cluster Analysis* tool within the visualisation software Ovito, using a cutoff distance of 5.5 Å. In each simulation, the number of Re or Os atoms within the clusters, as a percentage of the total number of Re or Os atoms in the simulation is plotted for each MC step. For the two simulations shown in figure 7.14 (b) and (c), the percentage of the Re and Os decorating the voids quickly saturates. The percentage of Os atoms decorating the void is higher, due to the stronger attractive interactions between Os and vacancies. Re decoration is also observed but the percentage of Re atoms decorating the voids is lower than the Os case, due to the weaker interaction with vacancies.

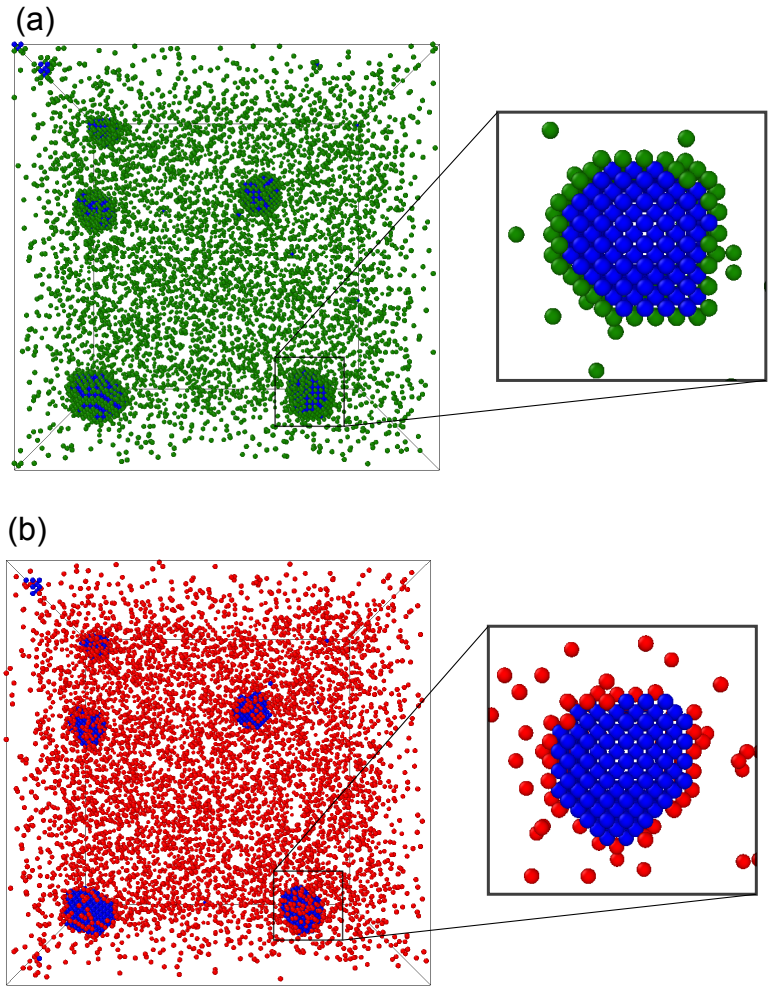


Figure 7.15: Canonical simulations for W box containing 0.5at.%vacancies, evolved with metropolis to form voids with (a) 1.4at.%Os and (b) 1.4at.%Re, as shown in figure 7.14 (c) and (b) respectively. A slice taken through the centre of one of the voids is shown, highlighting that solute atoms have not migrated into the centre of the vacancy cluster, as is shown in figure 7.2.

Figure 7.17 shows a canonical simulation in which realistic concentrations of Re and Os are used. This simulation cell is shown in figure 7.14(d) and contains 1.4at.%Re-0.1at.%Os, as was measured in the neutron irradiated W in chapter 3. Both Re and Os show an increase in the beginning of the simulation. Os quickly decorates the void until virtually 100% of the Os atoms are decorating the void. Re decoration also increases but then shows a slight decrease at around 2×10^6 MC steps. This reduction in Re as Os

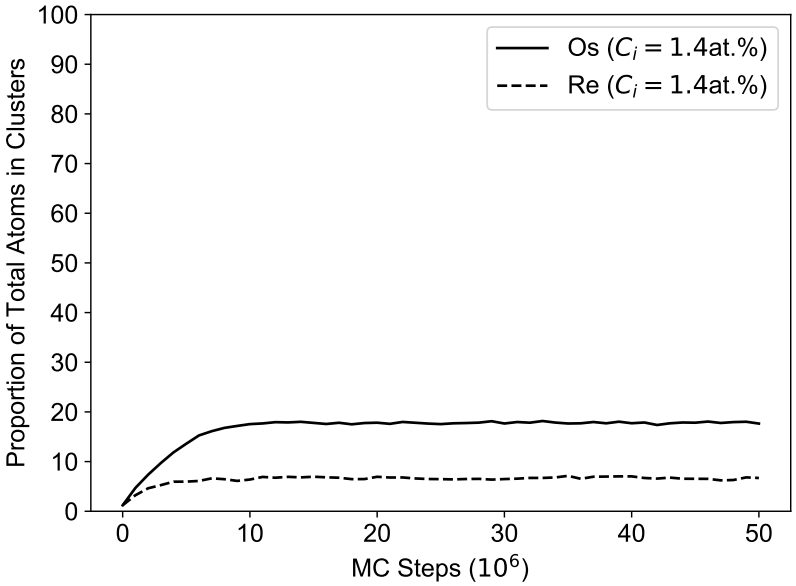


Figure 7.16: Proportion of solute atoms contained within clusters defined by a cutoff distance of 5.5 Å, in simulation cells with 1.4at.% Re and Os, after 5×10^7 MC steps, as shown in figure 7.14(b) and (c).

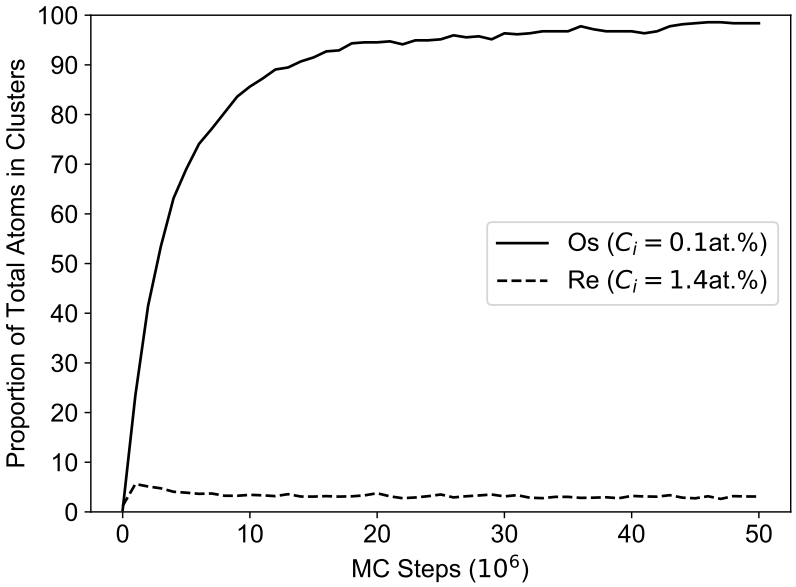


Figure 7.17: Proportion of solute atoms contained within clusters defined by a cutoff distance of 5.5 Å, in simulation cells with 1.4at.% Re - 0.1at.% Os, after 5×10^7 MC steps, as shown in figure 7.14 (d).

increases shows that Os is segregating to the voids preferentially to Re and may indicate some repulsion between Re and Os atoms.

The simulations shown in figure 7.14 indicate that there is some thermodynamic tendency for Os and Re to segregate to voids, however, this is more limited in the case of Re. The strong Re segregation seen experimentally to voids may therefore be a result of kinetic transport of Re to voids by a flux of point defects. This process was simulated in section 7.1.4 in which mixed W-Re interstitials transported Re to ideal point sinks. In this case, the voids formed may act as point defect sinks therefore creating a site for segregation to occur. The stronger Os interaction with interstitials and at the periphery of the void suggest that a core shell structure such as that seen in chapter 3 is likely to form due to competition between the transport of Re and Os.

These results indicate an improvement on existing models in terms of void formation. The simulations with voids and solute atoms are a good basis from which to carry out more substantial KMC simulations in order to try to reproduce the experimental core shell structures around voids.

Summary of Simulations

In part III of this study, interstitial defects were implemented into the SPPARKS code and a new broken-bond MC model for the study of radiation induced effects in W-Re-Os is presented. Our study of W-Re using a previously developed energy model for W-Re highlighted the importance of the W-Re mixed interstitial dumbbell for the precipitation of Re in W and supported the findings of previous studies. However, no homogeneous precipitation of Re due to mixed interstitial immobilisation was observed. SGMC simulations for the W-Re and W-Os binary systems both showed phase transitions at 50at.%, with a second transition to 75at.%Os observed in the case of W-Os. This model therefore suggests that a coherent metastable Re bcc phase may also be present in addition to the incoherent σ phase at 50at.%Re.

Pre-alloying with Re was shown to have limited effect on point defect trapping, and therefore Re cluster growth. More studies are required to investigate the impact of Os on this process, as Os binds more strongly to point defects and trapping is likely to be more effective. The Re pre-alloying simulation suggests that differences between the ion and neutron irradiated samples discussed in section 4.5, are likely caused by either the different dose rates, by differences in the ballistic effects between ions and neutrons, or by a combination of these effects.

To investigate the void decoration observed in chapter 3, a new energy model for W-Re-Os including both Vacancy and Interstitial type point defects was developed. A novel approach to parameterising the defect-atom interactions was used, based on the fitting of the enthalpy of mixing data from binary atom-vacancy systems calculated using DFT. Both void nucleation and growth was simulated which was not possible with the previous energy model. Decoration of these voids with both Re and Os was observed, supporting our experimental findings from chapter 3 and suggesting that voids may act as nucleation sites for precipitates in W, with mixed interstitials providing fast transport of Re and Os to those site.

Part III: Epilogue

8 Conclusions

In this thesis, a combination of experimental and computational techniques were used to investigate the radiation damage and transmutation induced precipitation of Re and Os in W. Precipitation of both Re and Os, and void formation was observed under neutron and heavy-ion irradiation, and was simulated using a new energy model for the W-Re-Os system containing both vacancy and interstitial type defects. This has provided valuable insight into how W components in a fusion reactor will undergo microstructural changes due to transmutation and radiation damage.

8.1 Tungsten and Nuclear Fusion

Nuclear fusion is a novel technology that addresses some of the problems with nuclear fission including the absence of a chain reaction and reduced long-lived nuclear waste production. As a means of combating climate change in the short-term, nuclear fusion appears to offer limited effectiveness due to its low technological readiness level, the scale of outstanding engineering challenges to its deployment and the urgency of decarbonisation. Fusion therefore offers a long-term solution but its place within a changing energy market is uncertain - with a move away from the base load supply model and an increase in renewable capacity in post-industrial economies.

Tungsten is the current leading candidate material for many of the PFCs. Despite ongoing interest in fusion, and the critical role of plasma facing materials, there is a lack of understanding of neutron irradiation effects in W - particularly at reactor relevant doses and transmutation rates. Complete validation of the material therefore requires a source of fusion spectrum neutrons to properly test component performance as the microstructure produced in neutron irradiation experiments appear to be highly sensitive to the neutron energy spectrum.

8.2 Effect of Neutron Irradiation on W

Single and polycrystalline W samples, neutron irradiated to 1.67dpa at 900 °C at HFR, were characterised using a combination of APT and STEM-EDX. The irradiation temperature is closer to a DEMO operating temperature than studied previously, and crucially the samples have a post-irradiation composition closer to the predicted DEMO level, leading to a more representative microstructure than in previous irradiations.

Analysis of the mass spectra produced during APT showed that transmutation had produced a composition of 1.263 ± 0.150 at.%Re, 0.083 ± 0.017 at.%Os and 0.009 ± 0.004 at.%Ta in the single crystal sample; and 1.090 ± 0.067 at.%Re, 0.080 ± 0.016 at.%Os and 0.009 ± 0.004 at.%Ta in the polycrystalline sample. The primary Re isotope was ^{187}Re, at 90.67 ± 0.718 at.% compared to 62.20% in its natural form. For Os, the primary signal came from ^{188}Os, at 92.24 ± 0.862% of the detected Os compared to

13.29% in its natural state. Comparison with FISPACT-II inventory modelling and EDX measurements were in agreement with the compositional measurements from APT. Comparison of the isotopic abundances between FISPACT-II and APT results clearly demonstrated that FISPACT-II is a very reliable way of quantifying transmutation in neutron irradiated W. This highlights that APT provides a method of analysing small samples with low activities, that can be used to validate specific FISPACT calculations.

APT and STEM of the neutron irradiated material measured the formation of Re and Os decorated voids, and isolated Re and Os rich precipitates. A single loop decorated primarily with Os was observed using APT. APT gave some indication of void formation, with high atomic density artefacts correlated with Re and Os rich regions in the data, likely being produced by trajectory aberrations at the periphery of the void during analysis. This study highlights the importance of using complementary techniques for nuclear materials in which void or bubble formation is expected, due to the demonstrated potential for atomic density artefacts to be introduced.

The majority of the clusters found in the APT data were found to contain a central core of Os and Re, surrounded by a shell of Re. Standard cluster analysis techniques using a maximum separation algorithm showed a range of compositions up to a maximum of around 20at.%Re and 5at.%Os, with a similar average cluster compositions to previous studies using low transmutation rate irradiations: 7.32 ± 4.42Re-0.36 ± 0.50Os for the single crystal and 6.81 ± 3.38Re-0.64 ± 0.44Os for the polycrystalline. Line profile

analysis of some of the clusters found that in the central region of some of the clusters, the concentration was as high as 50at.%Re and 5-10at.%Os, consistent with concentration of σ phase. The new model for W-Re-Os indicates that both a coherent metastable bcc phase and incoherent σ phase may be present at 50at.%Re, thus explaining the mixture of spherical and elongated precipitates observed using APT, following neutron irradiation. The strong clustering at low transmutation levels indicates that transmutation may cause problems during the early stages of component service in a reactor, not just after high doses.

8.3 Simulated Neutron Irradiation with Ions

Ion irradiated alloys of W-Re-Os were characterised and compared with the neutron irradiated material. Irradiation at 1173K was carried out at SNL, representing a higher temperature irradiation than carried out previously in W-Re-Os, and was more representative of fusion operating conditions. The microstructure following ion irradiation was very different from the neutron irradiated samples. Small clusters of Os were seen with limited Re segregation. Small voids were observed for the first time in alloys of W-Re-Os under ion irradiation.

Simulations of neutron and ion irradiation in chapter 7 showed that point defect trapping due to the presence of pre-alloyed solute atoms has no major effect on the growth of Re rich clusters. Differences between the ion and neutron irradiated material is therefore caused either by differences in

the dose rate between experiments, or by difference in the ballistic effects of ions vs neutrons. Cluster analysis using maximum separation techniques showed that the clusters were higher in Os than Re, with an average concentrations of 2.32 ± 0.72Re and 9.28 ± 1.52Os. The results from chapter 4, combined with the computational study in chapter 6, indicate that Os clustering occurs first due to the stronger binding with point defects. This could occur at point defect sinks such as voids. As the Os is depleted in the bulk, Re transport starts to be favoured as Re also binds strongly to vacancies and mixed interstitials. This results in the core shell structure seen in chapter 3. Transmutation of the Re at the cluster could also contribute to this effect.

8.4 Computational Modelling of Tungsten

In this work a broken bond model was used to carry out MC simulations in W-Re, and W-Re-Os with vacancy, self-interstitial and mixed interstitial dumbbells. In chapter 6 a new energy model for W-Re-Os-Vac-Interstitials was developed, extending concentration dependent interactions to include all solvent-solute atom interactions as well as all atom-vacancy interactions. With this model it was possible to correct the underestimation of vacancy interactions in previous models and simulate both void nucleation and growth. Decoration of voids with Re and Os was observed and also highlighted the importance of studying low Os concentration samples, due to the strong tendency of Os to segregate. This model provides the basis for further

study of the W-Re-Os system, and could be used to address some of the outstanding questions raised in this thesis.

8.5 Future Work

The experimental work discussed in chapters 3 and 4 highlight the importance of studying fusion relevant compositions on the resultant nanostructure. In particular more sample with low Os concentrations are needed, which may be possible through canister design. Further systematic study of reactor relevant compositions of W-Re-Os-Ta is needed to understand the effects of transmutation.

I recommend that more ion irradiation experiments be carried out at lower doses and high temperatures to further compare to neutron irradiation. It is possible that void growth could be accelerated by using a higher irradiation temperature. I also recommend more ion irradiation experiments of a range of W-Re-Os-Ta compositions to systematically study the effects of these elements. In particular, the Ta containing alloys produced in this study should be investigated to understand whether small quantities of Ta may offset the negative impacts of Re and Os. To further improve the use of heavy-ions as a surrogate for neutron irradiation, the suitability of using a temperature shift during ion irradiation to promote void and precipitate growth should be investigated.

More work is needed to fully understand the impact of voids on APT data. Correlative TEM/APT can be used to show the exact positions of the

voids and precipitates prior to APT. Comparing this data before and after APT will confirm which features are voids and which are precipitates. This could also be combined with diffraction pattern analysis to show whether σ phase has formed in the cluster centres. Void size likely plays an impact and these findings could be compared directly with recently developed electrostatic simulations which can be used to plot void size against the resultant increase in the atomic density after data reconstruction. Experimental data on void sizes and the magnitude of the resulting atomic density artefact could be used to benchmark these simulations.

More work is needed to develop the energy model discussed in chapter 6 in order to improve the fitting of the enthalpies of mixing and reduce the solute-vacancy binding energies, which at present are overestimated. To provide more effective comparison to experimental data, longer time simulations are required. If possible, improvements to the current model to make it less computationally expensive should be made.

KMC simulations using the new energy model should be carried out to investigate Re and Os transport to voids. This could be used to compare with the experimental data on void decoration to provide additional validation to the model. Metropolis simulations containing a GB could be used to investigate the void denuded zone observed in the polycrystalline neutron irradiated sample. It was suggested that this was due to the attractive binding between vacancies and Re, and the decoration of the GB with these elements. This hypothesis could be tested using the new energy model.

List of Figures

1.1 Neutron induced fission, and neutron absorption reaction cross sections for (a)^{235}U and (b)^{186}W targets respectively as a function of incident neutron energy. Plotted using data obtained from the Nuclear Energy Agency, Java-based Nuclear Data Information System (JANIS) [13]. Data plotted is taken from the Evaluated Nuclear Data File (ENDF) version B-V111.0 [14]. 16

1.2 Fusion cross section in barns for various fuels as a function of incident deuteron energy. Plotted using data obtained from the Nuclear Energy Agency, Java-based Nuclear Data Information System (JANIS) [13]. Data plotted is taken from the Evaluated Nuclear Data File (ENDF) version B-V1.8 [14]. 20

1.3 Photograph of the inside of the JET reactor, showing the position of the Beryllium first wall and W divertor, adapted from image obtained from [26]. 22

1.4 First wall neutron energy spectrum in a concept fusion power station vs a typical Pressurised Water Reactor (PWR) energy spectrum shown on both (a) a log-log scale and (b) with a standard x-axis scale [34]. 25

1.5 Schematic diagram of a damage cascade [35]. 26

1.6 Schematic diagram showing the difference in dose/depth profiles for neutron, heavy-ion and proton irradiation. The approximate dose profile from a neutron irradiation is plotted in red and indicates that on average, the long mean free path of neutrons in the material means that there is no variation in the dose as a function of depth. 27

1.7 Periodic table presented by Gilbert et. al, showing the total activity in Bq for each element in the periodic table following a 2 full-power year neutron irradiation with a DEMO FW neutron spectrum, and following 10 years of cooling [47]. . . 31

1.8 Level of activity in mSv from common elements found in steels, irradiated for 5 years in a 3.6 GW fusion power reactor, plotted as a function of time after removal from the reactor. Black line represents ITER administrative limit for hands on maintenance [48]. 32

2.1 Transmutation of a W FW component during a 5-year irradiation under DEMO fusion power-plant conditions assuming a spatially homogenous reactor structure and neutron flux [18, 19]. 43

2.2 Transmutation of initially pure W under a DEMO neutron spectrum for 5 full-power years showing the production of Re, Os and Ta through β decay as well as He and H production [18–20]. . . . 44
2.3 Comparison between transmutation rates in different fission irradiation experiments compared to the predicted transmutation level in a DEMO reactor after 1 and 2 years full-power irradiation at a dose rate of 5dpa/year [18]. . . . 47
2.4 Computationally derived equilibrium W-Re phase diagram adapted from [94]. . . . 50
2.5 Equilibrium phase diagrams for binary W-Re, W-Os and W-Ta alloy systems. Adapted from the imaged reproduced in [84] and originally sourced from [95, 96]. . . . 51
2.6 Ternary equilibrium phase diagram at 1873 K for the W-Re-Os system, showing partial phase region in which experimental data is available. Adapted from the images reproduced in [84] and originally sourced from [95]. . . . 53
2.7 Ternary equilibrium phase diagram at 1473 K for the W-Re-Ta system. Adapted from the images reproduced in [84] and originally sourced from [95]. The χ and σ phase regions are shown in black. . . . 53
2.8 Vickers hardness measured at room temperature for W-Re as a function of Re concentration [99]. . . . 56
2.9 DBTT measured using 3-point bend testing in pure-W, W-26Re and W-24Re as a function of recrystallised grain size [99]. . . . 56
2.10 Schematic illustration of observed microstructural evolution under neutron irradiation, showing the effects of dose and Re concentration. Reproduced from [90]. . . . 59
2.11 TEM image of polycrystalline W neutron irradiated at HFR to 1.67dpa at 1173 K showing voids and grain boundaries, reproduced from [91]. . . . 60
2.12 TEM images of single crystal W neutron irradiated at HFR to 1.67dpa at 1173 K showing (a) HAADF image of voids alongside EDX mapping of (b) W (c) Re and (d) Os, reproduced from [91]. . . . 60
2.13 TEM imaging of voids, precipitates and grain boundaries in initially pure W sample, neutron irradiated at HFIR to 1.5dpa at 1073 K. The HAADF image with the location of the voids and grain boundary highlighted, and with the corresponding EDX maps for W, Re and Os. Reproduced from [116]. . . . 61

2.14 Comparison between (i) Re atomic mapping from APT with (ii) Re isoconcentration surfaces and (iii) a TEM image of a different region of each sample. Shown in (a) is the data for initially pure W and (b) is the initially W-10Re alloy, both irradiated at Joyo to 0.96dpa at 811 K. Reproduced from [114]. 63
2.15 10 FIM images from a sequence of 18 images taken through a controlled evaporation of a void in neutron irradiated Mo, adapted from [124]. Panel 18 shows the perfect crystal structure in the underlying material beneath the void. Position of the void highlighted with blue circle. 66
2.16 STEM HAADF and reconstructed APT data at various rotations. In the APT data, high density regions are highlighted using isodensity contour surfaces at 50 atoms/nm^3. 67
2.17 4 nm slice through atom map of 6 samples, 3 irradiated at 573 K and 3 at 773 K. On the left most side in figures (a) and (b) are the W-2Re sample irradiated at 573 K and at 773 K respectively. (c) and (d) show the W-2Re-1Ta sample irradiated at 573 K and at 773 K respectively and (e) and (f) are the W-1Re-1Os sample irradiated at 573 K and at 773 K respectively. All are irradiated to a peak dose of 33 dpa calculated using the full-cascade model ($\approx$ 18 dpa under quick cascade mode). 71
2.18 1 Directional migration of a W-W interstitial dumbbell along the $< 111 >$ direction. Reproduced from [140]. 73
2.19 Migration of a mixed W-Re interstitial dumbbell via translation and migration. Reproduced from [140]. Mixed dumbbell migrates along $< 111 >$ direction and rotates to $< 1\bar{1}1 >$ direction. Following this process the dumbbell effectively migrates along the $< 100 >$ directions. 75
2.20 Comparison between irradiation induced hardening as a function of the (a) and (b) total solute concentration; (c) and (d) the total dose in dpa, and (e) and (f) the irradiation temperature. Solute concentration is Re + Os either from transmutation, pre-alloying or a combination of both. The marker size in both (a) and (b) is a measure of the dose, and otherwise a measure of the total solute concentration. 82
2.21 Hardening produced in initially pure W, neutron irradiated at JOYO, HFR and HFIR to doses of between 0.7 and 3dpa, at temperatures of between 1000 and 1200 K, plotted as a function of the rate of solute (Re + Os) production, per dpa in units of at.%/dpa. 86
2.22 Thermal resistivity (1/thermal conductivity) as a function of total amount of solute produced from transmutation in different reactors and irradiations. Reproduced from [89]. . . 89

2.23 Thermal diffusivity of W-Re alloys with open symbols showing the transient grating measurements taken by Hofmann et. al [165]. 89

3.1 Local neutron energy spectrum received by samples, overlaid over the averaged spectrum for the HFR reactor. 96
3.2 SEM images taken with the TLD detector during the lift-out of the polycrystalline neutron irradiated sample. 98
3.3 Averaged mass spectrum for (top) single crystal and (bottom) polycrystalline samples taken using APT. 103
3.4 Summary of (left) over and (right) under ranging strategy used to estimate the uncertainty due to varying peak identification between different operators. 104
3.5 Portions of the mass spectra between 58 and 65Da, showing the 3+ charge state ions taken from (a) neutron irradiated (b)W-1.4Re Saclay ion irradiated (c) W-1.4Re-0.1Os SNL ion irradiated and (d) W-1Re-1Os SIBC ion irradiated samples. 106
3.6 Summary of the 6 reconstructed APT data sets, taken from the single crystal neutron irradiated sample. W atoms are plotted in blue, with between 5 and 20% of atoms shown for visual clarity. Re isoconcentration surfaces at 5at.%Re are shown in red to highlight the positions of the precipitates. 100% of Os atoms are plotted in green but are not strongly visible because they are located primarily within the Re clusters. Each atom map shows a different sample analysed using APT. 111
3.7 Summary of the 6 reconstructed samples shown in figure 3.6 with all of the W atoms removed, and 100% of Re atoms plotted as red spheres of diameter 0.1 nm. Os isoconcentration surfaces at 1.5at.%Os are shown in green and highlight the position of the Os within the Re rich clusters. Each atom map shows a different sample analysed using APT. 112
3.8 Summary of the 5 reconstructed APT data sets taken from the polycrystalline neutron irradiated sample. W atoms are plotted in blue, with between 5 and 20% of atoms shown for visual clarity. Re isoconcentration surfaces at 5at.%Re are shown in red to highlight the positions of the precipitates. 100% of Os atoms are plotted in green but are not strongly visible because they are located primarily within the Re clusters. Each atom map shows a different sample analysed using APT. 113

3.9 Summary of the 5 reconstructed samples shown in figure 3.8 with all of the W atoms removed, and 100% of Re atoms plotted as red spheres of diameter 0.1 nm. Os isoconcentration surfaces at 1.5at.%Os are shown in green and highlight the position of the Os within the Re rich clusters. Each atom map shows a different sample analysed using APT. 114
3.10 APT reconstruction of single crystal neutron irradiated sample. (a) For visual clarity, only 1.3% of total detected W ions are shown in blue, all detected Re and Os ions are shown in red and green respectively. Red surfaces represent Re isoconcentration surfaces plotted at 5at.%Re. (b) Higher magnification of the region of interest showing Re isoconcentration surfaces at 5at.%Re and individual Os atoms as green squares. (c) Region of interest showing transparent Re isoconcentration surfaces and green Os isoconcentration surfaces at 1.5at.%Os.The positions of the Re and Os atoms are shown separately in (d) and (e) respectively. 115
3.11 APT reconstruction of polycrystalline neutron irradiated sample. (a) For visual clarity, 11% of total detected W ions are shown in blue, all detected Re and Os ions are shown in red and green respectively. Red surfaces represent Re isoconcentration surfaces plotted at 5at.%Re. (b) Higher magnification of the region of interest showing Re isoconcentration surfaces at 5at.%Re and individual Os atoms as green squares. (c) Region of interest showing transparent Re isoconcentration surfaces and green Os isoconcentration surfaces at 1.5at.%Os.The positions of the Re and Os atoms are shown separately in (d) and (e) respectively. 116
3.12 Cluster compositions in neutron irradiated single and polycrystalline W samples from HFR, plotted on the equilibrium ternary W-Re-Os phase diagram at 1873 K, with average cluster compositions from experiments at HFIR and Joyo [114, 199]. 118
3.13 High magnification image of the Re and Os atoms in the precipitate analysed in figure 3.14, plotted as spheres of radius 0.05nm. 100% of Re and Os atoms are shown respectively with all other atoms hidden for visual clarity. The boundary of the cluster was defined using a 5at.%Re isoconcentration surface. 119

3.14 Line profile taken through rod-shaped cluster in APT data, centred on a 25at.%Re isoconcentration surface. Cylindrical ROI of dimensions 1.64 nm radius, 15 nm long, binned into 152 bins along the z-direction of width 0.1 nm in IVAS, rebinned into 20 bins using Python. Errors plotted are both counting error from IVAS and the standard deviation on each bin. Inset image shows the ROI centred on the cluster core. An isoconcentration surface at 5at.%Re is shown with Os atoms plotted as green squares to highlight the central rod shape. . 120
3.15 Reconstruction of sample taken from polycrystalline neutron irradiated sample showing the decoration of the central GB with solute Re, Os and Fe atoms. 122
3.16 Line profile of concentration taken in the z-direction along a cylindrical ROI across the grain boundary showing enriched Re, Os and Fe concentration. 123
3.17 Line profile of concentration taken in the z-direction along a cylindrical ROI along the direction of the grain boundary, showing variation in the Re, Fe and Fe concentration. 123
3.18 Segregation of Re and Os transmutation products to a line dislocation in W-1.4Re-0.1Os irradiated to 1.67dpa at 1173K, measured using APT. Shown in (a) is the full data set with Re atoms plotted in red and Os atoms in green, with (b) a higher magnification section of the sample with the line dislocation highlighted with a 0.5at.%Os isoconcentration surface. Plotted in (b) are the ROIs used to analyse the segregation of Re and Os to the dislocation. The plots shown in (c) and (d) show the line profile concentrations from the ROIs shown in (b) for the transverse and in-line directions respectively. In (c) and (d), the circular red points represent Re and the square green points represent Os. The error bar is given by the standard error, $\sigma_{\bar{x}}$ for each of the bins, calculated using $\sigma_{\bar{x}} = \sigma/\sqrt{N}$ where N is the number of points in each bin, and σ is the standard deviation of the bin concentration. . . 126
3.19 Segregation of Re and Os transmutation products to a dislocation loop in W-1.4Re-0.1Os irradiated to 1.67dpa at 1173K, measured using APT, showing 8% of W atoms for visual clarity in addition to (a) Re atoms and (b) Os atoms. 127
3.20 Higher magnification image of the loop shown in figure 3.19, obtained by extracting a volume defined by a Re isoconcentration surface, showing two different orientations which are rotated 90° with respect to one another, with all W atoms removed. The Os atoms are plotted as larger spheres compared to the Re atoms. 127
3.21 SEM image of tip number M-21 imaged using both secondary electron and in lens detectors showing the presence of a small region of contrast corresponding to a void. 128

3.22 5nm cross section of the atom map shown in figure 3.10. (a) Density contour in number of atoms per cubic nm (b) Re concentration contour (c) Os concentration contour. Arrow indicates central precipitate with Os rich zone offset from higher density region. 129
3.23 EELS thickness measurement across a suspected void in STEM image (right), showing the drop in thickness in the darker region. 131
3.24 (a) High magnification HAADF image of a void in the single crystal neutron irradiated sample with (b) corresponding Fast-Fourier Transform (FFT) image showing the orientation of the void facets, which are aligned along the (110) directions. 132
3.25 Low magnification STEM-HAADF images of voids and precipitates in single crystal neutron irradiated sample. Raw images from two sites are shown in (a) and (b) and after background subtraction in ImageJ in (c) and (d). Voids are shown as regions of dark contrast. Voids are highlighted in (b) and (c) in red using a contrast threshold. 133
3.26 (a) Lower magnification and (b) high magnification High Angle Annular Dark Field (HAADF) images of voids in neutron irradiated single crystal W. EDX Maps of (c) W (d) Re and (e) Os showing the decoration of the central void. 134
3.27 (a) Low and (b) high magnification STEM-HAADF images of voids and (c) voids and precipitates in the polycrystalline neutron irradiated sample, with corresponding EDX maps of W, Re and Os. 135
3.28 Low magnification HAADF images of the neutron irradiated polycrystalline sample, showing voids as dark regions and grain boundaries as bright lines. Inset is a higher magnification image of a region containing a GB showing the void denuded zone and maximum void size region. 137
3.29 High magnification HAADF images of the neutron irradiated polycrystalline sample, showing voids as dark regions and grain boundaries highlighted in red. 138
3.30 Spatial distribution of voids near to the GB, showing (a) a graphical representation of voids as black spheres of area corresponding to the area obtained by contrast thresholding of the original image and the grain boundary highlighted in blue. Shown in (b) is the binned void size in nm^2 as a function of distance from the GB. 139
3.31 HAADF image of GB with adjacent voids with corresponding EDX maps of W, Re and Os respectively showing GB decoration with Re and Os. 139

3.32 Under and over focus conditions used to confirm the presence of voids. Images shown for one rotation condition at ±1000 µm from the in focus condition. Arrow shows presence of one void to illustrate the change from bright to dark contrast. 140

4.1 Simulated solute concentrations as a function of irradiation time for pure W tiles under a DEMO first wall neutron spectrum. Points show the transmutation concentrations at which pre-alloyed samples were made. 145
4.2 Ion irradiated sample from SNL showing (a) an enhanced contrast photograph showing the darker contrast from the central irradiated region and (b) a schematic illustration of the irradiated area shown in (a). The dashed line on (a) highlights the boundary between dark and light contrast on the sample surface, marking the boundary between irradiated and unirradiated material. 149
4.3 Thermal history of the sample during irradiation at SNL. . . 150
4.4 Dose as a function of depth into the sample surface estimated for the different self-ion irradiations conducted as part of this study and in previous work, estimated using SRIM with 3 displacement threshold energies: $E_d = 55$eV,$E_d = 68$eV and $E_d = 90$eV. 152
4.5 APT atom map of W-25Re ion implanted to 18 dpa at 773 K, showing 60% of Re atoms as red spheres of radius 0.1 nm. . . 157
4.6 Re-binned line profile taken along the direction of a rod shaped precipitate in the 18 dpa ion irradiated W-25Re sample. Cylindrical ROI of diameter 1.85 nm, length 26 nm, initially split into 262 bins of width 0.1 nm. Rebinned into 20 concentration bins. 159
4.7 Re and Os atom maps, showing 100% of Os atoms, and ≈10% of Re atoms, rendered as spheres of radius 0.22 nm, taken from a sample ion implanted by Xu et. al [134] to a peak dose of 18 dpa, at 773 K at the Surrey Ion Beam Centre. The sample surface is located on the left of the image and the underlying unirradiated material is on the right side of image. 160
4.8 Re and Os atom maps, showing 100% of Os atoms, and 100% of Re atoms, rendered as spheres of radius 0.22 nm, taken from a 5 nm slice through the centre of samples ion implanted by Xu et. al [134] and as part of this study to different irradiation conditions to illustrate the position of Re atoms with respect to Os clusters. 160

4.9 Re and Os atom maps, showing 100% of Os atoms, and 50% of Re atoms for 2 samples taken from the W-1.4Re-0.1Os sample irradiated at SNL, one from the unimplanted edge of the sample and one from the centre which received a peak dose of 1.7dpa. 161
4.10 APT reconstruction of W-1.4Re sample ion irradiated to 1.67dpa at 1073K. Re atoms shown in Red, all other atoms hidden. Grain boundary visible decorated with Re surrounded by a region depleted in Re compared to the bulk. An increase in the W signal also highlights the GB and is a result of artefacts from the APT process. 163
4.11 Re concentration across GB in Saclay ion implanted W-1.4Re sample. 164
4.12 SEM images showing the surface topography of ion implanted sample annealed for 12 hours under an Argon atmosphere. . 165
4.13 Comparison of ion irradiated W-1.4Re sample from Saclay (bottom) before and (top) after annealing at 1273 K for 24 hours. 167
4.14 Stitched STEM image of voids in the ion implanted W-1.4Re-0.1Os sample from SNL. The bottom right of the image is located approximately 300nm from the original sample surface. The top left of the image is the underlying unirradiated material. 168
4.15 Comparison between voids observed under ion and neutron irradiation showing voids in (left) the ion implanted W-1.4Re-0.1Os sample and (right) the polycrystalline neutron irradiated material. 168
4.16 Re and Os atom maps from APT reconstructions of samples taken from (a) Saclay irradiated W-1.4Re (b) near surface region of SNL irradiated W-1.4Re-0.1Os (c)subsurface region of SNL irradiated W-1.4Re-0.1Os and (d) the single crystal neutron irradiated sample from HFR. The tip shown in (b) starts from just below the original sample surface below the protective layer, but (c) had more material removed. The exact amount of material removed is not accurate but is between 200 and 500 nm. 174
4.17 Re isoconcentration surface analysis for single crystal neutron irradiated sample and ion irradiated W-1.4Re Saclay sample. 175

4.18 Comparison of cluster concentration determined using the maximum separation algorithm, in ion and neutron irradiated W and W-(Re/Os). Overlaid is a section of the W-Re-Os ternary equilibrium phase diagram at a 1873 K isotherm, between 0 and 30at.% solute. Shown in black is the region of solute concentration within which σ phase is predicted to form. Hollow markers represent the average cluster compositions obtained by Hwang et. al and Edmondson et. al [114, 202] using APT, from neutron irradiated samples from HFIR and Joyo. 179
4.19 Re to Os ratio for clusters in ion and neutron irradiated W. The red points represent the W-1Re-1Os samples ion irradiated to 18 dpa by Xu et. al [134]. The black points represent clusters in the SNL ion irradiated W-1.4Re-0.1Os sample, irradiated to 1.70dpa. The blue points represent clusters in the neutron irradiated single and polycrystalline samples which have a post-irradiation composition of W-1.2Re-0.1Os, and a damage level of 1.67dpa. 180

5.1 Schematic diagram showing time and length scales associated with (a) radiation induced phenomena and (b) multiscale materials modelling techniques, adapted from [203]. 189
5.2 Event selection in KMC, adapted from [147, 148]. 191

6.1 Enthalpy of mixing data from DFT calculations for the (a) W-Re (b) W-Os and (c) Re-Os binary systems, showing the convex hull and fitted polynomial function. Each hollow data point refers to a DFT calculation of a specific configuration of atoms. 213
6.2 Enthalpy of mixing data from DFT calculations for the (a) W-Vacancy, (b) Re-Vacancy and (c) Os-Vacancy binary systems constrained to a bcc lattice, showing the convex hull and fitted polynomial function. Each hollow data point refers to a DFT calculation of a specific configuration of atoms and vacancies. 214
6.3 Enthalpy of mixing, ΔH_{mix}, of the ternary W-Re-Os system, described by equation 6.22 as a function of Re, Os and W concentration. Overlaid in black are the enthalpy of mixing points for various concentrations. The opacity of the DFT points is a function of the number of configurations at that concentration point. 218
6.4 Comparison of binding energies of different vacancy clusters up to 15 vacancies calculated with new pair interaction model. Configurations taken from [138, 139] and a comparison of the formation energy of a 4 vacancy cluster as a function of box size. 222

6.5 Cluster binding energies for a single vacancy surrounded with Re and Os solute calculated using the new W-Re-Os-Vac energy model. 223
6.6 Vacancy solute cluster binding energies, calculated using new W-Re-Os energy parameterisation. Labels indicate the composition of the each cluster, with each point on the x-axis representing a different cluster composition. The first axis segment is comprised of vacancy clusters only. The second and third are vacancy-Re and vacancy-Os clusters respectively and the final axis segment is for mixed clusters of vacancy-Re-Os. The colour represents the number of vacancies in a cluster, as shown in the legend. The black points represent DFT data provided by Messina [145]. 225
6.7 Plot of chemical potential for Re atom exchange with solute reservoir as a function of Re concentration, calculated for the W-Re-Os energy parameterisation using the method outlined in section 5.4.2. 227
6.8 Plot of chemical potential for Os atom exchange with solute reservoir as a function of Os concentration, calculated for the W-Re-Os energy parameterisation using the method outlined in section 5.4.2. 227
6.9 Low vacancy concentration section of the W-Vacancy phase diagram predicted by new parameterisation. 230
6.10 Low vacancy concentration section of the W-Vacancy phase diagram predicted by new parameterisation, plotted on a log scale of vacancy concentration. 230
6.11 Void nucleation under new energy parameterisation, in a 64x64x64 W atom box, simulated using a metropolis algorithm (see section 5.4.1), with number of MC steps and vacancy concentration highlighted. Individual vacancies are shown in blue and are introduced with a dose rate of 1×10^{-2} per MC step. 232

7.1 Plot of equilibrated solute concentration in % as a function of the change in chemical potential $\Delta\mu$ for a range of temperatures. 236
7.2 Equilibriated configurations of W-Re-Vacancy and W-Re-Interstitial for a fixed starting defect concentration and change in chemical potential, $\Delta\mu$. 237
7.3 Vacancy diffusivity, D_v, as a function of temperature and Re concentration. Dashed line shows the Arrhenius relationship described by equation 7.1. 241

7.4 Solute and self-diffusivity, D_s, as a function of temperature and Re concentration. Dashed line shows the Arrhenius relationship described by equation 7.1 using an activation energy of 4.79eV. The black points represent experimental values for the self-diffusion of W in W taken from [212]. 242
7.5 Precipitation of Re around a point sink at 10 and 100s of irradiation in a W-2at.%Re alloy. A dose rate of 1×10^{-3} dpa/s was used at an irradiation temperature of 1800K which ensures that vacancies are mobile within our simulation. 244
7.6 Re concentration as a function of radius from an ideal point sink, in a W-2%Re alloy irradiated with a dose rate of 1×10^{-3} dpa/s and an irradiation temperature of 1800K. 245
7.7 Growth of cluster in terms of the number of atoms in the cluster as a function of irradiation time for the simulation shown in figure 7.5. 245
7.8 Segregation of Re in a 1.4at.%Re alloy to a planar ideal sink at 1800K after a total dose of 5.96×10^{-3}dpa with a dose rate of 1.19×10^{-3}dpa/s. 249
7.9 (top) Segregation of Re in a W-1.4at.%Re alloy to a planar ideal sink at 1800K after a total dose of 5.96×10^{-3}dpa with a dose rate of 1.19×10^{-3}dpa/s. (bottom) Segregation on GB in a W-1.4at.%Re alloy, observed experimentally using APT - as shown in figure 4.11. 250
7.10 Comparison before and after KMC for two samples containing pre-alloyed W-1.4Re and one in which W-1.4Re was introduced continuously with a fixed transmutation rate. All atoms are hidden apart from those contained within the largest cluster in the simulation cell which forms around an ideal sink shown in black. 251
7.11 Plot of maximum precipitate size in transmuted and pre-alloyed simulations, in terms of the total number of Re atoms contained within the cluster, defined by the cluster search function in Ovito using a cutoff distance of 5.5 Å. 252
7.12 Metropolis simulations at 1000K and 1800K, shown at 3×10^7 MC steps with vacancies shown in blue. Simulations were carried out using an initial vacancy concentration $C_V^i = 0.1$at.% and using a vacancy insertion rate corresponding to a final vacancy concentration of 0.1at.%. 254
7.13 Metropolis simulations with a vacancy concentration of 0.1 and 0.5at.% at 1800K. (a) and (b) show simulations carried out with an initial vacancy concentration of 0.1 and 0.5 at.% at respectively, whereas in (c) and (d), vacancies were inserted at a rate that resulted in a final vacancy concentration of 0.1 and 0.5 at.% at 3×10^7 MC steps respectively. 255

7.14 Canonical simulations for a W box containing 0.5at.%vacancies, evolved with metropolis to form voids as shown in (a). Canonical simulations were carried out for (b) W-1.4Re (c) W-1.4Os and (d) W-1.4Re-0.1Os, randomly distributed through the initial simulation cell shown in (a) at a temperature of 1800K. 257
7.15 Canonical simulations for W box containing 0.5at.%vacancies, evolved with metropolis to form voids with (a) 1.4at.%Os and (b) 1.4at.%Re, as shown in figure 7.14 (c) and (b) respectively. A slice taken through the centre of one of the voids is shown, highlighting that solute atoms have not migrated into the centre of the vacancy cluster, as is shown in figure 7.2.258
7.16 Proportion of solute atoms contained within clusters defined by a cutoff distance of 5.5 Å, in simulation cells with 1.4at.% Re and Os, after 5×10^7 MC steps, as shown in figure 7.14(b) and (c). 259
7.17 Proportion of solute atoms contained within clusters defined by a cutoff distance of 5.5 Å, in simulation cells with 1.4at.% Re - 0.1at.% Os, after 5×10^7 MC steps, as shown in figure 7.14 (d). 259

List of Tables

1.1 Predicted operating conditions for the first wall and divertor of a demonstration fusion reactor. Units of full-power years are used to describe operational lifetimes, and refer to years of continued exposure to neutron loading at temperature without maintenance. Peak loading and operating temperature refers to the expected conditions under a disruption lasting a short period of time. The operating temperature of PFCs are subject to variation because of many outstanding design choices. The operating temperature of the components will also depend on the type of coolant used, for example He or water. 23

2.1 Natural abundances of W isotopes [18]. 41
2.2 Natural abundances of Re, Os and Ta isotopes [18]. 48

3.1 Comparison between the calculated distribution of isotopes and the measured distribution from APT produced by transmutation from 208 day neutron irradiation at HFR and 6 years of cooling, as a percentage of the total number of atoms in the simulation and the total number of ranged ions in APT. The 11 most commonly occurring isotopes from the simulation are included, isotopes with lower concentration could not be separated from background using APT. Uncertainty on the concentration from APT is estimated by comparing different ranging approaches, background-to-background and at FWHM. 108

3.2 Bulk sample solute concentration from transmutation measured using APT. Uncertainty quantified using under and over ranging approach. Compared to FISPACT-II results [88] and EDX measurements [66]. 108

3.3 Average cluster compositions in the single crystal and polycrystalline neutron irradiated samples, measured using a maximum separation algorithm. The average compositions measured in the sample from JOYO and HFIR were also calculated on APT data using a maximum separation algorithm, details of which are given in [114]. The samples irradiated at JOYO and HFIR are polycrystalline pure-W and pre-alloyed W-10at.%Re [199]. The standard deviation of the Re and Os concentration around the average, σ_x, for the concentration of x is also given. 117

4.1 List of samples used in this study. Samples irradiated at SNL are indicated by a * symbol. Samples irradiated at Saclay by R. Abernethy are indicated by a † [109]. Samples marked with a ' were made in reference to [134]. 146
4.2 Comparison of doses in dpa measured at the Bragg peak in the W-1.4Re-0.1Os sample irradiated at SNL using 3 different displacement threshold energies. 152
4.3 Summary of irradiation conditions used in this study. Dose for ion implanted samples taken at the Bragg peak. For the SIBC and Saclay samples, the dose is taken at the Bragg peak simulated using an E_d of 68eV, whereas for the neutron irradiated sample and the SNL ion irradiation, the Bragg peak dose is taken from the simulation using E_d=55eV. Sample composition for the neutron irradiated samples is the predicted post-irradiation composition predicted by FISPACT-II and measured experimentally in this study using APT. Approximate irradiation times for SIBC irradiation calculated form the flux and fluence. 153
4.4 Samples used to compare between ion and neutron irradiations at equivalent temperatures. The Saclay sample was implanted at 1073 K. The uncertainty in the dose is a measure of the spread of values calculating with SRIM for different displacement threshold energies. 170
4.5 Comparison between isotopic abundances in ion irradiated W-1.4Re-0.1Os from SNL and polycrystalline neutron irradiated sample from HFR (W-1.2Re-0.1Os) compared to the natural abundance of each element [18, 65]. Isotopic abundances are calculated as the number of ions ranged per isotope, as a percentage of the total number of atoms ranged as that element. Uncertainty on the concentration from APT is estimated by comparing different ranging approaches, background-to-background and at FWHM. 171

4.6 Cluster search parameters used for various samples in this analysis. A range of values for the SNL sample were used to capture the impact of different approaches on the cluster composition. Where applicable the exact value of each parameter used is given in future analyses in this section. 177
4.7 Average cluster compositions, $\bar{x}_i$, and size in number of atoms, N, and radius of gyration, $\bar{r}_g$, for ion and neutron irradiated samples. The variation in average cluster compositions is represented by the standard deviation, σ_i. 178

5.1 Possible events within the KMC and SGMC models. Lattice sites are designated as follows: V=Vacancy, A,B = Atoms, AA = SIA, AB = Mixed Interstitial, S = Sink Site. 205

6.1 Local solute and defect dependencies of the pair interactions parameterised in this study. 207
6.2 DFT energies used to fit the atom-atom interactions. 208
6.3 Loss function for each of the ternary systems studied in this project. 219

7.1 Diffusion coefficient, D_0 and activation energy, E_A for vacancy diffusion as a function of solute concentration, x. . . . 239
7.2 Diffusion coefficient, D_0 and activation energy, E_A for solute diffusion as a function of solute concentration, x. 239

A.1 Pair interactions calculated by Huang et. al [154]. Interaction marked with * has the form $\varepsilon = a/x + b$ 309

B.1 Pair interactions for the W-Re-Os system. 310

C.1 Compositional information predicted by FISPACT-II for the HFR samples. 312
C.2 Activity information per nuclide from FISPACT-II after 5 years cooling. 313

D.1 List of figures with corresponding APT data file 314

E.1 Chemical analysis of nominally pure W sample performed by ACI alloys following sample manufacture. 315
E.2 Chemical analysis of nominal W-1.4Re-0.1Os sample performed by ACI alloys following sample manufacture. 316

Bibliography

[1] N. Ab Manan, A. N. Aizuddin, and R. Hod. Effect of Air Pollution and Hospital Admission: A Systematic Review. *Annals of Global Health*, 84(4):670, 2018.

[2] *Renewable Energy in Europe – 2017 Update Recent Growth and Knock-On Effects*. EEA Report No. 23/2017. European Environment Agency (EEA), Copenhagen, 2017. ISBN 978-92-9213-934-6.

[3] R. W. Grimes and W. J. Nuttall. Generating the Option of a Two-Stage Nuclear Renaissance. *Science*, 329(5993):799–803, 2010.

[4] R. Duffey and I. Pioro. Ensuring the Future of Nuclear Power. *Mechanical Engineering*, 141(11):30–35, 2019.

[5] *Energy, Electricity and Nuclear Power Estimates for the Period up to 2050*. Reference Data Series No. 1. International Atomic Energy Agency (IAEA), Vienna, 2019. ISBN 978-92-0-109319-6.

[6] P. A. Kharecha and M. Sato. Implications of Energy and CO2 Emission Changes in Japan and Germany after the Fukushima Accident. *Energy Policy*, 132:647–653, 2019.

[7] *Energy White Paper: Powering our Net Zero Future*. Report No. CP 337. UK Government, Department for Business, Energy & Industrial Strategy, London, 2020. ISBN 978-1-5286-2219-6.

[8] A. Vaughan. Boris Johnson Jokes about UK being on the Verge of Nuclear Fusion. *New Scientist*, 2019 (Accessed September 2020). [online] https://www.newscientist.com/article/2218570-boris-johnson-jokes-about-uk-being-on-the-verge-of-nuclear-fusion/.

[9] T. E. G. Nicholas, T. P. Davis, F. Federici, J. Leland, B. S. Patel, C. Vincent, and S. H. Ward. Re-Examining the Role of Nuclear Fusion in a Renewables-based Energy Mix. *Energy Policy*, 149:112043.

[10] A. Sykes, A.E. Costley, C.G. Windsor, O. Asunta, G. Brittles, P. Buxton, V. Chuyanov, J.W. Connor, M.P. Gryaznevich, B. Huang, and J. Hugill. Compact Fusion Energy Based on the Spherical Tokamak. *Nuclear Fusion*, 58(1):016039, 2017.

[11] K. S. Krane and D. Halliday. *Introductory Nuclear Physics, 3rd Edition*. John Wiley & Sons, Inc., New York, 1987. ISBN 978-0-471-80553-3.

[12] M. Kikuchi, K. Lackner, and M. Q. Tran. *Fusion Physics*. International Atomic Energy Authority (IAEA), Vienna, 2012. ISBN 978–92–0–130410–0.

[13] Nuclear Energy Agency. *Java-based Nuclear Data Information System*, 17 February 2019 (accessed 24 August, 2020). [online] https://www.oecd-nea.org/janis/.

[14] D.A. Brown, M.B. Chadwick, R. Capote, A.C. Kahler, A. Trkov, M.W. Herman, A.A. Sonzogni, Y. Danon, A.D. Carlson, M. Dunn, D.L. Smith, G.M. Hale, G. Arbanas, R. Arcilla, C.R. Bates, B. Beck, B. Becker, F. Brown, R.J. Casperson, J. Conlin, D.E. Cullen, M.-A. Descalle, R. Firestone, T. Gaines, K.H. Guber, A.I. Hawari, J. Holmes, T.D. Johnson, T. Kawano, B.C. Kiedrowski, A.J. Koning, S. Kopecky, L. Leal, J.P. Lestone, C. Lubitz, J.I. Márquez Damián, C.M. Mattoon, E.A. McCutchan, S. Mughabghab, P. Navratil, D. Neudecker, G.P.A. Nobre, G. Noguere, M. Paris, M.T. Pigni, A.J. Plompen, B. Pritychenko, V.G. Pronyaev, D. Roubtsov, D. Rochman, P. Romano, P. Schillebeeckx, S. Simakov, M. Sin, I. Sirakov, B. Sleaford, V. Sobes, E.S. Soukhovitskii, I. Stetcu, P. Talou, I. Thompson, S. van der Marck, L. Welser-Sherrill, D. Wiarda, M. White, J.L. Wormald, R.Q. Wright, M. Zerkle, G. Žerovnik, and Y. Zhu. ENDF/B-VIII.0: The 8th Major Release of the Nuclear Reaction Data Library with CIELO-project Cross Sections, New Standards and Thermal Scattering Data. *Nuclear Data Sheets*, 148:1 – 142, 2018. ISSN 0090-3752. Special Issue on Nuclear Reaction Data.

[15] J-Ch. Sublet, J.W. Eastwood, J.G. Morgan, M.R. Gilbert, M. Fleming, and W. Arter. FISPACT-II: An Advanced Simulation System for Activation, Transmutation and Material Modelling. *Nuclear Data Sheets*, 139:77–137, 2017.

[16] G. S. Was. *Fundamentals of Radiation Materials Science: Metals and Alloys, Second Edition*. Springer, New York, NY, 2016. ISBN 978-1-4939-3436-2.

[17] M.R. Gilbert, J-Ch. Sublet, and S.L. Dudarev. Spatial Heterogeneity of Tungsten Transmutation in a Fusion Device. *Nuclear Fusion*, 57 (4):044002, 2017.

[18] M. R. Gilbert and J-Ch. Sublet. *Handbook of Activation, Transmutation, and Radiation Damage Properties of the Elements Simulated using FISPACT-II and TENDL-2015; Magnetic Fusion Plants*. Report No. CCFE-R(16)36. United Kingdom Atomic Energy Authority, Oxford, 2016.

[19] M. R. Gilbert and J-Ch. Sublet. Neutron-Induced Transmutation Effects in W and W-Alloys in a Fusion Environment. *Nuclear Fusion*, 51(4):043005, 2011.

[20] M. R. Gilbert, S. L. Dudarev, S. Zheng, L. W. Packer, and J-Ch. Sublet. An Integrated Model for Materials in a Fusion Power Plant: Transmutation, Gas Production, and Helium Embrittlement under Neutron Irradiation. *Nuclear Fusion*, 52(8):083019, 2012.

[21] J. Marian, C. S. Becquart, C. Domain, S. L. Dudarev, M. R. Gilbert, R. J. Kurtz, D. R. Mason, K Nordlund, A. E. Sand, L. L. Snead, T. Suzudo, and B. D. Wirth. Recent Advances in Computational Materials Modeling of Tungsten as Plasma-Facing Material for Fusion Energy Applications. *Nucl. Fusion*, 57, 2017.

[22] A. J. Koning, D. Rochman, J-Ch. Sublet, N. Dzysiuk, M. Fleming, and S. van der Marck. TENDL: Complete Nuclear Data Library for Innovative Nuclear Science and Technology. *Nuclear Data Sheets*, 155: 1 – 55, 2019. ISSN 0090-3752. Special Issue on Nuclear Reaction Data.

[23] C. L. Smith and S. Cowley. The Path to Fusion Power. *Philosophical Transactions of the Royal Society A: Mathematical, Physical and Engineering Sciences*, 368(1914):1091–1108, 2010.

[24] F. Romanelli on behalf of JET Contributors. Overview of the JET Results. *Nuclear Fusion*, 55(10):104001, 2015.

[25] S. C. Cowley. The Quest for Fusion Power. *Nature Physics*, 12(5): 384–386, 2016.

[26] EUROfusion. *Media Library*, 2020 (accessed 5 August, 2020). [online] https://www.euro-fusion.org/.

[27] G. Federici, R. Kemp, D. Ward, C. Bachmann, T. Franke, S. Gonzalez, C. Lowry, M. Gadomska, J. Harman, B. Meszaros, C. Morlock, F. Romanelli, and R. Wenninger. Overview of EU DEMO Design and R&D Activities. *Fusion Engineering and Design*, 89(7):882–889, 2014.

[28] M. Barbarino, International Atomic Energy Authority (IAEA), Department of Nuclear Sciences and Applications. *Charting the International Roadmap to a Demonstration Fusion Power Plant*, 11 May 2018 (accessed 7 August, 2020). [online] https://www.iaea.org/newscenter/news/charting-the-international-roadmap-to-a-demonstration-fusion-power-plant.

[29] United Kingdom Atomic Energy Authority and Department for Business, Energy and Industrial Strategy, and The Rt. Hon. A. Leadsom MP. *UK to take a Big STEP to Fusion Electricity*, 3 October 2019 (accessed 7 August, 2020). [online] https://www.gov.uk/government/news/uk-to-take-a-big-step-to-fusion-electricity.

[30] Z. Vizvary, W. Arter, C. Bachmann, T.R. Barrett, B. Chuilon, P. Cooper, E. Flynn, M. Firdaouss, T. Franke, J. Gerardin, R. Gowland, M. Kovari, F. Maviglia, M. L. Richiusa, E. V. Rosa Adame, C. Vorpahl, A. Wilde, and Y. Xue. European DEMO First Wall Shaping and Limiters Design and Analysis Status. *Fusion Engineering and Design*, 158:111676, 2020.

[31] H. Bolt, V. Barabash, W. Krauss, J. Linke, R. Neu, S. Suzuki, N. Yoshida, and ASDEX Upgrade Team. Materials for the Plasma-Facing Components of Fusion Reactors. *Journal of nuclear materials*, 329:66–73, 2004.

[32] M. Rieth, J.L. Boutard, S.L. Dudarev, T. Ahlgren, S. Antusch, N. Baluc, M.-F. Barthe, C.S. Becquart, L. Ciupinski, J.B. Correia, C. Domain, J. Fikar, E. Fortuna, C.-C. Fu, E. Gaganidze, T.L. Galán, C. García-Rosales, B. Gludovatz, H. Greuner, K. Heinola, N. Holstein, N. Juslin, F. Koch, W. Krauss, K.J. Kurzydlowski, J. Linke, Ch. Linsmeier, N. Luzginova, H. Maier, M.S. Martínez, J.M. Missiaen, M. Muhammed, A. Muñoz, M. Muzyk, K. Nordlund, D. Nguyen-Manh, P. Norajitra, J. Opschoor, G. Pintsuk, R. Pippan, G. Ritz, L. Romaner, D. Rupp, R. Schäublin, J. Schlosser, I. Uytdenhouwen, J.G. van der Laan, L. Veleva, L. Ventelon, S. Wahlberg, F. Willaime, S. Wurster, and M.A. Yar. Review on the EFDA Programme on Tungsten Materials Technology and Science. *Journal of Nuclear Materials*, 417(1-3):463–467, 2011.

[33] M. Rieth, S.L. Dudarev, S.M. Gonzalez de Vicente, J. Aktaa, T. Ahlgren, S. Antusch, D.E.J. Armstrong, M. Balden, N. Baluc, M.-F. Barthe, W.W. Basuki, M. Battabyal, C.S. Becquart, D. Blagoeva, H. Boldyryeva, J. Brinkmann, M. Celino, L. Ciupinski, J.B. Correia, A. De Backer, C. Domain, E. Gaganidze, C. García-Rosales, J. Gibson, M.R. Gilbert, S. Giusepponi, B. Gludovatz, H. Greuner, K. Heinola, T. Höschen, A. Hoffmann, N. Holstein, F. Koch, W. Krauss, H. Li, S. Lindig, J. Linke, Ch. Linsmeier, P. López-Ruiz, H. Maier, J. Matejicek, T.P. Mishra, M. Muhammed, A. Muñoz, M. Muzyk, K. Nordlund, D. Nguyen-Manh, J. Opschoor, N. Ordás, T. Palacios, G. Pintsuk, R. Pippan, J. Reiser, J. Riesch, S.G. Roberts, L. Romaner, M. Rosiński, M. Sanchez, W. Schulmeyer, H. Traxler, A. Ureña, J.G. van der Laan, L. Veleva, S. Wahlberg, M. Walter, T. Weber, T. Weitkamp, S. Wurster, M.A. Yar, J.H. You, and A. Zivelonghi. Recent Progress in Research on Tungsten Materials for Nuclear Fusion Applications in Europe. *Journal of Nuclear Materials*, 432(1-3):482–500, 2013.

[34] M. R. Gilbert, S. L. Dudarev, D. Nguyen-Manh, S. Zheng, L. W. Packer, and J-Ch. Sublet. Neutron-Induced dpa, Transmutations, Gas Production, and Helium Embrittlement of Fusion Materials. *Journal of Nuclear Materials*, 442(1-3):S755–S760, 2013.

[35] J. Knaster, A. Moeslang, and T. Muroga. Materials Research for Fusion. *Nature Physics*, 12(5):424, 2016.

[36] K. Nordlund. Historical Review of Computer Simulation of Radiation Effects in Materials. *Journal of Nuclear Materials*, 520:273 – 295, 2019.

[37] T. Diaz de la Rubia, R. S. Averback, R. Benedek, and W. E. King. Role of Thermal Spikes in Energetic Displacement Cascades. *Physical review letters*, 59(17):1930, 1987.

[38] K. Trachenko, E. Zarkadoula, I. T. Todorov, M. T. Dove, D. J. Dunstan, and K. Nordlund. Modeling High-Energy Radiation Damage in Nuclear and Fusion Applications. *Nuclear Instruments and Methods in Physics Research Section B: Beam Interactions with Materials and Atoms*, 277:6–13, 2012.

[39] F. Granberg S. J. Zinkle R. Stoller R. S. Averback T. Suzudo L. Malerba F. Banhart W. J. Weber F. Willaime S. Dudarev K. Nordlund, A. E. Sand and D. Simeone. *Primary Radiation Damage in Materials: Review of Current Understanding and Proposed New Standard Displacement Damage Model to Incorporate in Cascade Defect Production Efficiency and Mixing Effects*. NEA-NSC-DOC–2015-9. Nuclear Energy Agency (NEA) of the Organisation for Economic Cooperation and Development (OECD), Vienna, 2015.

[40] M. J. Norgett, M. T. Robinson, and I. M. Torrens. A Proposed Method of Calculating Displacement Dose Rates. *Nuclear engineering and design*, 33(1):50–54, 1975.

[41] J. F. Ziegler, J. P. Biersack, and M. D. Ziegler. The Stopping and Range of Ions in Matter. 2009. [online] http://www.srim.org.

[42] K. Nordlund, S. J. Zinkle, A. E. Sand, F. Granberg, R. S. Averback, R. E. Stoller, T. Suzudo, L. Malerba, F. Banhart, W. J. Weber, Francois W., S. L. Dudarev, and D. Simeone. Primary Radiation Damage: A Review of Current Understanding and Models. *Journal of Nuclear Materials*, 512:450–479, 2018.

[43] R. E. Stoller, M. B. Toloczko, G. S. Was, A. G. Certain, S. Dwaraknath, and F. A. Garner. On the use of SRIM for Computing Radiation Damage Exposure. *Nuclear Instruments and Methods in Physics Research Section B: Beam Interactions with Materials and Atoms*, 310:75–80, 2013.

[44] S. I. Maydet and K. C. Russell. Precipitate Stability under Irradiation: Point Defect Effects. *Journal of Nuclear Materials*, 64(1-2):101–114, 1977.

[45] R. Cauvin and G. Martin. Solid Solutions under Irradiation. I. A Model for Radiation-Induced Metastability. *Physical Review B*, 23 (7):3322, 1981.

[46] I. T. Chapman and A. W. Morris. UKAEA Capabilities to Address the Challenges on the Path to Delivering Fusion Power. *Philosophical Transactions of the Royal Society A*, 377(2141):20170436, 2019.

[47] M. R. Gilbert, M. Fleming, and J.-Ch. Sublet. Automated Inventory and Material Science Scoping Calculations under Fission and Fusion Conditions. *Nuclear Engineering and Technology*, 49(6):1346–1353, 2017.

[48] M. J. Gorley. Critical Assessment 12: Prospects for Reduced Activation Steel for Fusion Plant. *Materials Science and Technology*, 31(8): 975–980, 2015.

[49] J. W. Coenen, S. Antusch, M. Aumann, W. Biel, J. Du, J. Engels, S. Heuer, A. Houben, T. Hoeschen, B. Jasper, F. Koch, J. Linke, A. Litnovsky, Y. Mao, R. Neu, G. Pintsuk, J. Riesch, M. Rasinski, J. Reiser, M. Rieth, A. Terra, B. Unterberg, Th. Weber, T. Wegener, J.-H. You, and Ch. Linsmeier. Materials for DEMO and Reactor Applications—Boundary Conditions and New Concepts. *Physica Scripta*, 2016(T167):014002, 2015.

[50] S. Nogami, M. Toyota, W. Guan, A. Hasegawa, and Y. Ueda. Degradation of Tungsten Monoblock Divertor under Cyclic High Heat Flux Loading. *Fusion Engineering and Design*, 120:49–60, 2017.

[51] S. Krat, Y. Gasparyan, A. Pisarev, I. Bykov, M. Mayer, G. de Saint Aubin, M. Balden, C. P. Lungu, and A. Widdowson. Erosion at the Inner Wall of JET during the Discharge Campaign 2011–2012 in Comparison with Previous Campaigns. *Journal of Nuclear Materials*, 456:106 – 110, 2015.

[52] M. Mayer, S. Krat, W. Van Renterghem, A. Baron-Wiechec, S. Brezinsek, I. Bykov, P. Coad, Y. Gasparyan, K. Heinola, J. Likonen, A. Pisarev, C. Ruset, G. de Saint-Aubin, A. Widdowson, and JET Contributors. Erosion and Deposition in the JET Divertor during the First ILW Campaign. *Physica Scripta*, 2016(T167):014051, 2016.

[53] Y. Wan, J. Li, Y. Liu, X. Wang, V. Chan, C. Chen, X. Duan, P. Fu, X. Gao, K. Feng, S. Liu, Y. Song, P. Weng, B. Wan, F. Wan, H. Wang, S. Wu, M. Ye, Q. Yang, G. Zheng, G. Zhuang, Q. Li, and CFETR Team. Overview of the Present Progresses and Activities on the Chinese Fusion Engineering Test Reactor. *Nuclear Fusion*, 57(10): 102009, 2017.

[54] R. Hancox and G. J. Butterworth. The Management of Fusion Waste. *Fusion Engineering and Design*, 14(1):37–47, 1991. 16th Symposium on Fusion Technology.

[55] R. L. Klueh, D. S. Gelles, and T. A. Lechtenberg. Development of Ferritic Steels for Reduced Activation: the US Program. *Journal of Nuclear Materials*, 141-143:1081–1087, 1986.

[56] H. R. Brager, F. A. Garner, D. S. Gelles, and M. L. Hamilton. Development of Reduced Activation Alloys for Fusion Service. *Journal of Nuclear Materials*, 133-134:907 – 911, 1985.

[57] M. R. Gilbert, T. Eade, C. Bachmann, U. Fischer, and N. P. Taylor. Activation, Decay Heat, and Waste Classification Studies of the European DEMO Concept. *Nuclear Fusion*, 57(4):046015, 2017.

[58] M. Lukacs and L. G. Williams. Nuclear Safety Issues for Fusion Power Plants. *Fusion Engineering and Design*, 150:111377, 2020.

[59] B. S. Kim, B. C. Kim, K. Im, H.-T. Kim, S. Kwon, and J. Park. Assessment of the Activation Induced by Neutron Irradiation in K-DEMO and Thermal Response under the Decay Heat. *Fusion Engineering and Design*, 146:2323–2327, 2019.

[60] P. Lu, P. Pereslavtsev, F. Hernandez, and U. Fischer. Activation analysis for the HCPB blanket module in the European DEMO. *Fusion Engineering and Design*, 125:18–23, 2017.

[61] A. Ibarra, F. Arbeiter, D. Bernardi, W. Krolas, M. Cappelli, U. Fischer, R. Heidinger, F. Martin-Fuertes, G. Micciché, A. Muñoz, F. S. Nitti, T. Pinna, A. Aiello, N. Bazin, N. Chauvin, S. Chel, G. Devanz, S. Gordeev, D. Regidor, F. Schwab, and the full IFMIF-DONES team. The European Approach to the Fusion-like Neutron Source: the IFMIF-DONES Project. *Nuclear Fusion*, 59(6):065002, 2019.

[62] A. Ibarra, F. Arbeiter, D. Bernardi, M. Cappelli, A. García, R. Heidinger, W. Krolas, U. Fischer, F. Martin-Fuertes, G. Micciché, A. Muñoz, F.S. Nitti, M. Pérez, T. Pinna, and K. Tian. The IFMIF-DONES Project: Preliminary Engineering Design. *Nuclear Fusion*, 58(10):105002, 2018.

[63] S. M. González de Vicente, J.-L. Boutard, S. J. Zinkle, and H. Tanigawa. Materials Testing Facilities and Programmes for Fission and Ion Implantation Damage. *Nuclear Fusion*, 57(9):092011, 2017.

[64] D. Stork, R. Heidinger, T. Muroga, S. J. Zinkle, A. Moeslang, M. Porton, J.-L. Boutard, S. Gonzalez, and A. Ibarra. Towards a Programme

of Testing and Qualification for Structural and Plasma-Facing Materials in 'Fusion Neutron' Environments. *Nuclear Fusion*, 57(9):092013, 2017.

[65] M. R. Gilbert and J-Ch. Sublet. *Handbook of Activation, Transmutation, and Radiation Damage Properties of the Elements Simulated using FISPACT-II and TENDL-2015; Nuclear Fission plants (HFR focus)*. United Kingdom Atomic Energy Authority, Oxford, 2015.

[66] R. G. Abernethy, J. S. K.-L. Gibson, A. Giannattasio, J. D. Murphy, O. Wouters, S. Bradnam, L. W. Packer, M. R. Gilbert, M. Klimenkov, M. Rieth, H.-C. Schneider, C. D. Hardie, S. G. Roberts, and D. E. J. Armstrong. Effects of Neutron Irradiation on the Brittle to Ductile Transition in Single Crystal Tungsten. *Journal of Nuclear Materials*, 527:151799, 2019.

[67] O. Tissot, C. Pareige, E. Meslin, B. Decamps, and J. Henry. Influence of Injected Interstitials on α' Precipitation in Fe–Cr Alloys under Self-Ion Irradiation. *Materials Research Letters*, 5(2):117–123, 2017.

[68] M. P. Short, D. R. Gaston, M. Jin, L. Shao, and F. A. Garner. Modeling Injected Interstitial Effects on Void Swelling in Self-Ion Irradiation Experiments. *Journal of Nuclear Materials*, 471:200–207, 2016.

[69] R. W. Harrison. On the use of Ion Beams to Emulate the Neutron Irradiation Behaviour of Tungsten. *Vacuum*, 160:355 – 370, 2019.

[70] E. R. Reese, N. Almirall, T. Yamamoto, S. Tumey, G. R. Odette, and E. A. Marquis. Dose Rate Dependence of Cr Precipitation in an Ion-Irradiated Fe 18Cr Alloy. *Scripta Materialia*, 146:213–217, 2018.

[71] C. D. Hardie, C. A. Williams, S. Xu, and S. G. Roberts. Effects of Irradiation Temperature and Dose Rate on the Mechanical Properties of Self-Ion Implanted Fe and Fe–Cr Alloys. *Journal of Nuclear Materials*, 439(1):33 – 40, 2013.

[72] C. M. Logan, J. D. Anderson, and A. K. Mukherjee. Proton Simulation of Displacement Effects Induced in Metals by 14 MeV Neutrons. *Journal of Nuclear Materials*, 48(3):223–232, 1973.

[73] S. A. Maloy, M. R. James, W. Sommer Jr, G. J. Willcutt Jr, M. Lopez, T. J. Romero, and M. B. Toloczko. The Effect of 800 MeV Proton Irradiation on the Mechanical Properties of Tungsten at Room Temperature and at 475^{o}C. *Journal of nuclear materials*, 343(1-3):219–226, 2005.

[74] R. Rayaprolu, S. Moller, Ch. Linsmeier, and S. Spellerberg. Simulation of Neutron Irradiation Damage in Tungsten using Higher Energy Protons. *Nuclear Materials and Energy*, 9:29–35, 2016.

[75] D. E. J. Armstrong, P. D. Edmondson, and S. G. Roberts. Effects of Sequential Tungsten and Helium Ion Implantation on Nano-Indentation Hardness of Tungsten. *Applied Physics Letters*, 102(25): 251901, 2013.

[76] D. R. Lide. *CRC Handbook of Chemistry and Physics, 85th Edition*, volume 85. CRC press, Boca Raton, FL, 2005. ISBN 0-8493-0485-7.

[77] T. Tanabe, C. Eamchotchawalit, C. Busabok, S. Taweethavorn, M. Fujitsuka, and T. Shikama. Temperature Dependence of Thermal Conductivity in W and W–Re Alloys from 300 to 1000 K. *Materials Letters*, 57(19):2950–2953, 2003.

[78] M. J. Baldwin and R. P. Doerner. Helium Induced Nanoscopic Morphology on Tungsten under Fusion Relevant Plasma Conditions. *Nuclear Fusion*, 48(3):035001, 2008.

[79] W. Yih. *Tungsten: Sources, Metallurgy, Properties, and Applications*. Springer, New York, NY, 1979. ISBN 978-1-4899-5027-7.

[80] E. Clementi, D. L. Raimondi, and W. P. Reinhardt. Atomic Screening Constants from SCF Functions. II. Atoms with 37 to 86 Electrons. *The Journal of Chemical Physics*, 47(4):1300–1307, 1967.

[81] J. C. Slater. Atomic Radii in Crystals. *The Journal of Chemical Physics*, 41(10):3199–3204, 1964.

[82] T. Suzudo, M. Yamaguchi, and A. Hasegawa. Migration of Rhenium and Osmium Interstitials in Tungsten. *Journal of Nuclear Materials*, 467:418–423, 2015.

[83] P. L. Raffo. Yielding and Fracture in Tungsten and Tungsten-Rhenium Alloys. *Journal of the Less Common Metals*, 17(2):133–149, 1969.

[84] A. Xu. *A Thesis Submitted for the Degree of Doctor of Philosophy: Atomic Scale Characterisation of Radiation Damage and Radiation Induced Precipitation in Tungsten-Rhenium Alloys*. PhD thesis, Department of Materials, University of Oxford, 2015.

[85] B. Gludovatz, S. Wurster, T. Weingärtner, A. Hoffmann, and R. Pippan. Influence of Impurities on the Fracture Behaviour of Tungsten. *Philosophical Magazine*, 91(22):3006–3020, 2011.

[86] A. Gilbert. A Fractographic Study of Tungsten and Dilute Tungsten-Rhenium Alloys. *Journal of the Less Common Metals*, 10(5):328–343, 1966.

[87] J. M. Steichen. Tensile Properties of Neutron Irradiated TZM and Tungsten. *Journal of Nuclear Materials*, 60(1):13–19, 1976.

[88] M. J. Lloyd, R. G. Abernethy, M. R. Gilbert, I. Griffiths, P. A. J. Bagot, D. Nguyen-Manh, M. P. Moody, and D. E. J. Armstrong. Decoration of Voids with Rhenium and Osmium Transmutation Products in Neutron Irradiated Single Crystal Tungsten. *Scripta Materialia*, 173:96–100, 2019.

[89] Y. Katoh, L. L. Snead, L. M. Garrison, X. Hu, T. Koyanagi, C. M. Parish, P. D. Edmondson, M. Fukuda, T. Hwang, T. Tanaka, and A. Hasegawa. Response of Unalloyed Tungsten to Mixed Spectrum Neutrons. *Journal of Nuclear Materials*, 520:193–207, 2019.

[90] A. Hasegawa, M. Fukuda, K. Yabuuchi, and S. Nogami. Neutron Irradiation Effects on the Microstructural Development of Tungsten and Tungsten Alloys. *Journal of Nuclear Materials*, 471:175–183, 2016.

[91] M. Klimenkov, U. Jäntsch, M. Rieth, H. C. Schneider, D. E. J. Armstrong, J. Gibson, and S. G. Roberts. Effect of Neutron Irradiation on the Microstructure of Tungsten. *Nuclear Materials and Energy*, 9: 480–483, 2016.

[92] L. M. Garrison, Y. Katoh, J. W. Geringer, M. Akiyoshi, X. Chen, M. Fukuda, A. Hasegawa, T. Hinoki, X. Hu, T. Koyanagi, E. Lang, M. McAlister, J. McDuffee, T. Miyazawa, C. Parish, E. Proehl, N. Reid, J. Robertson, and H. Wang. PHENIX US-Japan Collaboration Investigation of Thermal and Mechanical Properties of Thermal Neutron–Shielded Irradiated Tungsten. *Fusion Science and Technology*, 75(6):499–509, 2019.

[93] M. C. Green, H. B. Skinner, and R. A. Tuck. Osmium-Tungsten Alloys and their Relevance to Improved M-Type Cathodes. *Applications of Surface Science*, 8(1-2):13–35, 1981.

[94] Z.-K. Liu and Y. A. Chang. Evaluation of the Thermodynamic Properties of the Re–Ta and Re–W Systems. *Journal of Alloys and Compounds*, 299(1-2):153–162, 2000.

[95] P. Villars, A. Prince, and H. Okamoto. *Handbook of Ternary Alloy Phase Diagrams: Mg-Ni-P to Y-Zn-Zr*. ASM International, Materials Park, OH, USA, 2006. ISBN 978-0-87170-525-9.

[96] Rempe, J. and Knudson, D. and Condie, K. and Cole, J. Long Duration Performance of High Temperature Irradiation Resistant Thermocouples. volume 4, 05 2007.

[97] A. Xu, D. E. J. Armstrong, C. Beck, M. P. Moody, G. D. W. Smith, P. A. J. Bagot, and S. G. Roberts. Ion-Irradiation Induced Clustering in W-Re-Ta, W-Re and W-Ta Alloys: An Atom Probe Tomography and Nanoindentation Study. *Acta Materialia*, 124:71–78, 2017.

[98] M. Muzyk, D. Nguyen-Manh, K. J. Kurzydłowski, N. L. Baluc, and S. L. Dudarev. Phase Stability, Point Defects, and Elastic Properties of W-V and W-Ta Alloys. *Physical Review B*, 84(10):104115, 2011.

[99] W. D. Klopp. *Review of Ductilizing of Group VIA Elements by Rhenium and Other Solutes*. NASA Technical Note, NASA TN D-4955. National Aeronautics and Space Administration, Washington D. C., USA, 1968.

[100] C. Ren, Z.Z. Fang, M. Koopman, B. Butler, J. Paramore, and S. Middlemas. Methods for Improving Ductility of Tungsten - A Review. *International Journal of Refractory Metals and Hard Materials*, 75:170 – 183, 2018.

[101] Y.-J. Hu, M. R. Fellinger, B. G. Butler, Y. Wang, K. A. Darling, L. J. Kecskes, D. R. Trinkle, and Z.-K. Liu. Solute-Induced Solid-Solution Softening and Hardening in bcc Tungsten. *Acta Materialia*, 141:304 – 316, 2017.

[102] W. D. Klopp. A Review of Chromium, Molybdenum, and Tungsten Alloys. *Journal of the Less Common Metals*, 42(3):261 – 278, 1975.

[103] R. K. Williams, F. W. Wiffen, J. Bentley, and J. O. Stiegler. Irradiation Induced Precipitation in Tungsten Based, W-Re Alloys. *Metallurgical Transactions A*, 14(3):655–666, 1983.

[104] V. K. Sikka and J. Moteff. Superlattice of Voids in Neutron-Irradiated Tungsten. *Journal of Applied Physics*, 43(12):4942–4944, 1972.

[105] J. Matolich, H. Nahm, and J. Moteff. Swelling in Neutron Irradiated Tungsten and Tungsten-25 Percent Rhenium. *Scripta Metallurgica*, 8 (7):837–841, 1974.

[106] R. C. Rau, R. L. Ladd, and J. Moteff. *Voids in Irradiated Tungsten and Molybdenum*. Technical Report, Report No. NSA-23-034025. General Electric Co., Cincinnati, Ohio. Missile and Space Div., United States, 1969.

[107] R. C. Rau, J. Moteff, and R. L. Ladd. Comparison of Microstructure with Mechanical Properties of Irradiated Tungsten. *Journal of nuclear materials*, 24(2):164–173, 1967.

[108] J. W. Davis, V. R. Barabash, A. Makhankov, L. Plöchl, and K. T. Slattery. Assessment of Tungsten for use in the ITER Plasma Facing Components. *Journal of nuclear materials*, 258:308–312, 1998.

[109] R. Abernethy. *A Thesis Submitted for the Degree of Doctor of Philosophy: Comparison of Ion and Neutron Irradiation of Tungsten for Fusion Applications*. PhD thesis, Department of Materials, University of Oxford, 2019.

[110] R. F. Mattas, M. I. Baskes, J. N. Brooks, J. P. Blanchard, A. M. Hassanein, and A. Tobin. Divertor Engineering Studies for the International Tokamak Reactor. *Fusion technology*, 10(3P1):364–381, 1986.

[111] Y. Nemoto, A. Hasegawa, M. Satou, and K. Abe. Microstructural Development of Neutron Irradiated W–Re Alloys. *Journal of nuclear materials*, 283:1144–1147, 2000.

[112] A. Hasegawa, T. Tanno, S. Nogami, and M. Satou. Property Change Mechanism in Tungsten under Neutron Irradiation in Various Reactors. *Journal of Nuclear Materials*, 417(1-3):491–494, 2011.

[113] T. Tanno, M. Fukuda, S. Nogami, and A. Hasegawa. Microstructure Development in Neutron Irradiated Tungsten Alloys. *Materials Transactions*, pages 1105231402–1105231402, 2011.

[114] T. Hwang, A. Hasegawa, K. Tomura, N. Ebisawa, T. Toyama, Y. Nagai, M. Fukuda, T. Miyazawa, T. Tanaka, and S. Nogami. Effect of Neutron Irradiation on Rhenium Cluster Formation in Tungsten and Tungsten-Rhenium Alloys. *Journal of Nuclear Materials*, 507:78–86, 2018.

[115] X. Hu, T. Koyanagi, M. Fukuda, Y. Katoh, L. L. Snead, and B. D. Wirth. Defect Evolution in Single Crystalline Tungsten following Low Temperature and Low Dose Neutron Irradiation. *Journal of Nuclear Materials*, 470:278–289, 2016.

[116] X. Hu, C. M. Parish, K. Wang, T. Koyanagi, B. P. Eftink, and Y. Katoh. Transmutation-Induced Precipitation in Tungsten Irradiated with a Mixed Energy Neutron Spectrum. *Acta Materialia*, 165: 51–61, 2019.

[117] R. Herschitz and D. N. Seidman. Radiation-Induced Precipitation in Fast-Neutron Irradiated Tungsten-Rhenium Alloys: An Atom-Probe Field-Ion Microscope Study. *Nuclear Instruments and Methods in Physics Research Section B: Beam Interactions with Materials and Atoms*, 7:137–142, 1985.

[118] R. Herschitz and D. N. Seidman. An Atomic Resolution Study of Homogeneous Radiation-Induced Precipitation in a Neutron Irradiated W-10at.% Re Alloy. *Acta Metallurgica*, 32(8):1141–1154, 1984.

[119] R. Herschitz and D. N. Seidman. An Atomic Resolution Study of Radiation-Induced Precipitation and Solute Segregation Effects in a Neutron-Irradiated W-25 at.% Re alloy. *Acta Metallurgica*, 32(8): 1155–1171, 1984.

[120] H. C. Eaton and H. Nordén. The Segregation of Osmium to Grain Boundary Dislocations in Tungsten. *Scripta metallurgica*, 17(8):1043–1046, 1983.

[121] D. J. Larson, B. Gault, B. P. Geiser, F. De Geuser, and F. Vurpillot. Atom Probe Tomography Spatial Reconstruction: Status and Directions. *Current Opinion in Solid State and Materials Science*, 17(5): 236–247, 2013.

[122] S. K. Suram and K. Rajan. Calibration of Reconstruction Parameters in Atom Probe Tomography using a Single Crystallographic Orientation. *Ultramicroscopy*, 132:136–142, 2013.

[123] C. Fletcher, M. P. Moody, and D. Haley. Towards Model-Driven Reconstruction in Atom Probe Tomography. *Journal of Physics D: Applied Physics*, 2020.

[124] S. S. Brenner and D. N. Seidman. Field Ion Microscope Observations of Voids in Neutron Irradiated Molybdenum. *Radiation Effects*, 24 (2):73–78, 1975.

[125] P. J. Birdseye, D. A. Smith, and G. D. W. Smith. Analogue Investigations of Electric Field Distribution and Ion Trajectories in the Field Ion Microscope. *Journal of Physics D: Applied Physics*, 7(12):1642, 1974.

[126] X. Wang, C. Hatzoglou, B. Sneed, Z. Fan, W. Guo, K. Jin, D. Chen, H. Bei, Y. Wang, W. J. Weber, Y. Zhang, B. Gault, K. L. More, F. Vurpillot, and J. D. Poplawsky. Interpreting Nanovoids in Atom Probe Tomography Data for Accurate Local Compositional Measurements. *Nature Communications*, 11(1):1–11, 2020.

[127] M. K. Miller, L. Longstreth-Spoor, and K. F. Kelton. Detecting Density Variations and Nanovoids. *Ultramicroscopy*, 111(6):469–472, 2011.

[128] M. Dagan, L. R. Hanna, A. Xu, S. G. Roberts, G. D. W. Smith, B. Gault, P. D. Edmondson, P. A. J. Bagot, and M. P. Moody. Imaging of Radiation Damage using Complementary Field Ion Microscopy and Atom Probe Tomography. *Ultramicroscopy*, 159:387–394, 2015.

[129] D. Melkonyan, C. Fleischmann, L. Arnoldi, J. Demeulemeester, A. Kumar, J. Bogdanowicz, F. Vurpillot, and W. Vandervorst. Atom Probe Tomography Analysis of SiGe Fins Embedded in SiO2: Facts and Artefacts. *Ultramicroscopy*, 179:100–107, 2017.

[130] X. Yi, M. L. Jenkins, M. Briceno, S. G. Roberts, Z. Zhou, and M. A. Kirk. In Situ Study of Self-Ion Irradiation Damage in W and W–5Re at 500 ^{o}C. *Philosophical Magazine*, 93(14):1715–1738, 2013.

[131] X. Yi, M. L. Jenkins, M. A. Kirk, Z. Zhou, and S. G. Roberts. In-situ TEM Studies of 150 keV W^+ Ion Irradiated W and W-alloys: Damage Production and Microstructural Evolution. *Acta Materialia*, 112:105–120, 2016.

[132] T Hwang, M Fukuda, S Nogami, A Hasegawa, H Usami, K Yabuuchi, K Ozawa, and H Tanigawa. Effect of self-ion irradiation on hardening and microstructure of tungsten. *Nuclear Materials and Energy*, 9: 430–435, 2016.

[133] F. Ferroni, X. Yi, K. Arakawa, S. P. Fitzgerald, P. D. Edmondson, and S. G. Roberts. High Temperature Annealing of Ion Irradiated Tungsten. *Acta Materialia*, 90:380–393, 2015.

[134] A. Xu, C. Beck, D. E. J. Armstrong, K. Rajan, G. D. W. Smith, P. A. J. Bagot, and S. G. Roberts. Ion-Irradiation-Induced Clustering in W–Re and W–Re–Os Alloys: A Comparative Study using Atom Probe Tomography and Nanoindentation Measurements. *Acta Materialia*, 87:121–127, 2015.

[135] Olof C. Hellman, Justin A. Vandenbroucke, Järg Rüsing, Dieter Isheim, and David N. Seidman. Analysis of three-dimensional atom-probe data by the proximity histogram. *Microscopy and Microanalysis*, 6(5):437–444, 2000. doi: 10.1007/S100050010051.

[136] S. P. Fitzgerald and D. Nguyen-Manh. Peierls Potential for Crowdions in the bcc Transition Metals. *Physical review letters*, 101(11):115504, 2008.

[137] D. Nguyen-Manh, A. P. Horsfield, and S. L. Dudarev. Self-Interstitial Atom Defects in bcc Transition Metals: Group-Specific Trends. *Physical Review B*, 73(2):020101, 2006.

[138] J. S. Wróbel, D. Nguyen-Manh, K. J. Kurzydłowski, and S. L. Dudarev. A First-Principles Model for Anomalous Segregation in Dilute Ternary Tungsten-Rhenium-Vacancy Alloys. *Journal of Physics: Condensed Matter*, 29(14):145403, 2017.

[139] D. R. Mason, D. Nguyen-Manh, and C. S. Becquart. An Empirical Potential for Simulating Vacancy Clusters in Tungsten. *Journal of Physics: Condensed Matter*, 29(50):505501, 2017.

[140] T. Suzudo, M. Yamaguchi, and A. Hasegawa. Stability and Mobility of Rhenium and Osmium in Tungsten: First Principles Study. *Modelling and Simulation in Materials Science and Engineering*, 22(7):075006, 2014.

[141] C. S. Becquart, C. Domain, U. Sarkar, A. Debacker, and M. Hou. Microstructural Evolution of Irradiated Tungsten: Ab Initio Parameterisation of an OKMC Model. *Journal of nuclear materials*, 403 (1-3):75–88, 2010.

[142] T. Suzudo and A. Hasegawa. Suppression of Radiation-Induced Point Defects by Rhenium and Osmium Interstitials in Tungsten. *Scientific reports*, 6:36738, 2016.

[143] N. Castin, P. Dwivedi, L. Messina, A. Bakaev, D. Terentyev, and G. Bonny. The Effect of Rhenium on the Diffusion of Small Interstitial Clusters in Tungsten. *Computational Materials Science*, 177:109580, 2020.

[144] L. Gharaee, J. Marian, and P. Erhart. The Role of Interstitial Binding in Radiation Induced Segregation in W-Re Alloys. *Journal of Applied Physics*, 120(2):025901, 2016.

[145] L. Messina, P. Olsson, N. Castin, G. Bonny, D. Nguyen-Manh, M. J. Lloyd, M. C. Marinica, A. Gorayeva, T. Schuler, M. Nastar, and A. Quaglino. *Transport Properties of Transmutation Products in Concentrated W-Re-Os Alloys by Smart Fitting of Ab Initio Datasets.* Presented at the 19th International Conference on Fusion Reactor Materials (ICFRM19), New Modeling Methods Symposium, San Diego, CA, USA. 2019.

[146] J. Fu, Y. Chen, J. Fang, N. Gao, W. Hu, C. Jiang, H.-B. Zhou, G.-. Lu, F. Gao, and H. Deng. Molecular Dynamics Simulations of High-Energy Radiation Damage in W and W–Re Alloys. *Journal of Nuclear Materials*, 524:9 – 20, 2019.

[147] A. F. Voter. Introduction to the Kinetic Monte Carlo Method. In *Radiation Effects in Solids*, pages 1–23. Springer Netherlands, Dordrecht, 2007. ISBN 978-1-4020-5295-8.

[148] K. E. Sickafus, E. A. Kotomin, and B. P. Uberuaga. *Radiation Effects in Solids.* NATO Science Series II: Mathematics, Physics and Chemistry. Springer Netherlands, 2007. ISBN 9781402052958.

[149] W. M. Young and E. W. Elcock. Monte Carlo Studies of Vacancy Migration in Binary Ordered Alloys: I. *Proceedings of the Physical Society*, 89(3):735, 1966.

[150] A. D. Le Claire. Solvent Self-Diffusion in Dilute bcc Solid Solutions. *Philosophical Magazine*, 21(172):819–832, 1970.

[151] R. Ngayam-Happy, C. S. Becquart, C. Domain, and L. Malerba. Formation and Evolution of MnNi Clusters in Neutron Irradiated Dilute Fe Alloys Modelled by a First Principle-based AKMC Method. *Journal of Nuclear Materials*, 426(1-3):198–207, 2012.

[152] E. Martínez, O. Senninger, C.-C. Fu, and F. Soisson. Decomposition Kinetics of Fe-Cr Solid Solutions during Thermal Aging. *Physical Review B*, 86(22):224109, 2012.

[153] O. Senninger, F. Soisson, E. Martínez, M. Nastar, C.-C. Fu, and Y. Bréchet. Modeling Radiation Induced Segregation in Iron–Chromium Alloys. *Acta Materialia*, 103:1–11, 2016.

[154] C.-H. Huang, L. Gharaee, Y. Zhao, P. Erhart, and J. Marian. Mechanism of Nucleation and Incipient Growth of Re Clusters in Irradiated W-Re Alloys from Kinetic Monte Carlo Simulations. *Physical Review B*, 96(9):094108, 2017.

[155] K. Reuter and M. Scheffler. First-Principles Kinetic Monte Carlo Simulations for Heterogeneous Catalysis: Application to the CO oxidation at RuO2 (110). *Physical Review B*, 73(4):045433, 2006.

[156] K. Reuter, S. Frenkel, and M. Scheffler. The Steady State of Heterogeneous Catalysis, Studied by First-Principles Statistical Mechanics. *Physical Review Letters*, 93(11):116105, 2004.

[157] F. Soisson and C.-C. Fu. Cu-Precipitation Kinetics in α-Fe from Atomistic Simulations: Vacancy-Trapping Effects and Cu-Cluster Mobility. *Physical Review B*, 76(21):214102, 2007.

[158] C.-H. Huang and J. Marian. A Generalized Ising Model for Studying Alloy Evolution under Irradiation and its use in Kinetic Monte Carlo Simulations. *Journal of Physics: Condensed Matter*, 28(42):425201, 2016.

[159] M. J. Lloyd, R. G. Abernethy, D. E. J. Armstrong, P. A. J. Bagot, M. P. Moody, E. Martinez, and D. Nguyen-Manh. Radiation-Induced Segregation in W-Re: from Kinetic Monte Carlo Simulations to Atom Probe Tomography Experiments. *The European Physical Journal B*, 92(10):241, 2019.

[160] D. R. Mason, X. Yi, M. A. Kirk, and S. L. Dudarev. Elastic Trapping of Dislocation Loops in Cascades in Ion-Irradiated Tungsten Foils. *Journal of Physics: Condensed Matter*, 26(37):375701, 2014.

[161] J. C. He, G. Y. Tang, A. Hasegawa, and K. Abe. Microstructural Development and Irradiation Hardening of W and W–(3–26) wt% Re Alloys after High-Temperature Neutron Irradiation to 0.15 dpa. *Nuclear fusion*, 46(11):877, 2006.

[162] Z. X. Zhang, D. S. Chen, W. T. Han, and A. Kimura. Irradiation Hardening in Pure Tungsten before and after Recrystallization. *Fusion Engineering and Design*, 98:2103–2107, 2015.

[163] D. E. J. Armstrong, A. J. Wilkinson, and S. G. Roberts. Mechanical Properties of Ion-Implanted Tungsten–5 wt% Tantalum. *Physica Scripta*, 2011(T145):014076, 2011.

[164] D. E. J. Armstrong and T. B. Britton. Effect of Dislocation Density on Improved Radiation Hardening Resistance of Nano-Structured Tungsten–Rhenium. *Materials Science and Engineering: A*, 611:388–393, 2014.

[165] F. Hofmann, D. R. Mason, J. K. Eliason, A. A. Maznev, K. A. Nelson, and S. L. Dudarev. Non-Contact Measurement of Thermal Diffusivity in Ion-Implanted Nuclear Materials. *Scientific Reports*, 5:16042, 2015.

[166] ASTM Standard E521, "Standard Practice for Neutron Radiation Damage Simulation by Charged-Particle Irradiation". Standard, ASTM International, West Conshohocken, PA, USA, 2009.

[167] F. Liu, H. Ren, S. Peng, and K. Zhu. Effect of Crystal Orientation on Low Flux Helium and Hydrogen Ion Irradiation in Polycrystalline Tungsten. *Nuclear Instruments and Methods in Physics Research Section B: Beam Interactions with Materials and Atoms*, 333:120–123, 2014.

[168] M. Fujitsuka, B. Tsuchiya, I. Mutoh, T. Tanabe, and T. Shikama. Effect of Neutron Irradiation on Thermal Diffusivity of Tungsten–Rhenium Alloys. *Journal of Nuclear Materials*, 283:1148–1151, 2000.

[169] I. Smid, M. Akiba, G. Vieider, and L. Plöchl. Development of Tungsten Armor and Bonding to Copper for Plasma-Interactive Components. *Journal of Nuclear Materials*, 258:160–172, 1998.

[170] M. Roedig, W. Kuehnlein, J. Linke, D. Pitzer, M. Merola, E. Rigal, B. Schedler, and E. Visca. Post Irradiation Testing of Samples from the Irradiation Experiments PARIDE 3 and PARIDE 4. *Journal of Nuclear Materials*, 329:766–770, 2004.

[171] A. Reza, H. Yu, K. Mizohata, and F. Hofmann. Thermal Diffusivity Degradation and Point Defect Density in Self-Ion Implanted Tungsten. *Acta Materialia*, 2020.

[172] E. Lassner and W.-D. Schubert. *Properties, Chemistry, Technology of the Element, Alloys, and Chemical Compounds*. Plenum Publishers, New York, NY, USA, 1999. ISBN 0-306-45053-4.

[173] D.-G. Liu, L. Zheng, L.-M. Luo, X. Zan, J.-P. Song, Q. Xu, X.-Y. Zhu, and Y.-C. Wu. An Overview of Oxidation-Resistant Tungsten Alloys for Nuclear Fusion. *Journal of Alloys and Compounds*, 765: 299–312, 2018.

[174] A. Litnovsky, T. Wegener, F. Klein, Ch. Linsmeier, M. Rasinski, A. Kreter, X. Tan, J. Schmitz, J. W. Coenen, Y. Mao, J. Gonzalez-Julian, and M. Bram. New Oxidation-Resistant Tungsten Alloys for use in the Nuclear Fusion Reactors. *Physica Scripta*, 2017(T170): 014012, 2017.

[175] T. Wegener, F. Klein, A. Litnovsky, M. Rasinski, J. Brinkmann, F. Koch, and Ch. Linsmeier. Development of Yttrium-Containing Self-Passivating Tungsten Alloys for Future Fusion Power Plants. *Nuclear Materials and Energy*, 9:394–398, 2016.

[176] F. Koch, J. Brinkmann, S. Lindig, T. P. Mishra, and Ch. Linsmeier. Oxidation Behaviour of Silicon-Free Tungsten Alloys for use as the First Wall Material. *Physica Scripta*, 2011(T145):014019, 2011.

[177] W. L. Phillips Jr. The Rate of Oxidation of Rhenium at Elevated Temperatures in Air. *Journal of the Less Common Metals*, 5(2):97–100, 1963.

[178] *Acute Exposure Guideline Levels (AEGLs): Osmium Tetroxide.* CAS Reg. No. 20816-12-0. United States Environment Protection Agency, 2016. [online] https://www.epa.gov/aegl/osmium-tetroxide-results-aegl-program (accessed 26 August, 2020).

[179] A. Paul, J. G. P. Binner, B. Vaidhyanathan, A. C. J. Heaton, and P. M. Brown. Oxyacetylene Torch Testing and Microstructural Characterization of Tantalum Carbide. *Journal of Microscopy*, 250(2): 122–129, 2013.

[180] G. Smith. *Materials for Fusion, with Special Reference to the Spherical Tokamak Design.* Presented at Fusion Energy using Tokamaks: Can Development be Accelerated, Royal Society 26-27 March 2018, London, UK.

[181] A. Litnovsky, T. Wegener, F. Klein, Ch. Linsmeier, M. Rasinski, A. Kreter, X. Tan, J. Schmitz, Y. Mao, J. W. Coenen, M. Bram, and J. Gonzalez-Julian. Advanced Smart Tungsten Alloys for a Future Fusion Power Plant. *Plasma physics and controlled fusion*, 59(6): 064003, 2017.

[182] A. Litnovsky, J. Schmitz, F. Klein, K. De Lannoye, S. Weckauf, A. Kreter, M. Rasinski, J. W. Coenen, C. Linsmeier, J. Gonzalez-Julian, M. Bram, I. Povstugar, T. Morgan, D. Nguyen-Manh, M. Gilbert, D. Sobieraj, and J. S. Wróbel. Smart Tungsten-based Alloys for a First Wall of DEMO. *Fusion Engineering and Design*, 159:111742, 2020.

[183] F. Hofmann, D. Nguyen-Manh, M. R. Gilbert, C. E. Beck, J. K. Eliason, A. A. Maznev, W. Liu, D. E. J. Armstrong, K. A. Nelson, and S. L. Dudarev. Lattice Swelling and Modulus Change in a Helium-Implanted Tungsten Alloy: X-ray Micro-Diffraction, Surface Acoustic Wave Measurements, and Multiscale Modelling. *Acta Materialia*, 89: 352–363, 2015.

[184] J. Matějíček, V. Weinzettl, M. Vilémová, T. W. Morgan, G. De Temmerman, M. Dimitrova, J. Cavalier, J. Adámek, J. Seidl, and A. Jäger. ELM-Induced Arcing on Tungsten Fuzz in the COMPASS Divertor Region. *Journal of Nuclear Materials*, 492:204–212, 2017.

[185] A. M Ito, A. Takayama, Y. Oda, T. Tamura, R Kobayashi, T. Hattori, S. Ogata, N. Ohno, S. Kajita, M. Yajima, Y. Noiri, Y. Yoshimoto, S. Saito, S. Takamura, T. Murashima, M. Miyamoto, and H. Nakamura. Hybrid Simulation Research on Formation Mechanism of Tungsten Nanostructure induced by Helium Plasma Irradiation. *Journal of Nuclear Materials*, 463:109–115, 2015.

[186] G. M. Wright, D. Brunner, M. J. Baldwin, R. P. Doerner, B. Labombard, B. Lipschultz, J. L. Terry, and D. G. Whyte. Tungsten Nano-Tendril Growth in the Alcator C-Mod Divertor. *Nuclear Fusion*, 52 (4):042003, 2012.

[187] D. Nishijima, M. J. Baldwin, R. P. Doerner, and J. H. Yu. Sputtering Properties of Tungsten 'Fuzzy' Surfaces. *Journal of Nuclear Materials*, 415(1):S96–S99, 2011.

[188] R. G. Abernethy. Predicting the Performance of Tungsten in a Fusion Environment: A Literature Review. *Materials Science and Technology*, 33(4):388–399, 2017.

[189] X. Yi, L. Zhang, W. Han, J. Chen, P. Liu, Y. Lv, J. Song, L. Xue, D. Geng, K. Yoshida, T. Toyama, Q. Zhan, F. Wan, S. Ohnuki, and Y. Nagai. Defect Characterization, Mechanical and Thermal Property Evaluation in CVD-W after Low-Dose Neutron Irradiation. *International Journal of Refractory Metals and Hard Materials*, 85:105004, 2019.

[190] J. D. Murphy, A. Giannattasio, Z. Yao, C. J. D. Hetherington, P. D. Nellist, and S. G. Roberts. The Mechanical Properties of Tungsten Grown by Chemical Vapour Deposition. *Journal of Nuclear Materials*, 386:583–586, 2009.

[191] R. Neu, J. Riesch, J. W. Coenen, J. Brinkmann, A. Calvo, S. Elgeti, C. Garca-Rosales, H. Greuner, T. Hoeschen, G. Holzner, F. Klein, F. Koch, Ch. Linsmeier, A. Litnovsky, T. Wegener, S. Wurster, and J.-H. You. Advanced Tungsten Materials for Plasma-Facing Components of DEMO and Fusion Power Plants. *Fusion Engineering and Design*, 109:1046–1052, 2016.

[192] A. v. Müller, G. Schlick, R. Neu, C. Anstätt, T. Klimkait, J. Lee, B. Pascher, M. Schmitt, and C. Seidel. Additive Manufacturing of Pure Tungsten by means of Selective Laser Beam Melting with Substrate Preheating Temperatures up to 1000°C. *Nuclear Materials and Energy*, 19:184–188, 2019.

[193] M. K. Miller, K. F. Russell, and G. B. Thompson. Strategies for Fabricating Atom Probe Specimens with a Dual Beam FIB. *Ultramicroscopy*, 102(4):287–298, 2005.

[194] B. Gault, M. P. Moody, J. M. Cairney, and S. P. Ringer. *Atom Probe Microscopy*. Springer Series in Materials Science. Springer New York, 2012.

[195] A. J. London. Quantifying Uncertainty from Mass-Peak Overlaps in Atom Probe Microscopy. *Microscopy and Microanalysis*, 25(2):378–388, 2019.

[196] D. Haley, P. Choi, and D. Raabe. Guided Mass Spectrum Labelling in Atom Probe Tomography. *Ultramicroscopy*, 159:338–345, 2015.

[197] *AtomProbeLab: Matlab-based Analysis of Atom Probe Data*, 30/06/2016 (accessed 27 August, 2020). [online] https://sourceforge.net/projects/atomprobelab/.

[198] *APTTools: A Collection of Utilities for Atom Probe Tomography Analysis*, 30-06-2020 (accessed March, 2020). [online] https://sourceforge.net/projects/posgen.apttools.p/.

[199] M. Fukuda, T. Tanno, S. Nogami, and A. Hasegawa. Effects of Re Content and Fabrication Process on Microstructural Changes and Hardening in Neutron Irradiated Tungsten. *Materials Transactions*, 53(12):2145–2150, 2012.

[200] L. Uray and M. Menyhard. The Segregation of Iron in Tungsten. *Physica Status Solidi (A)*, 84(1):65–72, 1984.

[201] *LEAP 5000 : 3D Atom Probe Microscope*, (accessed 7 January, 2021). [online] https://www.cameca.com/.

[202] P. D. Edmondson, B. Gault, and M. R. Gilbert. An Atom Probe Tomography and Inventory Calculation Examination of Second Phase Precipitates in Neutron Irradiated Single Crystal Tungsten. *Nuclear Fusion*, 60(12):126013, 2020.

[203] K. Nordlund and F. Djurabekova. Multiscale Modelling of Irradiation in Nanostructures. *Journal of Computational Electronics*, 13(1):122–141, 2014.

[204] M. Nastar and F. Soisson. Atomistic Modeling of Phase Transformations: Point-Defect Concentrations and the Time-Scale Problem. *Physical Review B*, 86(22):220102, 2012.

[205] F. Soisson, A. Barbu, and G. Martin. Monte Carlo Simulations of Copper Precipitation in Dilute Iron-Copper Alloys during Thermal Ageing and under Electron Irradiation. *Acta Materialia*, 44(9):3789–3800, 1996.

[206] M. Levesque, E. Martínez, C.-C. Fu, M. Nastar, and F. Soisson. Simple Concentration-dependent Pair Interaction Model for Large-Scale Simulations of Fe-Cr Alloys. *Physical Review B*, 84(18):184205, 2011.

[207] S. Plimpton, C. Battaile, M. Chandross, L. Holm, A. Thompson, V. Tikare, G. Wagner, E. Webb, X. Zhou, C. G. Cardona, and A. Slepoy. Crossing the Mesoscale No-Man's Land via Parallel Kinetic Monte Carlo. *Sandia Report SAND2009-6226*, 2009.

[208] D. Frenkel and B. Smit. *Understanding Molecular Simulation: From Algorithms to Applications*. Elsevier Science, 2001. ISBN 9780080519982.

[209] R. Swendsen. *An Introduction to Statistical Mechanics and Thermodynamics: Second Edition*. Oxford Graduate Texts. Oxford University Press, 2020. ISBN 9780198853237.

[210] P. Warczok, J. Ženíšek, and E. Kozeschnik. Atomistic and Continuums Modeling of Cluster Migration and Coagulation in Precipitation Reactions. *Computational materials science*, 60:59–65, 2012.

[211] *scipy.optimize.curve_fit*, 2020 (accessed 23 September, 2020). [online] https://docs.scipy.org/doc/scipy/reference/generated/scipy.optimize.curve_fit.html.

[212] J. N. Mundy, S. J. Rothman, N. Q. Lam, H. A. Hoff, and L. J. Nowicki. Self-Diffusion in Tungsten. *Physical Review B*, 18(12):6566, 1978.

Appendices

A Huang Energy Model

Table A.1 shows a summary of the pair interaction coefficients, ε derived for the W-Re system. The subscripts A and B here refer to W and Re atoms respectively. The pair interactions are listed by the two components. a and b that give $\varepsilon = ax + b$, excluding $\varepsilon^{(1)}_{\text{B-V}}$ which has the form $\varepsilon = a/x + b$. Where $a = 0$ the pair interaction coefficient is not concentration dependent. For more information the reader is referred to the published works on this model [154].

Quantity	Description	$\varepsilon = ax + b$ a	b
$\varepsilon^{(1)}_{\text{A-A}}$	Cohesive Energy	0	-1.5815
$\varepsilon^{(2)}_{\text{A-A}}$	Cohesive Energy	0	-0.6672
$\varepsilon^{(1)}_{\text{B-B}}$	Cohesive Energy	0	-1.4067
$\varepsilon^{(2)}_{\text{B-B}}$	Cohesive Energy	0	-0.5935
$\varepsilon^{(1)}_{\text{A-B}}$	ΔH_{mix}	-0.0219	-1.5090
$\varepsilon^{(2)}_{\text{A-B}}$	ΔH_{mix}	-0.0092	-0.6366
$\varepsilon^{(1)}_{\text{A-V}}$	Formation Energy	0	-0.4898
$\varepsilon^{(2)}_{\text{A-V}}$	Formation Energy	0	-0.2067
$\varepsilon^{(1)}_{\text{B-V}}$	Formation Energy	-0.009432*	-0.4898
$\varepsilon^{(2)}_{\text{B-V}}$	Formation Energy	0.036	-0.3311
$\varepsilon^{(1)}_{\text{V-V}}$	Binding Energy	0	0.5873
$\varepsilon^{(2)}_{\text{V-V}}$	Binding Energy	0	0.5566
$\varepsilon^{(1)}_{\text{AA-A}}$	Formation Energy	0	0.1740
$\varepsilon^{(2)}_{\text{AA-A}}$	Formation Energy	0	0.0734
$\varepsilon^{(1)}_{\text{AB-A}}$	Formation Energy	0	0.1104
$\varepsilon^{(2)}_{\text{AB-A}}$	Formation Energy	0	0.0466
$\varepsilon^{(1)}_{\text{AA-B}}$	Binding Energy	0	-0.2750
$\varepsilon^{(2)}_{\text{AA-B}}$	Binding Energy	0	-0.1160
$\varepsilon^{(1)}_{\text{AB-B}}$	Binding Energy	0	-0.3486
$\varepsilon^{(2)}_{\text{AB-B}}$	Binding Energy	0	-0.1470
$\varepsilon^{(1)}_{\text{AA-AA}}$	Binding Energy	0	-0.1905
$\varepsilon^{(2)}_{\text{AA-AA}}$	Binding Energy	0	-0.0804
$\varepsilon^{(1)}_{\text{AB-AA}}$	Binding Energy	0	-0.2505
$\varepsilon^{(2)}_{\text{AB-AA}}$	Binding Energy	0	-0.1057
$\varepsilon^{(1)}_{\text{AB-AB}}$	Binding Energy	0	-1.3977
$\varepsilon^{(2)}_{\text{AB-AB}}$	Binding Energy	0	-0.5897

Table A.1: Pair interactions calculated by Huang et. al [154]. Interaction marked with * has the form $\varepsilon = a/x + b$.

B W-Re-Os-Vac Energy Model

Table B.1 summarised the pair interactions calculated for the W-Re-Os system in chapter 6. The subscripts A, B and C refer to W, Re and Os atoms respectively. Vacancy interactions are denoted V. The interactions are listed by the value of a, b, c and d as discussed in section 6.2.2 and 6.3. The value of these parameters are given by equations 6.16, 6.17, 6.18 and 6.19. Where interaction parameters were not calculated as part of this study, the corresponding publication is listed as the reference. Note that interaction coefficients are not yet calculated for interstitial defects with C atoms.

Quantity	Description	a	b	c	d	Reference
$\varepsilon^{(1)}_{\text{A-A}}$	Cohesive Energy	0	0	0	-1.5975	This Study
$\varepsilon^{(2)}_{\text{A-A}}$	Cohesive Energy	0	0	0	-0.6672	This Study
$\varepsilon^{(1)}_{\text{B-B}}$	Cohesive Energy	0	0	0	-1.4231	This Study
$\varepsilon^{(2)}_{\text{B-B}}$	Cohesive Energy	0	0	0	-0.6004	This Study
$\varepsilon^{(1)}_{\text{C-C}}$	Cohesive Energy	0	0	0	-1.4107	This Study
$\varepsilon^{(2)}_{\text{C-C}}$	Cohesive Energy	0	0	0	-0.5935	This Study
$\varepsilon^{(1)}_{\text{A-B}}$	ΔH_{mix}(W-Re)	0	0	-0.0112	-1.5266	This Study
$\varepsilon^{(2)}_{\text{A-B}}$	ΔH_{mix}(W-Re)	0	0	-0.0047	-0.6440	This Study
$\varepsilon^{(1)}_{\text{A-C}}$	ΔH_{mix}(W-Os)	0	0	-0.0662	-1.5221	This Study
$\varepsilon^{(2)}_{\text{A-C}}$	ΔH_{mix}(W-Os)	0	0	-0.0279	-0.6422	This Study
$\varepsilon^{(1)}_{\text{B-C}}$	ΔH_{mix}(Re-Os)	0	0	0.0007	-1.4359	This Study
$\varepsilon^{(2)}_{\text{B-C}}$	ΔH_{mix}(Re-Os)	0	0	0.0003	-0.6058	This Study
$\varepsilon^{(1)}_{\text{A-V}}$	ΔH_{mix}(W-Vac)	-0.0143	-0.9539	0.9255	-0.5472	This Study
$\varepsilon^{(2)}_{\text{A-V}}$	ΔH_{mix}(W-Vac)	-0.0060	-0.4024	0.3905	-0.2309	This Study
$\varepsilon^{(1)}_{\text{B-V}}$	ΔH_{mix}(Re-Vac)	2.0347	-4.2840	2.7552	-0.9242	This Study
$\varepsilon^{(2)}_{\text{B-V}}$	ΔH_{mix}(Re-Vac)	0.8584	-1.8073	1.1624	-0.3899	This Study
$\varepsilon^{(1)}_{\text{C-V}}$	ΔH_{mix}(Os-Vac)	0	-1.9183	2.6751	-1.3951	This Study
$\varepsilon^{(2)}_{\text{C-V}}$	ΔH_{mix}(Os-Vac)	0	-0.8093	1.1286	-0.5886	This Study
$\varepsilon^{(1)}_{\text{AA-A}}$	Formation Energy			0	0.1740	[154]
$\varepsilon^{(2)}_{\text{AA-A}}$	Formation Energy			0	0.0734	[154]
$\varepsilon^{(1)}_{\text{AB-A}}$	Formation Energy			0	0.1104	[154]
$\varepsilon^{(2)}_{\text{AB-A}}$	Formation Energy			0	0.0466	[154]
$\varepsilon^{(1)}_{\text{AA-B}}$	Binding Energy			0	-0.2750	[154]
$\varepsilon^{(2)}_{\text{AA-B}}$	Binding Energy			0	-0.1160	[154]
$\varepsilon^{(1)}_{\text{AB-B}}$	Binding Energy			0	-0.3486	[154]
$\varepsilon^{(2)}_{\text{AB-B}}$	Binding Energy			0	-0.1470	[154]
$\varepsilon^{(1)}_{\text{AA-AA}}$	Binding Energy			0	-0.1905	[154]
$\varepsilon^{(2)}_{\text{AA-AA}}$	Binding Energy			0	-0.0804	[154]
$\varepsilon^{(1)}_{\text{AB-AA}}$	Binding Energy			0	-0.2505	[154]
$\varepsilon^{(2)}_{\text{AB-AA}}$	Binding Energy			0	-0.1057	[154]
$\varepsilon^{(1)}_{\text{AB-AB}}$	Binding Energy			0	-1.3977	[154]
$\varepsilon^{(2)}_{\text{AB-AB}}$	Binding Energy			0	-0.5897	[154]

Table B.1: Pair interactions for the W-Re-Os system.

C FISPACT-II HFR Data

Tables C.2 and C.1 contain the output data for the FISPACT-II simulations for the neutron irradiated W material from HFR discussed in chapter 3. Table C.1 summarises the compositional information used to predict the post-irradiation composition of the samples and compare to experimental observation. For more information on the code used to calculate these results the reader is directed to [15].

Nuclide	Atoms	Grams	Dose Rate (Sv/hr)	Ingestion Dose (Sv)	Inhalation Dose (Sv)
H 1	8.31E+15	1.39E-08	0.00E+00	0.00E+00	0.00E+00
H 2	1.29E+14	4.32E-10	0.00E+00	0.00E+00	0.00E+00
H 3	7.62E+12	3.82E-11	0.00E+00	5.70E-07	3.53E-06
He 3	2.53E+12	1.27E-11	0.00E+00	0.00E+00	0.00E+00
He 4	4.82E+16	3.20E-07	0.00E+00	0.00E+00	0.00E+00
Yb172	3.86E+03	1.10E-18	0.00E+00	0.00E+00	0.00E+00
Yb173	9.51E+05	2.73E-16	0.00E+00	0.00E+00	0.00E+00
Yb174	1.45E+08	4.20E-14	0.00E+00	0.00E+00	0.00E+00
Yb176	3.22E+08	9.42E-14	0.00E+00	0.00E+00	0.00E+00
Lu174	5.14E+02	1.49E-19	5.88E-17	8.57E-16	1.33E-14
Lu175	3.52E+08	1.02E-13	0.00E+00	0.00E+00	0.00E+00
Lu176	3.97E+08	1.16E-13	5.55E-21	3.93E-19	1.53E-17
Lu177	4.29E+02	1.26E-19	4.50E-16	2.75E-13	6.22E-13
Lu177m	4.39E+04	1.29E-17	2.82E-14	3.74E-12	3.52E-11
Hf174	4.88E+03	1.41E-18	0.00E+00	4.13E-27	1.93E-26
Hf175	3.72E+00	1.08E-21	9.27E-18	1.75E-16	5.12E-16
Hf176	1.95E+13	5.70E-09	0.00E+00	0.00E+00	0.00E+00
Hf177	1.22E+14	3.59E-08	0.00E+00	0.00E+00	0.00E+00
Hf178	6.69E+14	1.98E-07	0.00E+00	0.00E+00	0.00E+00
Hf178m	3.10E+01	9.17E-21	4.22E-10	2.10E-13	4.25E-13
Hf178n	7.59E+09	2.24E-12	6.90E-10	2.53E-08	1.40E-06
Hf179	3.32E+16	9.88E-06	0.00E+00	0.00E+00	0.00E+00
Hf179n	1.02E+05	3.03E-17	2.22E-12	3.92E-11	1.24E-10
Hf180	5.02E+16	1.50E-05	0.00E+00	0.00E+00	0.00E+00
Hf181	1.35E+03	4.05E-19	1.35E-14	2.81E-13	1.28E-12
Hf182	4.56E+13	1.38E-08	8.21E-13	3.34E-10	3.45E-08
Ta179	3.14E+15	9.33E-07	5.30E-06	2.78E-03	2.40E-02
Ta180m	8.18E+14	2.44E-07	2.83E-19	8.38E-18	2.59E-16
Ta181	6.57E+20	1.97E-01	0.00E+00	0.00E+00	0.00E+00
Ta182	5.02E+13	1.52E-08	1.10E-03	5.27E-03	3.51E-02
W 180	>3.20E+21	9.57E-01	0.00E+00	0.00E+00	0.00E+00
W 181	1.15E+16	3.45E-06	1.20E-04	5.78E-02	2.05E-02
W 182	>8.32E+23	2.51E+02	0.00E+00	0.00E+00	0.00E+00
W 183	>4.91E+23	1.49E+02	0.00E+00	2.16E-09	3.43E-06
W 184	>1.01E+24	3.10E+02	0.00E+00	6.69E-09	1.78E-09
W 185	1.12E+14	3.43E-08	3.67E-09	5.24E-03	1.43E-03
W 186	>8.86E+23	2.73E+02	0.00E+00	3.63E-10	5.60E-07
W 188	1.47E+12	4.59E-10	9.80E-09	3.55E-04	9.63E-05
Re183	2.60E+04	7.89E-18	5.40E-15	2.26E-12	5.36E-12
Re184	1.18E+11	3.60E-11	4.63E-06	2.67E-05	5.08E-05
Re184m	5.91E+11	1.80E-10	1.43E-06	4.23E-05	1.83E-04
Re185	3.15E+21	9.68E-01	0.00E+00	0.00E+00	0.00E+00
Re186	3.44E+10	1.06E-11	1.73E-08	1.11E-04	8.10E-05
Re186m	6.70E+17	2.07E-04	1.84E-08	1.62E-04	8.84E-04
Re187	4.25E+22	1.32E+01	0.00E+00	1.09E-07	1.35E-07
Re188	1.51E+10	4.70E-12	1.13E-06	2.39E-04	9.22E-05
Os184	2.91E+10	8.88E-12	0.00E+00	3.19E-19	5.13E-16
Os185	1.16E+09	3.55E-13	1.25E-08	5.05E-08	1.58E-07
Os186	3.36E+20	1.04E-01	0.00E+00	1.03E-09	9.58E-10
Os187	3.98E+18	1.24E-03	0.00E+00	0.00E+00	0.00E+00
Os188	3.22E+21	1.01E+00	0.00E+00	0.00E+00	0.00E+00

Os189	6.39E+19	2.00E-02	0.00E+00	0.00E+00	0.00E+00
Os190	3.97E+18	1.25E-03	0.00E+00	0.00E+00	0.00E+00
Os192	5.32E+14	1.70E-07	0.00E+00	0.00E+00	0.00E+00
Os194	5.01E+08	1.61E-13	1.93E-14	4.41E-09	1.56E-07
Ir191	1.37E+16	4.36E-06	0.00E+00	0.00E+00	0.00E+00
Ir192	1.31E+08	4.17E-14	1.10E-09	1.99E-08	9.38E-08
Ir192n	8.14E+10	2.59E-11	7.76E-13	2.30E-09	2.89E-07
Ir193	5.76E+14	1.85E-07	0.00E+00	0.00E+00	0.00E+00
Ir194	1.84E+05	5.93E-17	2.30E-11	2.39E-09	1.03E-09
Pt190	3.33E+03	1.05E-18	0.00E+00	9.22E-25	2.59E-23
Pt192	1.40E+15	4.45E-07	0.00E+00	0.00E+00	0.00E+00
Pt193	5.34E+11	1.71E-10	3.86E-11	7.27E-09	4.93E-09
Pt194	3.06E+13	9.85E-09	0.00E+00	0.00E+00	0.00E+00
Pt195	1.87E+11	6.06E-11	0.00E+00	0.00E+00	0.00E+00
Pt196	2.82E+09	9.18E-13	0.00E+00	0.00E+00	0.00E+00
Pt198	1.49E+03	4.91E-19	0.00E+00	0.00E+00	0.00E+00
Au197	8.01E+05	2.62E-16	0.00E+00	0.00E+00	0.00E+00
Hg198	1.84E+04	6.05E-18	0.00E+00	0.00E+00	0.00E+00
Hg199	9.45E+03	3.12E-18	0.00E+00	0.00E+00	0.00E+00
Hg200	8.76E+02	2.91E-19	0.00E+00	0.00E+00	0.00E+00
Hg201	2.42E+00	8.08E-22	0.00E+00	0.00E+00	0.00E+00

Table C.1: Compositional information predicted by FISPACT-II for the HFR samples.

Nuclide	Activity (Bq)	B-Energy (kW)	A-Energy (kW)	G-Energy (kW)	Half Life (seconds)
H 1	0.00E+00	0.00E+00	0.00E+00	0.00E+00	Stable
H 2	0.00E+00	0.00E+00	0.00E+00	0.00E+00	Stable
H 3	1.36E+04	1.24E-14	0.00E+00	0.00E+00	3.89E+08
He 3	0.00E+00	0.00E+00	0.00E+00	0.00E+00	Stable
He 4	0.00E+00	0.00E+00	0.00E+00	0.00E+00	Stable
Yb172	0.00E+00	0.00E+00	0.00E+00	0.00E+00	Stable
Yb173	0.00E+00	0.00E+00	0.00E+00	0.00E+00	Stable
Yb174	0.00E+00	0.00E+00	0.00E+00	0.00E+00	Stable
Yb176	0.00E+00	0.00E+00	0.00E+00	0.00E+00	Stable
Lu174	3.17E-06	2.28E-23	0.00E+00	5.93E-23	1.12E+08
Lu175	0.00E+00	0.00E+00	0.00E+00	0.00E+00	Stable
Lu176	2.18E-10	1.04E-26	0.00E+00	1.68E-26	1.26E+18
Lu177	5.18E-04	1.22E-20	0.00E+00	2.78E-21	5.74E+05
Lu177m	2.20E-03	2.89E-20	0.00E+00	5.91E-20	1.39E+07
Hf174	5.36E-20	0.00E+00	2.15E-35	0.00E+00	6.31E+22
Hf175	4.26E-07	3.11E-24	0.00E+00	2.48E-23	6.05E+06
Hf176	0.00E+00	0.00E+00	0.00E+00	0.00E+00	Stable
Hf177	0.00E+00	0.00E+00	0.00E+00	0.00E+00	Stable
Hf178	0.00E+00	0.00E+00	0.00E+00	0.00E+00	Stable
Hf178m	5.38E+00	1.22E-16	0.00E+00	8.67E-16	4.00E+00
Hf178n	5.38E+00	6.35E-17	0.00E+00	1.05E-15	9.78E+08
Hf179	0.00E+00	0.00E+00	0.00E+00	0.00E+00	Stable
Hf179n	3.26E-02	9.74E-19	0.00E+00	4.81E-18	2.17E+06
Hf180	0.00E+00	0.00E+00	0.00E+00	0.00E+00	Stable
Hf181	2.55E-04	8.36E-21	0.00E+00	2.17E-20	3.66E+06
Hf182	1.11E-01	5.73E-19	0.00E+00	4.26E-18	2.84E+14
Ta179	4.28E+07	5.07E-11	0.00E+00	2.01E-10	5.08E+07
Ta180m	9.98E-09	2.01E-25	0.00E+00	8.99E-25	5.68E+22
Ta181	0.00E+00	0.00E+00	0.00E+00	0.00E+00	Stable
Ta182	3.51E+06	1.22E-10	0.00E+00	7.22E-10	9.91E+06
W 180	0.00E+00	0.00E+00	0.00E+00	0.00E+00	Stable
W 181	7.61E+08	1.55E-09	0.00E+00	5.02E-09	1.05E+07
W 182	0.00E+00	0.00E+00	0.00E+00	0.00E+00	Stable
W 183	9.80E-02	0.00E+00	1.86E-17	0.00E+00	3.47E+24
W 184	5.57E-02	0.00E+00	1.48E-17	0.00E+00	1.26E+25
W 185	1.19E+07	2.42E-10	0.00E+00	9.58E-14	6.49E+06
W 186	3.30E-02	1.29E-18	2.97E-18	0.00E+00	1.86E+25
W 188	1.69E+05	2.70E-12	0.00E+00	5.18E-14	6.03E+06

Re183	2.98E-03	5.19E-20	0.00E+00	7.70E-20	6.05E+06
Re184	2.67E+04	2.34E-13	0.00E+00	3.88E-12	3.06E+06
Re184m	2.82E+04	6.35E-13	0.00E+00	1.76E-12	1.45E+07
Re185	0.00E+00	0.00E+00	0.00E+00	0.00E+00	Stable
Re186	7.37E+04	3.98E-12	0.00E+00	2.47E-13	3.24E+05
Re186m	7.37E+04	8.05E-13	0.00E+00	7.08E-13	6.30E+12
Re187	2.15E+04	2.27E-15	0.00E+00	0.00E+00	1.37E+18
Re188	1.71E+05	2.13E-11	0.00E+00	1.58E-12	6.11E+04
Os184	1.14E-11	1.33E-27	2.71E-27	0.00E+00	1.77E+21
Os185	9.89E+01	2.91E-16	0.00E+00	1.14E-14	8.10E+06
Os186	3.69E-03	0.00E+00	1.67E-18	0.00E+00	6.31E+22
Os187	0.00E+00	0.00E+00	0.00E+00	0.00E+00	Stable
Os188	0.00E+00	0.00E+00	0.00E+00	0.00E+00	Stable
Os189	0.00E+00	0.00E+00	0.00E+00	0.00E+00	Stable
Os190	0.00E+00	0.00E+00	0.00E+00	0.00E+00	Stable
Os192	0.00E+00	0.00E+00	0.00E+00	0.00E+00	Stable
Os194	1.84E+00	9.51E-18	0.00E+00	6.77E-19	1.89E+08
Ir191	0.00E+00	0.00E+00	0.00E+00	0.00E+00	Stable
Ir192	1.42E+01	4.95E-16	0.00E+00	1.86E-15	6.38E+06
Ir192n	7.42E+00	1.96E-16	0.00E+00	3.67E-18	7.61E+09
Ir193	0.00E+00	0.00E+00	0.00E+00	0.00E+00	Stable
Ir194	1.84E+00	2.39E-16	0.00E+00	2.68E-17	6.95E+04
Pt190	1.12E-16	0.00E+00	5.85E-32	0.00E+00	2.05E+19
Pt192	0.00E+00	0.00E+00	0.00E+00	0.00E+00	Stable
Pt193	2.35E+02	2.95E-16	0.00E+00	1.27E-15	1.58E+09
Pt194	0.00E+00	0.00E+00	0.00E+00	0.00E+00	Stable
Pt195	0.00E+00	0.00E+00	0.00E+00	0.00E+00	Stable
Pt196	0.00E+00	0.00E+00	0.00E+00	0.00E+00	Stable
Pt198	0.00E+00	0.00E+00	0.00E+00	0.00E+00	Stable
Au197	0.00E+00	0.00E+00	0.00E+00	0.00E+00	Stable
Hg198	0.00E+00	0.00E+00	0.00E+00	0.00E+00	Stable
Hg199	0.00E+00	0.00E+00	0.00E+00	0.00E+00	Stable
Hg200	0.00E+00	0.00E+00	0.00E+00	0.00E+00	Stable
Hg201	0.00E+00	0.00E+00	0.00E+00	0.00E+00	Stable

Table C.2: Activity information per nuclide from FISPACT-II after 5 years cooling.

D APT Experimental Data

Figure	Data Files
3.6/3.7	R83_06792.RHIT
3.6/3.7	R83_06738.RHIT
3.6/3.7	R83_06743.RHIT
3.6/3.7	R83_06797.RHIT
3.6/3.7	R83_06749.RHIT
3.6/3.7	R83_06740.RHIT
3.6/3.7	R83_06792.RHIT
3.8/3.9	R83_07222.RHIT
3.6/3.7	R83_07220.RHIT
3.6/3.7	R5083_07444.HITS
3.6/3.7	R5083_07447.HITS
3.6/3.7	R5083_07456.HITS
3.10	R83_06743.RHIT
3.11	R83_07220.RHIT
3.13	R83_06797.RHIT
3.14	R83_06797.RHIT
3.15	R5083_07453.HITS
3.18	R83_06749.RHIT
3.19	R83_06740.RHIT
3.20	R83_06740.RHIT
3.22	R83_06743.RHIT
4.5	R83_05849.RHIT
4.7	R83_07149.RHIT
4.8	R5083_09804.HITS
4.8	R14_18507.RHIT
4.9	R5083_09804.HITS
4.9	R5083_09660.HITS
4.10	R83_07144.RHIT
4.13	R83_06093.RHIT
4.13	R5083_09170.HITS
4.16	R83_06093.RHIT
4.16	R5083_10230.HITS
4.16	R5083_09984.HITS
4.16	R5083_09804.HITS
4.16	R83_06797.RHIT
4.17	R83_06797.RHIT
4.17	R83_06093.RHIT

Table D.1: List of figures with corresponding APT data file

E ACI Alloy Samples

E.1 Chemical Analysis of Pure-W

Element	Composition (wt.%)	Element	Composition (wt.%)
Ag	Not Detected	O	0.005
Al	0.0025	Os	Not Detected
As	Not Detected	P	Not Detected
Au	Not Detected	Pb	Not Detected
B	Not Detected	Pd	Not Detected
Ba	Not Detected	Pr	Not Detected
Be	Not Detected	Pt	Not Detected
Bi	Not Detected	Re	Not Detected
Br	Not Detected	Rh	Not Detected
C	0.005	Ru	Not Detected
Ca	Not Detected	S	Not Detected
Cd	Not Detected	Sb	Not Detected
Ce	Not Detected	Sc	Not Detected
Cl	Not Detected	Se	Not Detected
Co	Not Detected	Si	0.004
Cr	0.002	Sm	Not Detected
Cu	0.001	Sn	Not Detected
Dy	Not Detected	Sr	Not Detected
Er	Not Detected	Ta	Not Detected
Eu	Not Detected	Tb	Not Detected
F	Not Detected	Te	Not Detected
Fe	0.003	Ti	Not Detected
Ga	Not Detected	Tl	Not Detected
Gd	Not Detected	Tm	Not Detected
Ge	Not Detected	V	Not Detected
H	Not Detected	W	99.9
Hf	Not Detected	Y	Not Detected
Hg	Not Detected	Yb	Not Detected
Ho	Not Detected	Zn	Not Detected
I	Not Detected	Zr	Not Detected
In	Not Detected		
Ir	Not Detected		
K	0.002		
La	Not Detected		
Li	Not Detected		
Lu	Not Detected		
Mg	Not Detected		
Mn	Not Detected		
Mo	0.005		
N	Not Detected		
Na	0.002		
Nb	Not Detected		
Nd	Not Detected		
Ni	0.003		

Table E.1: Chemical analysis of nominally pure W sample performed by ACI alloys following sample manufacture.

E.2 Chemical Analysis of W-1.4Re-0.1Os

Element	Composition (wt.%)	Element	Composition (wt.%)
Ag	Not Detected	O	Not Detected
Al	Not Detected	Os	0.1033
As	Not Detected	P	Not Detected
Au	Not Detected	Pb	Not Detected
B	Not Detected	Pd	Not Detected
Ba	Not Detected	Pr	Not Detected
Be	Not Detected	Pt	Not Detected
Bi	Not Detected	Re	1.4161
Br	Not Detected	Rh	Not Detected
C	Not Detected	Ru	Not Detected
Ca	0.0005	S	0.0012
Cd	Not Detected	Sb	Not Detected
Ce	Not Detected	Sc	Not Detected
Cl	Not Detected	Se	Not Detected
Co	0.0002	Si	Not Detected
Cr	0.0084	Sm	Not Detected
Cu	Not Detected	Sn	Not Detected
Dy	Not Detected	Sr	Not Detected
Er	Not Detected	Ta	0.0005
Eu	Not Detected	Tb	Not Detected
F	Not Detected	Te	Not Detected
Fe	0.0096	Ti	0.0002
Ga	Not Detected	Tl	Not Detected
Gd	Not Detected	Tm	Not Detected
Ge	Not Detected	V	0.0002
H	Not Detected	W	98.3809
Hf	Not Detected	Y	Not Detected
Hg	Not Detected	Yb	Not Detected
Ho	Not Detected	Zn	Not Detected
I	Not Detected	Zr	Not Detected
In	Not Detected		
Ir	Not Detected		
K	Not Detected		
La	Not Detected		
Li	Not Detected		
Lu	Not Detected		
Mg	Not Detected		
Mn	Not Detected		
Mo	0.0075		
N	Not Detected		
Na	0.0008		
Nb	Not Detected		
Nd	Not Detected		
Ni	0.0014		

Table E.2: Chemical analysis of nominal W-1.4Re-0.1Os sample performed by ACI alloys following sample manufacture.